Search for baryon and lepton number violating decays $D \to p\ell$ in Belle and calculation of slow-pion relative tracking efficiency using $B^0 \to D^*\pi$ decays in Belle II

Thesis submitted to the
Indian Institute of Technology Bhubaneswar
For award of the degree

Doctor of Philosophy

by

Souvik Maity
(Registration no. S16PH09004)

under the guidance of

Dr. Seema Bahinipati

School of Basic Sciences
Indian Institute of Technology Bhubaneswar

APPROVAL OF THE VIVA-VOCE BOARD

Date:

Certified that the thesis entitled **Search for baryon and lepton number violating decays $D \to p\ell$ in Belle and calculation of slow-pion relative tracking efficiency using $B^0 \to D^*\pi$ decays in Belle II**, submitted by **Souvik Maity** to the Indian Institute of Technology Bhubaneswar, for the award of the degree of Doctor of Philosophy has been accepted by the external examiners and that the student has successfully defended the thesis in the viva-voce examination held today.

(Member of DSC) (Member of DSC) (Member of DSC)

(Supervisor)

(External Examiner) (Chairman)

CERTIFICATE

This is to certify that the thesis entitled "**Search for baryon and lepton number violating decays $D \to p\ell$ in Belle and calculation of slow-pion relative tracking efficiency using $B^0 \to D^*\pi$ decays in Belle II**" submitted by **Souvik Maity** to Indian Institute of Technology, Bhubaneswar, is a record of bona fide research work under my supervision and I consider it worthy of consideration for the award of the degree of Doctor of Philosophy of the Institute.

Dr. Seema Bahinipati
Associate Professor
Indian Institute of Technology Bhubaneswar, India

Declaration of Authorship

I, Souvik Maity, declare that this thesis titled, "Search for baryon and lepton number violating decays $D \to p\ell$ in Belle and calculation of slow-pion relative tracking efficiency using $B^0 \to D^*\pi$ decays in Belle II" and the work presented in it are my own. I confirm that:

- This work was done wholly or mainly while in candidature for a research degree at this University.
- Where any part of this thesis has previously been submitted for a degree or any other qualification at this University or any other institution, this has been clearly stated.
- Where I have consulted the published work of others, this is always clearly attributed.
- Where I have quoted from the work of others, the source is always given. With the exception of such quotations, this thesis is entirely my own work.
- I have acknowledged all main sources of help.
- Where the thesis is based on work done by myself jointly with others, I have made clear exactly what was done by others and what I have contributed myself.

Signed: ____

Date: ____

Acknowledgments

First and foremost, I would like to praise and thank God, the Almighty, who has granted countless blessings, knowledge, and opportunity to me, so that I have been finally able to accomplish the thesis.

Apart from the efforts of me, the success of this thesis depends largely on the encouragement and guidelines of many others. I take this opportunity to express my gratitude to the people who have been instrumental in the successful completion of this thesis.

I extend my deepest gratitude to my advisor, Dr. Seema Bahinipati, whose guidance, support, and insightful feedback have been invaluable throughout this research journey. Your expertise and encouragement have shaped this thesis and my growth as a researcher.

I had a great opportunity to work closely with Dr. Vishal Bhardwaj at IISER Mohali and his evaluation of my research, constructive comments, constant encouragement, and suggestions have helped me to improve this study.

I would like to thank the members of my dissertation committee, Dr. Chandrasekhar Bhamidipati, Dr. Tarakant Nayak, Dr. Kishor Kumar Sahu, and Dr. Rajan Jha, Head of the School of Basic Sciences for their constructive feedback and valuable suggestions that enhanced the quality of this work.

I also acknowledge support from IIT Bhubaneswar, SERB DST, CICS, and KEK(Japan) for the financial, necessary resources and infrastructure essential for the successful completion of this research. I would like to express my sincere thanks to our internal reviewers, Prof. Prell, Soeren A, Dr. Hwanbae Park, and Dr. Dmytro Levit Andrea for giving their time and knowledge in the completion of this analysis during review time.

I formally wish to thank Prof. G. Mohanty, Yoshi Sakai-san, Mikihiko Nakao-san, Alan Schwartz, Bruce Yabsley, Leo Piilonen, Youngjoon Kwon, and Takanori Hara-San for their valuable suggestions.

I would like to express my gratitude towards all the Belle India group members who encouraged and supported me during my Ph.D. career and also for organizing BAW (Belle Analysis Workshop). This gave me an opportunity to interact with the Belle members across the globe which allowed me to understand various aspects of theoretical and experimental particle physics.

I am grateful to my colleagues and fellow researchers (Rajesh, Soumen, Dr. Renu, Dr. Sourav, Dr. Manish, Samarendra, Risabh, and Varsha) who have provided support and camaraderie throughout the ups and downs of this doctoral journey. Your shared insights and discussions have contributed significantly to the development of my ideas.

Heartfelt appreciation goes to my family for their unwavering support, love, and understanding. Your encouragement sustained me during challenging times, and I am deeply thankful for your belief in my abilities.

Lastly, this thesis stands as a testament to the collective support and encouragement I have received. I am truly fortunate to have had such a supportive network, and I look forward to contributing to the academic community in the future.

Souvik Maity

Abstract

The Belle detector is a sophisticated particle physics apparatus designed for experiments at the High Energy Accelerator Research Organization (KEK) in Japan. It played a pivotal role in the exploration of fundamental particles and their interactions. The detector was a key component of the Belle experiment, which aimed Charge-conjugation-Parity (CP) violation asymmetry of the decays of B and D mesons. It featured state-of-the-art technologies such as a highly segmented electromagnetic calorimeter, a precise tracking system, and a powerful magnet of producing magnetic field of 1.5 T. The integrated luminosity collected by the Belle detector more than 1000 fb^{-1} (1 ab^{-1}) from 1999 to 2010.

The Belle II detector is a second generation B-factory particle physics experiment located at the SuperKEKB accelerator facility in Tsukuba, Japan. The design luminosity of the machine is 6×10^{35} cm^{-2}s^{-1} and the Belle II experiment aims to record 50 ab^{-1} of data, a factor of 50 more than its predecessor. The Belle II experiment possesses unique capabilities to search directly for dark-matter particles in the MeV to GeV range and to explore for indirect events in heavy quark and τ physics, which are sensitive to greater energy than direct searches. Belle II, with its high accuracy and advanced technology, is poised to make a major contribution to our understanding of the fundamental forces of the universe by illuminating some of the most deep problems in particle physics.

We search for the baryon and lepton number violating charm decays, $D \to p\ell$, where D is either a D^0 or a $\overline{D}^0$ and ℓ is a muon or an electron, using a data sample of 921 fb^{-1} collected by the Belle detector at the KEKB asymmetric energy e^+e^- collider at center of mass energy $\sqrt{s} \approx 10.58$ GeV. The branching fraction is determined with respect to the well measured cabibbo favored decay $D^0 \to K^-\pi^+$. Branching fraction for the $\mathcal{B}(D \to p\ell)$ is calculated as:

$$\mathcal{B}(D \to p\ell) = \frac{N_{p\ell}}{N_{K\pi}}.\frac{L_{K\pi}}{L_{p\ell}}.\frac{\epsilon_{K\pi}}{\epsilon_{p\ell}}.\mathcal{B}(D^0 \to K^-\pi^+) \tag{1}$$

where $N_{p\ell}$ and $N_{K\pi}$ are the number of D^0 mesons for the signal modes and control mode respectively. $L_{K\pi}$ and $L_{p\ell}$ are the integrated luminosities of the MC analysed for the control mode and signal modes respectively. $\epsilon_{p\ell}$ and $\epsilon_{K\pi}$ are the efficiencies of signal mode and control mode, respectively. The branching fraction for the D^0 decay into kaon and pion is $\mathcal{B}(D^0 \to K^-\pi^+) = (3.946 \pm 0.030) \times 10^{-2}$.

In the absence of significant signals, we set upper limits on the branching fractions in the range $(5 - 8) \times 10^{-7}$ at a 90% confidence level, depending on the decay mode. The obtained upper limits are the most stringent to date. The limits on the $D \to p\mu$ modes are the first such results.

We study $B^0 \to D^{*-}\pi^+$ and $B^0 \to D^{*-}\rho^+$ decay modes to calculate the slow-pion relative tracking efficiency, where the D^{*-} further goes to $\overline{D^0}$ and π^-. Owing to its limited phase space, the pion from D^* decay is traditionally referred to as the slow pion due to a small mass difference between the D^* and $\overline{D^0}$. We have considered two sets of different final states for $\overline{D}^0$. In the first case , $\overline{D}^0$ decays into the following three clean channels: $K^+\pi^-$, $K_s^0\pi^+\pi^-$, and $K^+\pi^-\pi^-\pi^+$ and in second case, it decays to $K^+\pi^-$, $K^+\pi^-\pi^0$, and $K^+\pi^-\pi^-\pi^+$, respectively. We report herein a measurement of efficiency in the momentum region of 50–320 MeV/c using $B^0 \to D^{*-}\pi^+$ and $B^0 \to D^{*-}\rho^+$ decay modes.

Abstract

বেল ডিটেক্টর হল জাপানের হাই এনার্জি অ্যাক্সিলারেটর রিসার্চ অর্গানাইজেশনে (KEK) পরীক্ষার জন্য ডিজাইন করা একটি পরিশীলিত কণা পদার্থবিদ্যার যন্ত্রপাতি। এটি মৌলিক কণা এবং তাদের মিথস্ক্রিয়াগুলির অনুসন্ধানে একটি গুরুত্বপূর্ণ ভূমিকা পালন করেছে। আবিষ্কারকটি বেল পরীক্ষার একটি মূল উপাদান ছিল, যার লক্ষ্য ছিল চার্জ-সংযোজন-প্যারিটি (CP) লঙ্ঘন B এবং D মেসনের ক্ষয়ের অসাম্য। এটিতে অত্যাধুনিক প্রযুক্তি যেমন একটি উচ্চ বিভাজিত ইলেক্ট্রোম্যাগনেটিক ক্যালোরিমিটার, একটি সুনির্দিষ্ট ট্র্যাকিং সিস্টেম এবং 1.5 T এর চৌম্বক ক্ষেত্র তৈরির একটি শক্তিশালী চুম্বক বৈশিষ্ট্যযুক্ত। বেল ডিটেক্টর দ্বারা সংগৃহীত সমন্বিত আলোকসজ্জা 1000 fb^{-1} (1 ab^{-1}) থেকে 1999 থেকে 2010।

বেল II আবিষ্কারক হল একটি দ্বিতীয় প্রজন্মের বি-ফ্যাক্টরি কণা পদার্থবিদ্যা পরীক্ষা যা জাপানের সুকুবাতে সুপারকেকেবি এক্সিলারেটর সুবিধায় অবস্থিত। মেশিনের ডিজাইনের উজ্জ্বলতা হল 6×10^{35} সেমি$^{-2}$$s^{-1}$ এবং বেল II পরীক্ষার লক্ষ্য 50 ab^{-1} ডেটা রেকর্ড করা, যা এর পূর্বসূরীর থেকে 50 বেশি একটি ফ্যাক্টর। বেল II পরীক্ষাটি MeV থেকে GeV পরিসরে ডার্ক-ম্যাটার কণাগুলির জন্য সরাসরি অনুসন্ধান করার এবং ভারী কোয়ার্ক এবং τ পদার্থবিদ্যায় পরোক্ষ ঘটনাগুলির জন্য অন্বেষণ করার অনন্য ক্ষমতার অধিকারী, যা সরাসরি অনুসন্ধানের চেয়ে বেশি শক্তির প্রতি সংবেদনশীল। বেল II, এর উচ্চ নির্ভুলতা এবং উন্নত প্রযুক্তি সহ, কণা পদার্থবিদ্যার সবচেয়ে গভীর কিছু সমস্যাকে আলোকিত করে মহাবিশ্বের মৌলিক শক্তি সম্পর্কে আমাদের বোঝার ক্ষেত্রে একটি বড় অবদান রাখতে প্রস্তুত।

আমরা বেল ডিটেক্টর দ্বারা সংগৃহীত 921 fb^{-1} এর ডেটা নমুনা ব্যবহার করে, $D \to pl(e,\mu)$, যেখানে D হল D^0 বা একটি anti-D এবং l একটি muon বা একটি ইলেকট্রন, লঙ্ঘনকারী ব্যারিয়ন এবং লেপটন নম্বরের জন্য অনুসন্ধান করি ভর শক্তি $\sqrt{s} \approx 10.58$ GeV কেন্দ্রে KEKB অপ্রতিসম শক্তি e^+e^- কোলাইডার। শাখা ভগ্নাংশ সম্মান সঙ্গে নির্ধারিত হয় ভালোভাবে পরিমাপ করা ক্যাবিবোর পক্ষপাতী ক্ষয় $D^0 \to K^-\pi^+$।

উল্লেখযোগ্য সংকেতের অনুপস্থিতিতে, আমরা ক্ষয় মোডের উপর নির্ভর করে 90% আত্মবিশ্বাসের স্তরে $(5 - 8) \times 10^{-7}$ রেঞ্জের শাখা ভগ্নাংশের উপরের সীমা নির্ধারণ করি। প্রাপ্ত উপরের সীমাগুলি এখন পর্যন্ত সবচেয়ে কঠোর। $D \to p\mu$ মোডের সীমাগুলি প্রথম এই ধরনের ফলাফল।

আমরা $B^0 \to D^{*-}\pi^+$ এবং $B^0 \to D^{*-}\rho^+$ ধীর-পায়ন আপেক্ষিক ট্র্যাকিং দক্ষতা গণনা করার জন্য ক্ষয় মোড অধ্যয়ন করি, যেখানে D^{*-} আরও D^0 এবং π^--তে যায়। এর সীমিত পর্যায়ে স্থানের কারণে, D^* এবং D^0 এর মধ্যে একটি ছোট ভরের পার্থক্যের কারণে D^* ক্ষয় থেকে পাওয়া পাইনকে ঐতিহ্যগতভাবে ধীর পাইন হিসাবে উল্লেখ করা হয়। আমরা দুটি সেট বিবেচনা করেছি D এর জন্য বিভিন্ন চূড়ান্ত অবস্থা। প্রথম ক্ষেত্রে, D নিম্নলিখিত তিনটি পরিষ্কার চ্যানেলে ক্ষয়প্রাপ্ত হয়: $K^+\pi^-$, $K_s\pi^+\pi^-$, এবং $K^+\pi^-\pi^-\pi^+$, এবং দ্বিতীয় ক্ষেত্রে, এটি $K^+\pi^-$, $K^+\pi^-\pi^0$, এবং $K^+\pi^-\pi^-\pi^+$ -এ ক্ষয় হয়, যথাক্রমে। আমরা এখানে $B^0 \to D^{*-}\pi^+$ এবং $B^0 \to D^{*-}\rho^+$ ক্ষয় মোড ব্যবহার করে 50-320 MeV/c ভরবেগ অঞ্চলে দক্ষতার পরিমাপের প্রতিবেদন করি।

List of Publications

Journal publications related to Ph.D. thesis

[1] *Search for the baryon and lepton number violating decays $D \to p\ell$*
S. Maity, R. Garg, S. Bahinipati, V. Bhardwaj *et al.* (The Belle Collaboration), **(Phys. Rev. D 109, L031101 – Published 5 February 2024)**, [arXiv:2310.07412].

[2] *The Design, Construction, Operation and Performance of the Belle II Silicon Vertex Detector* **Adamczyk, K.** *et al.* (The Belle II Collaboration), [JINST **17**, P11042 (2022)] [arXiv: 2201.09824].

[3] *Slow-Pion Relative Tracking Efficiency Studies at Belle II*
S. Maity, N. S. Ipsita, and S. Patra (The Belle II Collaboration), [**454**, Part of the Springer Proceedings in Physics book series (SPPHY,volume 277)].

List of other publication

[1] *Measurement of the Λ_c^+ Lifetime*
F. Abudinén *et al.* (The Belle II Collaboration), Phys. Rev. Lett. **130**, 071802 – Published 16 February 2023.

[2] *Determination of $|V_{cb}|$ using $\overline{B}^0 \to D^{*+}\ell^-\overline{\nu}_l$ decays with Belle II*
I. Adachi *et al.* (Belle II Collaboration), Phys. Rev. D **108**, 092013 – Published 29 November 2023.

[3] *Measurement of CP Violation in $B^0 \to K_S^0\pi^0$ Decays at Belle II*
I. Adachi *et al.* (Belle II Collaboration), Phys. Rev. Lett. **131**, 111803 – Published 14 September 2023.

[4] *Search for $B^+ \to K^+\nu\bar{\nu}$ Decays Using an Inclusive Tagging Method at Belle II*
F. Abudinén *et al.* (The Belle II Collaboration), Phys. Rev. Lett. **127**, 181802 – Published 27 October 2021.

Contents

Certification of Approval iii

Declaration of Authorship vii

Acknowledgments ix

Abstract xii

Abstract xv

List of Figures xxiii

List of Tables xxxi

Abbreviations xxxv

Symbols xxxvii

1 Introduction **1**
- 1.1 The Standard Model . . . 1
  - 1.1.1 Force Particles . . . 4
    - 1.1.1.1 Electromagnetic Interaction . . . 4
    - 1.1.1.2 Strong Interaction . . . 5
    - 1.1.1.3 The Weak Interaction . . . 6
  - 1.1.2 Symmetries and Conservation laws . . . 9
    - 1.1.2.1 Baryon Number Conservation . . . 9
    - 1.1.2.2 Lepton Number Conservation . . . 10
  - 1.1.3 Approximate conservation laws . . . 11
  - 1.1.4 Limitations of Standard Model . . . 15
  - 1.1.5 Leptoquarks . . . 18
  - 1.1.6 The D mesons . . . 19
  - 1.1.7 Branching Fraction and Upper Limits . . . 20
  - 1.1.8 Literature Survey . . . 21

2 Experimental setup and Analysis strategy of $D \to p\ell$ 25

2.1 The KEKB accelerator complex . . . 26

2.2 The Belle Detector . . . 32

2.2.1 Silicon Vertexing Detector (SVD) . . . 35

2.2.2 Central Drift Chamber (CDC) . . . 37

2.2.3 Aerogel Cerenkov Counter (ACC) and Time of Flight (TOF) detector . . . 40

2.2.4 Electromagnetic Calorimeter (ECL) . . . 44

2.2.5 Superconducting Magnet . . . 47

2.2.6 K_L^0 and Muon Detection System (KLM) . . . 48

2.2.7 Extreme Forward Calorimeter (EFL) . . . 49

2.3 Overview of the Analysis . . . 51

2.3.1 Data sample . . . 53

2.3.2 Analysis strategy . . . 53

2.3.3 **Preliminary selection criteria** . . . 54

2.3.4 **Signal MC study** . . . 55

2.4 **Generic MC study** . . . 59

2.4.1 **Optimisation** . . . 59

2.4.2 **Best Candidate Selection** . . . 67

2.4.3 **Efficiency determination** . . . 70

2.4.4 **Background Study** . . . 75

2.4.4.1 $D^0 \to pe^-$ . . . 77

2.4.4.2 $\bar{D}^0 \to pe^-$ . . . 78

2.4.4.3 $D^0 \to \bar{p}e^+$ . . . 79

2.4.4.4 $\bar{D}^0 \to \bar{p}e^+$ . . . 80

2.4.4.5 $D^0 \to p\mu^-$ . . . 81

2.4.4.6 $\bar{D}^0 \to p\mu^-$ . . . 82

2.4.4.7 $D^0 \to \bar{p}\mu^+$ . . . 83

2.4.4.8 $\bar{D}^0 \to \bar{p}\mu^+$ . . . 84

2.5 Fit Validation . . . 86

2.6 **Upper Limit Estimation** . . . 95

2.7 **Control mode $D^0 \to K^-\pi^+$study** . . . 97

2.8 **Data-MC comparison:** . . . 100

2.9 Systematic study . . . 103

2.9.1 Pion mis-identification . . . 103

2.9.2 Proton mis-identification . . . 103

2.9.3 Electron misidentification . . . 105

2.9.4 Muon misidentification . . . 105

2.9.5 PDF shape . . . 105

2.9.6 Tracking . . . 106

2.9.6.1 Total Systematics . . . 107

2.10 **Box Open** . . . 107

2.10.1 Systematics study . . . 113

2.11 **Conclusion** . . . 114

3 Calculation of relative slow pion tracking efficiency using $B^0 \to D^*\pi$ and $B^0 \to D^*\rho$ decays 115

3.1 The SuperKEKB experiment . . . 115
3.2 The Belle II Detector . . . 117
3.2.1 Pixel Detector . . . 118
3.2.2 Silicon Vertex Detector . . . 120
3.2.3 Central Drift Chamber (CDC) . . . 122
3.2.4 Particle Identification Detectors (PID) . . . 124
3.2.5 Electromagnetic Calorimeter (ECL) . . . 125
3.2.6 Solenoid . . . 127
3.2.7 K_L^0 and Muon Detector (KLM) . . . 127
3.3 Motivation for Low Momentum Tracking . . . 129
3.4 Study of slow-pion relative tracking efficiency using $B^0 \to D^*\pi$ and $B^0 \to D^*\rho$ decays . . . 130
3.4.1 Data and Monte Carlo Samples . . . 132
3.4.2 Results for $B^0 \to D^{*-}\pi^+$ decays (Clean Channel) . . . 132
3.4.2.1 Using $M_{\rm bc}$ Fitting Method . . . 135
3.4.2.2 Using ΔE Fitting Method . . . 138
3.4.3 Results for $B^0 \to D^{*-}\pi^+$ decays (π^0 added) . . . 143
3.4.3.1 Using $M_{\rm bc}$ Fitting Method . . . 144
3.4.3.2 Using ΔE Fitting Method . . . 148
3.4.4 Measured Branching Fraction . . . 152
3.4.5 **Systematic study** . . . 153
3.4.6 Conclusion . . . 155

4 $D \to p\ell$: Future Prospects at Belle II **157**

A Background details of the $D \to p\ell$ study **161**
A.1 Background details . . . 161
A.2 Background contribution from different samples . . . 164
A.3 Significance (Including Systematic) . . . 165

B Relative tracking efficiency for $B^0 \to D^{*-}\rho^+$ decay **167**
B.1 $B^0 \to D^{*-}\rho^+$ decay (Clean channels) . . . 168
B.2 $B^0 \to D^{*-}\rho^+$ mode (π^0 added) . . . 174
B.3 Systematic study . . . 178

Bibliography **181**

List of Figures

1.1 $uu\gamma$ and $ee\gamma$ interaction. 5
1.2 Gluon line, gluon-gluon interaction, and quark-gluon interactions are shown in diagrams. 6
1.3 Meson production caused by rapidly separating quarks. A similar mechanism forms baryon-antibaryon pairs. 7
1.4 The charged current interaction of quarks with the same coupling constant g. 8
1.5 Helicity of neutrino and antineutrino. 14
1.6 (a) and (c) are the Feynman diagram of the proton decay as described in $SU(5)$. Right-hand plots (b) and (d) are the possible decay diagrams of $D^0 \to \bar{p}e^+$. 24

2.1 The KEKB accelerator complex. 26
2.2 Event topology of a $B^0 \to J/\psi k^0_S$ event, with two displaced vertexes separated by a distance proportional to Δt. 27
2.3 Head-on collision due to crab crossing scheme despite having finite crossing angle. 29
2.4 Cross section (in nb) of various Υ resonances from e^+e^- collision. 29
2.5 Schematic of the Belle detector. 32
2.6 Detector configuration of SVD1. 35
2.7 Detector configuration of SVDII. 36
2.8 Comparison of the impact parameter resolutions in the directions of $r - \phi$ (left) and z (right) measured with cosmic ray data. 37
2.9 Overview of the CDC. 39
2.10 Measured dE/dx vs. momentum in collision data. 39
2.11 p_t resolution studied using cosmic rays. 40
2.12 Configuration of ACC and TOF system. 41
2.13 Pulse-height spectra in units of photoelectrons observed by ACC for electrons and kaons show a good agreement between data-MC. 42
2.14 Time resolution of the TOF for $e^+e^- \to \mu^+\mu^-$ events. 43
2.15 Distributions of hadron masses calculated from measured time-of-flight for particles with momenta less than 1.25 GeV/c. The histogram corresponds to MC distribution. 43
2.16 Momentum coverage of each detector used for K/π separation. 44
2.17 Kaon identification efficiency and pion fake rate as a function of momentum. 45
2.18 Configuration of the ECL. 45
2.19 Energy resolutions measured from $e^+e^- \to \gamma\gamma$ event samples for overall, barrel, forward-endcap, and backward-endcap. E and E_γ are measured and calculated γ energies, respectively. 47

2.20 The Belle Kaon and Muon detector. 49
2.21 Configuration of the EFC. 50
2.22 The above plots (a-d) are for M_{D^0} distributions and (e-h) are for ΔM distributions for all the electronic modes in simulated sample. 56
2.23 The above plots (a-d) are for M_{D^0} distributions and (e-h) are for ΔM distributions for all the muonic modes in simulated sample. 58
2.24 Two dimensional distribution between M_{D^0} [GeV/c^2] and ΔM [GeV/c^2] for the channel $D^0 \to pe^-$ is signal MC. 60
2.25 Distribution of variables in signal MC and generic MC of the decay $D^0 \to pe^-$ for the optimized variables (a)proton id w.r.t. kaon, (b)proton id w.r.t. pion, (c)electron id, (d)proton momentum, (e)electron momentum and (f)D^* momentum in center of mass frame. 61
2.26 Distribution of variables in signal MC and generic MC of the decay $D^0 \to p\mu^-$ for the optimized variables (a)proton id w.r.t. kaon, (b)proton id w.r.t. pion, (c)muon id, (d)proton momentum, (e)muon momentum and (f)D^* momentum in center of mass frame. 62
2.27 Figure of merit distribution of the decay $D^0 \to pe^-$ for the variables (a)proton id w.r.t. kaon, (b)proton id w.r.t. pion, (c)electron id, (d)proton momentum, (e)electron momentum, (f)D^* momentum in center of mass frame. 63
2.28 Figure of merit distribution of the decay $D^0 \to p\mu^-$ for the variables (a)proton id w.r.t. kaon, (b)proton id w.r.t. pion, (c)muon id, (d)proton momentum, (e)muon momentum and (f)D^* momentum in center of mass frame 64
2.29 Figure of merit distribution of the decay $D^0 \to \bar{p}e^+$ for the variables (a)anti-proton id w.r.t. kaon, (b)anti-proton id w.r.t. pion, (c)positron id, (d)anti-proton momentum, (e)positron momentum, (f)D^* momentum in center of mass frame 65
2.30 Figure of merit distribution of the decay $D^0 \to \bar{p}\mu^+$ for the variables (a)anti-proton id w.r.t. kaon, (b)anti-proton id w.r.t. pion, (c)anti-muon id, (d)anti-proton momentum, (e)anti-muon momentum and (f)D^* momentum in center of mass frame 66
2.31 Multiplicity of the decay modes (a) $D^0 \to pe^-$, (b) $\overline{D^0} \to pe^-$ (c) $D^0 \to \bar{p}e^+$ (d) $\overline{D^0} \to \bar{p}e^+$ (e) $D^0 \to p\mu^-$ (f) $\overline{D^0} \to p\mu^-$ (g) $D^0 \to \bar{p}\mu^+$ and (h) $\overline{D^0} \to \bar{p}\mu^+$. 68
2.32 Two dimensional fit between M_{D^0} and ΔM in signal MC (a),(b) $D^0 \to pe^-$, (c),(d) $\overline{D^0} \to pe^-$ (e),(f) $D^0 \to \bar{p}e^+$ and (g),(h) $\overline{D^0} \to \bar{p}e^+$. 73
2.33 Two dimensional fit between M_{D^0} and ΔM in signal MC (a)(b) $D^0 \to p\mu^-$ (c),(d) $\overline{D^0} \to p\mu^-$ (e),(f) $D^0 \to \bar{p}\mu^+$ and (g),(h) $\overline{D^0} \to \bar{p}\mu^+$. 74
2.34 Two dimensional distribution between M_{D^0}[GeV/c^2] and ΔM[GeV/c^2 of peaking component $\bar{D}^0 \to K^+e^-\overline{\nu_e}$ for the mode $\bar{D}^0 \to pe^-$ in generic MC. 76
2.35 Distribution of (a)M_{D^0}[GeV/c^2] and (b)ΔM[GeV/c^2] for the channel $D^0 \to pe^-$ after applying the optimised set of cuts. Bottom plots are for two-dimensional fit results between (c)M_{D^0}[GeV/c^2] and (d)ΔM[GeV/c^2] using 6×711 fb^{-1} of generic MC. The red color is the combinatorial background component both in M_{D^0} and ΔM in the fitted diagram. 77

2.36 Distribution of (a)M_{D^0}[GeV/c^2] and (b)ΔM[GeV/c^2] for the channel $\bar{D}^0 \to pe^-$ after applying the optimised set of cuts. The peaking component is shown in the red color in (b). The cyan component is the combinatorial background shown in all the diagrams. Bottom plots are for two-dimensional fit results between (c)M_{D^0}[GeV/c^2] and (d)ΔM[GeV/c^2] using 6×711 fb^{-1} of generic MC. 78

2.37 Distribution of (a)M_{D^0}[GeV/c^2] and (b)ΔM[GeV/c^2] for the channel $D^0 \to \bar{p}e^+$ after applying the optimised set of cuts. The peaking component is shown in the red color in (b). The cyan component is the combinatorial background shown in all the diagrams. Bottom plots are for two-dimensional fit results between (c)M_{D^0}[GeV/c^2] and (d)ΔM[GeV/c^2] using 6×711 fb^{-1} of generic MC. 79

2.38 Distribution of (a)M_{D^0}[GeV/c^2] and (b)ΔM[GeV/c^2] for the channel $\bar{D}^0 \to \bar{p}e^+$ after applying the optimised set of cuts. Bottom plots are for two-dimensional fit results between (c)M_{D^0}[GeV/c^2] and (d)ΔM[GeV/c^2] using 6×711 fb^{-1} of generic MC. The red color is the combinatorial background component both in M_{D^0} and ΔM in the fitted diagram. 80

2.39 Distribution of (a)M_{D^0}[GeV/c^2] and (b)ΔM[GeV/c^2] for the channel $D^0 \to p\mu^-$ after applying the optimised set of cuts. Bottom plots are for two-dimensional fit results between (c)M_{D^0}[GeV/c^2] and (d)ΔM[GeV/c^2] using 6×711 fb^{-1} of generic MC. The red color is the combinatorial background component both in M_{D^0} and ΔM in the fitted diagram. 81

2.40 Distribution of (a)M_{D^0}[GeV/c^2] and (b)ΔM[GeV/c^2] for the channel $\bar{D}^0 \to p\mu^-$ after applying the optimised set of cuts. The peaking component is shown in the red color in (b). The cyan component is the combinatorial background shown in all the diagrams. Bottom plots are for two-dimensional fit results between (c)M_{D^0}[GeV/c^2] and (d)ΔM[GeV/c^2] using 6×711 fb^{-1} of generic MC. 82

2.41 Distribution of (a)M_{D^0}[GeV/c^2] and (b)ΔM[GeV/c^2] for the channel $D^0 \to \bar{p}\mu^+$ after applying the optimised set of cuts. The peaking component is shown in the red color in (b). The cyan component is the combinatorial background shown in all the diagrams. Bottom plots are for two-dimensional fit results between (c)M_{D^0}[GeV/c^2] and (d)ΔM[GeV/c^2] using 6×711 fb^{-1} of generic MC. 83

2.42 Distribution of (a)M_{D^0}[GeV/c^2] and (b)ΔM[GeV/c^2] for the channel $\bar{D}^0 \to \bar{p}e^+$ after applying the optimised set of cuts. Bottom plots are for two-dimensional fit results between (c)M_{D^0}[GeV/c^2] and (d)ΔM[GeV/c^2] using 6×711 fb^{-1} of generic MC. The red color is the combinatorial background component both in M_{D^0} and ΔM in the fitted diagram. 84

2.43 Results of the Toy MC study for the decay $D^0 \to pe^-$: (a) extracted signal yield (b) pull distribution (c) input versus output signal yield fitted with first-order polynomial (d) input signal yield versus pull mean, the (blue) dashed line shows the behavior of pull means in ideal case. 87

2.44 Results of the Toy MC study for the decay $\overline{D^0} \to pe^-$: (a) extracted signal yield (b) pull distribution (c) input versus output signal yield fitted with first-order polynomial (d) input signal yield versus pull mean, the (blue) dashed line shows the behavior of pull means in ideal case. 88

2.45 Results of the Toy MC study for the decay $D^0 \to \bar{p}e^+$: (a) extracted signal yield (b) pull distribution (c) input versus output signal yield fitted with first-order polynomial (d) input signal yield versus pull mean, the (blue) dashed line shows the behavior of pull means in ideal case. 89
2.46 Results of the Toy MC study for the decay $\overline{D^0} \to \bar{p}e^+$: (a) extracted signal yield (b) pull distribution (c) input versus output signal yield fitted with first-order polynomial (d) input signal yield versus pull mean, the (blue) dashed line shows the behavior of pull means in an ideal case. 90
2.47 Results of the Toy MC study for the decay $D^0 \to p\mu^-$: (a) extracted signal yield (b) pull distribution (c) input versus output signal yield fitted with first-order polynomial (d) input signal yield versus pull mean, the (blue) dashed line shows the behavior of pull means in ideal case. 91
2.48 Results of the Toy MC study for the decay $\overline{D^0} \to p\mu^-$: (a) extracted signal yield (b) pull distribution (c) input versus output signal yield fitted with first-order polynomial (d) input signal yield versus pull mean, the (blue) dashed line shows the behavior of pull means in ideal case. 92
2.49 Results of the Toy MC study for the decay $D^0 \to \bar{p}\mu^+$: (a) extracted signal yield (b) pull distribution (c) input versus output signal yield fitted with first-order polynomial (d) input signal yield versus pull mean, the (blue) dashed line shows the behavior of pull means in ideal case. 93
2.50 Results of the Toy MC study for the decay $\overline{D^0} \to \bar{p}\mu^+$: (a) extracted signal yield (b) pull distribution (c) input versus output signal yield fitted with first-order polynomial (d) input signal yield versus pull mean, the (blue) dashed line shows the behavior of pull means in ideal case. 94
2.51 Upper limit on yield at 90% C.L. of the decay modes without (with) systematics (a) $D^0 \to pe^-$, (b) $\overline{D^0} \to pe^-$ (c) $D^0 \to \bar{p}e^+$ (d) $\overline{D^0} \to \bar{p}e^+$ (e) $D^0 \to p\mu^-$ (f) $\overline{D^0} \to p\mu^-$ (g) $D^0 \to \bar{p}\mu^+$ and (h) $\overline{D^0} \to \bar{p}\mu^+$. Cyan line gives the U.L. at 90% C.L. 96
2.52 Distribution of (a) M_{D^0}[GeV/c^2] and (b) ΔM[GeV/c^2] for the channel $D^0 \to K^-\pi^+$ after applying the optimised set of cuts. Green color is the signal, red is the peaking component in M_{D^0} and violet is the peaking component in ΔM and rest are combinatorial backgrounds. 98
2.53 Two dimensional fit between (a) M_{D^0}[GeV/c^2] and (b) ΔM[GeV/c^2] for the channel $D^0 \to K^-\pi^+$ after applying the optimised set of cuts in 921 fb^{-1} of generic MC. The green color is the signal in both the fitted diagrams and the cyan and red colors are the peaking and combinatorial backgrounds respectively in both the diagrams. 99
2.54 Two-dimensional fit between (a) M_{D^0}[GeV/c^2] and (b) ΔM[GeV/c^2] for the channel $D^0 \to K^-\pi^+$ to determine efficiency after applying the optimized set of cuts in one million signal MC events. 99
2.55 M_{D^0} and ΔM distributions without the signal region for the mode $D^0 \to pe^-$ in generic MC. 100
2.56 Data and MC comparison plots where left plots are for M_{D^0} in the side band of ΔM and right plots are for ΔM in the side band of M_{D^0} distributions for all the electronic modes. 101
2.57 Data and MC comparison plots where left plots are for M_{D^0} in side band of ΔM and right plots are for ΔM distributions in side band of M_{D^0} for all the muonic modes. 102

2.58 Two dimensional fit between (a) M_{D^0}[GeV/c^2] and (b) ΔM[GeV/c^2] for the channel $D^0 \to K^-\pi^+$ after applying the optimised set of cuts in 921 fb^{-1} of data. The green dotted curves show the fit function for the signal, the violate dashed curves show the fit function for the peaking background, and the red dashed curves show the combinatorial background of the fit functions in M_{D^0}. The green dotted curves show the fit function for the signal, the violate dashed curves show the fit function for the peaking background, and the cyan dashed curves show the combinatorial background of the fit functions in ΔM. 108

2.59 Two dimensional fit results between M_{D^0} and ΔM for the elelctronic modes using 921 fb^{-1} data. In Fig. 2.59 (A), (B), (G) and (H), the red dotted curves show the fit function for the combinatorial background, the green dashed curves show the fit function for the signal. In Fig. 2.59 (C), (D), (E) and (F), the red dotted curves show the fit function for the peaking background, the green dashed curves show the fit function for the signal and the cyan dotted curves show the fit function for the combinatorial background. The blue solid line represent the total fit function for all the plots. 109

2.60 Two dimensional fit results between M_{D^0} and ΔM for the muonic modes using 921 fb^{-1} data. In Fig. 2.60 (A), (B), (G) and (H), the red dotted curves show the fit function for the combinatorial background, the green dashed curves show the fit function for the signal. In Fig. 2.60 (C), (D), (E) and (F), the red dotted curves show the fit function for the peaking background, the green dashed curves show the fit function for the signal and the cyan dotted curves show the fit function for the combinatorial background. The blue solid line represent the total fit function for all the plots. 110

2.61 Upper limit on yield at 90% C.L. of the decay modes without(with) systematics (a)$D^0 \to pe^-$, (b)$\overline{D^0} \to pe^-$ (c)$D^0 \to \bar{p}e^+$ (d)$\overline{D^0} \to \bar{p}e^+$ (e)$D^0 \to p\mu^-$ (f)$\overline{D^0} \to p\mu^-$ (g)$D^0 \to \bar{p}\mu^+$ and (h)$\overline{D^0} \to \bar{p}\mu^+$. Cyan line gives the U.L. at 90% C.L. 111

3.1 Schematic diagram of the SuperKEKB collider with its high energy electron ring (HER, blue) and low energy positron ring (LER, red), as well as the added positron damping ring and the Belle II detector. The electron and positron beams collide at the interaction point in the Tsukuba straight section. 118

3.2 Layout of the Belle II detector. The inner part is called the vertex detector (PXD and SVD). The vertex detector is enclosed in the Central Drift Chamber (CDC). It is followed by a time of propagation detector (TOP) in the barrel region and a particle identification (PID) detector in the forward direction (to the right-hand side). The next layer is the Electromagnetic Calorimeter (ECL) and the outermost detector is called K_L^0 and muon detector (KLM). The interaction point (IP) is at the center. 119

3.3 (a) The schematic cross-sectional view of the VXD. The SVD is red, the PXD is light blue, and the IP beam pipe diamonds are pink circles. (b) The ladder numbering scheme of the SVD is sketched on the xy plane. Figure courtesy of the Belle II Collaboration. 121

3.4 Working principle of an SVD sensor. The n-side strips (blue rectangles at the top) are perpendicular to the p-side strips (red rectangles at the bottom). Adapted from [105]. 121
3.5 Wire configuration of Belle-II CDC and comparison with Belle CDC. . . . 124
3.6 Working principle of the ARICH (left) and TOP (right) detectors. 124
3.7 A schematic view and a picture of a crystal equipped with photodetectors. 127
3.8 The sketch of an RPC. Two highly resistive electrodes enclose a gas volume. High voltage is applied to the electrodes. 129
3.9 Depiction of the time development of the signal generation inside a RPC. a) A charged particle ionized the gas forming an avalanche. b) As the avalanche grows photons start to contribute to the avalanche. A streamer mode evolves. c) An avalanche hits the electrodes. d) The electric field on the electrodes is drastically decreased. 129
3.10 Distribution of π_s momentum for $B^0 \to D^{*-}\pi^+$ in generic MC events. Signal and background candidates are shown by the blue and red hatched histograms, respectively. 133
3.11 Distributions of $M_{\rm bc}$ (left) and ΔE (right) for $B^0 \to D^{*-}\pi^+$ in generic MC events. Correctly reconstructed events and backgrounds are shown by the green and red hatched histograms, respectively. 133
3.12 Distribution of $M_{\rm bc}$ for $B^0 \to D^{*-}\pi^+$ in Generic MC sample after the background investigation using the generator level information. 134
3.13 Top plots show the fitted distribution of $M_{\rm bc}$ for $B^0 \to D^{*-}\pi^+$ in generic MC [left] and data [right]. The PDF for the signal (background) component is shown by the blue (green) dotted curve. The total fit PDF is shown by the solid blue curve. The yellow part shows the peaking background contribution. The bottom plot shows the signal yields obtained from an $M_{\rm bc}$ fit in the bins of π_s momentum. The red error bar corresponds to data yields and the blue error bar corresponds to generic MC yields. 135
3.14 Fitted distribution of $M_{\rm bc}$ for $B^0 \to D^{*-}\pi^+$ in generic MC in slow pion momentum bins (a) Bin 1, (b) Bin 2, (c) Bin 3 and (d) Bin 4. The points with error bars and all color curves are the same as in Fig. 3.13. 136
3.15 Fitted distribution of $M_{\rm bc}$ for $B^0 \to D^{*-}\pi^+$ in data in π_s momentum bins (a) Bin 1, (b) Bin 2, (c) Bin 3, and (d) Bin 4. The points with error bars and all color curves are the same as in Fig. 3.13. 137
3.16 Slow pion relative tracking efficiency ratio of data to MC in bins of slow pion momentum in lab frame for $M_{\rm bc}$ for $B^0 \to D^{*-}\pi^+$. 138
3.17 Top plots show the fitted distribution of ΔE for $B^0 \to D^{*-}\pi^+$ in generic MC [left] and data [right]. The sum of the PDF for signal and background component is shown by the blue dotted curve. The yellow part shows the peaking background contribution. The bottom plot shows the signal yields obtained from an ΔE fit in the bins of π_s momentum. The red error bar corresponds to Data yields and the blue error bar corresponds to MC yield. 139
3.18 Fitted distribution of ΔE for $B^0 \to D^{*-}\pi^+$ in generic MC in slow pion momentum bins (a) Bin 1, (b) Bin 2, (c) Bin 3 and (d) Bin 4. The points with error bars and all color curves are the same as in Fig. 3.17. 140

3.19 Fitted distribution of ΔE for $B^0 \to D^{*-}\pi^+$ in data in π_s momentum bins (a) Bin 1, (b) Bin 2, (c) Bin 3, and (d) Bin 4. The points with error bars and all color curves are the same as in Fig. 3.17 . . . 141
3.20 Slow pion relative tracking efficiency ratio of data to MC in bins of slow pion momentum in lab frame for ΔE for $B^0 \to D^{*-}\pi^+$. . . . 142
3.21 Distributions of $M_{\rm bc}$ for $B^0 \to D^{*-}\pi^+$ in generic MC events. All and correctly reconstructed events are shown by the blue and red hatched histograms, respectively. . . . 143
3.22 Distribution of $M_{\rm bc}$ for $B^0 \to D^{*-}\pi^+$ in Generic MC sample after the background investigation using GenMC Tagging tool and isSignal. . . . 143
3.23 Top plots show the fitted distribution of $M_{\rm bc}$ for $B^0 \to D^{*-}\pi^+$ in both generic MC (left) and data (right). The PDF for the signal (background) component is shown by the blue (green) dotted curve. The yellow part shows peaking background contribution Total fit PDF is shown by the solid blue curve. The bottom plot shows the signal yields obtained from an $M_{\rm bc}$ fit in the bins of π_s momentum. . . . 145
3.24 Fitted distribution of $M_{\rm bc}$ for $B^0 \to D^{*-}\pi^+$ in generic MC in slow pion momentum bins (a) Bin 1, (b) Bin 2, (c) Bin 3 and (d) Bin 4. The points with error bars and all color curves are the same as in Fig. 3.23 . . . 146
3.25 Fitted distribution of $M_{\rm bc}$ for $B^0 \to D^{*-}\pi^+$ in data in π_s momentum bins (a) Bin 1, (b) Bin 2, (c) Bin 3, and (d) Bin 4. The points with error bars and all color curves are the same as in Fig. 3.23. . . . 147
3.26 Slow pion relative tracking efficiency ratio of data to MC in bins of slow pion momentum in lab frame for $M_{\rm bc}$ for $B^0 \to D^{*-}\pi^+$. . . . 147
3.27 Top plot shows the fitted distribution of ΔE for $B^0 \to D^{*-}\pi^+$ in generic MC (left) and data (right), respectively. The sum of the PDF for signal and background component is shown by the blue dotted curve. The total fit PDF is shown by the solid blue curve. The bottom plot shows the signal yields obtained from an ΔE fit in the bins of π_s momentum. The red error bar corresponds to Data yields and the blue error bar corresponds to Generic MC yield. . . . 148
3.28 Fitted distribution of ΔE for $B^0 \to D^{*-}\pi^+$ in generic MC in slow pion momentum bins (a) Bin 1, (b) Bin 2, (c) Bin 3 and (d) Bin 4. The points with error bars and all color curves are the same as in Fig. 3.27 . . . 149
3.29 Fitted distribution of ΔE for $B^0 \to D^{*-}\pi^+$ in data in π_s momentum bins (a) Bin 1, (b) Bin 2, (c) Bin 3, and (d) Bin 4. The points with error bars and all color curves are the same as in Fig. 3.27 . . . 150
3.30 Slow pion relative tracking efficiency ratio of data to MC in bins of slow pion momentum in lab frame for ΔE for $B^0 \to D^{*-}\pi^+$. . . . 151

A.1 The breakdown of backgrounds for each sample where left plots are for M_{D^0} and right plots are for ΔM distributions for all the electronic modes. 162
A.2 The breakdown of backgrounds for each sample where left plots are for M_{D^0} and right plots are for ΔM distributions for all the muonic modes. . 163
A.3 Distribution of M_{D^0} and ΔM after using pre-selection cuts in generic MC for all the electronic modes. . . . 164
A.4 Distribution of M_{D^0} and ΔM after using pre-selection cuts in generic MC for all the muonic modes. . . . 165

B.1 Distribution of π_s momentum for for $B^0 \to D^{*-}\rho^+$ in generic MC events. All (correctly reconstructed) candidates are shown in the blue (red) hatched histogram. . . . 168
B.2 Distributions of $|(cos\theta_{hl}|$, M_{bc} and R2 for $B^0 \to D^{*-}\rho^+$ in generic MC events. . . . 169
B.3 Distribution of $M_{\rm bc}$ for $B^0 \to D^{*-}\rho^+$ decay mode in Generic MC sample after the background investigation using generator level information. . . . 169
B.4 Top plots show the fitted distribution of $M_{\rm bc}$ for $B^0 \to D^{*-}\rho^+$ in both generic MC (left) and data (right). The fit PDFs for signal (background)components are shown in blue (green) dotted curves. The total fit PDF is shown in the solid blue curve. The bottom plot shows the signal yields obtained from an $M_{\rm bc}$ fit in the bins of π_s momentum. . . . 170
B.5 Fitted distribution of $M_{\rm bc}$ for $B^0 \to D^{*-}\rho^+$ in generic MC in slow pion momentum bins (a) Bin 1, (b) Bin 2, (c) Bin 3 and (d) Bin 4. The points with error bars and all color curves are the same as in Fig. B.4. . . . 171
B.6 Fitted distribution of $M_{\rm bc}$ for $B^0 \to D^{*-}\rho^+$ in data in slow pion momentum bins (a) Bin 1, (b) Bin 2, (c) Bin 3 and (d) Bin 4. . . . 172
B.7 Slow pion relative tracking efficiency ratio of data to MC in bins of slow pion momentum in lab frame for $M_{\rm bc}$ for $B^0 \to D^{*-}\rho^+$. . . . 173
B.8 Distributions of M_{bc} for $B^0 \to D^{*-}\rho^+$ in generic MC events. . . . 174
B.9 Distribution of $M_{\rm bc}$ for $B^0 \to D^{*-}\rho^+$ decay mode in Generic MC sample after the background investigation using generator level information. . . . 174
B.10 Top plots show the fitted distribution of $M_{\rm bc}$ for $B^0 \to D^{*-}\rho^+$ in both generic MC (left) and data (right). The fit PDFs for signal (background) components are shown in green (yellow) dotted curves. The total fit PDF is shown in the solid blue curve. The bottom plot shows the signal yields obtained from an $M_{\rm bc}$ fit in the bins of π_s momentum. . . . 175
B.11 Fitted distribution of $M_{\rm bc}$ for $B^0 \to D^{*-}\rho^+$ in generic MC in slow pion momentum bins (a) Bin 1, (b) Bin 2, (c) Bin 3 and (d) Bin 4. The points with error bars and all color curves are the same as in Fig. B.10. . . . 176
B.12 Fitted distribution of $M_{\rm bc}$ for $B^0 \to D^{*-}\rho^+$ in data in slow pion momentum bins (a) Bin 1, (b) Bin 2, (c) Bin 3 and (d) Bin 4. . . . 177
B.13 Slow pion relative tracking efficiency ratio of data to MC in bins of slow pion momentum in lab frame for $M_{\rm bc}$ for $B^0 \to D^{*-}\rho^+$. . . . 178

List of Tables

1.1 The quark and lepton families, their masses, and their charges Q. All are spin-$\frac{1}{2}$ fermions. The corresponding anti-particles have the same masses as the particles, but the opposite charges. 3
1.2 The fundamental forces and their strengths, ranges, and mediators. 3
1.3 Possible leptoquarks and their quantum numbers. 19
1.4 List of D meson properties. 20

2.1 Summary of the integrated luminosity in each resonance. 30
2.2 Main parameters of KEKB. 30
2.3 Properties measure by each sub-detector. 31
2.4 Performance of the detector and sub-systems. p and p_t in GeV/c, E in GeV. 34
2.5 Upper limits of branching fractions with a 90% confidence level for the combine decays of D^0 and $\overline{D^0}$ by CLEO. 52
2.6 Upper limits of branching fractions with a 90% confidence level for the decays of D^0 by BESIII. 52
2.7 Percentage of correctly reconstructed events for each decay mode. 57
2.8 Sets of final selection cuts for the decay $D^0 \to pe^-$ 67
2.9 Sets of final selection cuts for the decay $D^0 \to p\mu^-$ 67
2.10 Percentage of multiplicity and BCS efficiency for each decay mode. $\bar{\epsilon}_{BCS}$ is the BCS efficiency considering multiplicity=1. 69
2.11 Efficiency values for all the decay modes after two-dimensional fits between M_{D^0} and ΔM using signal MC. 70
2.12 Summary of the mean and widths of the PDFs from fit of M_{D^0} in the Fig. 2.32 and Fig. 2.33. `a2a` is the fraction of the core gaussian w.r.t. the second gaussian. 71
2.13 Summary of the mean and widths of the PDFs from the fit of ΔM in the Fig. 2.32 and Fig. 2.33. `a2a_dm1` is the fraction of the core gaussian w.r.t. the second gaussian. `a2a_dm` is the fraction for the addition of the first two gaussians with the third gaussian. `a2a_dm2` is the fraction for the addition of the first three gaussians with the fourth gaussian. 72
2.14 Summary of the background level for each mode in M_{D^0} distributions in signal enhanced region of ΔM. 85
2.15 Summary of the background level for each mode in ΔM distributions in signal enhanced region of M_{D^0}. 85
2.16 Summary of the yields and U.L. at 90% confidence level for each mode where MC is scaled to data luminosity. 95
2.17 Sets of final selection cuts for the decay $D^0 \to K^-\pi^+$ 97
2.18 Systematics uncertainty due to pion misidentification. 103

2.19 Systematics uncertainty due to proton misidentification. 104
2.20 Systematics uncertainty due to electron identification. 105
2.21 Systematics uncertainty due to muon identification. 105
2.22 Summary of systematic uncertainties(%) arising from PDF parameters for electronic modes. 105
2.23 Summary of systematic uncertainties(%) arising from PDF parameters for muonic modes. 106
2.24 Summary of systematic uncertainties (%) 107
2.25 Summary of the yields and U.L. at 90% confidence level for each mode in data. 112
2.26 Summary of systematic uncertainties (%) due to normalization mode $D^0 \to K^-\pi^+$ (Norm), proton (p) and lepton (ℓ) identification, PDF used for signal extraction, fit bias from toy study ('-' denotes negligible bias) and tracking for $D^0 \to p\ell$ decay modes. 113

3.1 Main parameters of the Belle CDC and the CDC upgrade for Belle II. Taken from [105]. 123
3.2 Percentage of background contributing in M_{bc} distribution for $B^0 \to D^{*-}\pi^+$ decays where SCF (self-cross feed events) and Fake D corresponds to the mis-reconstructed signal events and the background coming from the wrong D^* and D^0 respectively. 134
3.3 Yields in different bins of slow pion momentum in the generic MC sample for $B^0 \to D^{*-}\pi^+$ decays. 135
3.4 Signal yields in different bins of slow pion momentum in data for $B^0 \to D^{*-}\pi^+$ decays. 136
3.5 Summary of slow pion relative tracking efficiency data-MC ratio in bins of slow pion momentum for $B^0 \to D^{*-}\pi^+$. 138
3.6 Yields in different bins of slow pion momentum in the generic MC sample for $B^0 \to D^{*-}\pi^+$ decays. 140
3.7 Signal yields in different bins of slow pion momentum in data for $B^0 \to D^{*-}\pi^+$ decays. 140
3.8 Summary of slow pion relative tracking efficiency data-MC ratio in bins of slow pion momentum for $B^0 \to D^{*-}\pi^+$. 142
3.9 Percentage of background contributing in M_{bc} distribution for $B^0 \to D^{*-}\pi^+$ decays where SCF (self-cross feed events) and Fake D corresponds to the mis-reconstructed signal events and the background coming from the wrong D^* and D^0 respectively. 144
3.10 Yields in different bins of slow pion momentum in the generic MC sample for $B^0 \to D^{*-}\pi^+$ decays. 144
3.11 Signal yields in different bins of slow pion momentum in data for $B^0 \to D^{*-}\pi^+$ decays. 144
3.12 Summary of slow pion relative tracking efficiency data-MC ratio in bins of slow pion momentum for $B^0 \to D^{*-}\pi^+$. 146
3.13 Yields in different bins of slow pion momentum in the generic MC sample for $B^0 \to D^{*-}\pi^+$ decays. 149
3.14 Signal yields in different bins of slow pion momentum in data for $B^0 \to D^{*-}\pi^+$ decays. 149
3.15 Summary of slow pion relative tracking efficiency data-MC ratio in bins of slow pion momentum for $B^0 \to D^{*-}\pi^+$. 151

3.16 The Branching fraction ($\mathcal{B}$) of $B^0 \to D^{*-}\pi^+$ (K_s^0 added) decay modes from datasets and PDG [2020] . . . 152
3.17 The Branching fraction ($\mathcal{B}$) of $B^0 \to D^{*-}\pi^+$ (π^0 added) decay modes from datasets and PDG [2020] . . . 152
3.18 Total Systematic Uncertainty of $B^0 \to D^{*-}\pi^+$ (K_s^0 added) mode using $M_{\rm bc}$ fitting method . . . 153
3.19 Total Systematic Uncertainty of $B^0 \to D^{*-}\pi^+$ (K_s^0 added) mode using ΔE fitting method . . . 153
3.20 Total Systematic Uncertainty of $B^0 \to D^{*-}\pi^+$ (π^0 added) mode using $M_{\rm bc}$ fitting method . . . 154
3.21 Total Systematic Uncertainty of $B^0 \to D^{*-}\pi^+$ (π^0 added) mode using ΔE fitting method . . . 154

4.1 Summary of expected systematic uncertainties (%) on $D^0 \to p\ell$ decay modes in Belle-II. . . . 159

A.1 Summary of the background level for each mode in the whole region of M_{D^0} and ΔM. . . . 161

B.1 Percentage of background contributing in $M_{\rm bc}$ distribution for $B^0 \to D^{*-}\rho^+$ decays where SCF (self-cross feed events) and Fake D corresponds to the mis-reconstructed signal events and the background coming from the wrong D^* and D^0 respectively. . . . 170
B.2 Signal yields in different bins of slow pion momentum in the Generic MC sample for $B^0 \to D^{*-}\rho^+$ decays. . . . 171
B.3 Yields in different bins of slow pion momentum in data for $B^0 \to D^{*-}\rho^+$ decays . . . 171
B.4 Summary of slow pion relative tracking efficiency ratio of data to MC in bins of slow pion momentum in lab frame for $B^0 \to D^{*-}\rho^+$. . . . 173
B.5 Percentage of background contributing in $M_{\rm bc}$ distribution for $B^0 \to D^{*-}\rho^+$ decays where SCF (self-cross feed events) and Fake D corresponds to the mis-reconstructed signal events and the background coming from the wrong D^* and D^0 respectively. . . . 175
B.6 Signal yields in different bins of slow pion momentum in the generic MC sample for $B^0 \to D^{*-}\rho^+$ decays. . . . 176
B.7 Yields in different bins of slow pion momentum in data for $B^0 \to D^{*-}\rho^+$ decays . . . 177
B.8 Summary of slow pion relative tracking efficiency ratio of data to MC in bins of slow pion momentum in lab frame for $B^0 \to D^{*-}\rho^+$. . . . 178
B.9 Total Systematic Uncertainty of $B^0 \to D^*\rho$ (π^0 added) mode using $M_{\rm bc}$ fitting method. . . . 179
B.10 Total Systematic Uncertainty of $B^0 \to D^*\rho$ (k_s^0 added) mode using $M_{\rm bc}$ fitting method. . . . 179

Abbreviations

SM	**S**tandard **M**odel
BSM	**B**eyond **S**tandard **M**odel
BNV	**B**aryon **N**umber **V**iolation
LNV	**L**epton **N**umber **V**iolation
LFU	**L**epton **F**lavor **U**niversality
LFV	**L**epton **F**lavor **V**iolation
NP	**N**ew **P**hysics
U.L.	**U**pper **L**imit
BF	**B**ranching **F**raction
C	**C**harge symmetry
P	**P**arity symmetry
CP	**C**harge symmetry **P**arity symmetry
CF	**C**abibbo **F**avored
Eq.	**E**quation
PDG	**P**article **D**ata **G**roup
Ref.	**R**eferences
C.L.	**C**onfidence **L**evel

Symbols

u	Up quark	q	Quark
d	Down quark	μ	Muon
c	charm quark	τ	Tau
s	Strange quark	ν_e	Electron neutrino
b	Bottom quark	ν_μ	Muon neutrino
t	Top quark	ν_τ	Tau neutrino
e	Electron	γ	Photon
K	Kaon	D	D meson
π	pion	Z^0	Z boson
$\Upsilon(4\mathrm{S})$	$\Upsilon(4\mathrm{S})$ meson	$\mathrm{W}^\pm$	W boson
CM	Center of mass frame	Planck's constant	h
E_{beam}	beam energy in CM frame	Speed of Light	c
M_{bc}	Beam constrained mass	$\mathcal{B}$	Branching fraction
B	B meson	J/ψ	J/psi meson
p	Proton	π^0	Neutral pion
g	Coupling strength	θ_C	Cabibbo angle
L	Lepton number	a_μ	Muon magnetic moment

Dedicated to my parents

Chapter 1

Introduction

The Standard Model of physics is the theory of particles, fields and the fundamental forces that govern them. It tells us about how families of elementary particles group together to form larger composite particles, and how one particle can interact with another, and how particles respond to the fundamental forces of nature. It serves as the foundation for theoretical physics and has produced accurate predictions, like as the existence of the Higgs boson. Standard Model is as a family tree for particles whuch tells us how the atoms that make up our bodies are made of protons and neutrons, which in turn are made of elementary particles called quarks.

In this chapter we describe the fundamental constituents of matter, forces, symmetries, conservation laws and limitations of Standard Model.

1.1 The Standard Model

In fundamental research of elementary particle physics we are guided by the endeavor to find answers to the fundamental questions of the Universe: what are we made of? What are the basic building blocks of the universe from which we are all made? The theory that ties all of this together is the pinnacle of 350 years of scientific endeavor. It is, by any measure, the most successful scientific theory of all time—Standard Model. Standard Model (SM) of particle physics provides the most accurate description of nature at the subatomic level. It is the result of theories and discoveries developed and made since the 1930s. It is based on the quantum theory of fields. In the quantum field theory there is one field for each type of particle - be it matter particles or force particles. With precision experiments performed at previous and current colliders, SM has been established as a physics theory tested to the highest precision at the quantum level. With the discovery of the Higgs boson, we now have a consistent mathematical framework to describe physics all the way up to the Planck scale. The fundamental matter particles in the Standard Model are quarks and leptons. All are spin-half point-like fermions. Quarks are confined to hadrons only as they carry a color charge.

The second type of matter particles is leptons. These are also spin-$\frac{1}{2}$ fermions but unlike the quarks, they do not interact via strong interactions, because they do not carry a color charge. Like the quarks, there are three families of leptons. The lightest generation contains the electron e^- and its partner electron neutrino (ν_e). The second generation consists of the muon μ^- and its partner neutrino (ν_μ). The muon is similar to the electron with the same electric charge but is about 207 times heavier. Muons are highly penetrating. High energy muons created in the upper atmosphere are able to pass through the atmosphere and can be observed on the earth's surface. The muon lifetime is 2.2 μs after which it decays as

$$\mu^- \to e^- + \bar{\nu}_e + \nu_\mu$$

The third generation contains the tau τ^- and its neutrino ν_τ. The tau also has a '-e' electric charge and it is 3500 times heavier than the electron. It decays much more rapidly than other members of the lepton family with a lifetime of 2.9 $\times$ 10^{-13} s. It can decay to either an electron or a muon with an associated neutrino pair.

$$\tau^- \rightarrow e^- + \bar{\nu}_e + \nu_\tau$$

$$\tau^- \rightarrow \mu^- + \bar{\nu}_\mu + \nu_\tau$$

Since it has the highest mass in the lepton family, a wide range of decay options are available for τ. A brief summary of some of the most important properties of the six quarks and six leptons can be found in Table 1.1.

TABLE 1.1: The quark and lepton families, their masses, and their charges Q. All are spin-$\frac{1}{2}$ fermions. The corresponding anti-particles have the same masses as the particles, but the opposite charges.

	Quarks		Leptons	
Generations	Q $= -\frac{1}{3}$	Q $= -\frac{2}{3}$	Q=-1	Q=0
First	down (d) $\sim$ 5 MeV	up (u) $\sim$ 2.5 MeV	electron (e) $\sim$ 0.511 MeV	e neutrino (ν) $<$ 1 eV
Second	strange (s) $\sim$ 101 MeV	charm (c) $\sim$ 1270 MeV	muon (μ) $\sim$ 105.7 MeV	μ neutrino (ν_μ) $<$ 1 eV
Third	bottom (b) $\sim$ 4200 MeV	top (t) $\sim$ 172 GeV	tau (τ) $\sim$ 1777 MeV	τ neutrino (ν_τ) $<$ 1 eV

TABLE 1.2: The fundamental forces and their strengths, ranges, and mediators.

Fundamental Forces	Strength	Range (m)	Mediators
Strong	1	10^{-15}	gluons, π(nucleons)
Electromagnetic	$\frac{1}{137}$	Infinite	photon (γ)
Weak	10^{-6}	10^{-18}	$W^{\pm}$, Z^0
Gravity	6×10^{-39}	Infinite	graviton

1.1.1 Force Particles

There are four fundamental forces that act on the matter particles. They are electromagnetic, weak nuclear force, strong nuclear force, and gravitational force. The comparison between all forces is shown in Table 1.2.

The gravitational force is a special case. It is very familiar, but at the level of individual subatomic particles is so much weaker than the other forces that it has a negligible effect. This makes it difficult to study, and so the microscopic mechanism behind gravitation is yet to be fully understood. We will not discuss it further in the coming section. Each of the other three forces is known to be carried by an intermediate particle and they are known as mediators. They are all spin-1 particles and termed as bosons.

1.1.1.1 Electromagnetic Interaction

The quantum of the electromagnetic force is the photon, which is a massless boson with no electrical charge. It is through virtual photons that electromagnetic forces are transmitted between charges. The quantum theory of electromagnetism is known as quantum electrodynamics or QED. The electromagnetic interaction is felt by all charged particles. The vertex factor for a particle with charge quantum number Q is g_{EM} where $\frac{g_{EM}^2}{4\pi} = \alpha_{EM}$. For example, the u-quark has charge Q $= \frac{2}{3}$, so the coupling strength in the $uu\gamma$ vertex is only two-thirds as large as that in the $ee\gamma$ vertex, and of the opposite sign.

The electromagnetic interaction does not change the quark flavor or lepton flavor. Flavor-changing vertices such as:

$$\mu^- + \gamma \to e^-$$

$$u + \gamma \to c$$

FIGURE 1.1: $uu\gamma$ and $ee\gamma$ interaction.

are forbidden in electromagnetism due to lepton flavor violation and quark flavor violation respectively. Decays that do not require changes in flavor quantum numbers may proceed via the electromagnetic interaction, for example, the decay of the neutral pion to two photons

$$\pi^0 \to \gamma + \gamma$$

1.1.1.2 Strong Interaction

The strong interaction is very strong but very short-ranged as compared to the other three types. It is basically attractive but can be effectively repulsive in some circumstances. The quantum theory of the strong force is known as quantum chromodynamics or QCD. The strong force is mediated by spin-1, massless particles known as gluons. The gluons couple to color charge, rather like the photons couple to electromagnetic charge. Since the leptons have no color charge, they do not interact with gluons and hence do not interact via the strong force. Quarks carry color, r, g, and b. These are not actual colors rather they are quantum numbers. Anti-quarks carry anti-colour $\bar{r}$, $\bar{g}$ and $\bar{b}$. Each gluon carries both colour and anti-colour. So, it is expected to have 3 $\times$ 3 = 9 gluons but one of those 9 combination

$$\frac{1}{\sqrt{3}}(|r\bar{r}\rangle + |g\bar{g}\rangle + |b\bar{b}\rangle)$$

is colorless. The color charge is conserved at each vertex, with any change in the color of the quark being introduced or carried away by the gluon. The strong interaction has a larger coupling constant than the electromagnetic force. However, the strong force is more than just a stronger version of the electromagnetic interaction. Gluons (unlike photons) can act as sources for their own field.

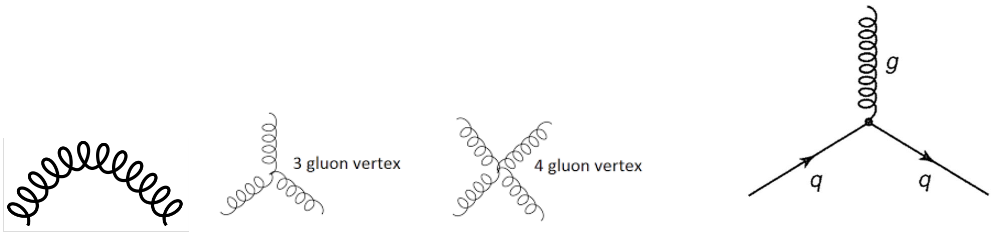

FIGURE 1.2: Gluon line, gluon-gluon interaction, and quark-gluon interactions are shown in diagrams.

This suggests that there is a gluon self-interaction force, involving a three or four-gluon interaction vertex. This makes a dramatic difference to the way the strong force works discussed below. The self-interactions of gluons help us better understand quark confinement. If one of the quarks in a given meson is pulled away from its neighbors, the color-force field "stretches" between that quark and its neighbors. In so doing, more and more energy is added to the color-force field as the quarks are pulled apart. At some point, it is energetically cheaper for the color-force field to "snap" into a new quark-antiquark pair. In doing so, energy is conserved because the energy of the color-force field is converted into the mass of the new quarks, and the color-force field can "relax" back to an unstretched state depicted in Fig. 1.3.

1.1.1.3 The Weak Interaction

The weak interaction is mediated by three particles, the charged $W^{\pm}$ bosons and the neutral Z^0 boson. The W^+ and W^- are antiparticles of one another, while the Z^0, like the photon, is its own antiparticle. The decay of β-emission is governed by weak interaction. Initially, such processes posed a serious puzzle: The observed emerging

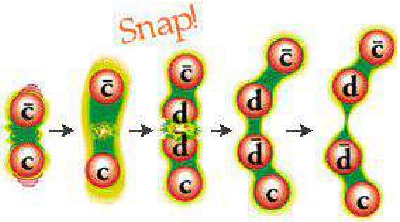

FIGURE 1.3: Meson production caused by rapidly separating quarks. A similar mechanism forms baryon-antibaryon pairs.

particles, electrons or positrons, did not come out with a definite energy equal to the mass difference between initial and final nuclei. Instead, they had an energy distribution with a maximal energy at the expected value. This led Niels Bohr to doubt that energy conservation could possibly be violated in quantum physics. But Wolfgang Pauli rescued it by suggesting the missing energy was carried off by a neutral particle, now called *neutrino*. Fig. 1.4 shows the possibilities of quark transition in families denoting their strength. In contrast, the diagram on the right-hand side shows the lepton families. For leptons, it is not possible to make a transition from one generation to another generation. If this were not the case, the K and λ particles would be completely stable (as it will hold good for some particles with b-quarks). Cabibbo[1] developed a theory when only three quarks were known namely u, d, and s. The theory states the charged current interaction of quarks proceeds with the same coupling constant g as for lepton interactions provided we associate a factor cosθ_C to $u \leftrightarrow d$ transitions and a factor sinθ_C to $u \leftrightarrow s$ transitions. But one problem still remain was $K_L^0 \rightarrow \mu^+\mu^-$ was predicted to go faster than measured experimentally. A solution to this paradox was given by GIM, Iliopoulos, and Miami (GIM). They introduced a fourth quark c into the theory with couplings cosθ_C for $c \leftrightarrow s$ transitions and -sinθ_C for $c \leftrightarrow d$ where θ_C is the Cabibbo angle and it was introduced to preserve the universality of the weak interaction. This produces a second Feynman diagram in the process $K_L \to \mu^+\mu^-$ which interferes destructively with the one involving only u, d, and s quarks and suppresses the decay as measured by the experiment. The main motivation of the GIM mechanism was to suppress weak interaction where flavor changes occur but not the quark charges change. So with four quarks, the GIM mechanism gives a nice conceptual picture of the weak interaction.

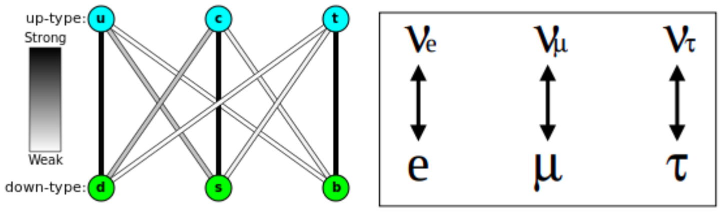

FIGURE 1.4: The charged current interaction of quarks with the same coupling constant g.

As shown in the above Fig. 1.4 , the scheme was extended to three quark generations with a 3×3 matrix, which was first proposed by Kobayashi and Maskawa known as CKM matrix[2].

$$\begin{pmatrix} d' \\ s' \\ b' \end{pmatrix} = \begin{pmatrix} V_{ud} & V_{us} & V_{ub} \\ V_{cd} & V_{cs} & V_{cb} \\ V_{td} & V_{ts} & V_{tb} \end{pmatrix} \times \begin{pmatrix} d \\ s \\ b \end{pmatrix}$$

In the weak interaction its the rotated states d',s' and b' which take part. The 3×3 matrix values[3] come from experiments and they are given as follows:

$$\begin{pmatrix} V_{ud} & V_{us} & V_{ub} \\ V_{cd} & V_{cs} & V_{cb} \\ V_{td} & V_{ts} & V_{tb} \end{pmatrix} = \begin{pmatrix} 0.97373 \pm 0.00031 & 0.2243 \pm 0.0008 & 0.00382 \pm 0.00020 \\ 0.221 \pm 0.004 & 0.975 \pm 0.006 & 0.0408 \pm 0.0014 \\ 0.0086 \pm 0.0002 & 0.0415 \pm 0.0009 & 1.014 \pm 0.029 \end{pmatrix}$$

The bottom row of the right-hand side is either close to zero or unity. Because the third generation does not interact much with the other two family members. This is why the decay of particles involving b-quarks is very slow. The top quark does not hadronize and the values are calculated assuming that the CKM matrix is unitary.

1.1.2 Symmetries and Conservation laws

We are already familiar with a number of conservation laws such as conservation of energy, momentum, charge, etc. These are known as exact conservation laws. These exact conservation laws control the occurrence of all the physical processes. In addition to that, certain other conservation laws hold good in the realm of particle physics to explain the non-occurrence of some processes even when they satisfy the well-known conservation laws. The discussion about the conservation laws is as follows.

1.1.2.1 Baryon Number Conservation

The baryon number denotes which particles are baryons and which particles are not. Each baryon has a baryon number of 1, and each antibaryon has a baryon number of -1. Other non-baryonic particles have a baryon number of 0. It is defined as

$$B = \frac{1}{3}(n_q - n_{\bar{q}}) \tag{1.1}$$

where n_q is the number of quarks, and $n_{\bar{q}}$ is the number of antiquarks. The baryon number is conserved in all the interactions of the Standard Model and it is an additive quantum number. The term conserved means that the sum of the baryon number of all incoming particles is the same as the sum of the baryon numbers of all particles resulting from the reaction. As per Sakharov conditions[4] a slight asymmetry in the laws of physics allowed baryons to be created in the Big Bang. The concepts of grand unified theory (GUT)[5] and supersymmetry[4] allow for the changing of a baryon into a lepton and an antiquark ($B - L$), thus violating the conservation of both baryon and lepton numbers. Thus proton decay[6] would be an example of such a process taking place, but has never been observed experimentally.

Conservation of baryon number prohibits a decay of the type

$$p + n \rightarrow p + \mu^+ + \mu^-$$

Protons and neutrons have B=1. On the right-hand side, we have only one proton. Leptons have a baryon number zero. So this decay is forbidden. With sufficient energy pair production in the reaction can occur:

$$p + n \rightarrow p + n + p + \bar{p}.$$

The fact that the decay

$$\pi^- \rightarrow \mu^- \bar{\nu}_\mu$$

is observed implies that there is no corresponding principle of conservation of meson number. The pion is a meson composed of a quark and an antiquark, and on the right side of the equation, there are only leptons. The baryon number assigned to a meson is always zero.

1.1.2.2 Lepton Number Conservation

Lepton number is a conserved quantum number representing the difference between the number of leptons and the number of antileptons in an elementary particle reaction. It is also an additive quantum number. Mathematically, the lepton number L is defined by

$$L = n_l - n_{\bar{l}}$$

where n_l and $n_{\bar{l}}$ are the number of leptons and antileptons. It was first introduced to explain the inverse beta decay

$$\bar{\nu} + p \rightarrow n + e^{+}$$

which conserves the lepton number, as the incoming antineutrino has lepton number -1, while the outgoing positron also has lepton number -1. The observation of the following two decay processes leads to the conclusion that there is a separate lepton number (L_μ) for muons which must also be conserved.

$$\pi^{-} \rightarrow \mu^{-} + \bar{\nu}_\mu$$

$$\mu^{-} \rightarrow e^{-} + \bar{\nu}_e + \nu_\mu$$

The same thing is also true for τ leptons, it has also a corresponding lepton number (L_τ).

1.1.3 Approximate conservation laws

These conservation laws are not obeyed by all the interactions, but these are useful in deciding the occurrence or otherwise of different types of reactions. These laws relate to the conservation of:
(a) Isospin, (b) Parity, (c) Strangeness, (d) Charge conjugation, and (e) Time-reversal.

Isospin: The concept of isospin arose from the idea that pairs of particles like nucleons and triplets like pions hardly differ in their mass and may be considered as isotopes and that their charges, differing from each other by unity, suggest space quantization similar to electron spin and orbit in a magnetic field. A multiplet number M is therefore assigned to such particles to indicate the number of their different charge states. For example, nucleons have M=2 (proton and neutron) and similarly M=3 for pions. We may relate isospin quantum number I with multiplicity M with the following relation,

$$M = 2I + 1$$

I is dimensionless and its z component (I_z or I_3) has allowed values

$$I, (I-1), (I-2), ..., -I$$

For nucleons, (M=2), I=(M-1)/2=$\frac{1}{2}$, with two components $I_3 = +\frac{1}{2}$ assigned to proton and I_3 = -$\frac{1}{2}$ assigned to neutron. Similarly for pion (M=3), I=(M-1)/2=1. Hence $I_3 = +1, 0, -1$; $I_3 = +1$ is assigned to π^+, $I_3 = 0$ to π^0 and $I_3 = -1$ is assigned to π^-. Isospin is conserved in strong interaction but violated in electromagnetic and weak interaction. The z-component of isospin, I_3 is conserved in strong and electromagnetic interactions, but not in weak interaction.

Hypercharge: The average charge $\bar{Q}$ of a particle in a multiplet group is the sum of the charge of each member in the group, divided by the multiplet number M

$$\bar{Q} = \sum Q_i/M \tag{1.2}$$

Therefore, the average charge $\bar{Q}$ on nucleon $= \frac{1}{2}(1+0) = \frac{1}{2}$. Charge quantum number is $Q = I_3 + \bar{Q}$. So, charge on proton, $Q = \frac{1}{2} + \frac{1}{2} = 1$ and that on a neutron $Q = -\frac{1}{2} + \frac{1}{2} = 0$. The quantum number called hypercharge, Y is defined as double of the average charge $\bar{Q}$ of the multiplet.

$$Y = 2\bar{Q} \tag{1.3}$$

The factor '2' ensures that hypercharge is always integral, instead of half-integral. In strong and electromagnetic interactions, the hypercharge is conserved. But it need not be conserved in the weak interaction.

Strangeness: Strangeness is another quantum number, first proposed by Pais and developed by Gell-Mann and Nishijima, to understand the strange behavior of K-mesons and hyperons (strange particles). Experimentally, it is found that K-meson and Λ, Σ, and Ω are produced by strong interaction. But they decay, contrary to expectation, only by weak interaction having a lifetime $\gg 10^{-23}$s. This inconsistency was resolved by the discovery of associated production - the strange particles being produced always in pairs.

Strangeness number S is defined by

$$S = Y - B \tag{1.4}$$

So we can write strangeness S in terms of baryon number (B) and isospin (I_3).

$$Q = I_3 + \frac{B+S}{2} \tag{1.5}$$

With this relation, the strangeness of a particle will be an integer.
For K^+ meson, $Q = +1$, $I_3 = +\frac{1}{2}$, $B = 0$, therefore, $S = +1$.
For Λ^0 and Σ^0 hyperons, $Q = 0$, $I_3 = 0$, $B = 0$, therefore $S = -1$. Strangeness is conserved in strong and electromagnetic interactions, but not in weak decay. For an weak interaction, S however can change but not more than ± 1 i.e.,

$$\Delta S = 0, \pm 1$$

This is not a conservation law rather it is called the selection rule.

Parity: Parity refers to an inherent property that has to do with the right-handedness and left-handedness of the particles. When particles like neutrinos are emitted during β-decay, they show a preferred spin direction. If the spin is in the direction in which a right-handed screw advances, it is said to possess a helicity +1; if the spin is in the direction of a left-handed screw, the helicity is -1 (Fig. 1.5).

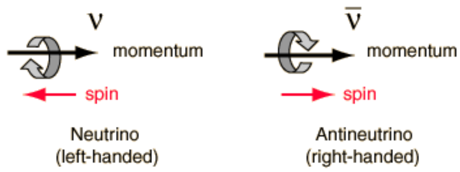

FIGURE 1.5: Helicity of neutrino and antineutrino.

As parity is related to the spin J, the two quantum numbers are generally combined and symbolized by J^p. So, $\frac{1}{2}^+$ means $J = \frac{1}{2}$ and $P = +1$ (even); $\frac{1}{2}^-$ means $J = \frac{1}{2}$ and $P = -1$ (odd).

In strong and electromagnetic interaction, parity is conserved but it is violated in weak interaction.

Charge conjugation: Charge conjugation means a reversal of the signs of all types of charge - electric, baryonic, and leptonic - of particles i.e. it converts a particle into its anti-particle and vice versa. If a physics law holding for a particle also holds for the corresponding antiparticle, then the principle of charge conjugation is said to be valid. Strong and electromagnetic interactions are invariant under charge conjugation operation. But weak interaction like β-decay violates charge conjugation.

Time reversal The operation T, i.e., time-reversal means replacing the time 't' by '$-t$' in all equations of motion, a reflection of the time axis at the origin of the time co-ordinate in a relativistic space-time continuum. It is thus, like parity a discrete change. It is also invariant under strong and electromagnetic interaction but in weak interaction, it is violated.

1.1.4 Limitations of Standard Model

The Standard Model agrees with all confirmed experimental data from accelerators but is theoretically very unsatisfactory. It is the most rigorous theory of particle physics, incredibly precise and accurate in its predictions. It mathematically lays out the 17 building blocks of nature: six quarks, six leptons, four force-carrier particles, and the Higgs boson. These are ruled by electromagnetic, weak, and strong forces. Despite its great predictive power, however, the Standard Model fails to answer a few crucial questions.

Why is there so much matter in the universe? Scientists suppose that when the universe was formed in the Big Bang, matter and antimatter should have been produced in equal parts. However, some mechanisms kept the matter and antimatter from their usual pattern of total destruction, and the universe around us is dominated by matter. In collider experiments also when a matter comes into being-usually its antimatter counterpart comes along with for the ride. When equal matter and antimatter particles meet, they annihilate one another. The Standard Model cannot explain the imbalance. The level of CP asymmetry is not sufficient to describe the observed matter anti-matter asymmetry present in the universe.

Why do neutrinos have mass? The Standard Model predicts that, like photons, neutrinos should have no mass. But experiments found that neutrinos also transform into one another, as they move. This is only possible if neutrinos have mass. Some experimental results also have suggested, for example, that there might be a fourth type of neutrino called a sterile neutrino that is yet to be discovered.

What is dark matter? The velocity of the outer star in a spiral galaxy is very high. To compensate it requires more mass than we observe. Something we can't see, which scientists have dubbed "dark matter," must be giving additional mass. Dark matter is thought to account for approximately 85% of the matter in the universe. But it is not included in the Standard Model. Our best model of particle physics explains only about

4% of the universe.

Why is the expansion of the universe accelerating? The latest measurements by the Hubble Space Telescope and the European Space Agency observatory Gaia [8] indicate that galaxies are moving away from us at 45 miles per second. This rate is believed to come from an unexplained property of space-time called dark energy, which is pushing the universe apart. Dark energy is thought to make up around 68% of the energy in the universe and is also not included in the standard model.

Gravity? It is not included in the Standard Model. This fourth and weakest force of nature does not seem to have any impact on the subatomic interactions. But theoretical physics suggests that a subatomic particle called a graviton might transmit gravity the same way particles called photons carry the electromagnetic force.

There are many more mysteries than the above ones for example lepton flavour violation (LFV) [9]. In the Standard Model, the electroweak gauge bosons Z and $W^{\pm}$ have identical couplings to all three lepton flavors. This means that branching fractions of decays involving different lepton families do not depend on lepton flavor but differ only by phase space and helicity-suppressed contributions. This is called lepton flavor universality (LFU) and is well tested in e.g. decays of tau leptons, light mesons, as well as gauge bosons. Any experimental evidence of Lepton Flavour Non-Universality would be a clear sign of physics beyond the SM (BSM). Semileptonic decays of heavy particles are an excellent sector to test for the LFU as all three generations can be accessed. Many models extending the SM contain additional interactions that could violate LFU. These are for example BSM theories involving leptoquarks [10] or Z' [11] particles. Processes with the third generation of quarks and leptons (B and tau) are well suited to search for LFU violation since many BSM theories with LFU violation predict stronger couplings to the third generation and experimental results have lower precision. Charged current decays $c \to c\ell\nu$ are precisely predicted in the SM. The strongest evidence for a possible violation of LFU is currently seen in the measurements of the branching fractions of semileptonic decays involving a tau lepton, in particular, the measurement of the observables

$$R(D) = \frac{\mathcal{B}(B^0 \to D^+ \tau^- \bar{\nu_\tau})}{\mathcal{B}(B^0 \to D^+ \mu^- \bar{\nu_\mu})} \quad (1.6)$$

$$R(D^*) = \frac{\mathcal{B}(B^0 \to D^{*+} \tau^- \bar{\nu_\tau})}{\mathcal{B}(B^0 \to D^{*+} \mu^- \bar{\nu_\mu})} \quad (1.7)$$

The result R(D*) = 0.336 ± 0.027(stat) ± 0.030(syst) [12] was the first measurement of b-hadron decays to tau leptons at a hadron collider and deviates by 2.1σ from the SM (0.252 ± 0.003) prediction [13–18]. This means that the searches for direct production of new particles at the LHC can probe a significant range of explanations for the LHCb anomalies. However, for many of the possibilities, the high-energy upgrade to the LHC or a future circular collider with much higher energy would be required for the new particles to be discovered or ruled out. A leptoquark model could explain R(D) and R(D*) anomalies. These models are based on modified versions of grand unified theories (GUTs). Since GUTs unify the leptons and quarks, some of the force carriers can change quarks to leptons and vice versa, i.e. some of the force carriers could be leptoquarks. While intriguing, the B-physics anomalies are by no means confirmed. None of the measurements have separately reached the five standard deviations needed to claim a discovery and, indeed, most are hovering around the 1–3σ mark. However, taken together, they form an interesting and consistent picture that something is potentially going on. We are in a position where new measurements are expected to be completed soon, some in a few months, others in a few years. First of all, the observables showing the discrepancy from the SM, R(D^*) will be measured more precisely at LHCb [19] [20] and at Belle II [21], which is currently ramping up at KEK in Japan. In addition, there are many related measurements that are planned. For instance, measuring the same transitions, but with different initial- and final-state hadrons, should give further insights into the structure of NP contributions. If the anomalies are confirmed, this would then set a clear target for the next collider such as the high-energy LHC [22] or the proposed proton–proton Future Circular Collider[23], since the new particles cannot be arbitrarily heavy. If the present flavor anomalies stand firm, they will become another important milestone on this historic list, offering a view of a new energy scale to explore.

1.1.5 Leptoquarks

Leptoquarks (LQ)[24] are hypothetical particles that would interact with quarks and leptons. Leptoquarks are color-triplet bosons that carry both lepton (L) and baryon numbers (B). Leptoquarks, if they exist, must be heavier than all the currently known elementary particles otherwise they would have already been discovered. Current experimental lower limits on LQ mass (depending on their type) are around 1 TeV/c^2. They have a very short lifetime and are not present in ordinary matter. However, they might be produced in high-energy particle collisions such as in particle colliders or from cosmic rays hitting Earth's atmosphere. The existence of pure leptoquarks would not spoil the baryon number conservation. However, some theories allow the leptoquark to also have a diquark interaction vertex. For example, a Q=2/3 charged leptoquark might also decay into two d-type antiquarks. The existence of such a leptoquark-diquark would cause protons to decay. The current limits on proton lifetime are strong probes of the existence of these leptoquark-diquarks. These fields emerge in Grand unification theories; for example, in the Georgi–Glashow SU(5) model[24], they are called X and Y bosons. Several kinds of leptoquarks, depending on their electric charge, can be considered. They are listed below in the Table 1.3[25] from this assumption [26]. Bounds on leptoquark states are obtained both directly and indirectly. Direct limits are from their production cross-sections at colliders, while indirect limits are calculated from bounds on leptoquark-induced four-fermion interactions, which are obtained from low-energy experiments, or from collider experiments below a threshold. These four-fermion interactions often cause lepton-flavor non-universalities in heavy quark decays as mentioned in the above section. Anomalies observed recently in the R_K and R_D ratios[27] in the semi-leptonic B decays may be explained in models with TeV scale leptoquarks. There are also new results reported by the Fermilab Muon $g-2$ experiment[28–30] on the anomalous magnetic moment[31–33] of the muon a_μ. The combined results with the one from the E821 experiment at BNL deviate from the standard model prediction by 4.2σ.

$$\Delta a_\mu = a_\mu^{exp} - a_\mu^{SM} = (251 \pm 59) \times 10^{-11} \tag{1.8}$$

There have been different proposals of theories beyond the standard model to explain the anomaly. These results R_K and $(g-2)_\mu$, which are naturally expected if new physics is around the multi-TeV scale, could help us to find a new direction for physics beyond the standard model. Moreover, the above-mentioned anomalies can be explained by the theory of minimal quark and lepton unification[34] which is based on leptoquarks.

TABLE 1.3: Possible leptoquarks and their quantum numbers.

Spin	$3B+L$	SU(3)$_c$	SU(2)$_W$	$U(1)_Y$
0	-2	$\bar{3}$	1	1/3
0	-2	$\bar{3}$	1	4/3
0	-2	$\bar{3}$	3	1/3
1	-2	$\bar{3}$	2	5/6
1	-2	$\bar{3}$	2	-1/6
0	0	3	2	7/6
0	0	3	2	1/6
1	0	3	1	2/3
1	0	3	1	5/3
1	0	3	3	2/3

1.1.6 The D mesons

D meson is the lightest meson which contains a charm quark, which is why it's a good example to study the quark transformation via weak interaction. The D mesons were discovered in 1976 by the Mark I detector [35] at the Stanford Linear Accelerator Center. There are many possible decay processes for the D meson because it has a lot of excess mass-energy. These all involve the weak interaction to change the charm quark, and the variety of W decays provides many paths for the process. It is confirmed with a significance of more than seven standard deviations, that the neutral D^0 meson spontaneously transforms into its own antiparticle and back [36]. A phenomenon that was first observed in B meson only and known as flavor oscillation. D mesons with strange quarks are an important probe for exploring quantum chromodynamics [37,38]. We can measure form factors taking V_{cx} from the CKM matrix and precisely test lattice QCD [39–41] in charm and extrapolate to beauty. Taking decay constant and form factor [42–44] from QCD prediction we can verify the unitarity of the CKM matrix. Various uncommon decay paths of the D mesons are sensitive to physics processes outside the standard model. Measuring these rare branching fractions can help the search for new particles. Details of D meson properties are shown in Table 1.4.

TABLE 1.4: List of D meson properties.

Particle symbol	Antiparticle symbol	Quark content	Rest mass(MeV/c^2)	Mean lifetime(s)
D^+	D^-	$c\bar{d}$	1869.62±0.20	$(1.040\pm0.007)\times10^{-12}$
D^0	$\overline{D}^0$	$c\bar{u}$	1864.84±0.17	$(4.101\pm0.015)\times10^{-13}$
D_s^+	D_s^-	$c\bar{s}$	1968.47±0.33	$(5.00\pm0.07)\times10^{-13}$
D^{*+}	D^{*-}	$c\bar{d}$	2010.27±0.17	$(6.9\pm1.9)\times10^{-21}$
D^{*0}	$\overline{D}^{*0}$	$c\bar{u}$	2006.97±0.19	$> 3.1\times10^{-22}$

1.1.7 Branching Fraction and Upper Limits

In particle physics, the branching ratio for a decay process is the ratio of the number of particles that decay via a specific decay mode with respect to the total number of particles that decay via all decay modes. It can also be defined as the ratio of the partial decay constant to the overall decay constant. The branching fraction of the decay $A \to B + C$ is

$$\mathcal{B}(A \to B + C) = \frac{\Gamma(A \to B + C)}{\Gamma_A^{tot}} \tag{1.9}$$

where Γ_A^{tot} is the total decay width of A. An example of calculating Branching Fraction is illustrated below.

D^{*+} meson decays into three different channels. D^{*+} meson decays 67.7% of the time in one of the three ways as $D^0\pi^+$, $D^+\pi^0$ and $D^+\gamma$. Each decay mode has its own matrix element M. Partial decay width can be defined as

$$\Gamma(D^{*+}) = \Gamma(D^{*+} \to D^0\pi^+) + \Gamma(D^{*+} \to D^+\pi^0) + \Gamma(D^{*+} \to D^+\gamma) \tag{1.10}$$

The branching fraction $\mathcal{B}$, is the fraction of time a particle decays to a particular final state for $D^{*+} \to D^0\pi^+$ is given as

$$\mathcal{B}(D^{*+} \to D^0\pi^+) = \frac{\Gamma(D^{*+} \to D^0\pi^+)}{\Gamma_{D^{*+}}} \tag{1.11}$$

In particle physics when we find no signal events, we assign an upper limit (U.L.) and this is based on the method of confidence intervals.

1.1.8 Literature Survey

The universe as a whole seems to have a nonzero positive baryon number density – that is, matter exists. The known universe is dominated by matter over antimatter. It is expected that the total baryon number should be zero as the particles and antiparticles were produced in equal amounts after the Big Bang. This imbalance is extremely small as most of the matter and antimatter were annihilated, what was left over was all the baryonic matter in the current universe, along with a much greater number of bosons. So, there has to be some underlying baryon number violating process (BNV), as required for a successful mechanism of baryogenesis [45]. Nevertheless Standard Model is not sufficient to fully explain the baryogenesis. Various grand unified theories (GUTs) [5,46] and many Standard Model extensions such as superstring models [4] and supersymmetry

(SUSY)[47] predict baryon number violation, and as a consequence, nucleons can have finite, if long, lifetimes [25]. In all these theories baryon (B) and lepton (L) number violations are allowed but the difference of baryon number and lepton number $\Delta(B-L)$ is conserved. There are three ingredients every model is required to have in order to produce a baryon asymmetry. These are described by the three Sakharov conditions[48]:

1. Baryon number violation.

2. C and CP violation.

3. Departure from thermal equilibrium.

One specific area where baryon and lepton number violation has been studied is in the decays of B and D mesons. These are heavy mesons composed of a bottom (b) or charm (c) quark and a lighter quark (typically an up, down, or strange quark). In the context of these decays, violations of baryon and lepton number conservation could manifest in rare processes such as meson decays into final states containing fewer baryons or leptons than the initial state. Experimental searches for such violations are ongoing, with the aim of both testing the predictions of the Standard Model and probing for signs of physics beyond the Standard Model. These searches typically involve studying the decay products of B and D mesons produced in high-energy particle collisions, such as those at facilities like the Large Hadron Collider (LHC) or Belle II experiment. A few searches[49,50] were already made for BNV decays in B mesons but no obvious signals were found and upper limits were set. Neutrinoless double beta decay ($0\nu\beta\beta$) is the process where two neutrons inside an atomic nucleus are transmuted into two protons and two electrons without the emission of neutrinos. An observation of this process would indicate that lepton number (L) is not a good symmetry of nature (ΔL $= 2$) and that the neutrino mass has a Majorana component, implying that the mass eigenfields are selfconjugate [51]. Observation of $0\nu\beta\beta$ would thus have profound implications on understanding the mechanism of neutrino mass generation [52–54], and would also give insight into leptogenesis scenarios for the generation of the matter-antimatter asymmetry in the universe[55]. Thus search for this neutrinoless double beta decay would provide a deep insight to the lepton number (L) violation where lepton number L is violated by two units. Along with neutrinoless double beta decay and proton decay, which are being explored vigorously, ΔB $\neq 0$ and Δ(B - L) $\neq 0$ process of neutron-antineutron oscillations ($n \to \bar{n}$) are a necessary component of a multifaceted effort to experimentally observe BNV. New physics related to $n \to \bar{n}$ mixing and ΔB=2 more generally has also been considered with implications for LHC searches baryogenesis[56–59]. Direct experimental limits are currently available from a free neutron search at the Institut LaueLangevin (ILL) some decades ago with a lower limit of $\tau_{n\bar{n}} \sim 10^8$ s[60].

Several models of proton decay, e.g. in GUT, superstrings, and SUSY as mentioned above, can provide predictions on possible decay mechanisms $D \to p\ell$. These above-mentioned models, predict branching fractions (BFs) for these kinds of decays at the level of 10^{-39} to 10^{-27} [61], compatible with the experimental limits from proton decay experiments. Many efforts are given in search for the proton decay experimentally as in SU(5) predicts proton decays to $p \to e^+\pi^0$. Biswal et al. [6] suggested five different decay diagrams. The decays are mediated by heavy hypothetical gauge bosons called X and Y. The X and Y bosons have electric charge $\frac{4}{3}e$ and $\frac{1}{3}e$ and couple a quark to a lepton, hence they are sometimes called "leptoquarks".

The diagrams[62] in Fig. 1.6 show some of the possible mechanisms of $D^0 \to \bar{p}e^+$ based on analogous couplings of $p \to e^+\pi^0$ in SU(5). No tree level diagram is possible for $D^0 \to \bar{p}e^+$. Arnowitt and Nath also predict proton decay in an R-parity violating[63] superstring-based model that can also accommodate $D^0 \to \bar{p}e^+$ decay[64]. Several BNV processes were searched for in τ, Λ, D, and B decays by the CLEO [65], CLAS[66] and BABAR[67] experiments, but no clear signal was found. In 2009, the CLEO[68] searched for the decays of $D^0(\bar{D^0}) \to \bar{p}e^+$ and $D^0(\bar{D^0}) \to pe^-$ and set an upper limits on the branching fraction to be $< 1.1 \times 10^{-5}$ and $< 1.0 \times 10^{-5}$ at 90% confidence level

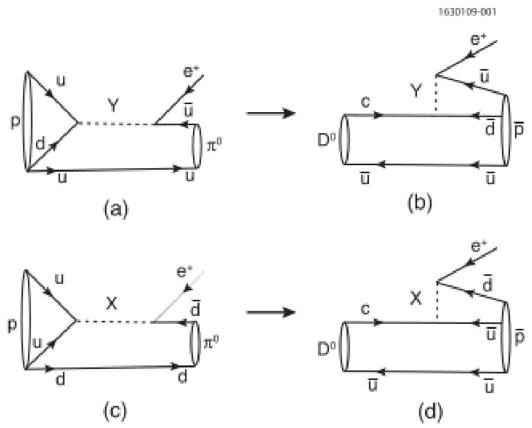

FIGURE 1.6: (a) and (c) are the Feynman diagram of the proton decay as described in $SU(5)$. Right-hand plots (b) and (d) are the possible decay diagrams of $D^0 \to \bar{p}e^+$.

(CL), respectively. Recently BESIII[69] also attempted to search for these decay modes $D^0 \to \bar{p}e^+$ and $D^0 \to pe^-$ and set an upper limit on branching fraction to be $< 1.2 \times 10^{-6}$ and $< 2.2 \times 10^{-6}$ respectively. The large data set accumulated by the Belle experiment led to the best sensitivity for investigating BNV decays of charmed mesons. In this thesis we present the most accurate search for the decays $D^0 \to pe^-$, $\overline{D}^0 \to pe^-$, $D^0 \to \bar{p}e^+$, $\overline{D}^0 \to \bar{p}e^+$, $D^0 \to p\mu^-$, $\overline{D}^0 \to p\mu^-$, $D^0 \to \bar{p}\mu^+$ and $\overline{D}^0 \to \bar{p}\mu^+$ performed with an e^+e^- collision data sample corresponding to an integrated sample 921 fb^{-1} with the Belle detector. Throughout this paper, Charge conjugate processes are included unless stated otherwise. A detailed description of the KEKB accelerator[70,71], as well as the Belle detector[75], is given in Chapter 2.

Chapter 2

Experimental setup and Analysis strategy of $D \to p\ell$

In this chapter, we discuss in detail the KEKB collider, Belle detector, and the details analysis of the $D \to p\ell$ study.

The KEKB[70,71], a double-ring collider with asymmetric energy of 3.5 GeV positrons and 8 GeV electrons, is built in the same tunnel as TRISTAN. KEKB was approved in 1994, and experiments started in 1999 and then continued through 2009. KEKB's energy is tuned around the resonance $\Upsilon(4S) = 10.56$ GeV to observe the asymmetry in the decay of B and $\bar{B}$ mesons. KEKB's luminosity reached 1.96×10^{34} cm^{-2}s^{-1} in 2009, which is twice as high as its design luminosity. The Belle detector surrounds the interaction region of the electron and positron beams. It covers a polar angle range (θ) from 17° to 150°, corresponding to 92% of the solid angle. Belle has also large data sets for charm physics. KEKB currently holds the world record on instantaneous peak luminosity of 2.11×10^{34} cm^{-2} s^{-1} during its tenure. The integrated luminosity collected by the Belle detector was more than 1000 fb^{-1} (1 ab^{-1}) from 1999 to 2010.

2.1 The KEKB accelerator complex

The KEKB complex[70,71], shown in Fig. 2.1, is a high-luminosity electron-positron collider located at the KEK (High Energy Accelerator Research Organization, Japan) consisting of a 600 m long linear accelerator (LINAC) connected with two storage rings.

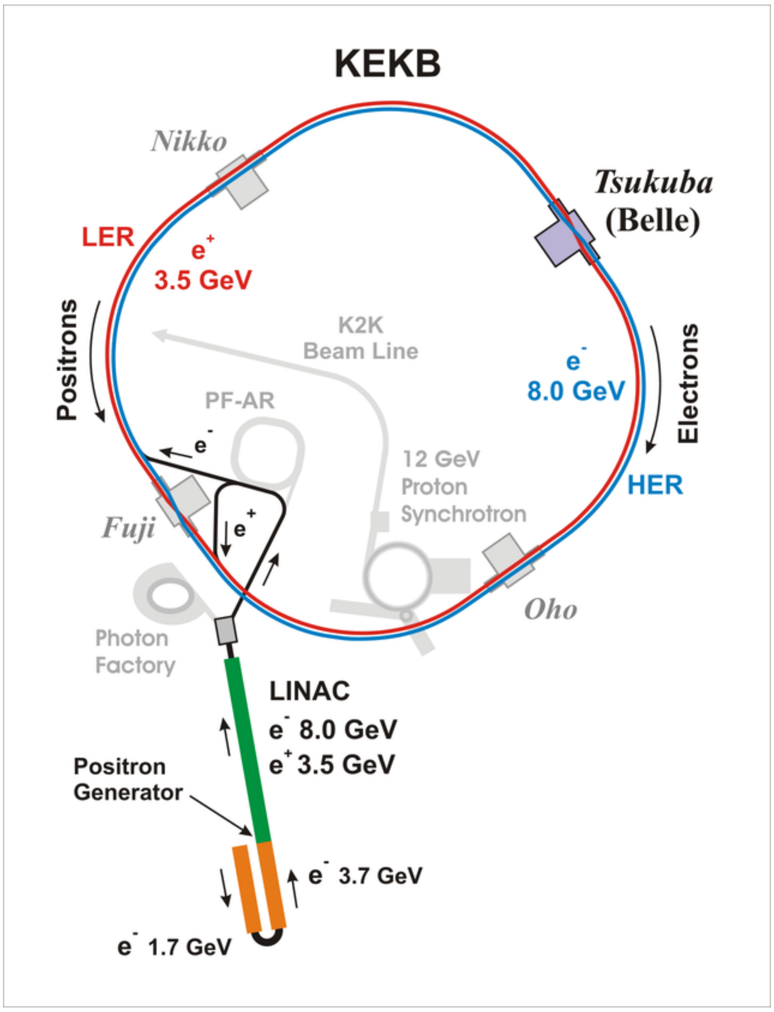

FIGURE 2.1: The KEKB accelerator complex.

It consists of two rings: a high-energy ring (HER) and a low-energy ring (LER). HER is an electron beam of energy 8.0 GeV and LER is for positron beam of energy 3.5 GeV. Electron and positron bunches are accelerated by the LINAC and they are injected into the two separated rings. KEKB is able to provide collision at energies in the CM frame ranging from 9.4 to 11 GeV, keeping a constant boost between the CM and the laboratory frame. The main physics goal of KEKB is to measure the CP asymmetry in the B meson system i.e. to measure the CKM angles[72,73] precisely. For example, $B^0 \to J/\psi K_S^0$ is golden mode for the measurement of $\phi_1 = arg(-\frac{V_{ud}V_{ub}^*}{V_{cd}V_{cb}^*})$. The event topology of the $B^0 \to J/\psi K_S^0$ is shown in the Fig. 2.2.

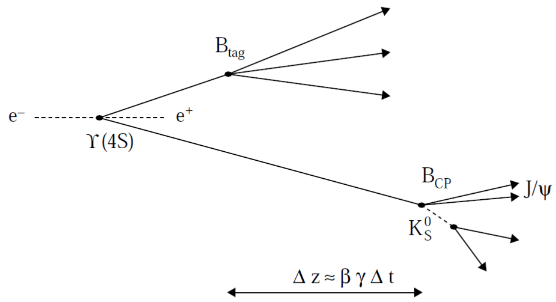

FIGURE 2.2: Event topology of a $B^0 \to J/\psi k_S^0$ event, with two displaced vertexes separated by a distance proportional to Δt.

Experimentally it is challenging to measure the distance between B meson production and decay vertex. In the ϒ(4S) reference frame, the average distance covered by B meson is $c\tau = 1.5 \times 10^{-12}$m. It is well below the typical tracking precision required to measure such a small separation. Therefore B vertex can not be distinguishable from the primary one if the $\Upsilon(4S)$ was produced at rest in the laboratory frame. So, a boost is required to magnify the path in the laboratory frame so that the separation between the vertices can be measured with well precision. The Lorentz boost factor used by the KEKB is

$$\beta\gamma = \frac{E_{e^-} - E_{e^+}}{\sqrt{s}} = 0.425$$

With this Lorentz boost the average decay length of a B^0 meson is

$$l = c\beta\gamma\tau_B = 200\ \mu m$$

, where τ_B is the B^0 meson lifetime. This length is measurable with the Belle vertex detector whose vertex resolution is of the order of 100 μm.

The conventional coordinate system in the Belle experiments is:

x horizontal direction: outward to the KEKB ring

y vertical direction: upward

z: direction of the electron beam

r $\sqrt{x^2 + y^2}$

θ polar angle with respect to the z-axis.

ϕ azimuthal angle around z axis.

The detailed description of the accelerator can be found here [70,71]. Two storage rings are situated side-by-side through which the beam is sent through LINAC. The circumference of the ring is 3 km which is buried 11 m below the surface. In the first stage of the linac, electrons are accelerated to an energy of 4 GeV. Then some of these electrons are allowed to make a collision with a thin tungsten mono-crystal target to produce photons. These high-energy photons create electron-positron pairs through pair creation and the positrons are collected and accelerated to 3.5 GeV. After the injection, three groups of radio-frequency cavities (two placed along the HER, and one along the LER) were used to sustain the energy of the beams. In order to avoid parasitic collision and keep the beam background as low as possible the beams had a crossing angle of 22 $mrad$ in the horizontal plane[74]. But a non-zero crossing angle between the two beams will reduce the luminosity which is maximum for head-on collision. To get rid of it, radio frequency crab cavities were installed near the interaction point. Its job was to rotate the beam bunches and provide the head-on collision despite the finite crossing angle between the lines. Fig. 2.3 shows how crab cavities[75] work and how they orient the bunches to make the collision head-on. With this scheme the total integrated luminosity accumulated by the KEKB reached in June 2010 the 1000 fb^{-1}.

Table 2.2 summarizes the design parameters of the KEKB accelerator. It has taken data at multiple resonances and they are listed in Table 2.1. A major part of the data was taken at $\Upsilon(4S)$ resonances and Fig. 2.4 shows the production cross-section of various Υ resonances. For each data-taking period of on-resonance, a set of *continuum*

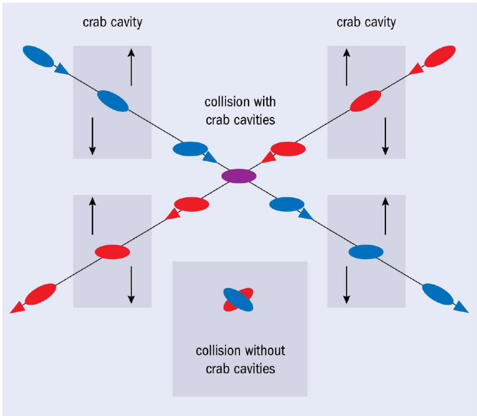

FIGURE 2.3: Head-on collision due to crab crossing scheme despite having finite crossing angle.

data was taken lowering the center of mass energy by 60 MeV in order to study the $q\bar{q}$ background. Short scan runs were taken to fine-tune the beam energies around the resonant peak position. During the entire period of data taking when beams were not available, cosmic ray events were recorded for calibration and alignment purposes[76].

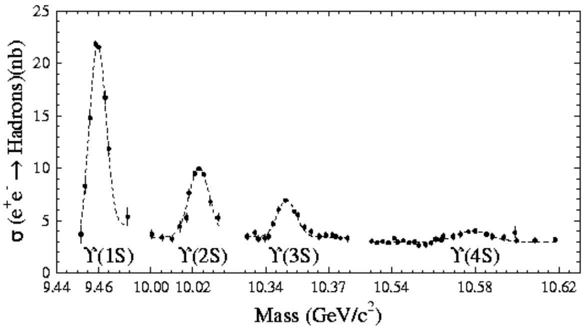

FIGURE 2.4: Cross section (in nb) of various Υ resonances from e^+e^- collision.

Table 2.1: Summary of the integrated luminosity in each resonance.

Resonances	Luminosity(fb^{-1})
$\Upsilon(1S)$/Off	5.7/1.2
$\Upsilon(2S)$/Off	24.9/1.7
$\Upsilon(3S)$/Off	2.9/0.2
$\Upsilon(4S)$/Off	710.5/89.4
$\Upsilon(5S)$/Off	121.1/1.7
scan	27.6

Table 2.2: Main parameters of KEKB.

Ring		LER	HER	unit
Particle		e^+	e^-	
Energy	E	3.5	8.0	GeV
Boost factor	$\beta\gamma$	0.425	0.425	
Circumference	C	3016.26	3016.26	m
Luminosity	L	1.6×10^{34}	1.6×10^{34}	$cm^{-2}s^{-1}$
Crossing angle	θ_x	± 11	± 11	mrad
Beam-beam parameters	ξ_x/ξ_y	0.113/0.074	0.072/0.057	
Vertical beam size at IP	σ_y^*	2.1	2.1	μm
Beta function at IP	β_x^*/β_y^*	59/0.52	56/0.65	cm
Beam current	I	1580	1200	mA
Natural bunch length	σ_z	0.4	0.4	cm
Number of bunches		1289	1289	
Energy spread	σ_ϵ	7.1×10^{-4}	6.7×10^{-4}	
Bunch spacing	s_b	2.34	2.34	m
Particle/bunch	N	3.3×10^{10}	1.4×10^{10}	
Emittance	ϵ_x/ϵ_y	18	24	nm
Synchrotron tune	ν_s	-0.0249	-0.0216	
Betatron tune	ν_x/ν_y	45.505/43.535	44.513/41.582	
Momentum	α_p	$1 \times 10^{-4} \sim 2 \times 10^{-4}$	$1 \times 10^{-4} \sim 2 \times 10^{-4}$	
RF voltage	V_e	8.0	14.0	MV
RF frequency	f_{RF}	508.887	508.887	MHz
Harmonic number	h	5120	5120	
HOM power	P_{HOM}	0.57	0.15	MW
Bending radius	ρ	16.3	104.5	m
Length of bending	l_B	0.915	5.86	m

TABLE 2.3: Properties measure by each sub-detector.

FSPs	Position	Momentum	Energy	Particle Identification
$e^{\pm}$	SVD, CDC	CDC	ECL	ECL, ACC, TOF, CDC
$\mu^{\pm}$	SVD, CDC	CDC	$\times$	KLM, ACC, TOF, CDC
$\pi^{\pm}$	SVD, CDC	CDC	$\times$	ACC, TOF, CDC
$K^{\pm}$	SVD, CDC	CDC	$\times$	ACC, TOF, CDC
p($\bar{p}$)	SVD, CDC	CDC	$\times$	ACC, TOF, CDC
γ	ECL	$\times$	ECL	ECL, CDC
K_L^0	KLM	$\times$	$\times$	KLM

2.2 The Belle Detector

The Belle detector[77] is a general-purpose 4π hermetic detector surrounding the interaction point (IP). In order to reconstruct all types of processes (spherical, jet-like) a hermetic detector was needed, capable of precisely reconstructing the global event shape. It consists of three components: a barrel, a forward, and a backward component. Fig. 2.5 shows the schematic diagram of the Belle detector.

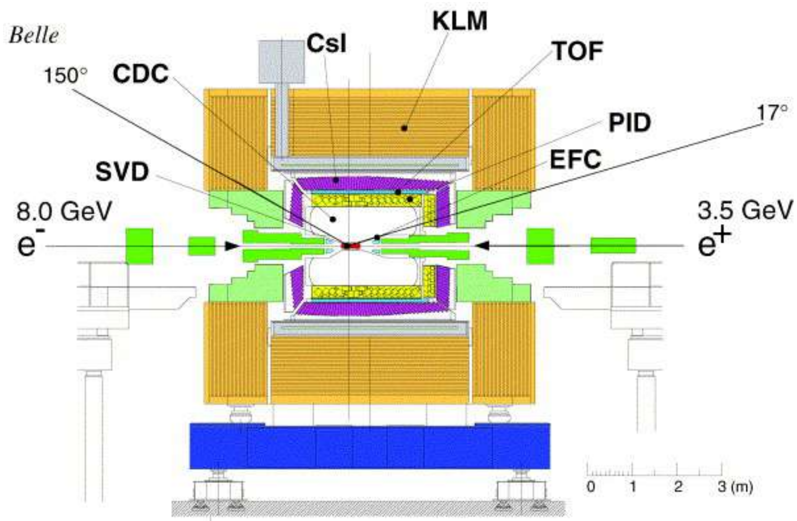

FIGURE 2.5: Schematic of the Belle detector.

The Belle Detector consists of a silicon vertex detector (SVD), a central drift chamber (CDC), a set of aerogel Cerenkov counters (ACC), a set of time-of-flight counters (TOF), an array of CsI(Tl) crystal calorimeters (ECL), a K_L^0 and muon detector (KLM), and a pair of BGO crystal arrays called the extreme forward calorimeter (EFC). In the Belle experiment, the final state particles of interest (FSP) are $K^{\pm}$, $\pi^{\pm}$, $e^{\pm}$, $\mu^{\pm}$, p, $\bar{p}$, K_L^0 and γ. The neutron and anti-neutron cannot be detected although they are also produced. The Belle detector is configured around a 1.5 T superconducting solenoidal magnet and iron structure surrounding the KEKB beams at the Tsukuba interaction region of accelerator as wide solid angle as possible. Each detector has its own purpose. Their main purposes are to measure position, momentum and energy, identify particle species of the decay products of B and D mesons. The detector covers the polar angle (θ) region extending from 17°-150°.

The tracking was performed by two sub-detector systems in a magnetic field parallel to the beam axis: a silicon vertex detector (SVD) located close to the beam pipe, surrounded by a large gas-filled drift chamber (CDC) able to provide information on both the particle's direction and particle identification based on dE/dx. Two PID-dedicated detectors were arranged around the CDC: a time of flight counter (TOF) made with two layers of fast scintilla-tors in the Barrel region and a Cherenkov threshold counter (ACC) which used aerogel tiles as a radiator. The latter one was installed in the Forward and Backward end-caps as well. Electromagnetic showers are detected in an array of CsI (Tl) crystals of Electromagnetic Calorimeter (ECL) located inside the solenoid coil covering both the barrel and the two end-caps regions. All the detector components mentioned so far are located inside a superconducting solenoid. Muon and K_L^0 are detected by a system of RPC included in the iron return yoke of the magnet (KLM). The EFC is placed on the surface of the cryostat of the final focusing quadrupole magnet (QCS) and provides coverage at small angles not covered by the other detectors. The purpose of sub-detectors in terms of the particle properties is listed in Table 2.3 and the performance of sub-detectors is listed in Table 2.4.

Table 2.4: Performance of the detector and sub-systems. p and p_t in GeV/c, E in GeV.

Detector	Type	Configuration	Readout	Performance
Beam pipe(SVD I) SVD II	Beryllium double wall	Cylindrical, $r = 20$ mm, 0.5/2.5/0.5 mm = Be/He/Be, He gas cooled		
SVD I	Double-sided Si strip	3-layers: 8/10/14 ladders, Strip pitch: 25(p)/50(n) μm	ϕ : 40.96 k, θ : 40.96 k,	$\sigma(\Delta z) \sim 100$ μm
SVD II	Double-sided Si strip	4-layers: 6/12/18/18 ladders, Strip pitch: 75(p)/50(n) μm (layer 1-3), 73(p)/65(n) μm (layer 4)	ϕ : 55.296 k, θ : 55.296 k	$\sigma(\Delta z) \sim 100$ μm
CDC	Small cell drift chamber	Anode: 50 layers, Cathode: 3 layers, $r = 8.3 - 87.4$ cm	A: 8.4k C:1.8k	$\sigma_{r\phi} = 130$ μm σ_{p_t}/p_t=0.3%$\sqrt{p_t^2+1}$ $\sigma_{dE/dx}$=6%
ACC	Threshold Cerenkov Silica aerogel $n = 1.01 - 1.03$	960 barrel, 228 endcaps, FM-PMT readout	1788	$N_{p.e.} \geq 6$ K/π separation at $1.2 < p < 3.5$ GeV/c
TOF/TSC	Plastic scintillator	128/64 ϕ segmentation, r = 120 cm, 3-m long	128 $\times$ 2/64	$\sigma_t = 100$ ps K/π separation at $p < 1.2$ GeV/c
ECL	CsI	$r = 125 - 162$ cm (Barrel), $z = -102$ cm (Backward Endcap), z = +196 cm (Forward Endcap)	6624 (B), 960 (BE), 1152 (FE)	σ_E/E = 0.066%/E
KLM	Resistive plate counters	14 layers (5 cm Fe + 4 cm gap), 2 RPCs for each gap, θ and ϕ strips	ϕ=16k $\theta = 16k$	$\Delta\phi$=$\Delta\theta$ = 30 mrad for K_L ~1% fake rate
EFC	BGO	Segmentation: 32 in ψ, 5 in θ	160 $\times$ 2	σ_E/E = (0.3 - 1)%/$\sqrt{E}$
Magnet	Super-conducting	Inner radius = 170 cm		$B = 1.5$ T

2.2.1 Silicon Vertexing Detector (SVD)

The SVD[78] is the innermost detector of the BELLE detector (just outside the beam pipe) and provides a very precise measurement of the position of the B mesons, which is crucial for the time-evolution study of the B mesons. In time-dependent CP asymmetry calculation, it is essential to obtain information on the difference between the flight length of the pair of B mesons in the z-direction, where z is the direction of the beam axis. The SVD also provides information to reconstruct D and τ decay vertices.

The SVD consisted of 3 layers of double-sided silicon strips (DSSD) arranged in a barrel-only geometry, with a polar angular coverage $23^\circ < \theta < 140^\circ$, where θ is defined as the polar angle from the z-axis. Its coverage corresponds to 86% of full solid angle. Its coverage is smaller than the outer detector's acceptance. The radii of the three layers are 30.0, 45.5, and 60.5 mm (the radius of the beam pipe is 2.0 cm) and the three layers are made up of 8, 10, and 14 ladders, from innermost to outermost. The resolution on the impact parameter σ_{IP} reconstructed with a multilayer detector strongly depends on the ratio of the inner layer radius to the outer layer radius. Fig. 2.6 shows the side and end views of the SVDI.

$$\sigma_{ip} \propto \frac{\sqrt{1 + \frac{r_1^2}{r_2^2}}}{1 - \frac{r_1}{r_2}}$$

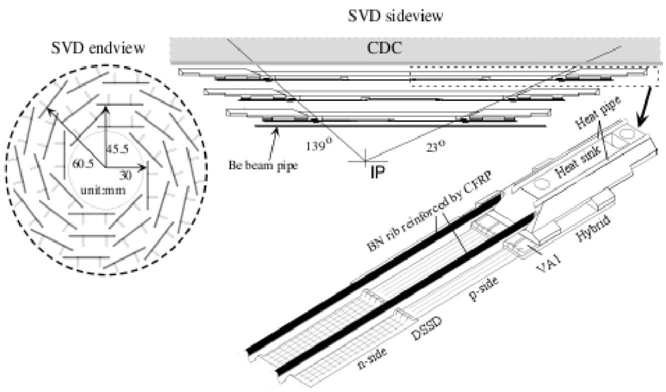

FIGURE 2.6: Detector configuration of SVD1.

These considerations, together with the need for a more radiation-hard design and a larger angular coverage, led to a radical modification of the SVD after four years of operation. Fig. 2.7 schematically shows the configuration of SVDII. SVDII consists of four concentric cylindrical layers and the polar angle acceptance is improved to cover $17° < \theta < 150°$ which is the same as CDC and corresponds to the 92% of the full solid angle. It is composed of 4 DSSD layers located at 20 mm, 44mm, 70 mm, and 88mm from the interaction point. Thanks to the new geometry, a reduction of the ratio of the inner radius to the outer radius (r_{in}/r_{ext}) from 0.50 to 0.23 was obtained, significantly improving the impact parameter resolution. SVD2 consists of 138 DSSDs in total.

A DSSD is basically a depleted p-n junction. When a charged particle passes through the junction, it knocks out electrons from the valence band into the conduction band creating an electron-hole pair. These pairs create currents in the p^+ and n^- strips respectively located on the surface of the DSSD. The impact parameter resolution for the reconstructed tracks is improved for SVDII[79] as compared to SVDI, mainly because of the smaller innermost layer. The distribution of impact parameter resolution with respect to the track momentum p (GeV/c) measured with SVDI and SVDII is shown in Fig. 2.8.

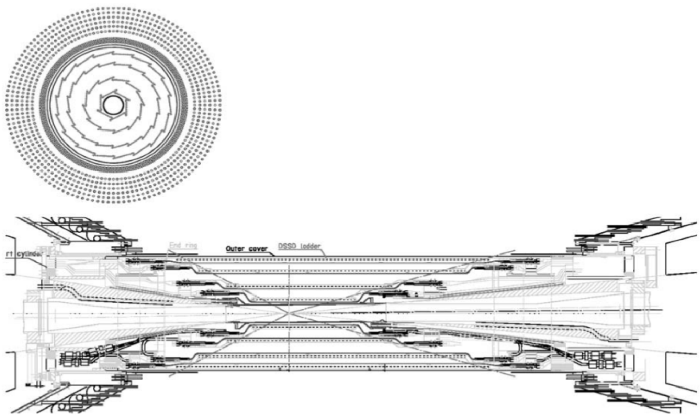

FIGURE 2.7: Detector configuration of SVDII.

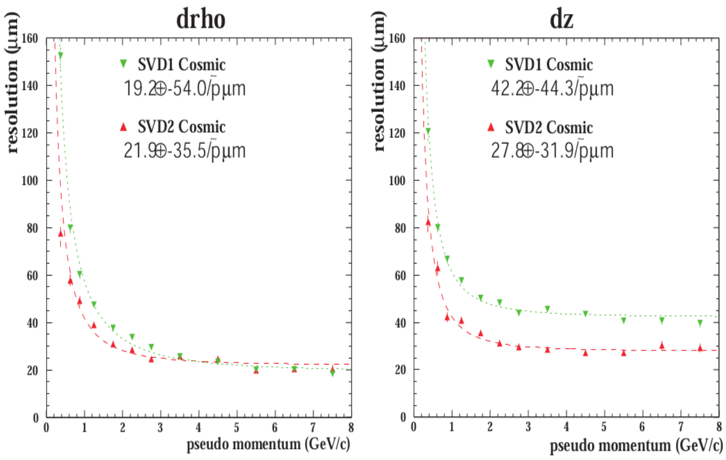

FIGURE 2.8: Comparison of the impact parameter resolutions in the directions of $r - \phi$ (left) and z (right) measured with cosmic ray data.

2.2.2 Central Drift Chamber (CDC)

The central drift chamber (CDC) is a gas-filled wire chamber and wires were arranged in 50 super-layers, each one comprising from three to six either axial or stereo layers and three cathode strip layers, for a total of 8400 drift cells. At the inner layers of the CDC, three cathode strip layers are made for higher precision z measurement at the position where the particles enter the CDC, which is especially beneficial for the trigger function. The primary role[80] of the Central Drift Chamber (CDC) is the determination of three-dimensional trajectories of charged particles and precise measurement of their momenta. The physics goals of the Belle experiment require a transverse momentum resolution of

$$\frac{\sigma_{p_t}}{p_t} \sim \sigma_{MS} \bigoplus \sigma_r \sim 0.5 \bigoplus 0.5 p_t \% \tag{2.1}$$

for all charged particles with $p_t \geq 0.1$ GeV/c in the polar angle region $17° < \theta < 150°$, which corresponds to 92% of the full solid angle. Here σ_{MS} denotes the error that comes from the multiple Coulomb scattering and shows contribution in the p_t region, and σ_r denotes the error proportional to p_t, which arises from the position measurement. CDC is placed in a 1.5 T magnetic field produced by the solenoidal coil, therefore a charged track follows a helicoidal trajectory in CDC. Transverse momentum p_t can be calculated from the radius of curvature r as

$$p_t = 0.3Br \tag{2.2}$$

where B is magnetic field in Tesla and r is in meter. The structure of the CDC is shown in Fig. 2.9. It is asymmetric in the z-direction. It is a cylindrical chamber with an inner radius of 77 mm, outer radius of 880 mm, and length 2400 mm and consists of 50 sense wire layers and three cathode strip layers. The sense wire layers are grouped into 11 super layers, where six of them are axial and five are small-angle stereo super layers. Each super layer consists of between three and six radial layers, all with the same number of drift cells in the azimuthal direction. The small-angle stereo layers are used in conjunction with the axial layers to provide z-coordinate measurements. Stereo layers also provide a highly efficient fast z-trigger combined with the cathode strips. The gas mixture[81] within CDC was chosen in order to minimize the coulomb scattering and the radiation absorption: the chosen 50% helium - 50% ethane mixture offered a long radiation length (640 m) and a velocity drift that saturates at the value of 4 cm/μm with an electric field of 1.6 kV/(cm.atm). CDC also helps with particle identification by measuring the energy loss (dE/dx). dE/dx provides information that can be used to distinguish particle species having equal momenta but with different masses.

Fig. 2.10 shows the measured dE/dx as a function of momentum, together with the expected mean values for different species. Populations of pions, kaons, protons, and electrons are clearly seen. The dE/dx resolution is measured to be 7.8% for pions in the momentum range from 0.4 to 0.6 GeV/c, while the resolution for Bhabha and muon pair events is measured to be about 6%. The momentum resolution of the CDC has been measured with cosmic rays, obtaining the distribution shown in Fig. 2.11. The upper result is for the case where we use only CDC information. In lower distribution, we use the SVD information in the track parameter fit. The resolution is substantially improved by including SVD. In the summer of 2003, the inner part structure of the CDC was jointly modified with the upgrade of the SVD. The three inner layers with cathode strips were removed to make the space for the upgraded SVD with a larger radius. Instead, two layers of smaller cells were installed, which we call small-cell CDC (sCDC). The inner radius after the modification is 104 mm, while the other geometry is unchanged.

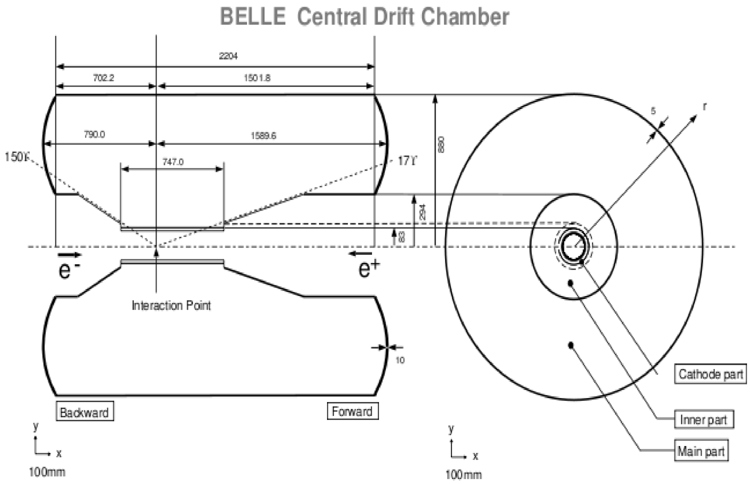

FIGURE 2.9: Overview of the CDC.

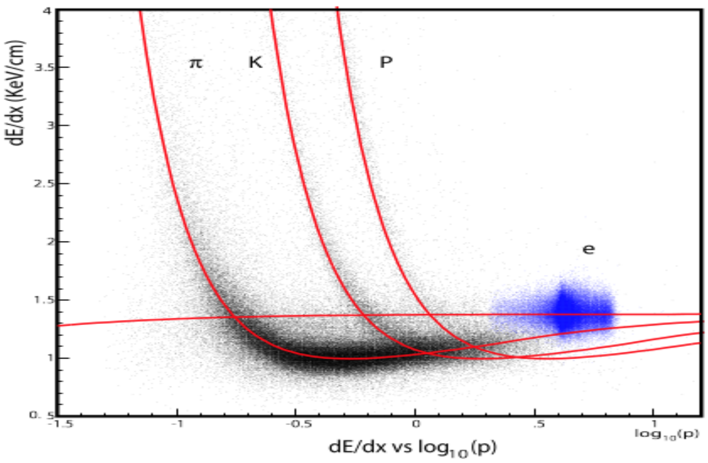

FIGURE 2.10: Measured dE/dx vs. momentum in collision data.

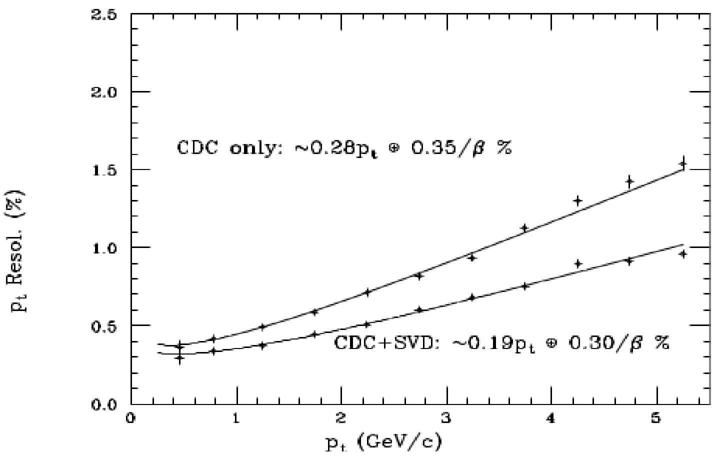

FIGURE 2.11: p_t resolution studied using cosmic rays.

2.2.3 Aerogel Cerenkov Counter (ACC) and Time of Flight (TOF) detector

Particle identification, particularly the identification of $\pi^{\pm}$ with respect to $K^{\pm}$, plays a crucial role in many measurements in B decays. The Aerogel Čerenkov Counter System (ACC) provides particle identification information (basically π/K separation) in the momentum range from 1.2 GeV/c to 3.5 GeV/c, where the CDC and TOF are not available for particle identification. It detects Cerenkov light from particles penetrating through a silica aerogel radiator. The Belle ACC is a threshold type of detector that identifies particle species according to whether Čerenkov light is emitted or not in the material. Cerenkov radiation is emitted in case of

$$n > \frac{1}{\beta} = \sqrt{1 + \frac{m^2}{p^2}} \tag{2.3}$$

where β, m, and p are the velocity, mass, and momentum of the charged particle, respectively, and n is the refractive index of the matter through which the particle is passing. Therefore there is a region where pions emit Cerenkov light but kaons or other heavier particles do not. Thus one can identify pion against kaon by choosing the proper refractive index n for the momentum of interest. For example, pions with momentum 2 GeV/c emit Čerenkov light in the matter if $n > 1.002$, while $n > 1.03$ is necessary for kaons with the same momentum.

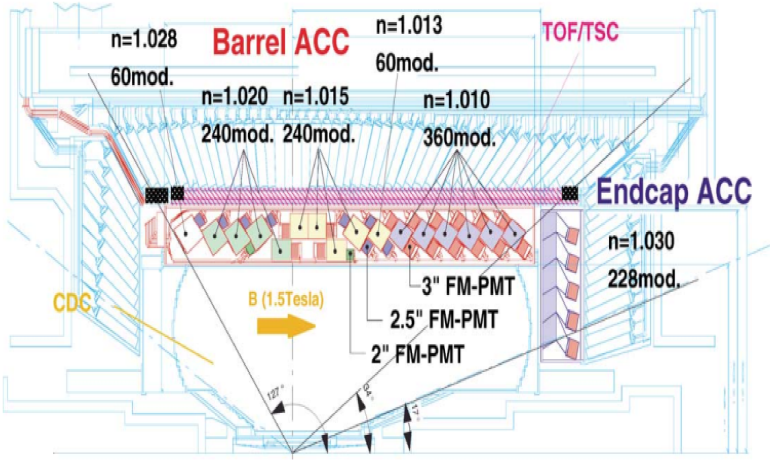

FIGURE 2.12: Configuration of ACC and TOF system.

The configuration of the ACC is shown in Fig. 2.12. The ACC consists of 960 counter modules segmented into 60 cells in the ϕ direction for the barrel part and 228 modules arranged in five concentric layers for the forward end-cap part of the detector [82]. All the modules are arranged in a semi-tower geometry, pointing to the IP. A typical ACC module consists of five aerogel tiles stacked in a thin (0.2 mm thick) aluminum box. To detect the Cerenkov light, two (one) fine-mesh type photomultiplier tubes (FM-PMTs) are attached to each module in the barrel (end-cap) part. These FM-PMTs are designed to operate in strong magnetic fields of 1.5 T [83].

Fig. 2.13 shows the measured pulse height distributions for barrel ACC for $e^{\pm}$ tracks in Bhabha events and $K^{\pm}$ candidates in hadronic events, together with the expectations from simulated data. $K^{\pm}$ tracks are selected by TOF and dE/dx measurements [84]. Clear separation can be seen from the distributions.

The time-flight-detector [85] subsystem provides particle identification information to distinguish charged kaons from pions in the low momentum region, below 1.2 GeV/c with a time resolution of 100 ps. The TOF also provides fast-timing signals for the trigger

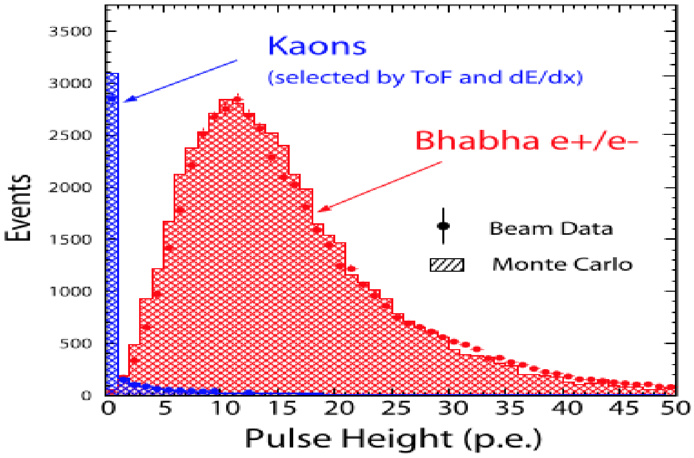

FIGURE 2.13: Pulse-height spectra in units of photoelectrons observed by ACC for electrons and kaons show a good agreement between data-MC.

system, together with thin trigger scintillation counters (TSC). The flight time T of a particle in length L is expressed as

$$T = \frac{L}{c}\sqrt{1 + c^2m^2/p^2} \tag{2.4}$$

Once the momentum is measured by the CDC, the time-of-flight can be used for particle identification by calculating the mass of the particle. For example, when $p = 1.2$ GeV/c, $T = 4.0$ ns for pions and $T = 4.3$ ns for kaons with $L = 1.2$ m. Thus, the time resolution of 100 ps would provide more than 3 standard deviation separation below 1.2 GeV/c. The Belle TOF system consists of 64 modules and each module consists of two trapezoidal-shaped TOF counters and one TSC counter (128 TOFs and 64 TSCs in total). The TOF/TSC modules are located at a radius of 1.2 m from the IP covering a polar angle range from 34° to 120°. The configuration of the TOF is shown in Fig. 2.12. Fig. 2.14 shows time resolutions as a function of z for forward and backward PMTs and for the weighted average. The resolution for the weighted average is about 100 ps with a small z dependence.

Fig. 2.15 shows the particle mass distribution calculated from measured time-of-flight

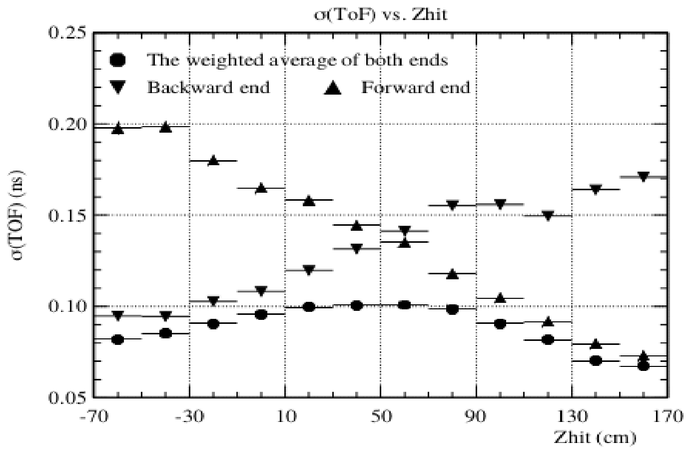

FIGURE 2.14: Time resolution of the TOF for $e^+e^- \to \mu^+\mu^-$ events.

for particles with momentum less than 1.25 GeV/c. Clear peaks corresponding to pions, kaons, and protons can be seen.

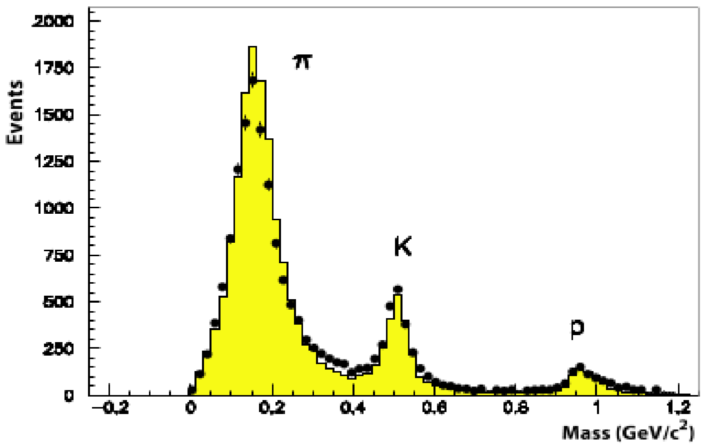

FIGURE 2.15: Distributions of hadron masses calculated from measured time-of-flight for particles with momenta less than 1.25 GeV/c. The histogram corresponds to MC distribution.

The kinematic upper limit of particle momenta from B decays in Belle is 3.5 GeV/c. The momentum coverage of each detector for K/π separation is shown in Fig. 2.16. We combine information from three independent measurements: energy loss (dE/dx) measurement in the CDC, time-of-flight measurement by the TOF, and the number of photoelectrons (N_{pe}) in the ACC. For each charged track, we calculate three likelihood functions using sub-detector information with kaon and pion hypothesis, L_h^{ACC}, L_h^{TOF}

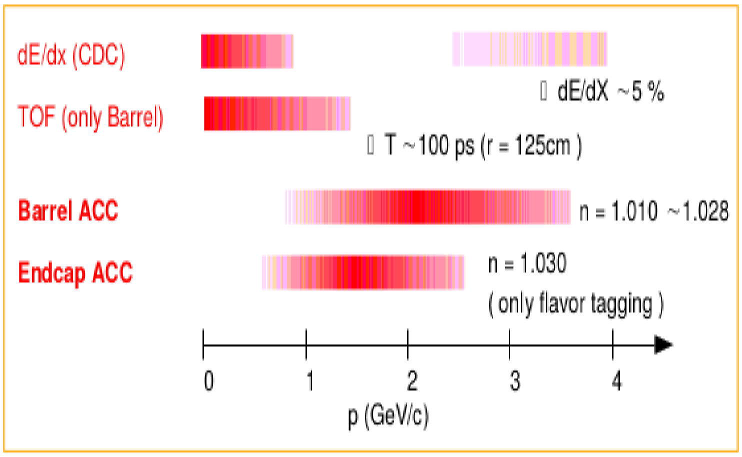

FIGURE 2.16: Momentum coverage of each detector used for K/π separation.

and L_h^{CDC}, where h denotes assumed particle species. Then, a combined likelihood is calculated by a product of these likelihood functions for a specific hadron species,

$$L_h = L_h^{ACC} \times L_h^{TOF} \times L_h^{CDC} \tag{2.5}$$

By combining all the information, a normalized likelihood function is calculated in such a way that a kaon-like particle gives about one and a pion-like particle gives a value close to zero.

$$R(K|\pi) = \frac{L_K}{L_K + L_\pi} \tag{2.6}$$

This ratio is used to separate out kaons from pions. Fig. 2.17 shows the kaon identification efficiency and fake rate as a function of momentum, measured using $D^{*+} \rightarrow D^0(K^-\pi^+)\pi^+$ decays. The $R(p|K)$ is defined in a similar manner as $R(\pi|K)$.

2.2.4 Electromagnetic Calorimeter (ECL)

When a high-energy electron or photon is incident on a calorimeter, it initiates an electromagnetic cascade as pair production and bremsstrahlung which generate more electrons and photons with lower energy. The main purpose of the ECL[86] is to detect

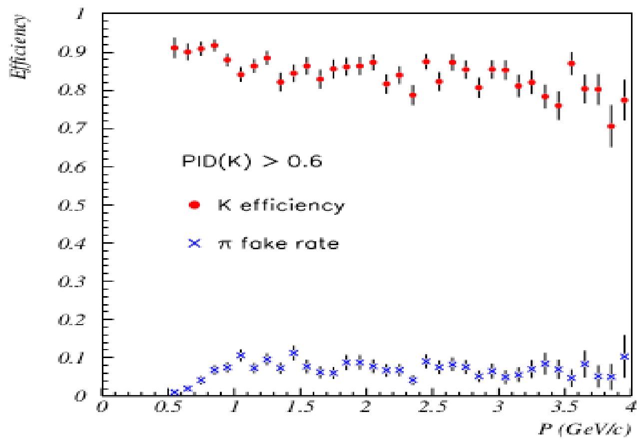

FIGURE 2.17: Kaon identification efficiency and pion fake rate as a function of momentum.

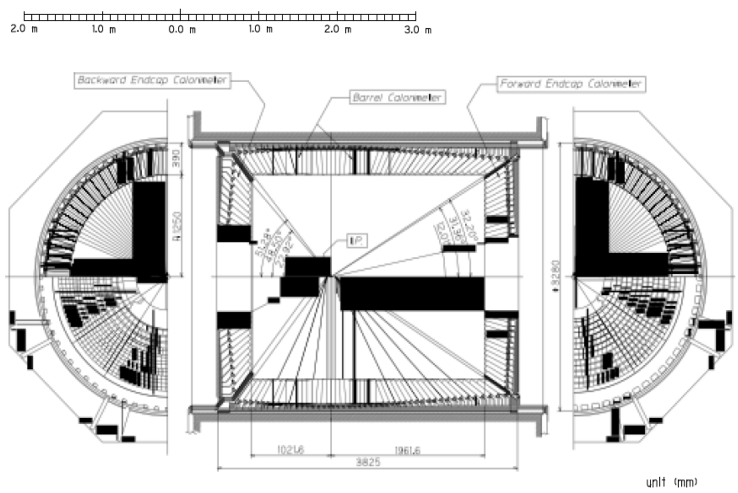

FIGURE 2.18: Configuration of the ECL.

and measure photons with high efficiency and good resolution in energy and position. Photons of interest in Belle mostly have relatively low energies (below 500 MeV) but photons in two-body decays of $B \to K^*\gamma$ and $B \to \pi^0\pi^0$ have energies up to 4 GeV. Therefore the ECL is required to cover a wide energy range of photon detection. It also plays a primary role in the electron identification at Belle. Electron identification at Belle primarily relies on the comparison of the charged particle momentum measured by the CDC and the energy deposit in the ECL. Electrons lose all their energies in the ECL crystals with electromagnetic showers, while other charged particles deposit only part of their energies in the ECL. Therefore, the ratio (E/p) of the cluster energy measured by the ECL to the momentum of the charged track momentum as measured by the CDC, E/p, is close to unity for electrons and smaller than unity for other particles. The overall configuration of the Belle calorimeter system, the ECL, is shown in Fig. 2.18. The ECL consisted in 8736 CsI(Tl) crystals with a typical dimension of (55×55)mm on the front face and 30 cm of depth, equivalent to 16.2 radiation lengths, arranged to point approximately to the primary vertex region[87]. The size of the crystals was arranged in such a way that approximately 80% of the total energy of a photon injected in its center remained contained in the crystal. The ECL was divided into three sections, the barrel and the two end-caps ("forward" and "backward" with respect to the HER beam direction). It has a coverage of 17° to 150° in the polar angle. The energy resolution is measured to be for a 5×5 block:

$$\frac{\sigma_E}{E} = \frac{0.0066(\%)}{E} + \frac{1.53(\%)}{E^{1/4}} + 1.18(\%) \tag{2.7}$$

For a 3×3 block, the resolution has the same functional form:

$$\frac{\sigma_E}{E} = \frac{0.066(\%)}{E} + \frac{0.81(\%)}{E^{1/4}} + 1.34(\%) \tag{2.8}$$

The photon reconstruction algorithm uses both the 5×5 and 3×3 block information. Fig. 2.19 shows the energy resolution measured from Bhabha events. The energy resolution of the photon was achieved to be 1.7% for the barrel ECL, 1.74%, and 2.85% for the forward and backward ECL, respectively. In addition to photon energy measurement and electron identification[88], ECL was used as a luminosity monitoring detector by counting the rate of Bhabha events.

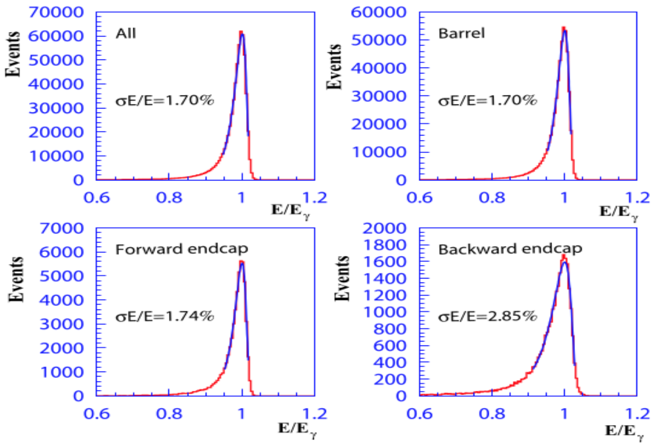

FIGURE 2.19: Energy resolutions measured from $e^+e^- \to \gamma\gamma$ event samples for overall, barrel, forward-endcap, and backward-endcap. E and E_γ are measured and calculated γ energies, respectively.

2.2.5 Superconducting Magnet

All the sub-detectors of the Belle detector described above are placed in a magnetic field of 1.5 T provided by a superconducting solenoid. The solenoid coil provides a magnetic field parallel to the beam pipe. The superconducting coil consists of a single layer of a niobium-titanium-copper alloy embedded in a high-purity aluminum stabilizer. It is cylindrical in volume of dimensions 4.4 m in length and 3.4 m in diameter. The coil is surrounded by a multi-layered iron structure that serves as the return path of the magnetic flux. When a charged particle enters a magnetic field with an angle λ with respect to the magnetic field B, it will have a trajectory that is described by a helix. The magnitude of the momentum can be determined from the radius of the curvature of the helix using the relation

$$p = 0.3 \times \frac{qBR}{cos\lambda} \tag{2.9}$$

where $q = \pm 1$ is the charge of the particle, R is radius of curvature in meter and p is the momentum of particle. The superconducting solenoid also acts as the absorber material for the KLM sub-detector.

2.2.6 K_L^0 and Muon Detection System (KLM)

KLM[89] is the outermost sub-detector and it is the only detector that is outside the solenoid magnetic field. It has two regions: one is barrel KLM and another is endcap (forward and endcap) KLM. It is designed to identify K_L^0's and muons with high efficiency over a broad momentum range greater than 600 MeV/c. The KLM consists of alternating layers of charged particle detectors and 4.7 cm-thick iron plates, with a total absorption length of 3.9 interaction lengths as shown in Fig. 2.20. The barrel-shaped region around the interaction point covers an angular range of 45° to 125° and endcaps in forward and backward directions extend this to 20° to 125°. The detection of charged particles is provided by glass-electrode-resistive plate counters (RPCs) and 4.7 cm-thick iron plates. There are 15 detector layers and 14 iron layers in the octagonal barrel region and 14 detector layers in each of the forward and backward end-caps. The iron layers also serve as a return yoke for the magnetic flux provided by the superconducting solenoid. Hadrons interacting with the iron plates produce a shower of ionizing particles that are detected by the RPC layers. The result is a cluster of hits deposited in the KLM.

A K_L^0 candidate can be distinguished from another charged hadron because it will not leave an associated track in the CDC. A muon, on the other hand, does leave a charged track in the CDC. However, muons can still be distinguished from charged and neutral hadrons because they are not affected by the strong interaction. Hadrons are more rapidly absorbed and deflected by strong interactions with iron, so wide clusters are observed. They are also stopped within a few layers of iron. Muons only experience electromagnetic multiple scattering and energy loss, so their clusters tend to be thinner and they have far greater penetration depth.

The KLM performance in muon detection was studied with cosmic rays with a momenta greater than 500 MeV/c, since particles with a momenta less than 500 MeV/c can not reach KLM due to the presence of a strong magnetic field. The pions were selected from

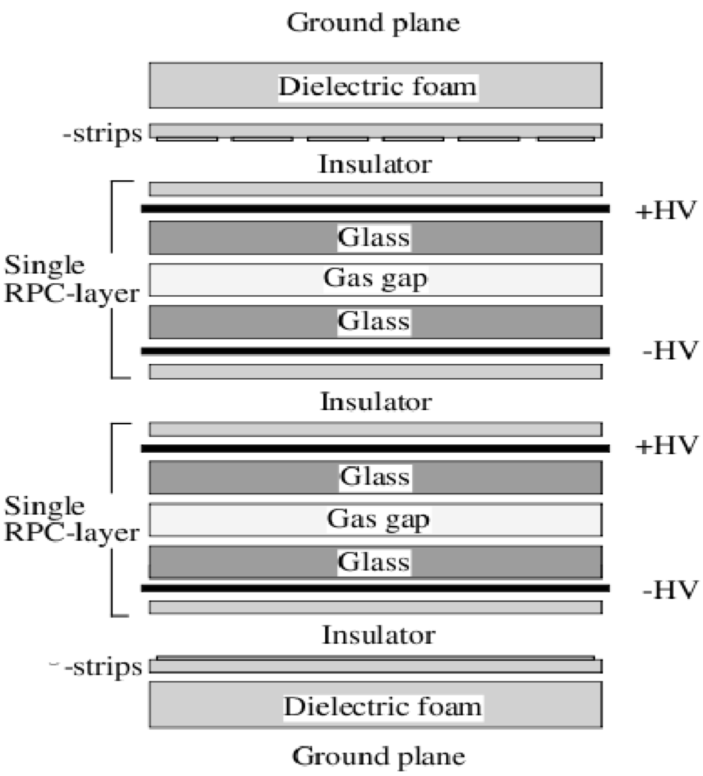

FIGURE 2.20: The Belle Kaon and Muon detector.

$K_s \to \pi^+\pi^-$ events in e^+e^- collisions. or muon with momentum above 1.5 GeV/c the identification efficiency is over 90% and the fake rate is less than 5%.

2.2.7 Extreme Forward Calorimeter (EFL)

EFC[90] is a calorimeter which further extends the polar angle coverage by ECL of 17° to 150°. The EFC covers the angular range from 6.4° to 11.5° in the forward region and 163.3° to 171.2° in the backward region. The EFC is also required as a beam mask to reduce backgrounds for the CDC. In addition, the EFC is used for a beam monitor in the KEKB control and a luminosity monitor for the Belle experiment[91]. The schematic diagram of EFC is shown in Fig 2.21. Since EFC is placed in a very high radiation-level area around the beam pipe near IP, it is required to be radiation-hard. Therefore, a radiation-hard BGO (Bismuth Germanate, $Bi_4Ge_3O_{12}$) crystal calorimeter is used for EFC. The EFC consists of BGO crystals segmented into 5 regions in θ-direction and 32 regions in the ϕ-direction in order to provide better position resolution. It also can be used as a tagging device for two-photon physics.

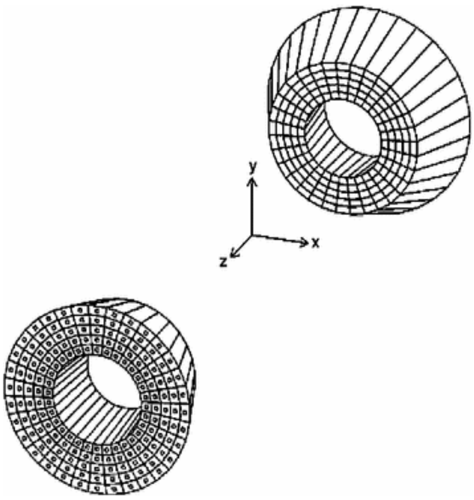

FIGURE 2.21: Configuration of the EFC.

2.3 Overview of the Analysis

In this analysis we search for the following semi-leptonic charm decays: $D^0 \to pe^-$, $\overline{D}^0 \to pe^-$, $D^0 \to \bar{p}e^+$, $\overline{D}^0 \to \bar{p}e^+$, $D^0 \to p\mu^-$, $\overline{D}^0 \to p\mu^-$, $D^0 \to \bar{p}\mu^+$ and $\overline{D}^0 \to \bar{p}\mu^+$. The branching fraction is determined relative to the decay $D^0 \to K^-\pi^+$. We consider eight different signal modes since such a choice decreases the background. The number of D^0 mesons that decay to proton and lepton can be written with the branching fraction $\mathcal{B}(D \to p\ell)$ as

$$N_{p\ell} = \sigma_{D^{*+}} L_{p\ell}.\mathcal{B}(D \to p\ell).\epsilon_{\pi}.\epsilon_{p\ell} \tag{2.10}$$

$\sigma_{D^{*+}}$ is the cross-section for the D^{*+} mesons production in the e^+e^- collisions, $L_{p\ell}$ is the integrated luminosity of the data analyzed for that channel, ϵ_π is the pion reconstruction efficiency and $\epsilon_{p\ell}$ the reconstruction efficiency for the decay $D \to p\ell$. Similarly, the number of D^0 mesons that decay to kaon and pion

$$N_{K\pi} = \sigma_{D^{*+}} L_{K\pi}.\mathcal{B}(D \to K\pi).\epsilon_{\pi}.\epsilon_{K\pi} \tag{2.11}$$

where $L_{K\pi}$ is the integrated luminosity of the data analyzed for that channel and $\epsilon_{K\pi}$ the reconstruction efficiency for the decay $D^0 \to K^-\pi^+$. By dividing the above two equations we can express the branching fraction for the decay into proton and lepton as

$$\mathcal{B}(D \to p\ell) = \frac{N_{p\ell}}{N_{K\pi}}.\frac{\epsilon_{K\pi}}{\epsilon_{p\ell}}.\mathcal{B}(D^0 \to K^-\pi^+) \tag{2.12}$$

The branching fraction for the D^0 decay into kaon and pion is $\mathcal{B}(D^0 \to K^-\pi^+) = (3.946 \pm 0.030) \times 10^{-2}$ [3]. As the branching fraction of the decay $D^0 \to K^-\pi^+$ is very high it is expected that we can reconstruct a large number of such decays from our data sample.

Decays of the type $D \to p\ell$ have not been observed; the current upper limits on branchings fractions are given in Table 2.5 and Table 2.6 obtained by CLEO [92] and BESIII [93] respectively.

TABLE 2.5: Upper limits of branching fractions with a 90% confidence level for the combine decays of D^0 and $\overline{D^0}$ by CLEO.

Channels	B.R.(90% CL)$\times 10^{-5}$
$D^0/\overline{D^0} \to pe^-$	< 1.0
$D^0/\overline{D^0} \to \bar{p}e^+$	< 1.1

TABLE 2.6: Upper limits of branching fractions with a 90% confidence level for the decays of D^0 by BESIII.

Channels	B.R.(90% CL)$\times 10^{-6}$
$D^0 \to pe^-$	< 2.2
$D^0 \to \bar{p}e^+$	< 1.2

2.3.1 Data sample

- For the efficiency determination, we generated 2 million monte carlo simulated samples for all the signal modes, and for the control mode, we generated 1 million simulated samples. Since the decay models for our signal modes are not well defined we have used PHSP in decay.dec files. We have used all the experiment numbers corresponding to various data-taking periods at Belle.

- We study the background using simulated samples corresponding to an integrated luminosity of about 4.5 times that of the Belle data sample.

- For the study in data we use the full data set i.e, 921 fb^{-1} for both signal modes and control mode $D^0 \to K^-\pi^+$.

2.3.2 Analysis strategy

- First we perform a simulated study to check our algorithm is working fine and also to calculate reconstruction efficiencies by using simulated samples. The signal MC sample for each decay mode is generated using EvtGen[94] where $e^+e^- \to q\bar{q}$ generated with Pythia[95] and PHOTOS[96] takes into account final state radiations. The produced particles are propagated with GEANT3[97] to simulate a detector response.

- Then we reconstruct our first mother particle D from the final state particles (FSP) whose lists are well defined in BASF[98] framework. Later we use those reconstructed D mesons to reconstruct $D^{*+} \to D^0\pi^+$ after combining with a slow pion (π_s).

- We perform a generic MC study to study for the possible backgrounds. There are four types of such events which are charged (B^+B^-), mixed ($B^0\bar{B}^0$), charm ($c\bar{c}$) and uds. By looking at the D^0 mass and ΔM=($M_{D^*} - M_D$) distributions, we apply a preliminary selection criteria.

- We use a simple cut-based technique to optimize our figure of merits to get the best possible selection criteria.

- Using those final selection criteria we check the final D^0 mass and ΔM distributions and identify the potential peaking backgrounds.

- We also perform control mode $D^0 \to K^-\pi^+$ study to extract the upper limits (U.L.) in branching fractions.

2.3.3 Preliminary selection criteria

In the following sub-section, we discuss the preliminary selection criteria applied at the reconstruction level. We utilize the HadronBJ skim data.

- **Charged particle selection**:

  Charged tracks are identified using a loose requirement on the distance of the closest approach with respect to the interaction point(IP) along the beam direction, $|dz| < 3$ cm, and in the transverse plane, $|dr| < 1.0$ cm. Apart from that, we ensure that charged tracks are reaching the SVD sub-detector by applying a criterion of at least two hits in the SVD. Additionally, we apply a PID cut greater than 0.1 on protons, electrons, and muons based on the information from the CDC, the TOF, and the ACC. We apply a PID cut ($Prob.(\pi : K) = \frac{L_\pi}{L_\pi + L_K}$) greater than 0.6 on slow pion to remove fake tracks. We have identified protons with respect to both kaons ($P_{p/K}$) and pions ($P_{p/\pi}$) where, $P_{i/j} = \mathcal{L}_i/(\mathcal{L}_i + \mathcal{L}_j)$ with $\mathcal{L}_i$ and $\mathcal{L}_j$ being the likelihood for the track to be identified as i and j, respectively. We make sure that PID cuts are greater than 0.1 for both cases. To recover the energy loss due to bremsstrahlung, gamma within a cone of radius 50 mrad around the momentum direction of the electron is added to the electron momentum.

- D **selection** We combine two oppositely-charged tracks, proton, and leptons (e, μ) to reconstruct a D. We select a loose cut on the D mass within [1.8, 1.9] GeV/c^2.

- D^* **selection** We combine π_s with D to reconstruct a D^*. While we are reconstructing D^* meson we make sure its momentum is greater than 2.5 GeV/c in the center-of-mass frame to reduce the backgrounds coming from $B\bar{B}$ events. With this cut, we also suppress the combinatorial backgrounds. We also ensure that ΔM $= M_{D^*} - M_D$ is less than 0.158 GeV/c^2, where M_{D^*} and M_D are the reconstructed mass of the D^* and D mesons respectively.

2.3.4 Signal MC study

We have generated 2 million $D^0 \to p\ell(e,\mu)$ and 1 million $D^0 \to K^-\pi^+$ simulated sample for the signal MC study. We use all the experiment numbers available starting from 7 to 65. In the decay.dec file we use PHOTOS+VSS for the decay $D^{*+} \to D^0\pi^+$ and phase space model for the D^0 decays. For the control mode $D^0 \to K^-\pi^+$ we also use PHSP. We then allow the generated events to pass through detector simulations where beam-induced backgrounds are added. Finally, we stored the events in mdst (micro data summary tapes) format.

Truth Matching

We performed a Monte Carlo truth matching study to separate out the correctly reconstructed events from the self-cross-feed candidates (SCF). This is done by the generated level information where we match the mother of the final state particles. The D^0 and ΔM distributions for the correctly reconstructed events and SCF are shown in Fig. 2.22 and Fig. 2.23 for M_{D^0} and ΔM respectively. The percentage of truth-matched signal candidates are listed in Table 2.7 for all the D^0 modes including control mode. Because of the loss of the bremsstrahlung photon in electron modes, we see a smaller number of correctly reconstructed events in electronic modes as compared to muonic modes.

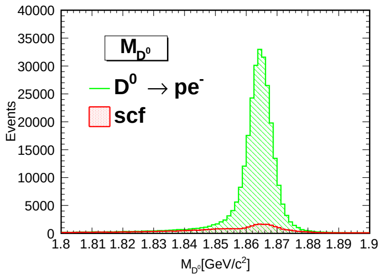

(A) $D^0 \to pe^-$

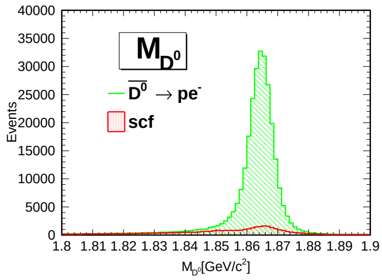

(B) $\overline{D^0} \to pe^-$

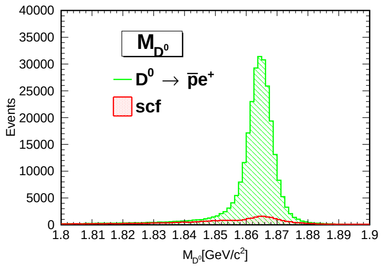

(C) $D^0 \to \bar{p}e^+$

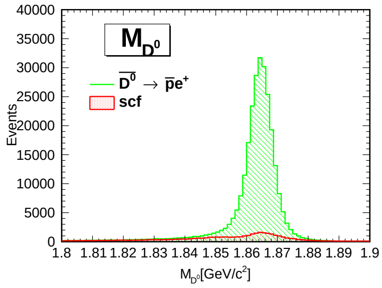

(D) $\overline{D^0} \to \bar{p}e^+$

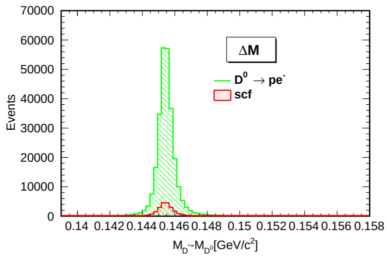

(E) $D^0 \to pe^-$

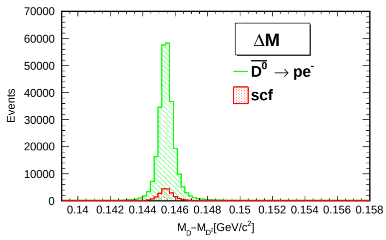

(F) $\overline{D^0} \to pe^-$

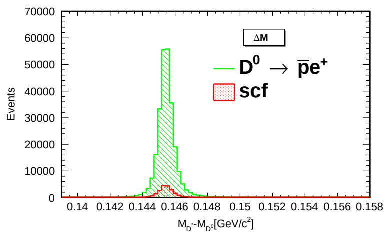

(G) $D^0 \to \bar{p}e^+$

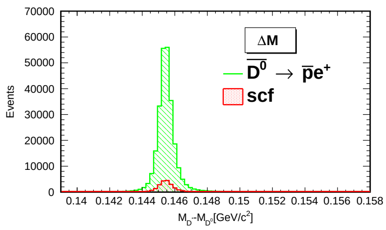

(H) $\overline{D^0} \to \bar{p}e^+$

FIGURE 2.22: The above plots (a-d) are for M_{D^0} distributions and (e-h) are for ΔM distributions for all the electronic modes in simulated sample.

Table 2.7: Percentage of correctly reconstructed events for each decay mode.

Channels	Correctly reconstructed Events(%)
$D^0 \to pe^-$	94.0
$\overline{D^0} \to pe^-$	93.8
$D^0 \to \bar{p}e^+$	95.1
$\overline{D^0} \to \bar{p}e^+$	94.2
$D^0 \to p\mu^-$	99.0
$\overline{D^0} \to p\mu^-$	99.0
$D^0 \to \bar{p}\mu^+$	99.0
$\overline{D^0} \to \bar{p}\mu^+$	99.0
$D^0 \to K^-\pi^+$	93.2

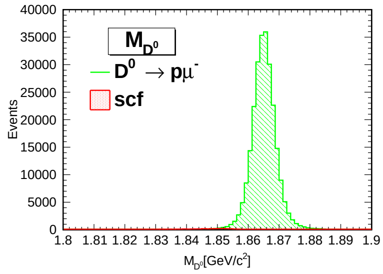

(A) $D^0 \to p\mu^-$

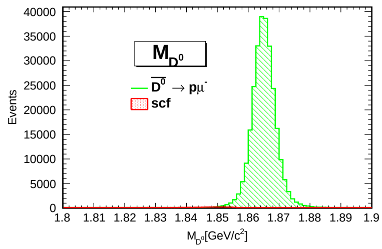

(B) $\overline{D^0} \to p\mu^-$

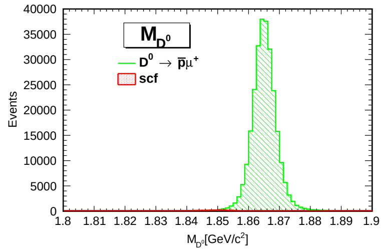

(C) $D^0 \to \bar{p}\mu^+$

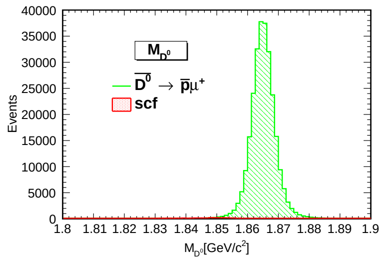

(D) $\overline{D^0} \to \bar{p}\mu^+$

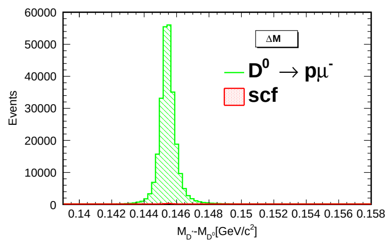

(E) $D^0 \to p\mu^-$

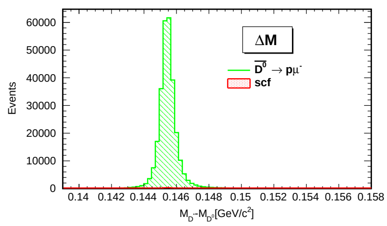

(F) $\overline{D^0} \to p\mu^-$

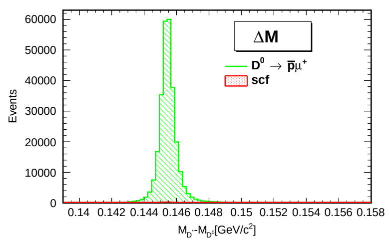

(G) $D^0 \to \bar{p}\mu^+$

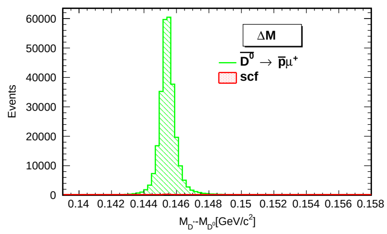

(H) $\overline{D^0} \to \bar{p}\mu^+$

FIGURE 2.23: The above plots (a-d) are for M_{D^0} distributions and (e-h) are for ΔM distributions for all the muonic modes in simulated sample.

2.4 Generic MC study

We looked at the generic MC sample, which consists of different types of events ($c\bar{c}, uds, b\bar{b}$, etc.) to study the background in detail. In our study, most of the backgrounds are coming from the charm sample. To get the best possible cut values of the variables, we optimize the figure of merit for particle identification variables, the momentum of the final state particles, and the D^* momentum in the center-of-mass frame. We do not choose optimal cuts for a few variables but rather loose cuts so that we can select more signals.

2.4.1 Optimisation

The distribution of the optimizing variables in generic MC are shown in Fig. 2.25 and Fig. 2.26 for $D^0 \to pe^-$ and $D^0 \to p\mu^-$ respectively. We maximize the figure of merit by varying the cuts. We have used a small signal approach [99] to optimize the figure of merits. The figure of merit (F.O.M.) is defined as

$$F.O.M. = \epsilon/(a/2 + \sqrt{N_{bkg}}) \tag{2.13}$$

where ϵ is the efficiency obtained from the signal MC and N_{bkg} is the number of backgrounds obtained from the background sample. As we are considering 90% confidence level, a is 3. For the optimization, we use signal enhance region which is defined as

$$1.85 < M_{D^0} < 1.875 \text{ GeV}/c^2$$

$$0.144 < \Delta M = (M_{D^*} - M_{D^0}) < 0.147 \text{ GeV}/c^2$$

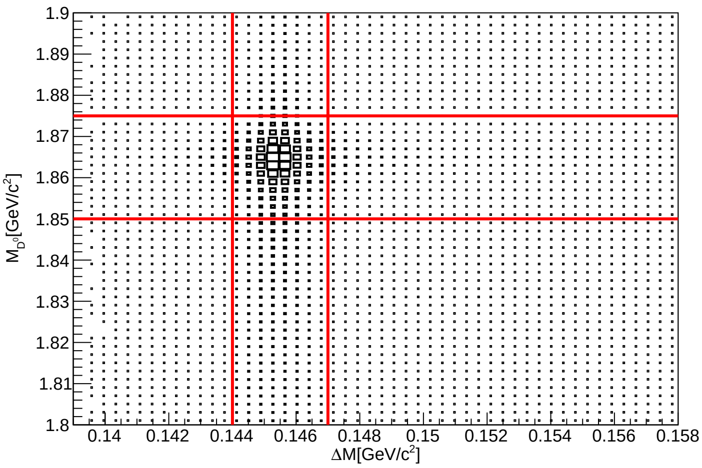

FIGURE 2.24: Two dimensional distribution between M_{D^0} [GeV/c^2] and ΔM [GeV/c^2] for the channel $D^0 \to pe^-$ is signal MC.

The selections cuts are 2.6σ, 2.3σ, respectively for ΔM and M_{D^0} distributions. These tight selection cuts are used to avoid the correlations between these two variables. The signal-enhanced region is visible in the Fig. 2.24.

The figure of merit curves of all the variables for electronic and muonic modes are shown below in Fig. 2.27 and Fig. 2.28.

We have listed all the final selection cuts in the Table 2.8 and Table 2.9 for the $D^0 \to pe^-$ and $D^0 \to p\mu^-$ respectively. We choose a little bit of loose cuts so that we can select more signals. We have followed this procedure for both modes. In the modes where we see the peaking background, we see similar optimized cuts like $D^0 \to p\ell^-$. In Fig. 2.29 and Fig. 2.30, we have shown the optimisation for the $D^0 \to \bar{p}e^+$ and $D^0 \to \bar{p}\mu^+$ modes respectively. The selection criteria mentioned in Table 2.8 and 2.9 is used for all electron and muon modes, respectively.

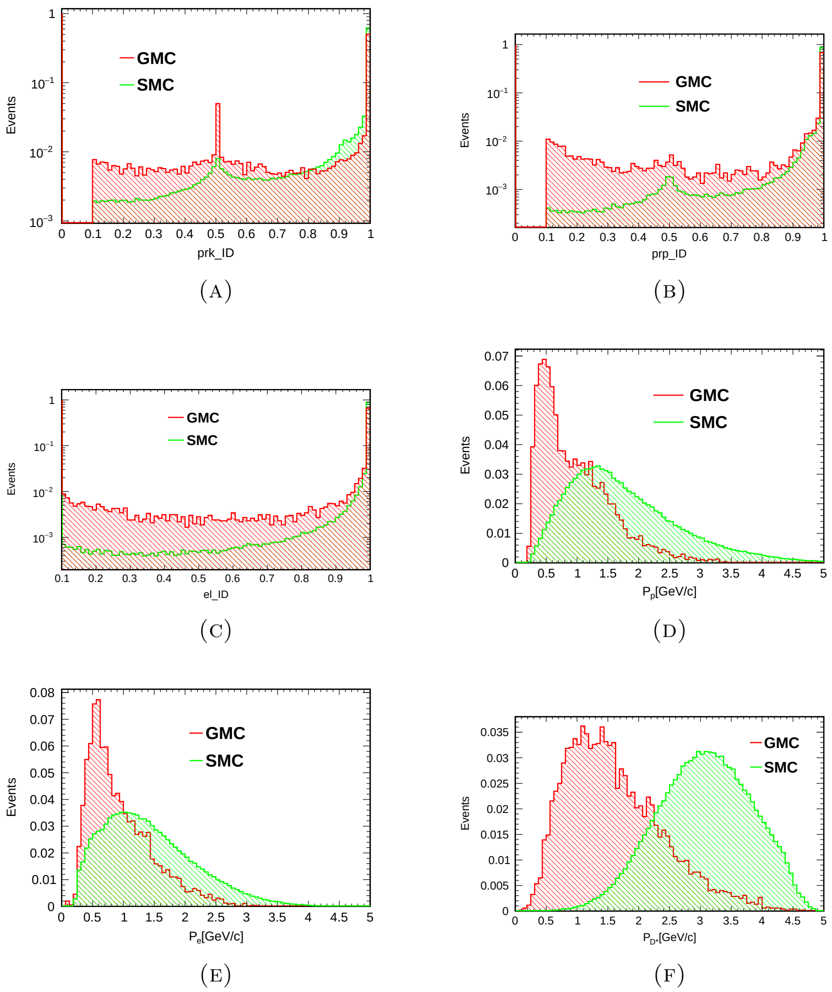

FIGURE 2.25: Distribution of variables in signal MC and generic MC of the decay $D^0 \to pe^-$ for the optimized variables (a)proton id w.r.t. kaon, (b)proton id w.r.t. pion, (c)electron id, (d)proton momentum, (e)electron momentum and (f)D^* momentum in center of mass frame.

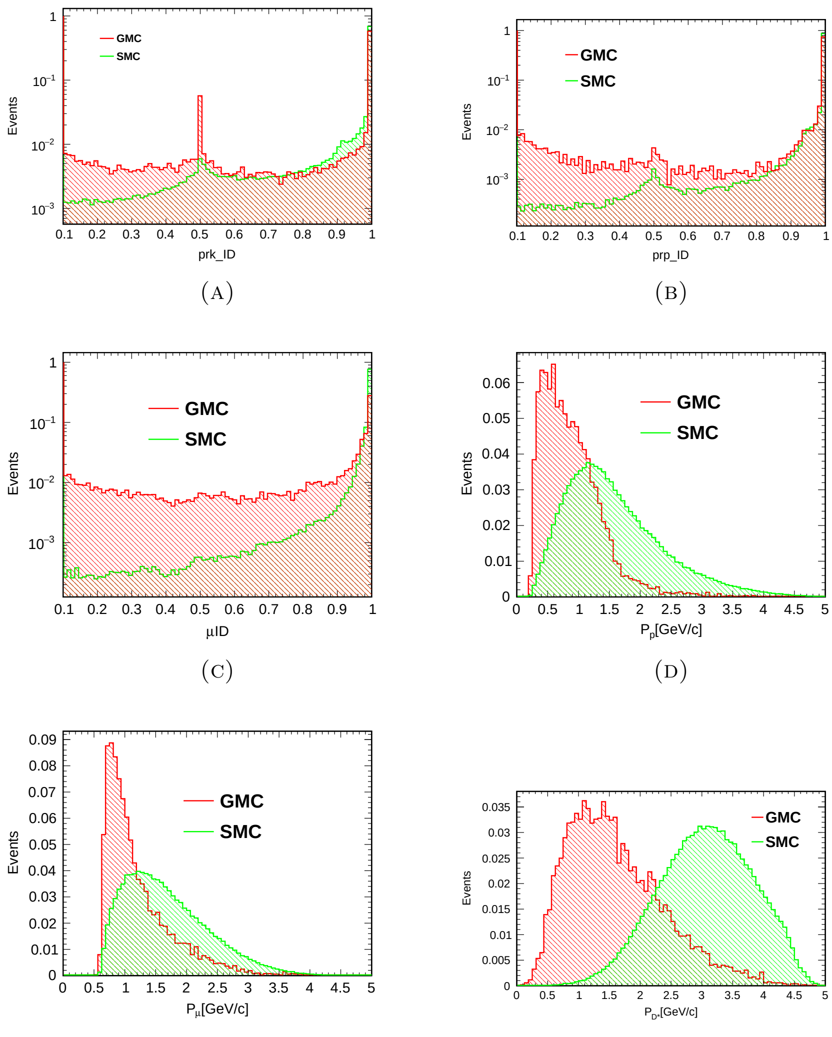

FIGURE 2.26: Distribution of variables in signal MC and generic MC of the decay $D^0 \to p\mu^-$ for the optimized variables (a)proton id w.r.t. kaon, (b)proton id w.r.t. pion, (c)muon id, (d)proton momentum, (e)muon momentum and (f)D^* momentum in center of mass frame.

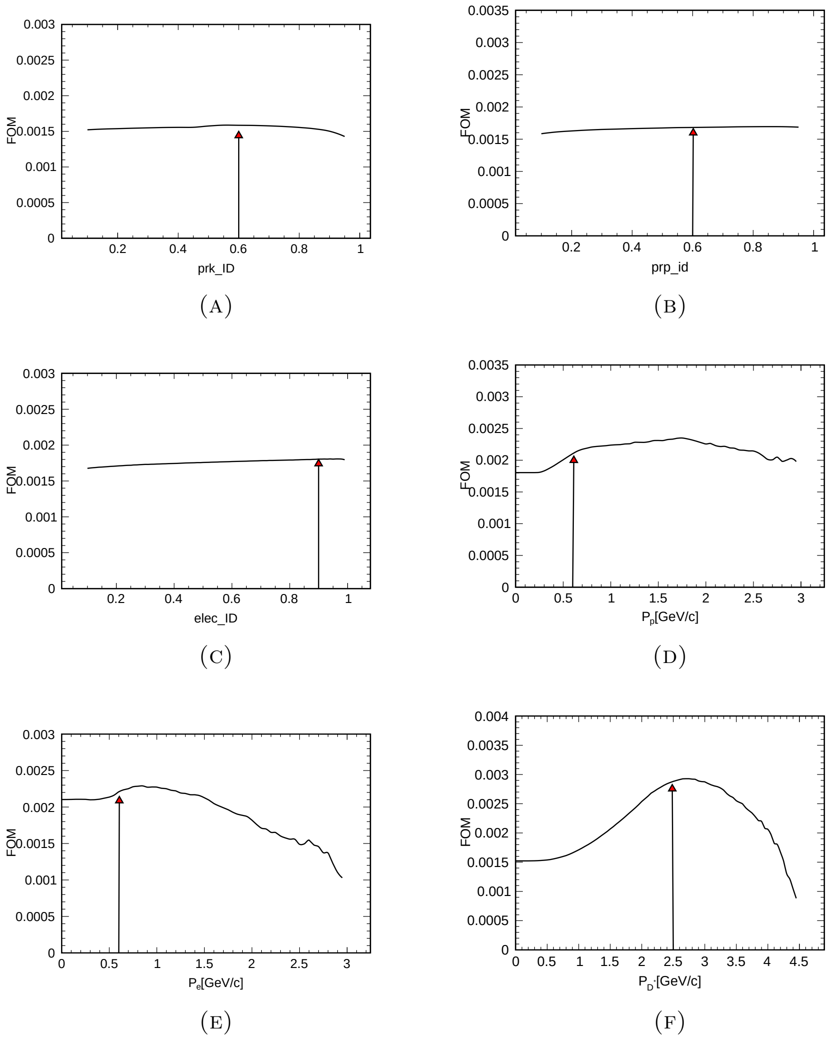

FIGURE 2.27: Figure of merit distribution of the decay $D^0 \to pe^-$ for the variables (a)proton id w.r.t. kaon, (b)proton id w.r.t. pion, (c)electron id, (d)proton momentum, (e)electron momentum, (f)D^* momentum in center of mass frame.

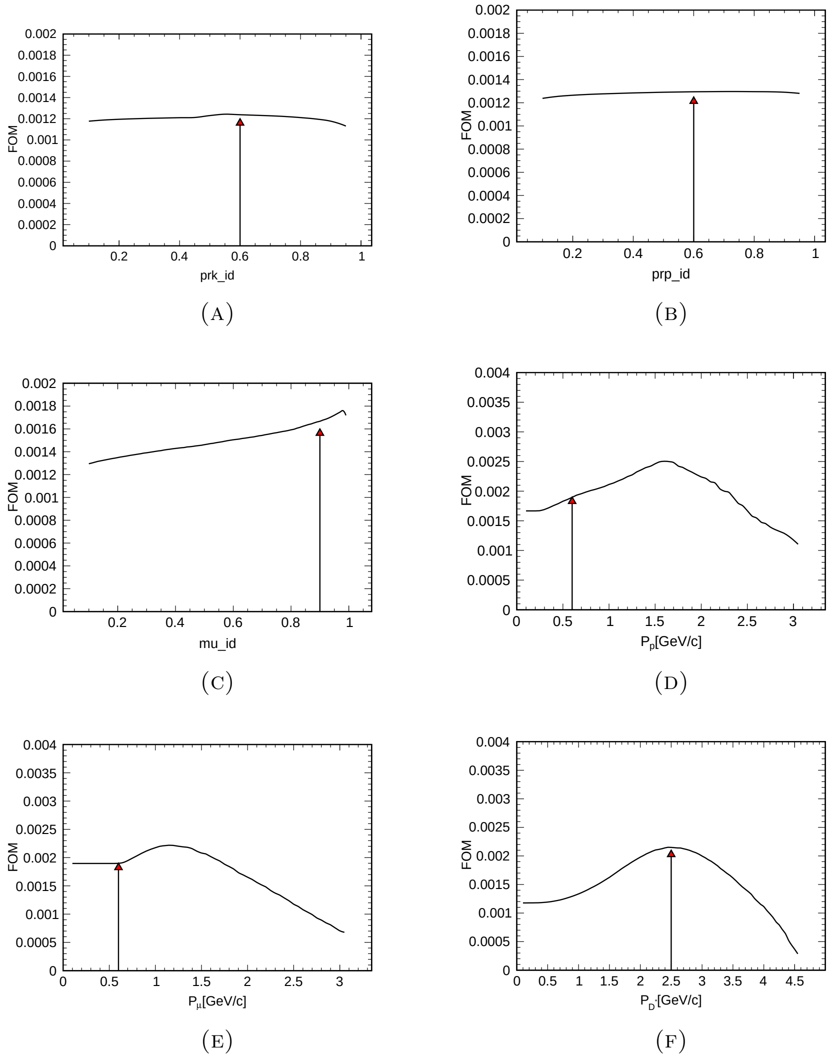

FIGURE 2.28: Figure of merit distribution of the decay $D^0 \rightarrow p\mu^-$ for the variables (a)proton id w.r.t. kaon, (b)proton id w.r.t. pion, (c)muon id, (d)proton momentum, (e)muon momentum and (f)D^* momentum in center of mass frame

.

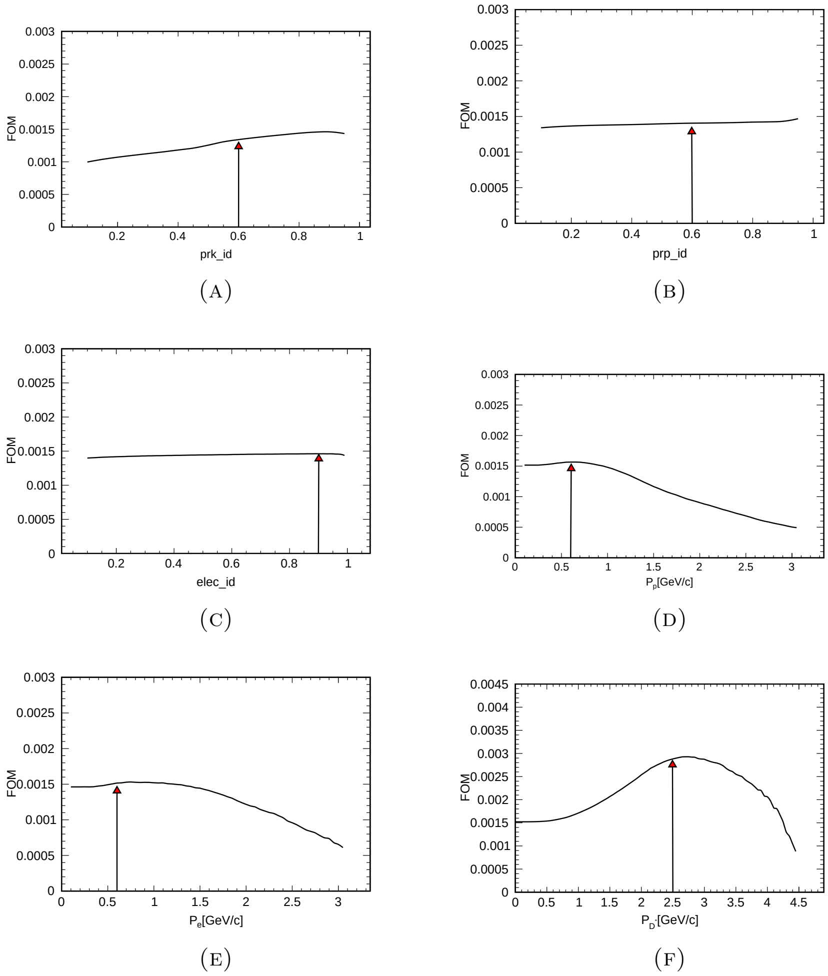

FIGURE 2.29: Figure of merit distribution of the decay $D^0 \to \bar{p}e^+$ for the variables (a)anti-proton id w.r.t. kaon, (b)anti-proton id w.r.t. pion, (c)positron id, (d)anti-proton momentum, (e)positron momentum, (f)D^* momentum in center of mass frame .

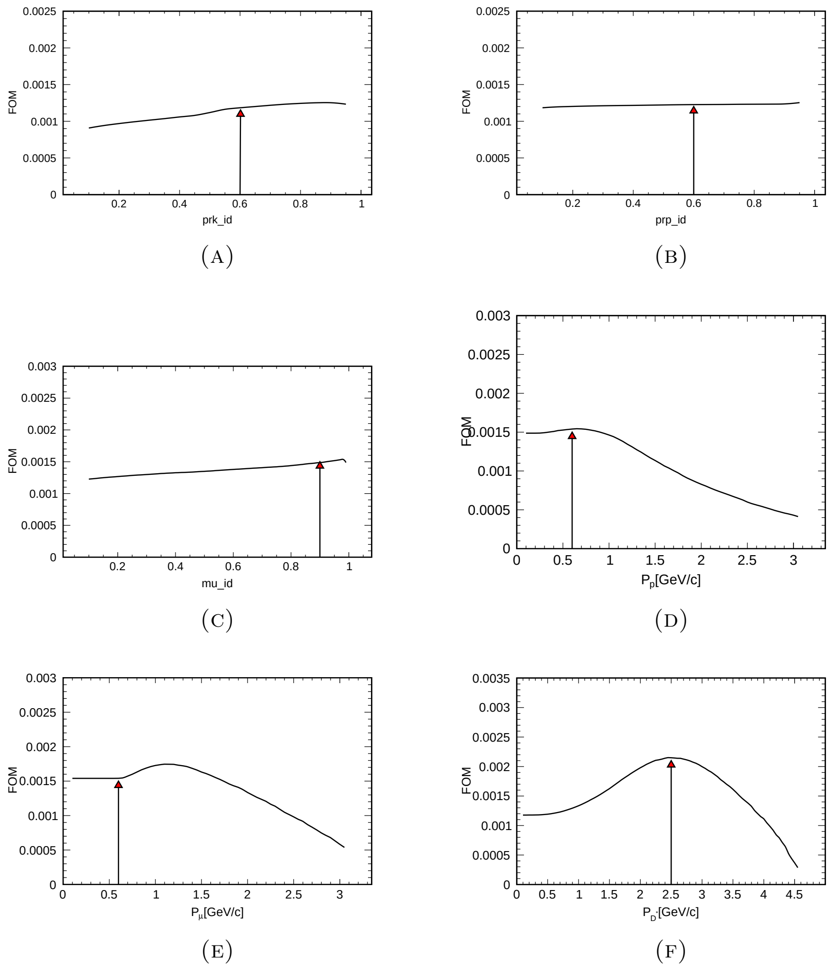

FIGURE 2.30: Figure of merit distribution of the decay $D^0 \to \bar{p}\mu^+$ for the variables (a)anti-proton id w.r.t. kaon, (b)anti-proton id w.r.t. pion, (c)anti-muon id, (d)anti-proton momentum, (e)anti-muon momentum and (f)D^* momentum in center of mass frame

.

TABLE 2.8: Sets of final selection cuts for the decay $D^0 \to pe^-$

channel	variables	optimised cuts
$D^0 \to pe^-$	$P_{p/K}$	> 0.6
	$P_{p/\pi}$	> 0.6
	eID=$\mathcal{L}_e/(\mathcal{L}_e + \mathcal{L}_{\bar{e}})$	> 0.9
	P_p	> 0.6 GeV/c
	P_e	> 0.6 GeV/c
	P_{D^*}	> 2.5 GeV/c

TABLE 2.9: Sets of final selection cuts for the decay $D^0 \to p\mu^-$

channel	variables	optimised cuts
$D^0 \to p\mu^-$	$P_{p/K}$	> 0.6
	$P_{p/\pi}$	> 0.6
	μID=$\mathcal{L}_\mu/(\mathcal{L}_\mu + \mathcal{L}_\pi + \mathcal{L}_K)$	> 0.9
	P_p	> 0.6 GeV/c
	P_μ	> 0.6 GeV/c
	P_{D^*}	> 2.5 GeV/c

2.4.2 Best Candidate Selection

The candidate multiplicity after applying the optimized set of cuts at the reconstruction level is shown in Fig. 2.31. After applying all sets of cuts, we have around 0.4% of events with multiple D^* candidates for all the modes. So we require an algorithm to pick the correct $D^* \to D\pi$, $D \to p\ell$ among all candidates. The D^0 candidate is selected having a smallest $\sum\chi^2$ where, $\sum\chi^2$ is related to the D^0 vertex fit. The final efficiency of best candidate selection(BCS) is defined as:

ϵ_{BCS} = Number of correct candidates selected in BCS/Number of events having multiplicity > 1, is found to be more than 80% for all the modes.

The percentage of multiple candidates and BCS efficiency are listed in Table 2.10.

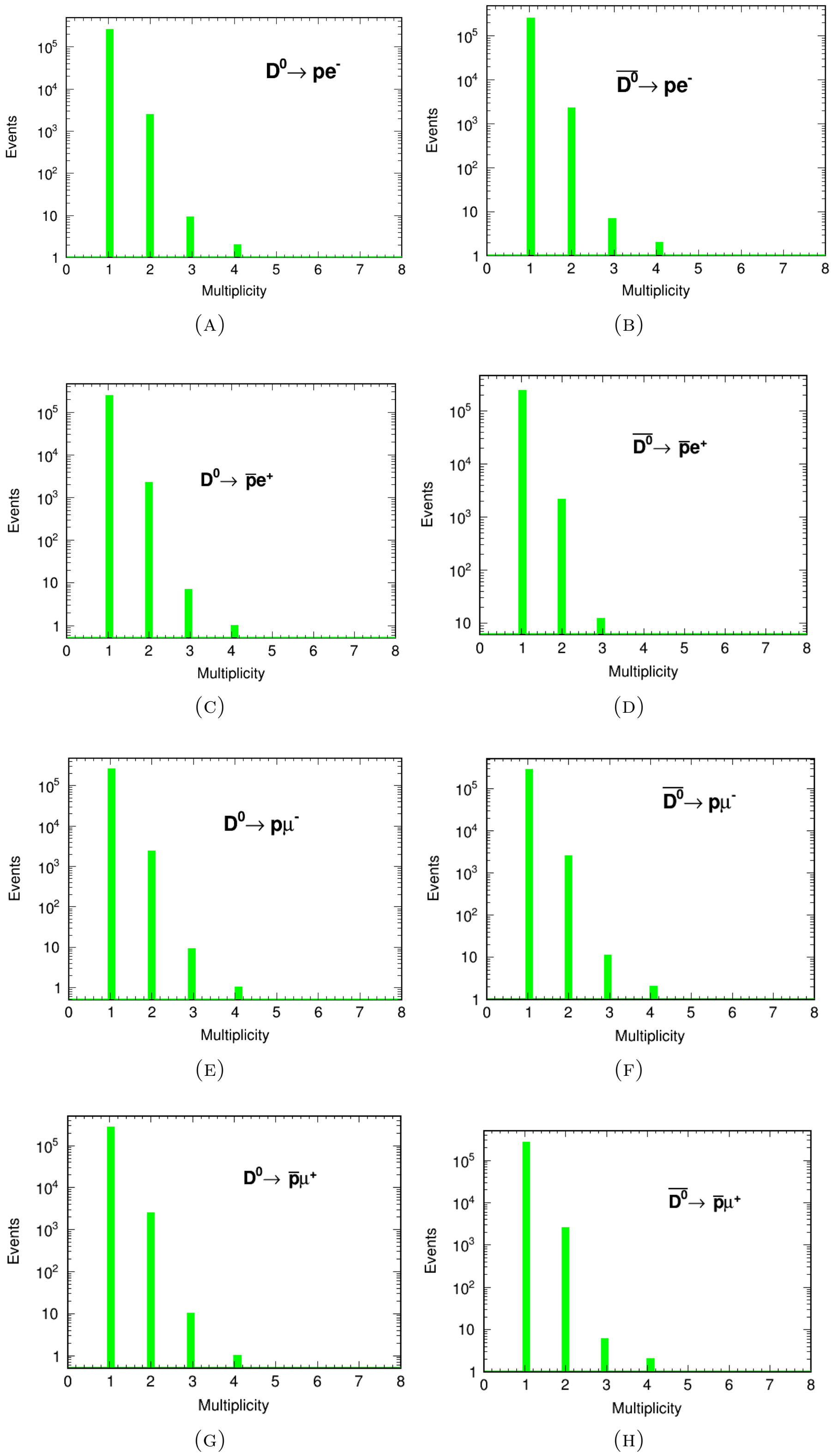

FIGURE 2.31: Multiplicity of the decay modes (a) $D^0 \rightarrow pe^-$, (b) $\overline{D^0} \rightarrow pe^-$ (c) $D^0 \rightarrow \bar{p}e^+$ (d) $\overline{D^0} \rightarrow \bar{p}e^+$ (e) $D^0 \rightarrow p\mu^-$ (f) $\overline{D^0} \rightarrow p\mu^-$ (g) $D^0 \rightarrow \bar{p}\mu^+$ and (h) $\overline{D^0} \rightarrow \bar{p}\mu^+$.

TABLE 2.10: Percentage of multiplicity and BCS efficiency for each decay mode. $\bar{\epsilon}_{BCS}$ is the BCS efficiency considering multiplicity=1.

Channels	multiplicity (%)	ϵ_{BCS}(%)	$\bar{\epsilon}_{BCS}$(%)
$D^0 \to pe^-$	0.4	86.1	92.4
$\overline{D^0} \to pe^-$	0.4	86.8	92.6
$D^0 \to \bar{p}e^+$	0.4	87.4	92.5
$\overline{D^0} \to \bar{p}e^+$	0.4	85.7	92.5
$D^0 \to p\mu^-$	0.4	94.5	99.4
$\overline{D^0} \to p\mu^-$	0.4	94.8	99.4
$D^0 \to \bar{p}\mu^+$	0.4	93.8	99.4
$\overline{D^0} \to \bar{p}\mu^+$	0.4	93.3	99.4

2.4.3 Efficiency determination

We have calculated the efficiency for our modes from the signal MC study. We perform a two-dimensional fit between M_{D^0} and ΔM. We generate two million signal MC for our signal modes and one million signal MC for the control mode. We plotted the projection of M_{D^0} in the signal enhanced region of ΔM which is defined as $0.144 < \Delta M < 0.147$ GeV/c^2 and also the projection of the ΔM is plotted in M_{D^0} signal enhanced region $1.85 < M_{D^0} < 1.875$ GeV/c^2. The fit distributions of M_{D^0} and ΔM are shown in Fig. 2.32 and Fig. 2.33 for electronic and muonic modes, respectively. We use the sum of two Gaussians and an Asymmetric Gaussian for the signal in M_{D^0} and for the signal in ΔM we use the sum of four Gaussians. To take into account the backgrounds we use the Chebychev polynomial and Threshold function for the M_{D^0} and ΔM respectively. The means and sigmas are listed in Table 2.12 and Table 2.13 for M_{D^0} and ΔM respectively. The efficiency values are listed in Table 2.11.

Table 2.11: Efficiency values for all the decay modes after two-dimensional fits between M_{D^0} and ΔM using signal MC.

Channels	Efficiency(%)
$D^0 \to pe^-$	10.58 ± 0.028
$\overline{D^0} \to pe^-$	10.54 ± 0.028
$D^0 \to \bar{p}e^+$	10.10 ± 0.027
$\overline{D^0} \to \bar{p}e^+$	10.04 ± 0.027
$D^0 \to p\mu^-$	11.27 ± 0.024
$\overline{D^0} \to p\mu^-$	11.22 ± 0.025
$D^0 \to \bar{p}\mu^+$	10.87 ± 0.024
$\overline{D^0} \to \bar{p}\mu^+$	10.81 ± 0.024

Table 2.12: Summary of the mean and widths of the PDFs from fit of M_{D^0} in the Fig. 2.32 and Fig. 2.33. `a2a` is the fraction of the core gaussian w.r.t. the second gaussian.

`Channels`	`mean1_md`	$M^{gen}_{D^0} - M^{rec}_{D^0}$	`a2a`	`sigma1_md`	`sigma2_mds`
$D^0 \to pe^-$	1.86458 ± 0.000013	0.00026	0.196 ± 0.0030	0.00315 ± 0.00002	0.00782 ± 0.00013
$\overline{D^0} \to pe^-$	1.86472 ± 0.000012	0.00012	0.401 ± 0.0087	0.00779 ± 0.00011	0.00328 ± 0.00002
$D^0 \to \bar{p}e^+$	1.86459 ± 0.000030	0.00025	0.430 ± 0.019	0.00758 ± 0.00015	0.00314 ± 0.00003
$\overline{D^0} \to \bar{p}e^+$	1.86462 ± 0.000011	0.00022	0.388 ± 0.016	0.00562 ± 0.00017	0.00304 ± 0.000039
$D^0 \to p\mu^-$	1.86499 ± 0.000008	-0.00015	0.170 ± 0.012	0.00530 ± 0.00015	0.00297 ± 0.00003
$\overline{D^0} \to p\mu^-$	1.86499 ± 0.000008	-0.00015	0.100 ± 0.0008	0.00274 ± 0.00002	0.00430 ± 0.00003
$D^0 \to \bar{p}\mu^+$	1.86498 ± 0.000008	-0.00014	0.100 ± 0.0012	0.00279 ± 0.00002	0.00429 ± 0.00003
$\overline{D^0} \to \bar{p}\mu^+$	1.86498 ± 0.000008	-0.00014	0.154 ± 0.008	0.00521 ± 0.00018	0.00295 ± 0.00003

TABLE 2.13: Summary of the mean and widths of the PDFs from the fit of ΔM in the Fig. 2.32 and Fig. 2.33. `a2a_dm1` is the fraction of the core gaussian w.r.t. the second gaussian. `a2a_dm` is the fraction for the addition of the first two gaussians with the third gaussian. `a2a_dm2` is the fraction for the addition of the first three gaussians with the fourth gaussian.

Channels	mean1_dm mean3_dm mean4_dm	ΔM^{gen}-ΔM^{rec}	sigma1_dm sigma2_dm sigma3_dm sigma4_dm	a2a_dm a2a_dm1 a2a_dm2
$D^0 \to pe^-$	0.1453988 ± 0.0000027 0.1454552 ± 0.0000037 0.146445 ± 0.000075	0.00004 -0.00002 -0.00101	0.0002429 ± 0.0000067 0.001053 ± 0.000044 0.0004650 ± 0.0000098 0.00308 ± 0.00011	0.415 ± 0.018 0.727 ± 0.028 0.9642 ± 0.0022
$\overline{D^0} \to pe^-$	0.1454065 ± 0.0000023 0.1454627 ± 0.0000045 0.146541 ± 0.000097	0.00003 -0.00003 -0.00111	0.0002556 ± 0.0000062 0.001110 ± 0.000063 0.000486 ± 0.000012 0.00318 ± 0.00014	0.457 ± 0.019 0.804 ± 0.024 0.9653 ± 0.0026
$D^0 \to \bar{p}e^+$	0.1453988 ± 0.0000026 0.1454565 ± 0.0000026 0.146728 ± 0.000092	0.00004 -0.00002 -0.00129	0.0002322 ± 0.0000043 0.001082 ± 0.000030 0.0004560 ± 0.0000046 0.00322 ± 0.00011	0.386 ± 0.012 0.704 ± 0.015 0.9663 ± 0.0017
$\overline{D^0} \to \bar{p}e^+$	0.1454088 ± 0.0000023 0.1454590 ± 0.0000043 0.14657 ± 0.00012	0.00003 -0.00002 -0.00114	0.0002565 ± 0.0000064 0.001143 ± 0.000061 0.000487 ± 0.000012 0.00332 ± 0.00018	0.462 ± 0.021 0.799 ± 0.023 0.9678 ± 0.0027
$D^0 \to p\mu^-$	0.1453994 ± 0.000002 0.145593 ± 0.000001 0.146479 ± 0.00006	0.00004 -0.00016 -0.00104	0.0002402 ± 0.0000047 0.0004556 ± 0.000007 0.000976 ± 0.000024 0.002968 ± 0.000027	0.8599 ± 0.0071 0.362 ± 0.018 0.9632 ± 0.0016
$\overline{D^0} \to p\mu^-$	0.1454105 ± 0.0000022 0.1454573 ± 0.0000029 0.146605 ± 0.000084	0.00002 -0.00002 -0.00117	0.0002491 ± 0.0000037 0.002742 ± 0.000021 0.001039 ± 0.000027 0.00323 ± 0.00011	0.457 ± 0.013 0.741 ± 0.013 0.9677 ± 0.0016
$D^0 \to \bar{p}\mu^+$	0.1454033 ± 0.0000020 0.1454711 ± 0.0000029 0.14747 ± 0.00092	0.00003 -0.00004 -0.00204	0.0002565 ± 0.0000029 0.001239 ± 0.000087 0.0005030 ± 0.0000061 0.0042 ± 0.0010	0.4777 ± 0.0099 0.7911 ± 0.0090 0.9777 ± 0.0051
$\overline{D^0} \to \bar{p}\mu^+$	0.1454041 ± 0.0000024 0.1454524 ± 0.0000034 0.146737 ± 0.000098	0.00003 -0.00002 -0.0013	0.0002383 ± 0.0000062 0.001034 ± 0.000034 0.0004602 ± 0.0000093 0.00335 ± 0.00013	0.430 ± 0.017 0.723 ± 0.026 0.9689 ± 0.0016

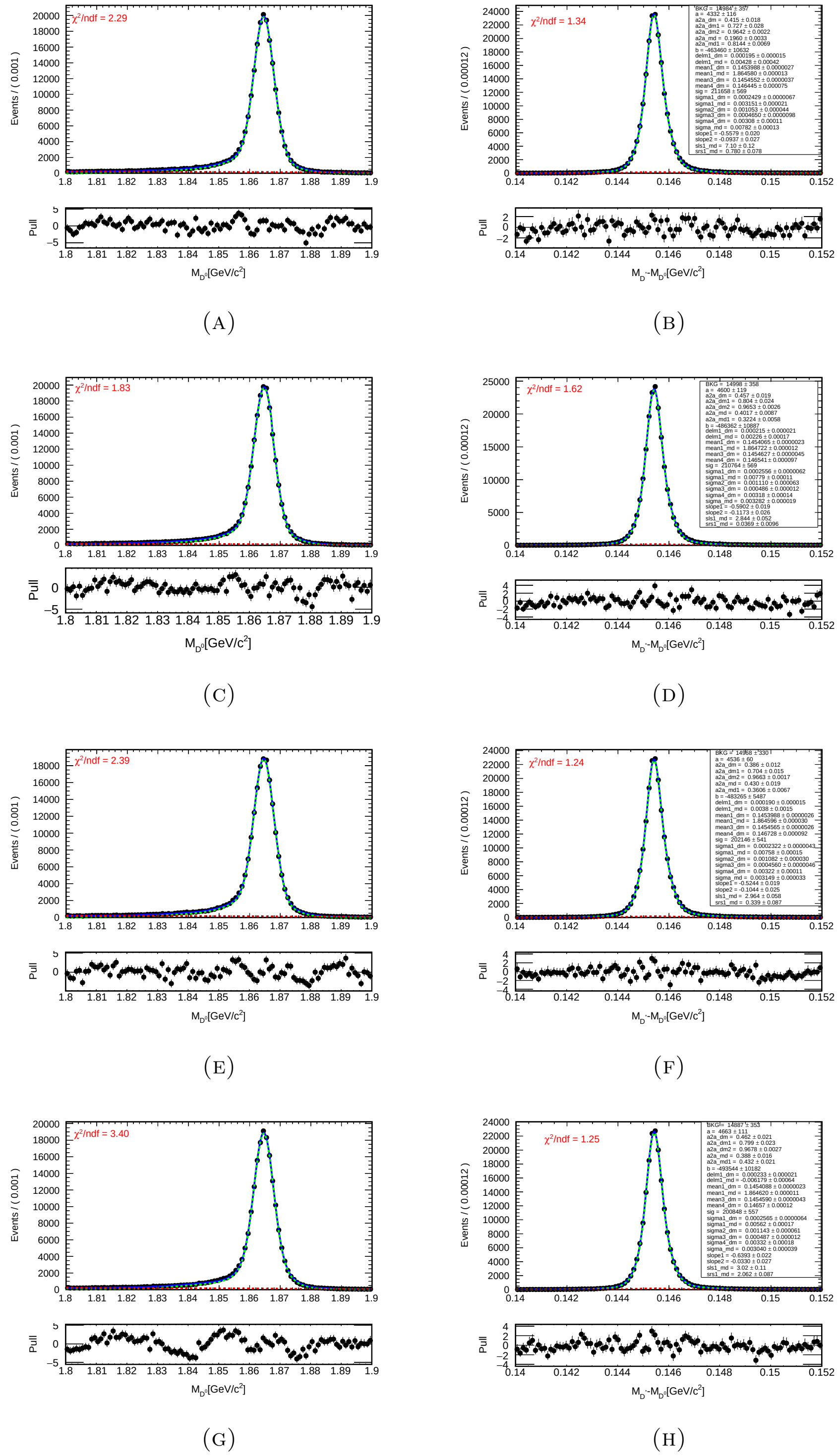

FIGURE 2.32: Two dimensional fit between M_{D^0} and ΔM in signal MC (a),(b) $D^0 \to pe^-$, (c),(d) $\overline{D^0} \to pe^-$ (e),(f) $D^0 \to \bar{p}e^+$ and (g),(h) $\overline{D^0} \to \bar{p}e^+$.

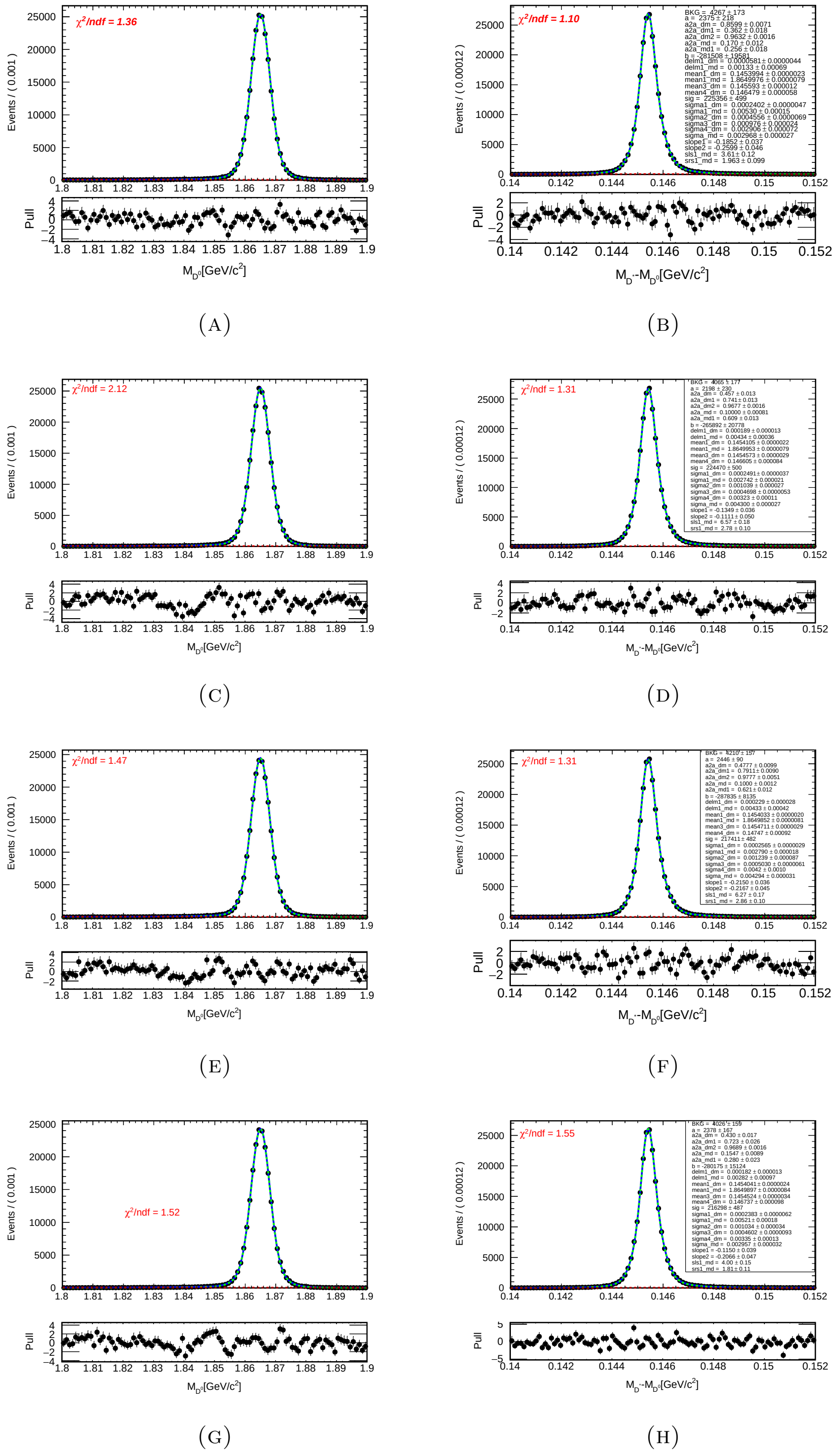

FIGURE 2.33: Two dimensional fit between M_{D^0} and ΔM in signal MC (a)(b) $D^0 \to p\mu^-$ (c),(d) $\overline{D^0} \to p\mu^-$ (e),(f) $D^0 \to \bar{p}\mu^+$ and (g),(h) $\overline{D^0} \to \bar{p}\mu^+$.

2.4.4 Background Study

As expected, the major background comes from the charm sample. We get peaking backgrounds in $\bar{D}^0 \to pe^-$, $D^0 \to \bar{p}e^+$, $D^0 \to p\mu^-$, $\bar{D}^0 \to p\mu^-$, $D^0 \to \bar{p}\mu^+$ and $\bar{D}^0 \to \bar{p}\mu^+$. For the $\bar{D}^0 \to pe^-$, $D^0 \to \bar{p}e^+$ modes we see peaking structures in the ΔM distributions which are due to the $D \to Ke\nu_e$. For the $\bar{D}^0 \to p\mu^-$, $D^0 \to \bar{p}\mu^+$ modes we see peaking structures in the ΔM distributions which are due to the $D \to K\rho$, $D \to K^*\pi$, $D \to KK$ in addition to the semileptonic D decays. We also see a tiny peaking structure coming from the $D \to KK$ for the $D^0 \to p\mu^-$ and $\bar{D}^0 \to \bar{p}\mu^+$ channels.

We see these peaking structures in the signal region because of the misidentification between the final state particles (FSPs). A two-dimensional scatter plot between M_{D^0} and ΔM of peaking component $\bar{D}^0 \to K^+e^-\overline{\nu_e}$ for the mode $\bar{D}^0 \to pe^-$ is shown in Fig. 2.34. Since we plan to do a two-dimensional fit between M_{D^0} and ΔM, we check both the distribution using a generic Monte Carlo sample. The distributions for the M_{D^0} and ΔM are shown in the Fig. 2.35 to Fig. 2.42 for all the modes. We have modeled the peaking background using a 1-D fit. The $D \to Ke\nu_e$ component in ΔM is modeled using two Asymmetric Gaussians and M_D is modeled by first-order polynomial for the electronic modes.

The $D \to K\mu\nu_\mu$, $D \to K\rho$, $D \to K^*\pi$ components in ΔM is modeled using two Asymmetric Gaussians and the $D \to KK$ component is modeled with double Gaussians. The peaking backgrounds in M_D are modeled by first-order polynomials for the muonic modes also.

The combinatorial background in ΔM is well modeled by a Threshold function, defined as

$$f(\Delta M) = (\Delta M - m_\pi)^a e^{-b(\Delta M - m_\pi)}, \tag{2.14}$$

,

where m_π is the known charged pion mass [3] and a, b are the shape parameters. We fix the Threshold parameter to the slow pion mass for all the fits. We also summarized the background level for each mode in the Table 2.14 and Table 2.15 in the signal-enhanced region of M_D and ΔM. In the overall two-dimensional fit between M_{D^0} and ΔM we fix all the parameters from the individual fits and we float the combinatorial background and signal events number for the modes where we see the peaking structure.

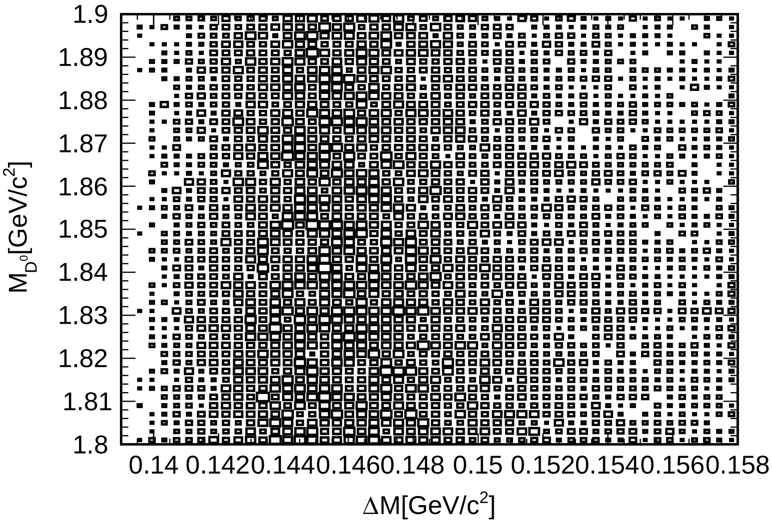

FIGURE 2.34: Two dimensional distribution between M_{D^0}[GeV/c^2] and ΔM[GeV/c^2 of peaking component $\bar{D^0} \to K^+ e^- \overline{\nu_e}$ for the mode $\bar{D^0} \to pe^-$ in generic MC.

- **2.4.4.1** $D^0 \to pe^-$

For the mode $D^0 \to pe^-$, the distribution of M_{D^0} and ΔM are shown in Fig. 2.35. We do not see any peaking component either in M_{D^0} or in ΔM. M_{D^0} can be well modeled by a Chebychev polynomial of the first order as the ΔM is modeled by a Threshold function. A two dimensional fit between M_{D^0} and ΔM is also shown in the Fig. 2.35.

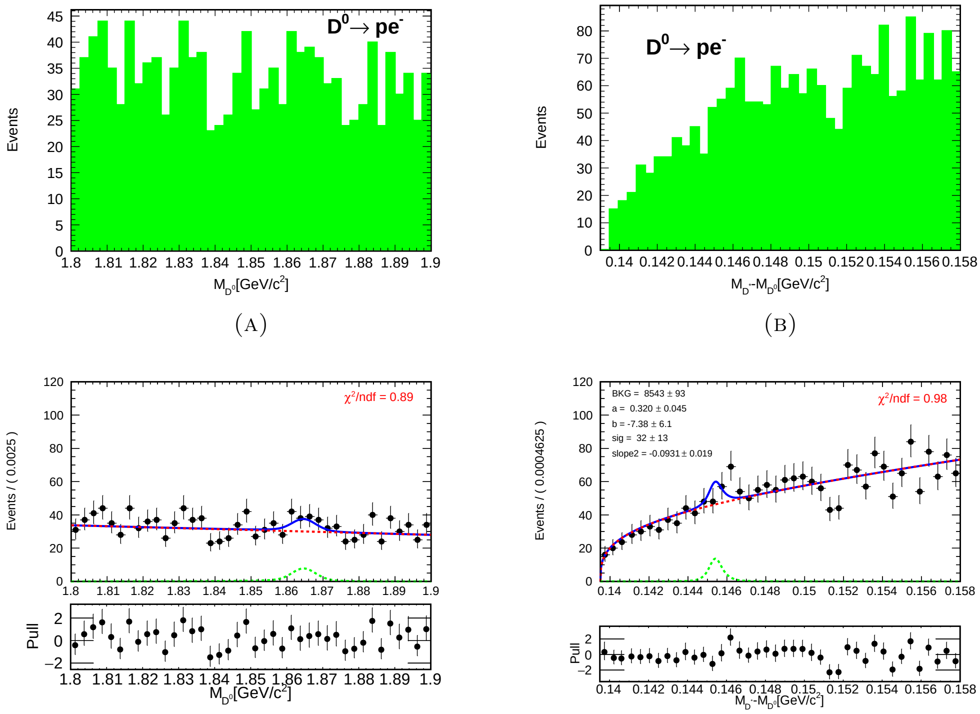

(A) (B)

(C) (D)

FIGURE 2.35: Distribution of (a)M_{D^0}[GeV/c^2] and (b)ΔM[GeV/c^2] for the channel $D^0 \to pe^-$ after applying the optimised set of cuts. Bottom plots are for two-dimensional fit results between (c)M_{D^0}[GeV/c^2] and (d)ΔM[GeV/c^2] using 6×711 fb^{-1} of generic MC. The red color is the combinatorial background component both in M_{D^0} and ΔM in the fitted diagram.

- **2.4.4.2** $\bar{D^0} \to pe^-$

For the mode $\bar{D^0} \to pe^-$, the distribution of M_{D^0} and ΔM are shown in Fig. 2.36. We see a peaking component in ΔM distribution coming from semileptonic D^0 decay mode $\bar{D^0} \to K^+e^-\overline{\nu_e}$. M_{D^0} can be well modeled by a Chebychev polynomial of the first order. The peaking component in ΔM is fitted by two asymmetric Gaussians with different mean. The combinatorial component in ΔM is well-fitted by a Threshold function. A two dimensional fit between M_{D^0} and ΔM is also shown in the Fig. 2.36.

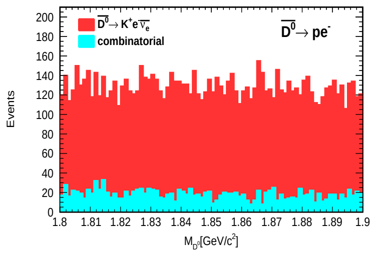

(A)

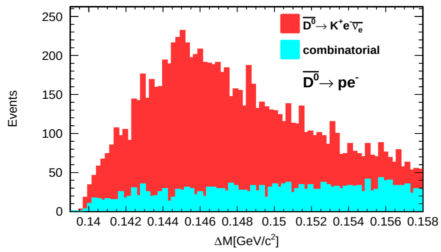

(B)

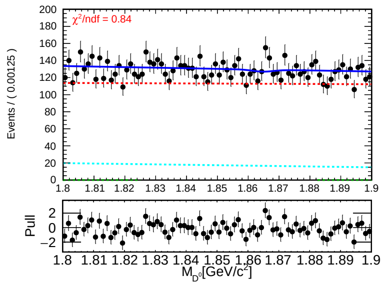

(C)

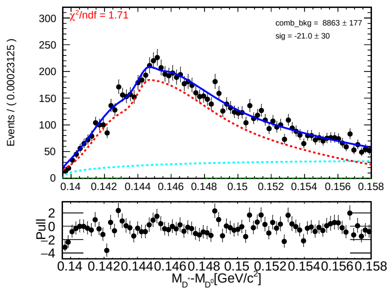

(D)

FIGURE 2.36: Distribution of (a)M_{D^0}[GeV/c^2] and (b)ΔM[GeV/c^2] for the channel $\bar{D^0} \to pe^-$ after applying the optimised set of cuts. The peaking component is shown in the red color in (b). The cyan component is the combinatorial background shown in all the diagrams. Bottom plots are for two-dimensional fit results between (c)M_{D^0}[GeV/c^2] and (d)ΔM[GeV/c^2] using 6×711 fb^{-1} of generic MC.

- **2.4.4.3** $D^0 \to \bar{p}e^+$

For the mode $D^0 \to \bar{p}e^+$, the distribution of M_{D^0} and ΔM are shown in Fig. 2.37. We see a peaking component in ΔM distribution originating from semileptonic D^0 decay mode $D^0 \to K^- e^+ \nu_e$. M_{D^0} can be well modeled by a Chebychev polynomial of first order. The peaking component in ΔM is fitted by two asymmetric Gaussians with different mean. The combinatorial component in ΔM is well-fitted by a Threshold function. A two dimensional fit between M_{D^0} and ΔM is also shown in the Fig. 2.37.

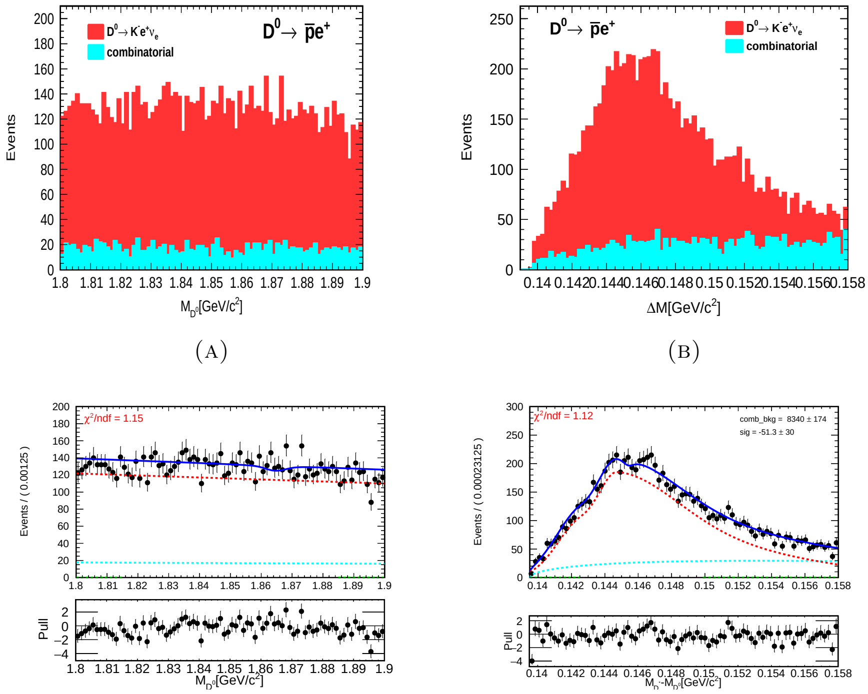

(A) (B) (C) (D)

FIGURE 2.37: Distribution of (a)M_{D^0}[GeV/c^2] and (b)ΔM[GeV/c^2] for the channel $D^0 \to \bar{p}e^+$ after applying the optimised set of cuts. The peaking component is shown in the red color in (b). The cyan component is the combinatorial background shown in all the diagrams. Bottom plots are for two-dimensional fit results between (c)M_{D^0}[GeV/c^2] and (d)ΔM[GeV/c^2] using 6×711 fb^{-1} of generic MC.

- **2.4.4.4** $\bar{D^0} \to \bar{p}e^+$

For the mode $\bar{D}^0 \to \bar{p}e^+$, the distribution of M_{D^0} and ΔM are shown in Fig. 2.38. We do not see any peaking component neither in M_{D^0} nor in ΔM like $D^0 \to pe^-$. M_{D^0} can be well modeled by a Chebychev polynomial of the first order as the ΔM is modeled by a Threshold function. A two dimensional fit between M_{D^0} and ΔM is also shown in the Fig. 2.38.

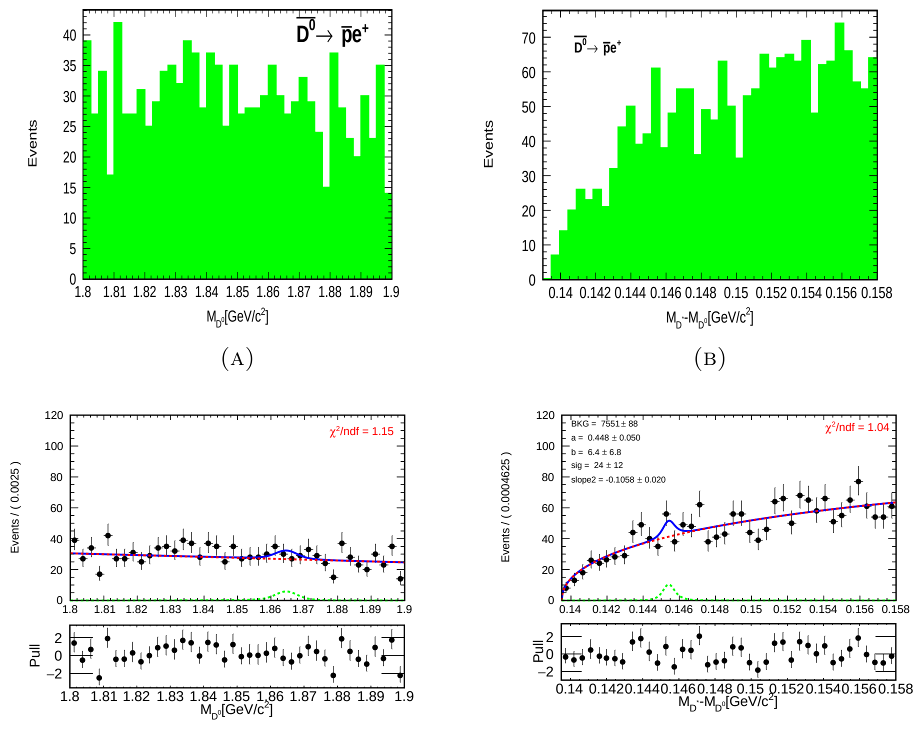

(A) (B)

(C) (D)

FIGURE 2.38: Distribution of (a)M_{D^0}[GeV/c^2] and (b)ΔM[GeV/c^2] for the channel $\bar{D^0} \to \bar{p}e^+$ after applying the optimised set of cuts. Bottom plots are for two-dimensional fit results between (c)M_{D^0}[GeV/c^2] and (d)ΔM[GeV/c^2] using 6×711 fb^{-1} of generic MC. The red color is the combinatorial background component both in M_{D^0} and ΔM in the fitted diagram.

- **2.4.4.5** $D^0 \to p\mu^-$

For the mode $D^0 \to p\mu^-$, the distribution of M_{D^0} and ΔM are shown in Fig. 2.39. Here we observe a peaking component in ΔM arising from $D^0 \to K^-K^+$. $D^0 \to K^-K^+$ component is well modeled by double Gaussians in ΔM and in M_{D^0} it is modeled by a Chebychev polynomial of the first order. The combinatorial background in M_{D^0} can be well modeled by a Chebychev polynomial of the first order whereas the ΔM is modeled by a Threshold function. A two dimensional fit between M_{D^0} and ΔM is also shown in the Fig. 2.39.

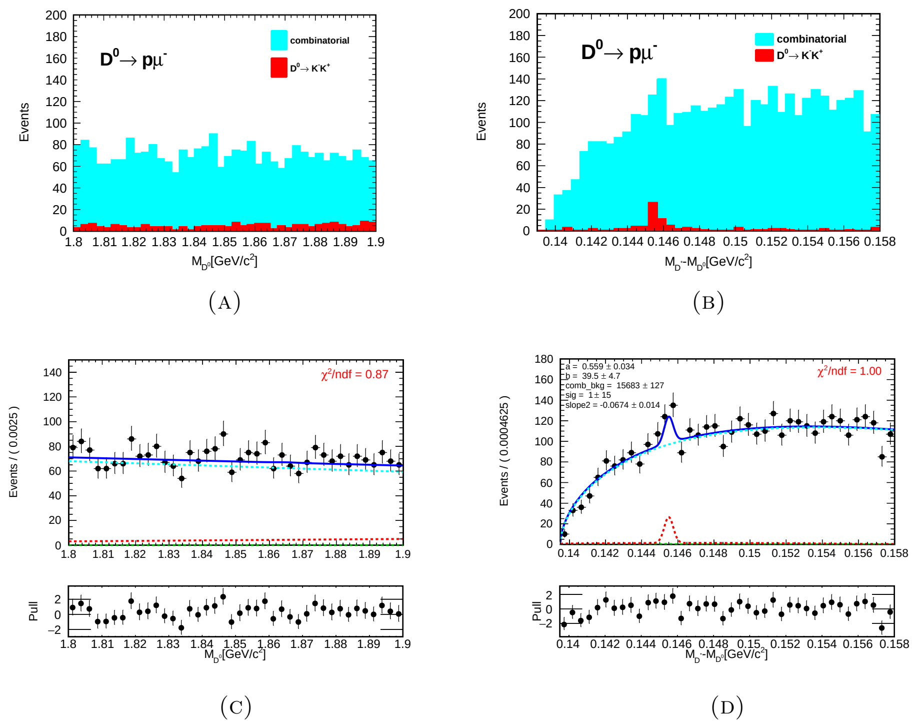

FIGURE 2.39: Distribution of (a)M_{D^0}[GeV/c^2] and (b)ΔM[GeV/c^2] for the channel $D^0 \to p\mu^-$ after applying the optimised set of cuts. Bottom plots are for two-dimensional fit results between (c)M_{D^0}[GeV/c^2] and (d)ΔM[GeV/c^2] using 6×711 fb^{-1} of generic MC. The red color is the combinatorial background component both in M_{D^0} and ΔM in the fitted diagram.

- **2.4.4.6** $\bar{D^0} \to p\mu^-$

For the mode $\bar{D^0} \to p\mu^-$, the distribution of M_{D^0} and ΔM are shown in Fig. 2.40. We see peaking structures in the ΔM distributions which are due to the $D \to K\rho$, $D \to K^*\pi$, $D \to KK$ in addition to the semileptonic D decays. The $D \to K\mu\nu_\mu$, $D \to K\rho$, $D \to K^*\pi$ components in ΔM are modeled by using two Asymmetric Gaussians and the $D \to KK$ component is modeled with double Gaussians. The peaking backgrounds in M_D are modeled by first-order polynomials. The combinatorial component in M_{D^0} can be well modeled by a Chebycheb polynomial of first order. The combinatorial component in ΔM is well-fitted by a Threshold function. A two dimensional fit between M_{D^0} and ΔM is also shown in the Fig. 2.40.

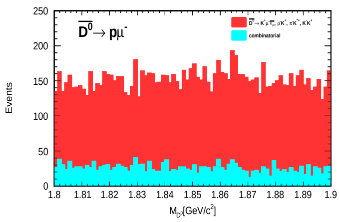

(A)

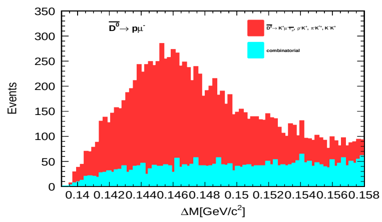

(B)

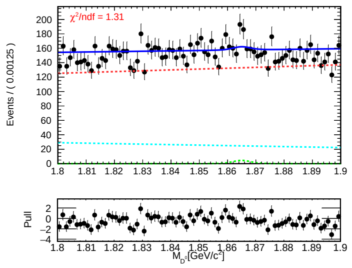

(C)

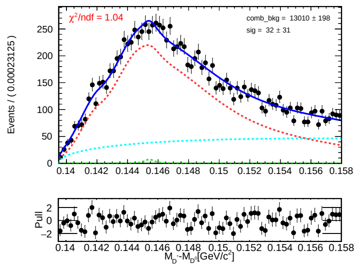

(D)

FIGURE 2.40: Distribution of (a)M_{D^0}[GeV/c^2] and (b)ΔM[GeV/c^2] for the channel $\bar{D^0} \to p\mu^-$ after applying the optimised set of cuts. The peaking component is shown in the red color in (b). The cyan component is the combinatorial background shown in all the diagrams. Bottom plots are for two-dimensional fit results between (c)M_{D^0}[GeV/c^2] and (d)ΔM[GeV/c^2] using 6×711 fb^{-1} of generic MC.

- **2.4.4.7** $D^0 \to \bar{p}\mu^+$

For the mode $D^0 \to \bar{p}\mu^+$, the distribution of M_{D^0} and ΔM are shown in Fig. 2.41. We see peaking structures in the ΔM distributions which are due to the $D \to K\rho$, $D \to K^*\pi$, $D \to KK$ in addition to the semileptonic D decays. The $D \to K\mu\nu_\mu$, $D \to K\rho$, $D \to K^*\pi$ components in ΔM are modeled by using two Asymmetric Gaussians and the $D \to KK$ component is modeled with double Gaussians. The peaking backgrounds in M_D are modeled by the first-order polynomial. The combinatorial component in M_{D^0} can also be well modeled by a Chebycheb polynomial of first order. The combinatorial component in ΔM is well fitted by a Threshold function. A two dimensional fit between M_{D^0} and ΔM is also shown in the Fig. 2.41.

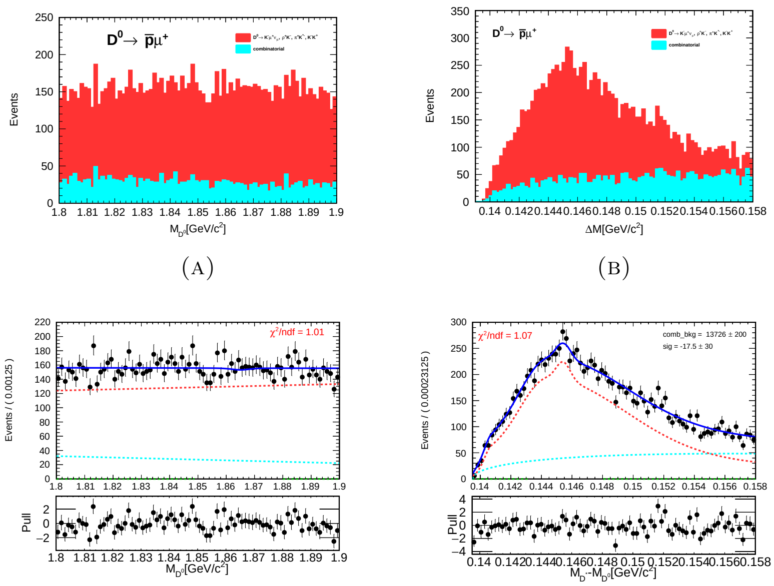

(A) (B) (C) (D)

FIGURE 2.41: Distribution of (a)M_{D^0}[GeV/c^2] and (b)ΔM[GeV/c^2] for the channel $D^0 \to \bar{p}\mu^+$ after applying the optimised set of cuts. The peaking component is shown in the red color in (b). The cyan component is the combinatorial background shown in all the diagrams. Bottom plots are for two-dimensional fit results between (c)M_{D^0}[GeV/c^2] and (d)ΔM[GeV/c^2] using 6×711 fb^{-1} of generic MC.

- **2.4.4.8** $\bar{D^0} \to \bar{p}\mu^+$

For the mode $\bar{D}^0 \to \bar{p}\mu^+$, the distribution of M_{D^0} and ΔM are shown in Fig. 2.42. Here we observe a peaking component in ΔM originating from $\bar{D^0} \to K^-K^+$. $\bar{D^0} \to K^-K^+$ component is well modeled by double Gaussians in ΔM and in M_{D^0} it is modeled by a Chebychev polynomial of the first order. The combinatorial background in M_{D^0} can also be well modeled by a Chebychev polynomial of the first order whereas the ΔM is modeled by a Threshold function. A two dimensional fit between M_{D^0} and ΔM is also shown in the Fig. 2.42.

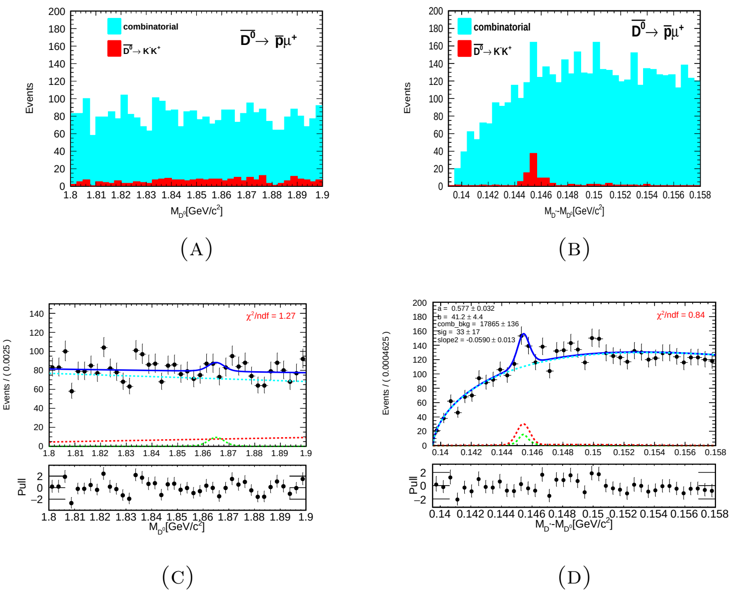

Figure 2.42: Distribution of (a)M_{D^0}[GeV/c^2] and (b)ΔM[GeV/c^2] for the channel $\bar{D^0} \to \bar{p}e^+$ after applying the optimised set of cuts. Bottom plots are for two-dimensional fit results between (c)M_{D^0}[GeV/c^2] and (d)ΔM[GeV/c^2] using 6×711 fb^{-1} of generic MC. The red color is the combinatorial background component both in M_{D^0} and ΔM in the fitted diagram.

TABLE 2.14: Summary of the background level for each mode in M_{D^0} distributions in signal enhanced region of ΔM.

	B^+B^-	B^0B^0	charm		uds
Channels	comb.	comb.	peaking	comb.	comb.
$D^0 \to pe^-$	391	243	-	417	287
$\overline{D^0} \to pe^-$	369	377	8793	581	149
$D^0 \to \bar{p}e^+$	341	337	8857	645	76
$\overline{D^0} \to \bar{p}e^+$	381	223	-	348	228
$D^0 \to p\mu^-$	439	307	195	1473	420
$\overline{D^0} \to p\mu^-$	432	413	10006	861	444
$D^0 \to \bar{p}\mu^+$	382	447	10029	880	646
$\overline{D^0} \to \bar{p}\mu^+$	439	263	241	1787	503

TABLE 2.15: Summary of the background level for each mode in ΔM distributions in signal enhanced region of M_{D^0}.

	B^+B^-	$B^0\bar{B}^0$	charm		uds
Channels	comb.	comb.	peaking	comb.	comb.
$D^0 \to pe^-$	679	471	-	525	417
$\overline{D^0} \to pe^-$	663	662	7212	608	220
$D^0 \to \bar{p}e^+$	611	594	7150	630	119
$\overline{D^0} \to \bar{p}e^+$	659	405	-	470	330
$D^0 \to p\mu^-$	764	532	78	1840	768
$\overline{D^0} \to p\mu^-$	757	729	8449	1006	742
$D^0 \to \bar{p}\mu^+$	631	715	8426	968	1016
$\overline{D^0} \to \bar{p}\mu^+$	755	486	93	2228	922

2.5 Fit Validation

In order to determine the stability of the fit procedure and to check fit bias, a Toy MC study is performed. We generated 2000 toys for each mode using the signal and background PDF parameters and yield obtained from the fit to generic MC (after including Poisson fluctuation in yield generation and also scaling the yields to data luminosity). After the toy generation, we fit each toy with the same PDFs and calculated the return yield. Finally, we check the pull distribution with respect to the input yields. In case the parameter is unbiased, the corresponding pull distribution is a Gaussian of zero mean and unity width.

$$Pull = \frac{Yield_{sig}^{fit} - Yield_{sig}^{gen}}{\sigma_{fit}} \tag{2.15}$$

As a consistency check, we also perform a linearity test by changing the signal yields. Here also, we generate 2000 toys at each step and we see fitter is well stable. The distribution of toys for each mode can be seen from Fig. 2.43 to Fig. 2.50.

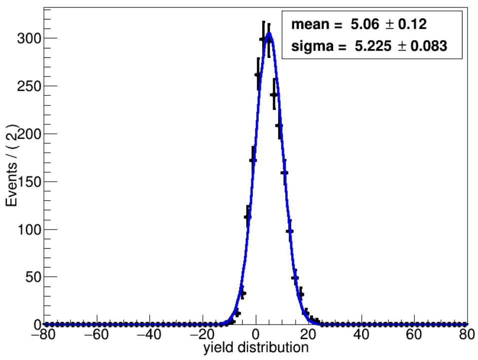

(A)

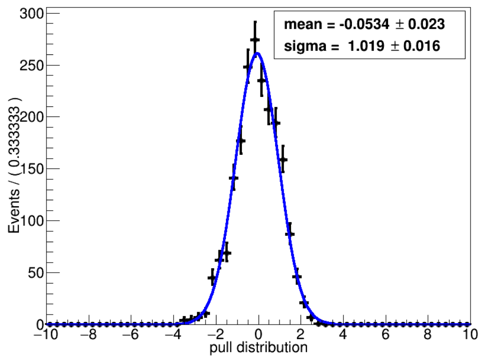

(B)

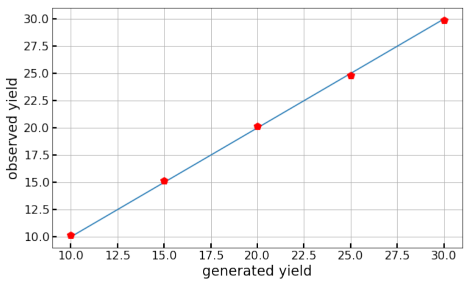

(C)

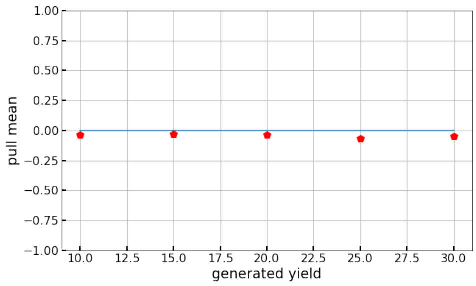

(D)

FIGURE 2.43: Results of the Toy MC study for the decay $D^0 \to pe^-$: (a) extracted signal yield (b) pull distribution (c) input versus output signal yield fitted with first-order polynomial (d) input signal yield versus pull mean, the (blue) dashed line shows the behavior of pull means in ideal case.

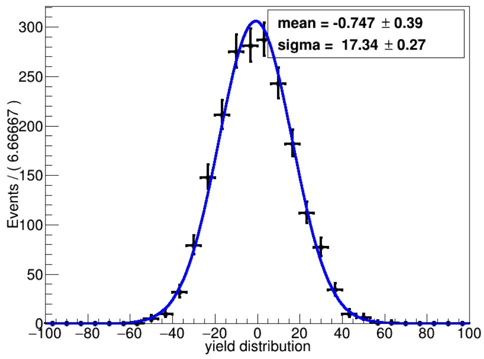

(A)

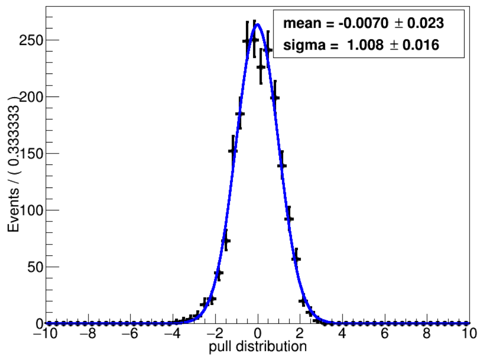

(B)

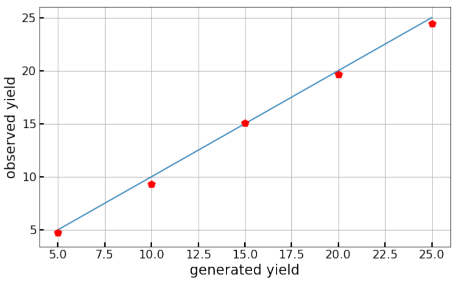

(C)

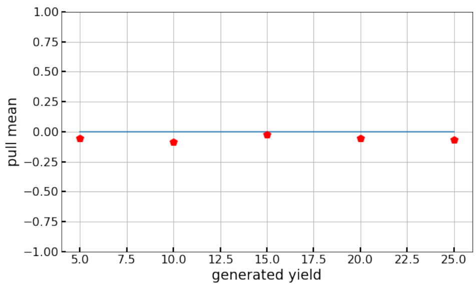

(D)

FIGURE 2.44: Results of the Toy MC study for the decay $\overline{D^0} \to pe^-$: (a) extracted signal yield (b) pull distribution (c) input versus output signal yield fitted with first-order polynomial (d) input signal yield versus pull mean, the (blue) dashed line shows the behavior of pull means in ideal case.

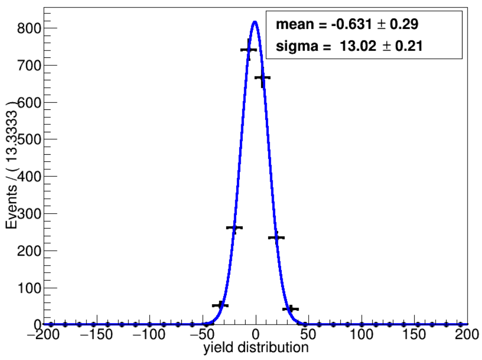

(A)

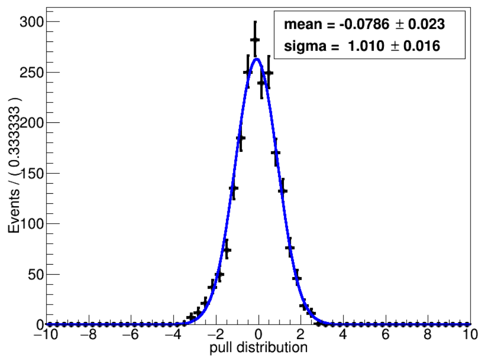

(B)

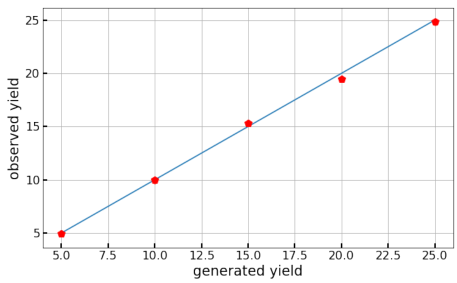

(C)

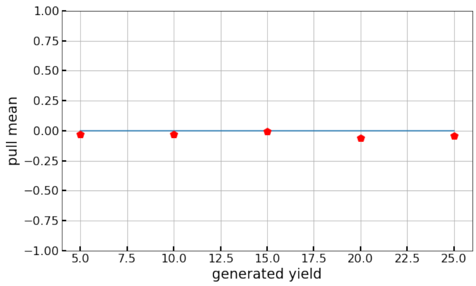

(D)

FIGURE 2.45: Results of the Toy MC study for the decay $D^0 \to \bar{p}e^+$: (a) extracted signal yield (b) pull distribution (c) input versus output signal yield fitted with first-order polynomial (d) input signal yield versus pull mean, the (blue) dashed line shows the behavior of pull means in ideal case.

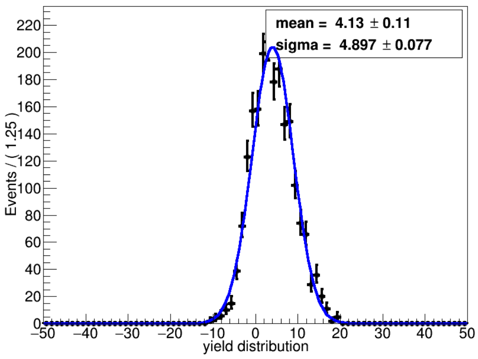

(A)

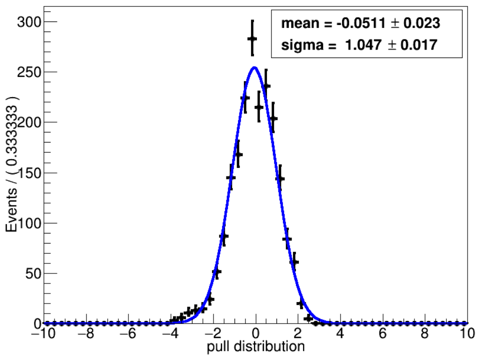

(B)

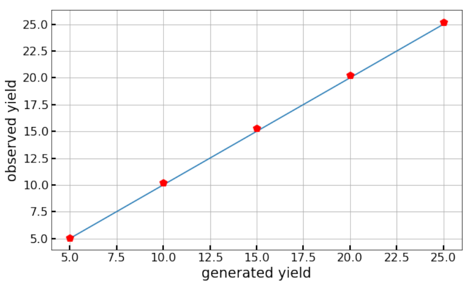

(C)

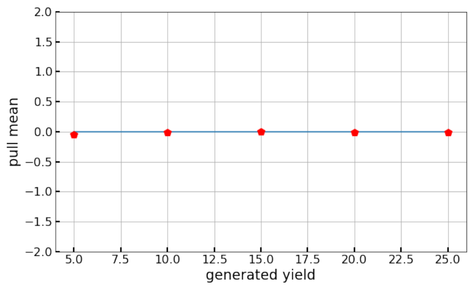

(D)

FIGURE 2.46: Results of the Toy MC study for the decay $\overline{D^0} \to \bar{p}e^+$: (a) extracted signal yield (b) pull distribution (c) input versus output signal yield fitted with first-order polynomial (d) input signal yield versus pull mean, the (blue) dashed line shows the behavior of pull means in an ideal case.

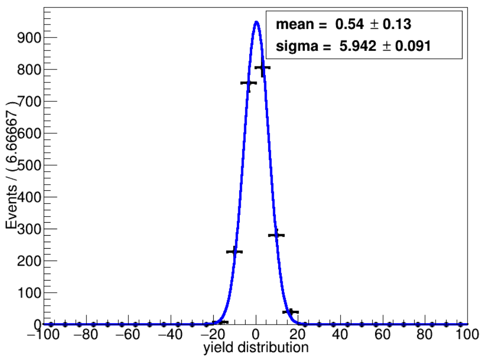

(A)

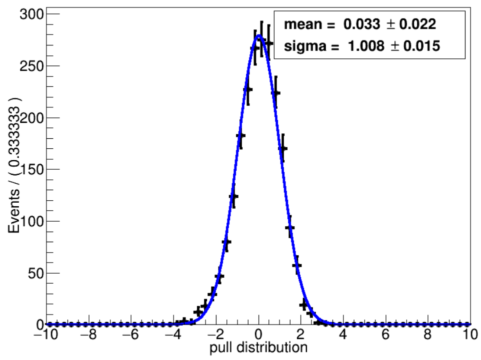

(B)

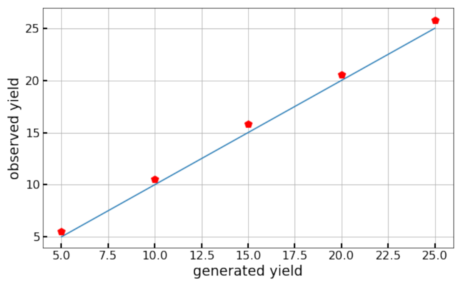

(C)

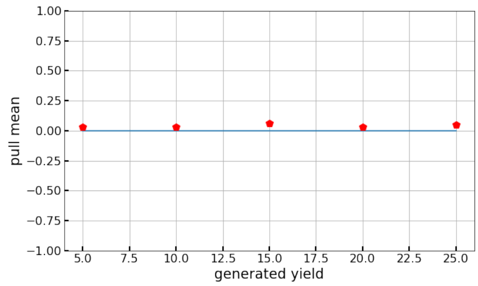

(D)

FIGURE 2.47: Results of the Toy MC study for the decay $D^0 \to p\mu^-$: (a) extracted signal yield (b) pull distribution (c) input versus output signal yield fitted with first-order polynomial (d) input signal yield versus pull mean, the (blue) dashed line shows the behavior of pull means in ideal case.

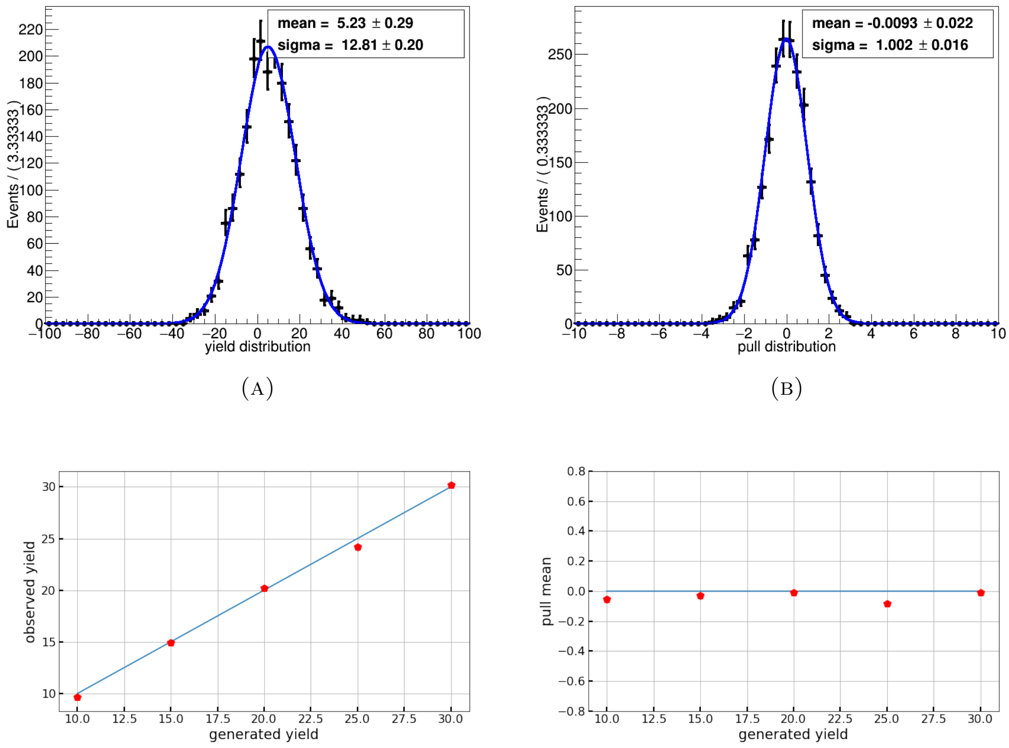

(a)

(b)

(c)

(d)

FIGURE 2.48: Results of the Toy MC study for the decay $\overline{D^0} \to p\mu^-$: (a) extracted signal yield (b) pull distribution (c) input versus output signal yield fitted with first-order polynomial (d) input signal yield versus pull mean, the (blue) dashed line shows the behavior of pull means in ideal case.

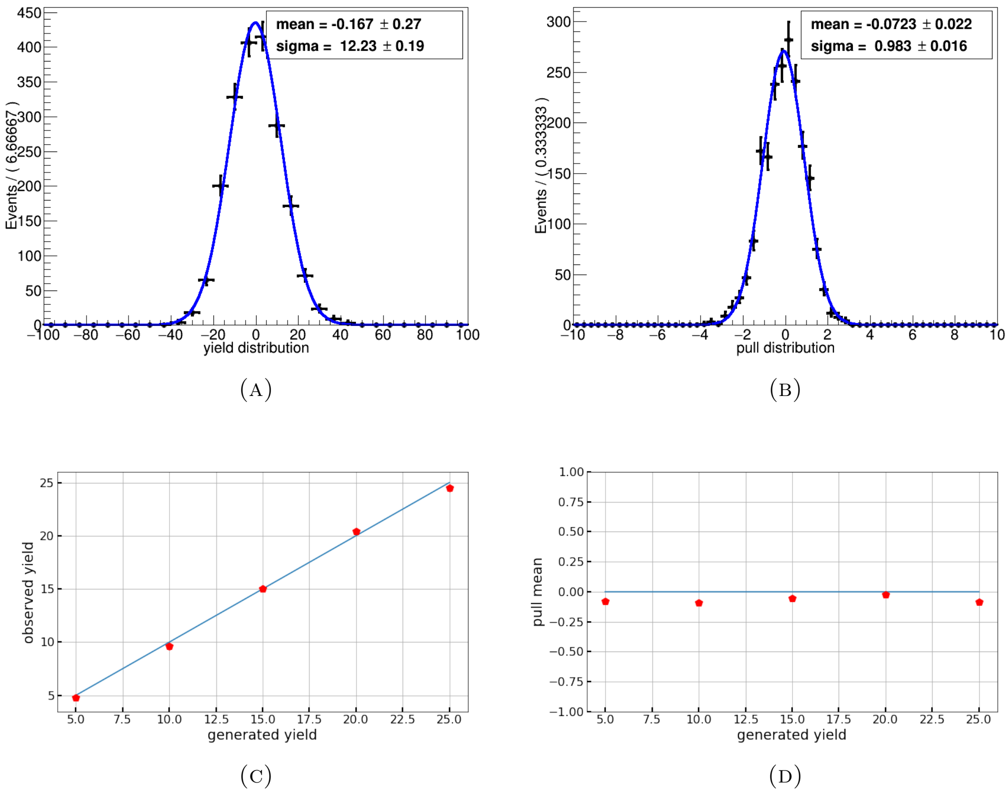

FIGURE 2.49: Results of the Toy MC study for the decay $D^0 \to \bar{p}\mu^+$: (a) extracted signal yield (b) pull distribution (c) input versus output signal yield fitted with first-order polynomial (d) input signal yield versus pull mean, the (blue) dashed line shows the behavior of pull means in ideal case.

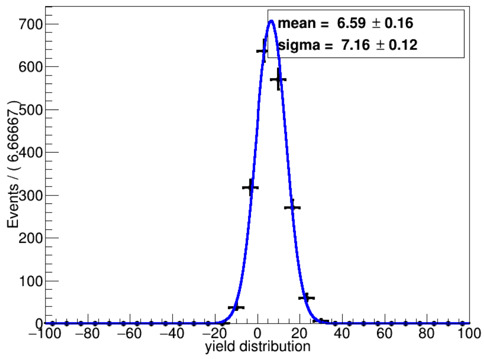

(A)

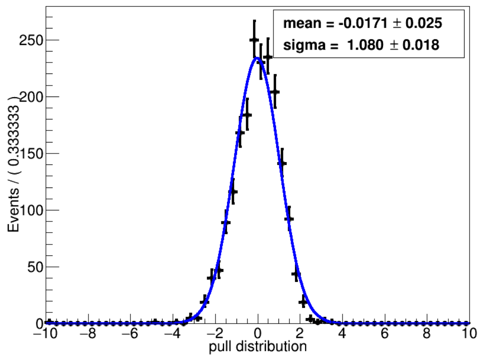

(B)

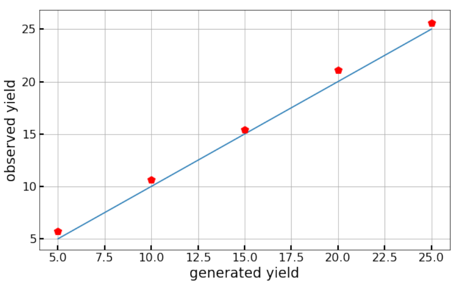

(C)

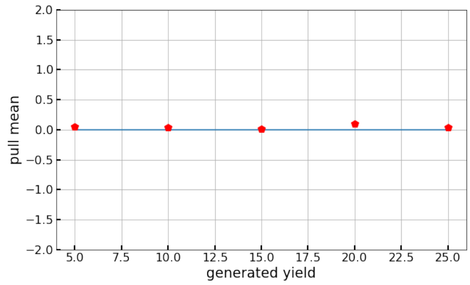

(D)

FIGURE 2.50: Results of the Toy MC study for the decay $\overline{D^0} \to \bar{p}\mu^+$: (a) extracted signal yield (b) pull distribution (c) input versus output signal yield fitted with first-order polynomial (d) input signal yield versus pull mean, the (blue) dashed line shows the behavior of pull means in ideal case.

2.6 Upper Limit Estimation

This analysis method is tested on the 6×711 fb^{-1} of generic MC. We have used signal MC PDFs in our generic MC fit and obtained some numbers for signal yields.

After scaling to data luminosity, we didn't observe significant signals. So, we have provided the Upper Limit (UL) at 90% confidence level (CL) on the signal yield for each signal decay mode using the frequentist method. We generated the 2000 samples of different signal yields using PDFs. Fit is performed on the generated samples and CL is calculated as the fraction of samples where the yield (from ToyMC) is more than the signal yield. Then, we smeared the yield distribution obtained from Toy MC by systematic uncertainty to include the systematic uncertainty as shown in Fig. 2.51. Signal yields, U.L. on the signal yields without and with systematics are given in Table 2.16. We have also estimated the upper limit on branching fractions at 90% confidence level and summarized in Table 2.16. We will use this method in data to measure upper limits.

All the values necessary for the calculation of the branching fraction are listed in Table 2.11 and Table 2.16. The branching fraction of the normalisation channel is $\mathcal{B}_{D^0\to K^-\pi^+} = 3.89 \times 10^{-2}$ (taken from DECAY.DEC). We see an improvement of order in magnitude as expected.

TABLE 2.16: Summary of the yields and U.L. at 90% confidence level for each mode where MC is scaled to data luminosity.

Channels	Expected yields	U.L.(w/o syst.)	U.L.(with syst.)	Branching Fraction (@ 90% C.L.)
$D^0 \to pe^-$	5.33 ± 2.16	13	14	3.9×10^{-7}
$\overline{D^0} \to pe^-$	-3.55 ± 5	17.5	18.5	5.2×10^{-7}
$D^0 \to \bar{p}e^+$	-8.55 ± 5	18.5	20.2	5.9×10^{-7}
$\overline{D^0} \to \bar{p}e^+$	4 ± 2	11.0	12.3	3.6×10^{-7}
$D^0 \to p\mu^-$	0.166 ± 2.5	9.0	11.2	2.9×10^{-7}
$\overline{D^0} \to p\mu^-$	5.33 ± 5.16	23	24.9	6.6×10^{-7}
$D^0 \to \bar{p}\mu^+$	-2.91 ± 5	17.5	18.9	5.2×10^{-7}
$\overline{D^0} \to \bar{p}\mu^+$	5.5 ± 2.63	17	17.9	4.9×10^{-7}

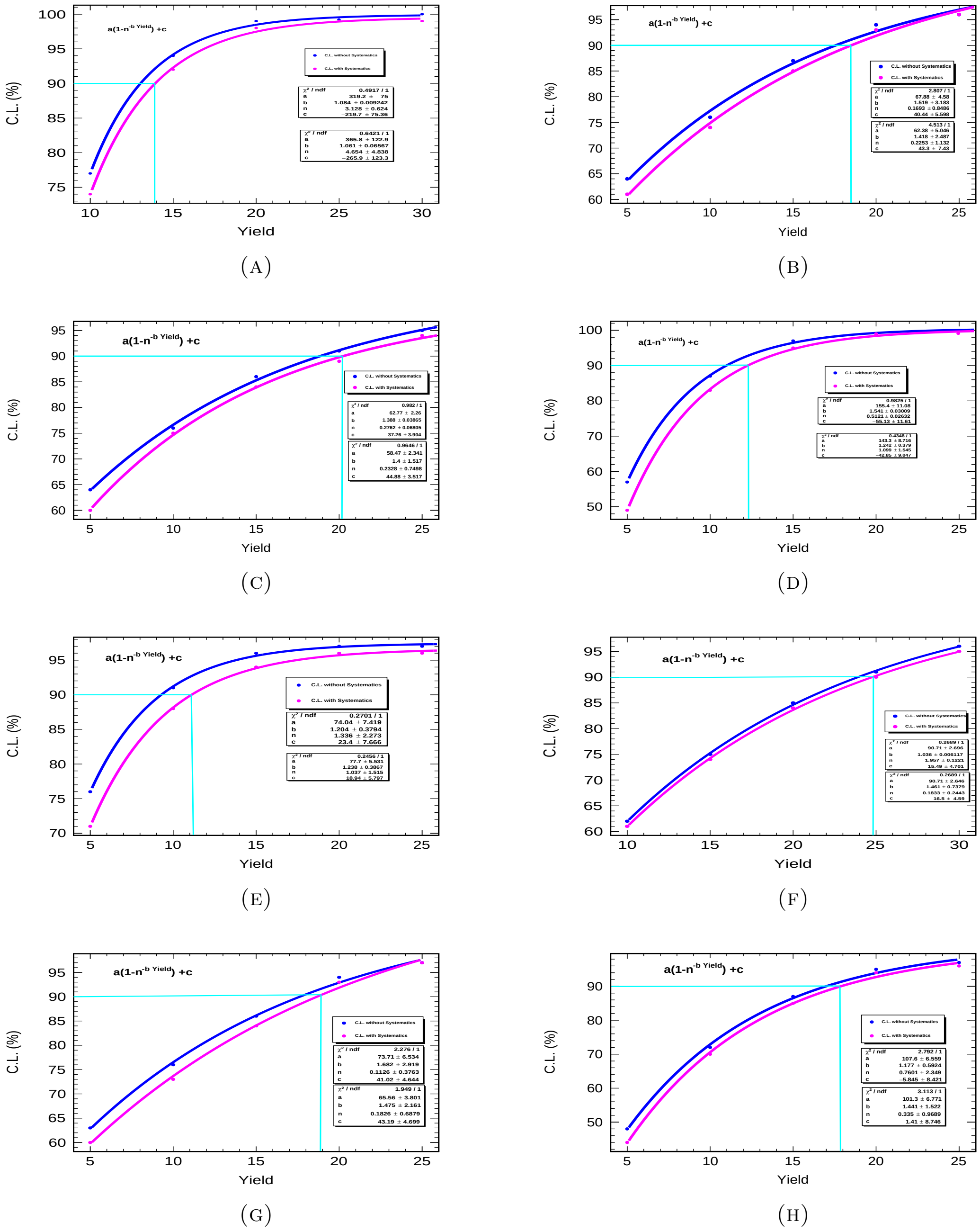

(a) (b) (c) (d) (e) (f) (g) (h)

Figure 2.51: Upper limit on yield at 90% C.L. of the decay modes without (with) systematics (a) $D^0 \to pe^-$, (b) $\overline{D^0} \to pe^-$ (c) $D^0 \to \bar{p}e^+$ (d) $\overline{D^0} \to \bar{p}e^+$ (e) $D^0 \to p\mu^-$ (f) $\overline{D^0} \to p\mu^-$ (g) $D^0 \to \bar{p}\mu^+$ and (h) $\overline{D^0} \to \bar{p}\mu^+$. Cyan line gives the U.L. at 90% C.L.

2.7 Control mode $D^0 \to K^-\pi^+$study

For our analysis, we use $D^0 \to K^-\pi^+$ decay mode as a control mode to calculate the upper limit of the decay $D \to p\ell$. Though we optimize the cuts for $D^0 \to K^-\pi^+$ channel we try to keep the cuts to be identical to those used for the signal modes. The final sets of cuts are listed in Table 2.17. Vertex fitting is also done for this mode and we obtained the BCS efficiency to be 83%. We perform a two-dimensional fit between M_{D^0} and ΔM to extract yield like our signal modes. For efficiency determination, we have generated a 1 Million signal MC sample and it comes out to be 14.52%. The fit result is attached in Fig. 2.54. We check the background structure both in M_{D^0} and ΔM. We observe a peaking background contribution originating from random slow pion in M_{D^0} distribution and a peaking background coming from three body decay in ΔM distribution. The distribution of signal and backgrounds are shown in Fig. 2.52. We model both backgrounds using a Gaussian function. The combinatorial background in M_{D^0} is modeled by a second-order polynomial and in ΔM it is well modeled by a combination of threshold function and second-order polynomial. We finally use a two-dimensional bin fitting to extract the yield for $D^0 \to K^-\pi^+$ mode. The two-dimensional fit results are shown in Fig. 2.53 and the extracted yield in generic MC is 2445040±2420.

TABLE 2.17: Sets of final selection cuts for the decay $D^0 \to K^-\pi^+$

channel	variables	optimised cuts
$D^0 \to K^-\pi^+$	$\frac{L_K}{L_K+L_\pi}$	> 0.6
	$\frac{L_\pi}{L_K+L_\pi}$	> 0.6
	P_{D^*}	> 2.5 GeV/c

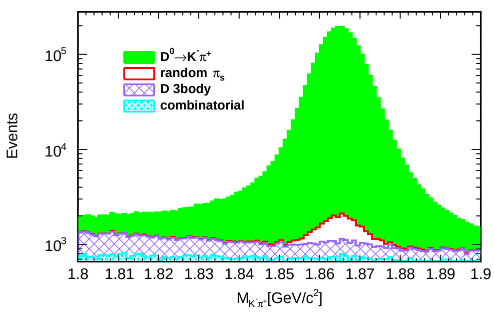

(A)

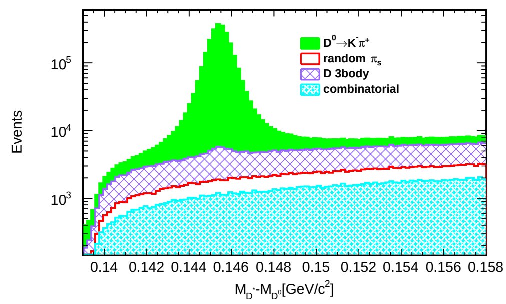

(B)

FIGURE 2.52: Distribution of (a) M_{D^0}[GeV/c^2] and (b) ΔM[GeV/c^2] for the channel $D^0 \to K^-\pi^+$ after applying the optimised set of cuts. Green color is the signal, red is the peaking component in M_{D^0} and violet is the peaking component in ΔM and rest are combinatorial backgrounds.

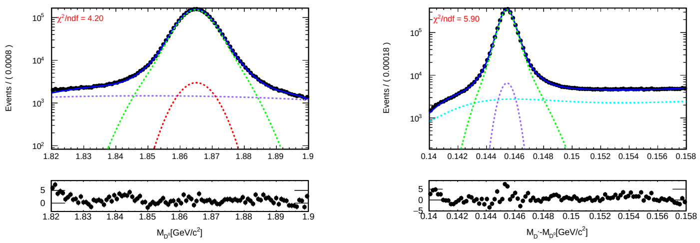

(A) (B)

FIGURE 2.53: Two dimensional fit between (a) M_{D^0}[GeV/c^2] and (b) ΔM[GeV/c^2] for the channel $D^0 \rightarrow K^-\pi^+$ after applying the optimised set of cuts in 921 fb^{-1} of generic MC. The green color is the signal in both the fitted diagrams and the cyan and red colors are the peaking and combinatorial backgrounds respectively in both the diagrams.

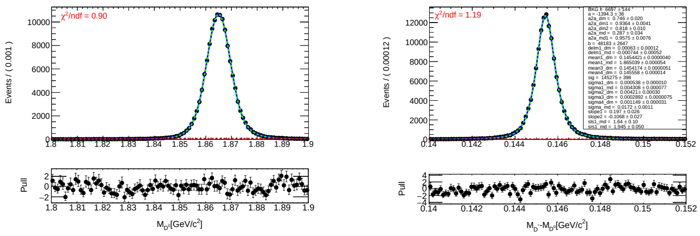

(A) (B)

FIGURE 2.54: Two-dimensional fit between (a) M_{D^0}[GeV/c^2] and (b) ΔM[GeV/c^2] for the channel $D^0 \rightarrow K^-\pi^+$ to determine efficiency after applying the optimized set of cuts in one million signal MC events.

2.8 Data-MC comparison:

We compare data with generic MC in the side-band using 711 fb^{-1} of data. We plot M_{D^0} (ΔM) in the side band of ΔM (M_{D^0}). The comparisons are shown in Fig. 2.56 and Fig. 2.57. We find good agreement in data and generic MC both in M_{D^0} and ΔM.

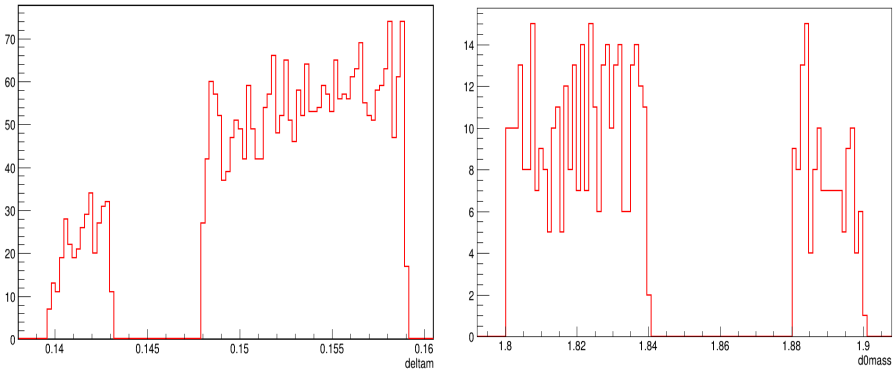

FIGURE 2.55: M_{D^0} and ΔM distributions without the signal region for the mode $D^0 \rightarrow pe^-$ in generic MC.

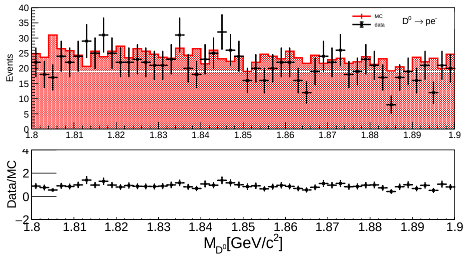

(A) $D^0 \to pe^-$

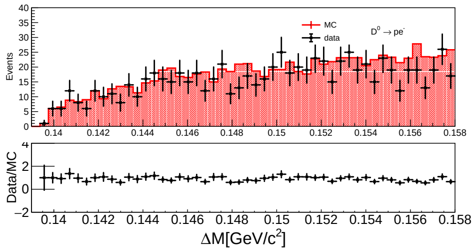

(B) $D^0 \to pe^-$

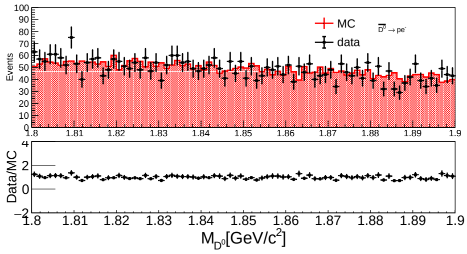

(C) $\overline{D^0} \to pe^-$

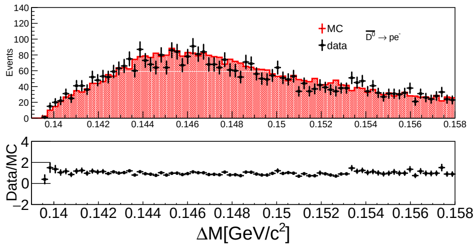

(D) $\overline{D^0} \to pe^-$

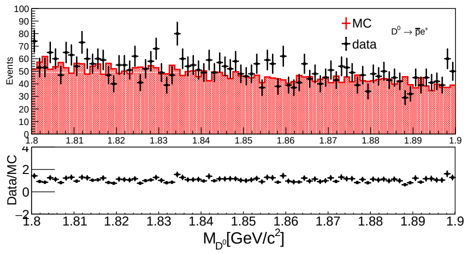

(E) $D^0 \to \bar{p}e^+$

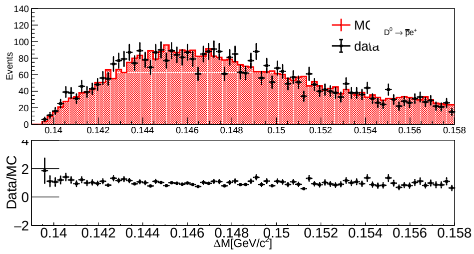

(F) $D^0 \to \bar{p}e^+$

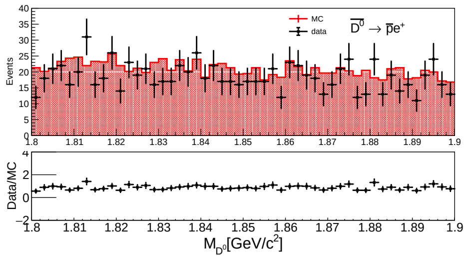

(G) $\overline{D^0} \to \bar{p}e^+$

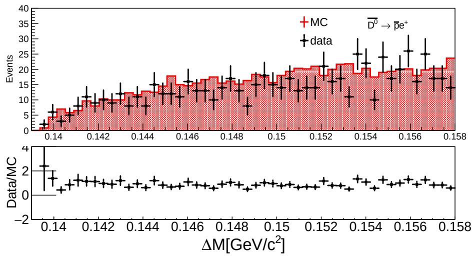

(H) $\overline{D^0} \to \bar{p}e^+$

FIGURE 2.56: Data and MC comparison plots where left plots are for M_{D^0} in the side band of ΔM and right plots are for ΔM in the side band of M_{D^0} distributions for all the electronic modes.

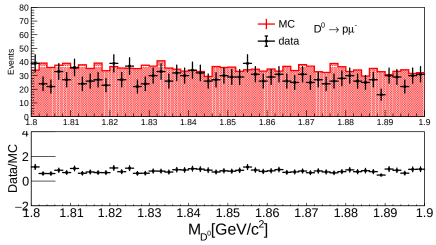

(A) $D^0 \to p\mu^-$

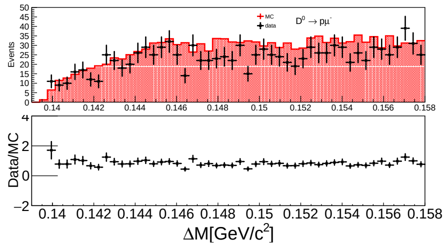

(B) $D^0 \to p\mu^-$

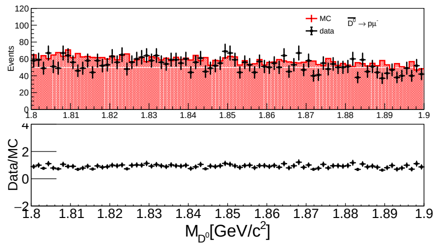

(C) $\overline{D^0} \to p\mu^-$

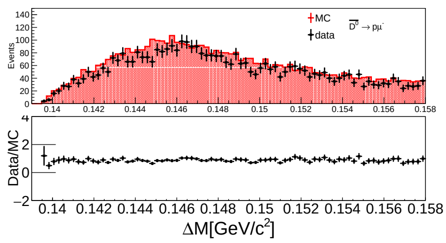

(D) $\overline{D^0} \to p\mu^-$

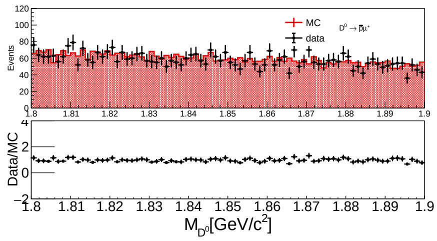

(E) $D^0 \to \bar{p}\mu^+$

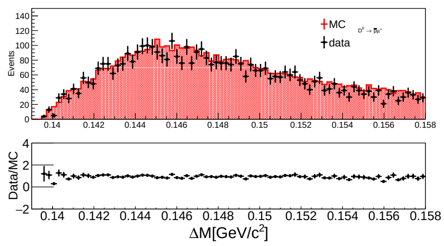

(F) $D^0 \to \bar{p}\mu^+$

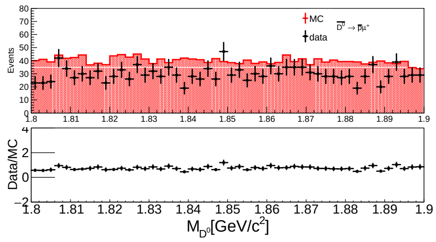

(G) $\overline{D^0} \to \bar{p}\mu^+$

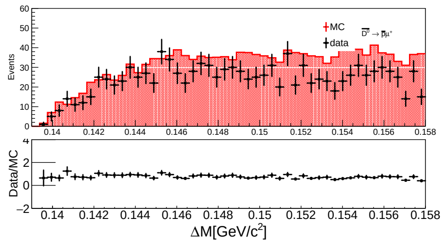

(H) $\overline{D^0} \to \bar{p}\mu^+$

FIGURE 2.57: Data and MC comparison plots where left plots are for M_{D^0} in side band of ΔM and right plots are for ΔM distributions in side band of M_{D^0} for all the muonic modes.

2.9 Systematic study

In addition to statistical uncertainties, we have to consider various sources of systematic uncertainties as well. For the particle identification efficiencies, calibration factors are obtained using $D^{*+} \to D^0\pi^+_+$ ($D^0 \to K^-\pi^+$), $\gamma\gamma \to \ell\ell$, and $\Lambda \to p\pi^-$ control samples for pion, leptons, and protons, respectively, to account for the differences between data and simulation[101]. The contribution due to several systematic sources will get canceled because we are calculating the upper limit with respect to control mode $D^0 \to K^-\pi^+$. However, the following systematic sources have to be considered: systematic sources due to pion misidentification, lepton misidentification, PDF parameters, and track finding. We will use the frequentist method to estimate the upper limit. We will generate the random numbers between yield(1-negsys) and yield(1+possys) and use that to calculate the upper limit.

2.9.1 Pion mis-identification

TABLE 2.18: Systematics uncertainty due to pion misidentification.

Channels	Correction factor	Systematic error(%)
$D^0 \to pe^-$	0.9943	0.2
$\overline{D^0} \to pe^-$	0.9949	0.2
$D^0 \to \bar{p}e^+$	0.9997	0.2
$\overline{D^0} \to \bar{p}e^+$	0.9943	0.2
$D^0 \to p\mu^-$	0.9994	0.8
$\overline{D^0} \to p\mu^-$	0.9997	1.0
$D^0 \to \bar{p}\mu^+$	1.0006	0.9
$\overline{D^0} \to \bar{p}\mu^+$	1.0005	0.9

2.9.2 Proton mis-identification

Table 2.19: Systematics uncertainty due to proton misidentification.

Channels	Correction factor	Systematic error(%)
$D^0 \to pe^-$	0.9905	0.30
$\overline{D^0} \to pe^-$	0.9926	0.31
$D^0 \to \bar{p}e^+$	0.9877	0.31
$\overline{D^0} \to \bar{p}e^+$	0.9887	0.34
$D^0 \to p\mu^-$	0.9943	0.40
$\overline{D^0} \to p\mu^-$	0.9932	0.31
$D^0 \to \bar{p}\mu^+$	0.9845	0.32
$\overline{D^0} \to \bar{p}\mu^+$	0.9841	0.31

2.9.3 Electron misidentification

Table 2.20: Systematics uncertainty due to electron identification.

Channels	Correction factor	Systematic error(%)
$D^0 \to pe^-$	0.9752	1.6
$\overline{D^0} \to pe^-$	0.9751	1.6
$D^0 \to \bar{p}e^+$	0.9750	1.6
$\overline{D^0} \to \bar{p}e^+$	0.9750	1.6

2.9.4 Muon misidentification

Table 2.21: Systematics uncertainty due to muon identification.

Channels	Correction factor	Systematic error(%)
$D^0 \to p\mu^-$	0.96	1.8
$\overline{D^0} \to p\mu^-$	0.9617	2.0
$D^0 \to \bar{p}\mu^+$	0.9780	1.5
$\overline{D^0} \to \bar{p}\mu^+$	0.9780	1.6

2.9.5 PDF shape

We fix a number of PDF parameters to a certain value when we extract yield. These fixed parameters have some uncertainty that affects the signal yield. To estimate this uncertainty, fixed parameters of PDFs are varied by $\pm\ 1\sigma$ one at a time and calculated yield. The PDF shape contribution for the signal mode to the systematic are summarised in Table 2.22 and Table 2.24.

Table 2.22: Summary of systematic uncertainties(%) arising from PDF parameters for electronic modes.

Sources(%)	$D^0 \to pe^-$	$\overline{D^0} \to pe^-$	$D^0 \to \bar{p}e^+$	$\overline{D^0} \to \bar{p}e^+$
Signal PDF	2.05 -2.05	0	0	0
Bkg. PDF	0	+4.95 -4.91	+12.00 -10.56	0
Fit bias	-1.2	0	0	-3.2

Table 2.23: Summary of systematic uncertainties(%) arising from PDF parameters for muonic modes.

Sources(%)	$D^0 \to p\mu^-$	$\overline{D^0} \to p\mu^-$	$D^0 \to \bar{p}\mu^+$	$\overline{D^0} \to \bar{p}\mu^+$
Signal PDF	+2.29	0	0	0
Bkg. PDF	+1.5 -8.30	+19.03 -11.73	+22.94 -19.53	+8.06
Fit bias	0	-4.6	0	-9.8

2.9.6 Tracking

The detection efficiency for the charged particle track has an uncertainty of about 0.35% per track and reconstruction of charged particle tracks are studied using partially reconstructed $D^{*+} \to D^0(K_S^0(\pi^+\pi^-)\pi^+\pi^-)\pi^+$ decay mode with $p_T > 200$MeV/c[102]. We have a total of two charged tracks for each mode. So, the total uncertainty associated with tracking is 0.70% for each mode.

2.9.6.1 Total Systematics

TABLE 2.24: Summary of systematic uncertainties (%)

Channel	Pion		proton		ℓ		PDF (%)	Tracking	Total	
	Corr.	Err (%)	Corr.	Err (%)	Corr.	Err (%)			Corr.	Sys (%)
$D^0 \to pe^-$	0.9943	0.2	0.9905	0.30	0.9752	1.6	$^{+2.05}_{-2.37}$	0.70	0.9604	$^{+2.71}_{-2.37}$
$\overline{D^0} \to pe^-$	0.9949	0.2	0.9926	0.31	0.9751	1.6	$^{+4.95}_{-4.91}$	0.70	0.9629	$^{+5.26}_{-4.91}$
$D^0 \to \bar{p}e^+$	0.9997	0.2	0.9877	0.31	0.9750	1.6	$^{+12.0}_{-10.56}$	0.70	0.9627	$^{+12.13}_{-10.56}$
$\overline{D^0} \to \bar{p}e^+$	0.9943	0.2	0.9887	0.31	0.9750	1.6	-3.2	0.70	0.9584	$^{+1.78}_{-3.2}$
$D^0 \to p\mu^-$	0.9994	0.8	0.9943	0.40	0.9600	1.8	$^{+2.70}_{-8.30}$	0.70	0.9539	$^{+3.43}_{-8.30}$
$\overline{D^0} \to p\mu^-$	0.9997	1.0	0.9932	0.31	0.9617	2.0	$^{+19.03}_{-12.59}$	0.70	0.9548	$^{+19.17}_{-12.59}$
$D^0 \to \bar{p}\mu^+$	1.0006	0.9	0.9845	0.32	0.9780	1.5	$^{+22.94}_{-19.53}$	0.70	0.9686	$^{+23.01}_{-19.53}$
$\overline{D^0} \to \bar{p}\mu^+$	1.0005	0.9	0.9841	0.31	0.9780	1.6	$^{+8.06}_{-9.80}$	0.70	0.9672	$^{+8.30}_{-9.30}$

2.10 Box Open

After confirming that there is no unexpected background from the sideband study, we looked at the data and performed the two-dimensional UML fit between M_{D^0} and ΔM for all the signal modes. The difference between data and signal MC for the mean and sigma is calculated from a control sample called the correction factor. The calibrated mean and sigma for signal modes are calculated from the correction factor.

$$\mu_{calibrated} = \mu_{MC} + (\mu_{data} - \mu_{MC})_{control\ mode} \tag{2.16}$$

$$\sigma_{calibrated} = \sigma_{MC} \times (\frac{\sigma_{data}}{\sigma_{MC}})_{control\ mode} \tag{2.17}$$

To calculate correction factors we use the normalization mode $D^0 \to K^-\pi^+$. Fit results for the signal modes are shown in Fig. 2.59 and Fig. 2.60. We have also listed out the yields in the Table 2.25. As seen from Fig. 2.59 and Fig. 2.60 no significant signal is found for any of the modes. So, we provide an upper limit (@ 90% C.L.) for all the modes using the frequentist method. We generated the 2000 samples of different signal and background events (as per data) using PDFs. Fit is performed on the generated samples and confidence level is measured as the fraction of samples where the signal is more than the data. We smear the yield distributions (which are obtained from ToyMC) by systematic uncertainty to include the systematic uncertainty. We have shown the U.L.

distributions for all the modes in Fig. 2.61. Upper limit on the $\mathcal{B.R.}$ based on @90% C.L. are obtained as of the order of 10^{-7} for all the modes. Statistical significance is estimated from $\sqrt{-2ln(\frac{\mathcal{L}_0}{\mathcal{L}_{max}})}$ where $\mathcal{L}_{max}$ ($\mathcal{L}_0$) denotes the likelihood value when the yield is allowed to vary (fixed to zero). The method used for significance is explained in Appendix C.

- $D^0 \to K^-\pi^+$ **study**

We also perform two two-dimensional UML fit for the control mode to extract yield. Fig. 2.58 shows the fit results in 921 fb^{-1} of data.

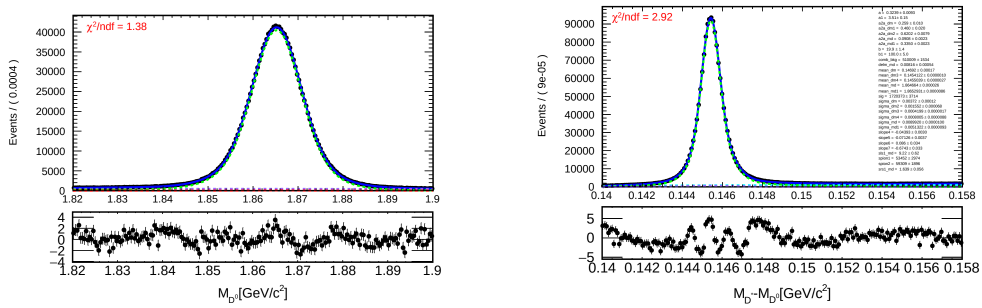

(A) (B)

FIGURE 2.58: Two dimensional fit between (a) M_{D^0}[GeV/c^2] and (b) ΔM[GeV/c^2] for the channel $D^0 \to K^-\pi^+$ after applying the optimised set of cuts in 921 fb^{-1} of data. The green dotted curves show the fit function for the signal, the violate dashed curves show the fit function for the peaking background, and the red dashed curves show the combinatorial background of the fit functions in M_{D^0}. The green dotted curves show the fit function for the signal, the violate dashed curves show the fit function for the peaking background, and the cyan dashed curves show the combinatorial background of the fit functions in ΔM.

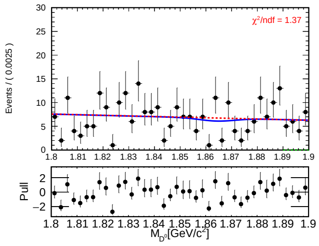

(A) $D^0 \to pe^-$

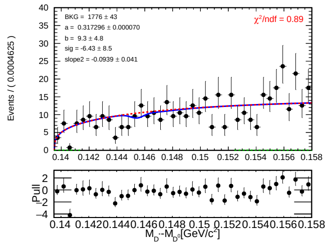

(B) $D^0 \to pe^-$

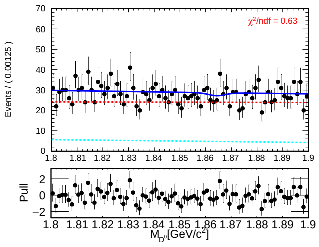

(C) $\overline{D^0} \to pe^-$

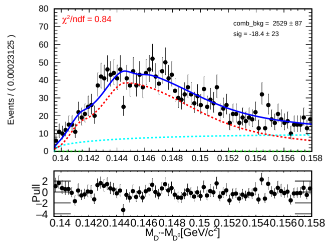

(D) $\overline{D^0} \to pe^-$

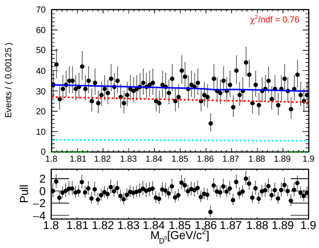

(E) $D^0 \to \bar{p}e^+$

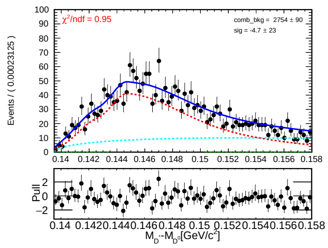

(F) $D^0 \to \bar{p}e^+$

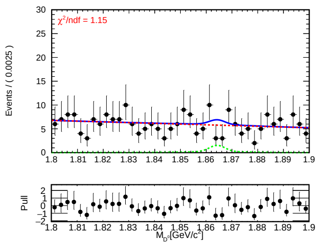

(G) $\overline{D^0} \to \bar{p}e^+$

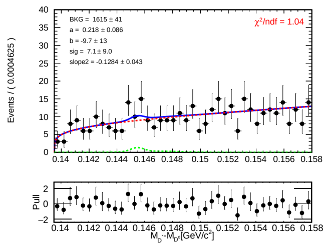

(H) $\overline{D^0} \to \bar{p}e^+$

FIGURE 2.59: Two dimensional fit results between M_{D^0} and ΔM for the elelctronic modes using 921 fb^{-1} data. In Fig. 2.59 (A), (B), (G) and (H), the red dotted curves show the fit function for the combinatorial background, the green dashed curves show the fit function for the signal. In Fig. 2.59 (C), (D), (E) and (F), the red dotted curves show the fit function for the peaking background, the green dashed curves show the fit function for the signal and the cyan dotted curves show the fit function for the combinatorial background. The blue solid line represent the total fit function for all the plots.

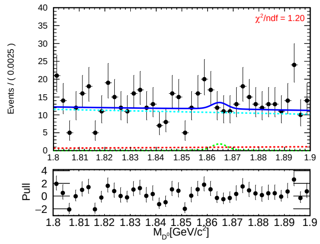

(A) $D^0 \to p\mu^-$

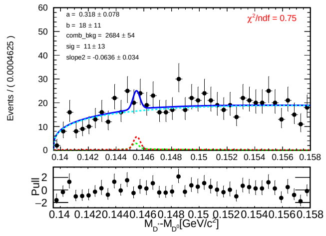

(B) $D^0 \to p\mu^-$

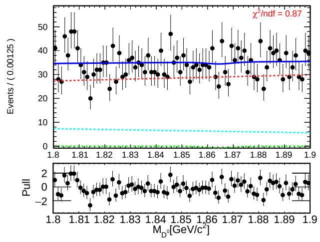

(C) $\overline{D^0} \to p\mu^-$

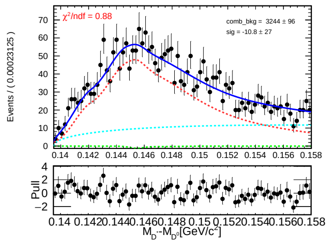

(D) $\overline{D^0} \to p\mu^-$

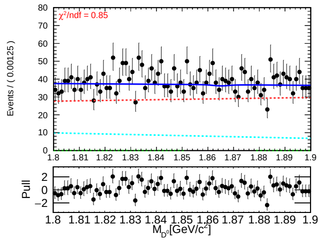

(E) $D^0 \to \bar{p}\mu^+$

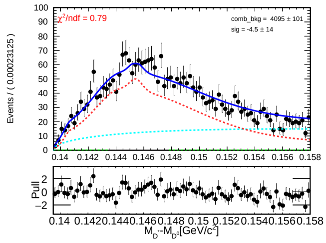

(F) $D^0 \to \bar{p}\mu^+$

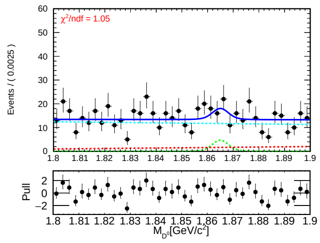

(G) $\overline{D^0} \to \bar{p}\mu^+$

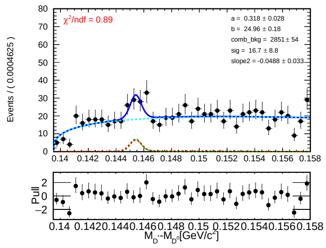

(H) $\overline{D^0} \to \bar{p}\mu^+$

FIGURE 2.60: Two dimensional fit results between M_{D^0} and ΔM for the muonic modes using 921 fb^{-1} data. In Fig. 2.60 (A), (B), (G) and (H), the red dotted curves show the fit function for the combinatorial background, the green dashed curves show the fit function for the signal. In Fig. 2.60 (C), (D), (E) and (F), the red dotted curves show the fit function for the peaking background, the green dashed curves show the fit function for the signal and the cyan dotted curves show the fit function for the combinatorial background. The blue solid line represent the total fit function for all the plots.

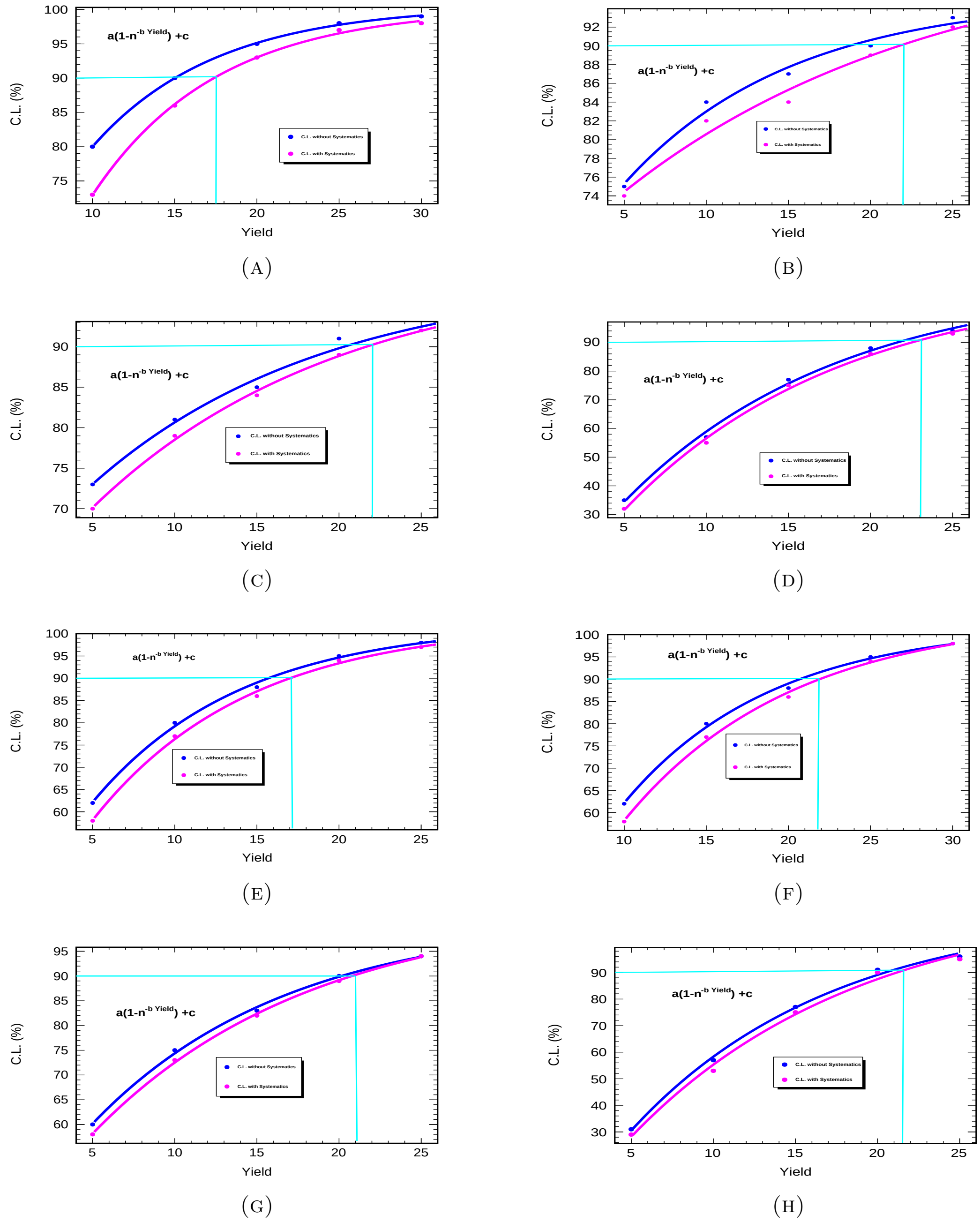

FIGURE 2.61: Upper limit on yield at 90% C.L. of the decay modes without(with) systematics (a)$D^0 \rightarrow pe^-$, (b)$\overline{D^0} \rightarrow pe^-$ (c)$D^0 \rightarrow \bar{p}e^+$ (d)$\overline{D^0} \rightarrow \bar{p}e^+$ (e)$D^0 \rightarrow p\mu^-$ (f)$\overline{D^0} \rightarrow p\mu^-$ (g)$D^0 \rightarrow \bar{p}\mu^+$ and (h)$\overline{D^0} \rightarrow \bar{p}\mu^+$. Cyan line gives the U.L. at 90% C.L.

Table 2.25: Summary of the yields and U.L. at 90% confidence level for each mode in data.

Channels	Expected yields	U.L.(@90%C.L.)	Branching Fraction (@ 90% C.L.)	Significance ($\mathcal{S}$)
$D^0 \to pe^-$	-6.43 ± 8.5	17.5	5.5×10^{-7}	—
$\overline{D^0} \to pe^-$	-18.4 ± 23	22.0	6.9×10^{-7}	—
$D^0 \to \bar{p}e^+$	-4.7 ± 23	22.0	7.2×10^{-7}	—
$\overline{D^0} \to \bar{p}e^+$	7.1 ± 9.0	23.0	7.6×10^{-7}	0.60
$D^0 \to p\mu^-$	11 ± 23	17.1	5.1×10^{-7}	0.95
$\overline{D^0} \to p\mu^-$	-10.8 ± 27	21.8	6.5×10^{-7}	—
$D^0 \to \bar{p}\mu^+$	-4.5 ± 14	21.1	6.3×10^{-7}	—
$\overline{D^0} \to \bar{p}\mu^+$	16.7 ± 8.8	21.4	6.5×10^{-7}	1.56

2.10.1 Systematics study

The origin of the systematic study is similar as mentioned in Section 2.9. Only systematics due to PDF shape and fit bias have to be modified. The uncertainties on the PDF shapes are obtained by varying each of the fixed parameters by $\pm 1\sigma$ and the ratio of the differences in obtained and nominal signal yield to the latter is added in quadrature to calculate the total systematic uncertainty from PDF modeling. The fit procedures are validated in simulated MC samples. Small observed biases of $(1-2)\%$ are taken as systematic uncertainties. The uncertainties due to pion and kaon identification are 1.1% and 0.8%, respectively, for the normalization mode $D^0 \to K^-\pi^+$. The uncertainty on $\mathcal{B}(D^0 \to K^-\pi^+)$ is 0.03%. These uncertainties are taken into account to determine the upper limit on the branching fraction. The uncertainty on the π_s efficiency cancels between the signal and normalization mode. All systematic uncertainties are added in quadrature to obtain the total systematic uncertainty.

TABLE 2.26: Summary of systematic uncertainties (%) due to normalization mode $D^0 \to K^-\pi^+$ (Norm), proton (p) and lepton (ℓ) identification, PDF used for signal extraction, fit bias from toy study ('-' denotes negligible bias) and tracking for $D^0 \to p\ell$ decay modes.

Decay mode	Norm	p	ℓ	PDF	Fit Bias	Tracking	Total
$D^0 \to pe^-$	1.8	0.3	1.6	$^{+4.7}_{-1.1}$	-	0.7	$^{+5.3}_{-2.8}$
$\overline{D}^0 \to pe^-$	1.8	0.3	1.6	$^{+8.2}_{-9.2}$	-	0.7	$^{+8.6}_{-9.5}$
$D^0 \to \overline{p}e^+$	1.8	0.3	1.6	$^{+11.1}_{-8.1}$	-	0.7	$^{+11.4}_{-8.5}$
$\overline{D}^0 \to \overline{p}e^+$	1.8	0.3	1.6	$^{+6.4}_{-2.0}$	1.7	0.7	$^{+7.1}_{-3.6}$
$D^0 \to p\mu^-$	1.8	0.4	1.8	$^{+3.7}_{-7.8}$	2.2	0.7	$^{+5.1}_{-8.5}$
$\overline{D}^0 \to p\mu^-$	1.8	0.3	2.0	$^{+21.3}_{-12.3}$	-	0.7	$^{+21.5}_{-12.6}$
$D^0 \to \overline{p}\mu^+$	1.8	0.3	1.5	$^{+21.7}_{-18.2}$	-	0.7	$^{+21.8}_{-18.4}$
$\overline{D}^0 \to \overline{p}\mu^+$	1.8	0.3	1.6	6.0	2.4	0.7	6.9

2.11 Conclusion

We have searched for the baryon and lepton number violating decays $D^0 \to pe^-$, $\overline{D^0} \to pe^-$, $D^0 \to \bar{p}e^+$, $\overline{D^0} \to \bar{p}e^+$, $D^0 \to p\mu^-$, $\overline{D^0} \to p\mu^-$, $D^0 \to \bar{p}\mu^+$, $\overline{D^0} \to \bar{p}\mu^+$. We found no excess numbers in the data. To determine the branching fraction upper limits we used $\mathcal{B}(D^0 \to K^-\pi^+) = (3.946 \pm 0.030) \times 10^{-2}$ as normalization channel. The results are of the order of 10^{-7} improved by an order for all the modes as compared to the recent BESIII results and the values are listed in Table 2.25.

Chapter 3

Calculation of relative slow pion tracking efficiency using $B^0 \to D^*\pi$ and $B^0 \to D^*\rho$ decays

3.1 The SuperKEKB experiment

The SuperKEKB[103,104] is an asymmetric energy electron-positron double-ring collider constructed by upgrading the KEKB[70,71] B-Factory. The KEKB achieved the world highest luminosity ($2.11\times10^{34}\,\mathrm{cm}^{-2}\mathrm{s}^{-1}$) operating from 1998 to 2010; total integrated luminosity accumulated by the Belle detector[77] reached 1.04 ab^{-1}. Belle succeeded in validating certain predictions of the Kobayashi-Maskawa theory and obtained a variety of experimental results in elementary high energy physics. Based on the success of KEKB, an upgrade to SuperKEKB was inevitable to seek for the new physics, and also in order to compete with other experiments like LHCb[106] the luminosity of the experiment has to be upgraded. The instantaneous luminosity of the SuperKEKB is 8×10^{35} $\mathrm{cm}^{-2}\mathrm{s}^{-1}$; 40 times higher than its predecessor and the final goal is to accumulate an integrated luminosity of 50 ab^{-1}. The following will give an overview of the collider and the mechanism that is used to generate particles. The SuperKEKB[103,104] collider complex consists of two rings: A electron beam with an energy of 7 GeV is called high energy ring (HER) and a positron beam with an energy of 4 GeV is called low energy ring (LER). An injector linear accelerator (linac) is used with an energy 1.1. GeV positron damping ring (DR). as shown in Fig. 3.1. These two beams collide at a point known as the interaction point (IP). The extremely high luminosity of SuperKEKB required significant upgrades to the HER, LER, and final-focus system of KEKB. The injector linac also required significant upgrades for injection beams with high current and low emittance, as well as for improving simultaneous top-up injections. To achieve higher luminosity in collider experiments requires higher beam currents $I_{\pm}$, larger vertical beam-beam parameters $\xi^*_{y\pm}$, and smaller vertical beta function at the interaction point $\beta^*_{y\pm}$. Luminosity L depends on several machine-related parameters and is defined as:

$$L = \frac{\gamma_{\pm}}{2er_e}(1 + \frac{\sigma^*_y}{\sigma^*_x})(\frac{I_{\pm}\xi_{y\pm}}{\beta^*_y})(\frac{R_L}{R_{\xi_y}}) \tag{3.1}$$

where $\gamma_{\pm}$ are denoted as Lorentz factors, r_e is the classical electron radius, and $\sigma^*_{x,y}$ is the beam size at the interaction point. Parameters R_L and $R_{\xi y}$ are correction factors for the geometrical loss due to the hourglass effect and the crossing angle at the IP. In this equation, $\sigma^*_{x,y}$ and β^*_y are assumed to be equal in both rings. So to achieve higher luminosity we pursued much smaller values of β^*_y. In SuperKEKB the beam currents are doubled, its ξ_y is almost the same as KEKB, and its β^*_y are reduced by a factor of 1/20. Thus, we can expect 40 times higher luminosity than that of KEKB. The higher energy in the LER was selected to improve the Touschek beam lifetime and suppress emittance growth due to intra-beam scattering. The lower energy for the HER decreases the horizontal emittance and synchrotron radiation power. Though the energy asymmetry is lowered it is still acceptable for the physics experiment.

To upgrade KEKB to SuperKEKB, a lot of new equipment was employed to meet the challenges of SuperKEKB, whereas a lot of things have been reused from KEKB:

existing tunnel, infrastructure, accelerator components, etc. The main dipole magnets were replaced with longer ones in LER. For the new collision scheme with extremely low vertical β_y^* function, a new final-focus superconducting magnet system (QCS) was employed. To cope with the electron cloud effect (ECE) in the LER, various measures are taken, including the replacement of beam pipes in most of the ring with new antechamber pipes with an internal TiN coating, groove-shaped surfaces in the dipole magnets, and clearing electrodes in the wiggler magnets and solenoids in field-free regions. To increase beam currents to twice that achieved in KEKB, vacuum components are upgraded for lower impedance and higher thermal strength. The RF system is reinforced to deliver higher power to the beam.

The beam position monitors, beam size monitors, bunch-by-bunch feedback system, and collision feedback system, are upgraded to provide the higher performance required for the lower emittance beams and smaller beam size at the IP. For the required beam quality and injection efficiencies into the LER and HER, the injector linac was upgraded. After 5.5 years of construction, the beam commissioning of SuperKEKB started without the Belle II detector (Phase I) in 2016. After Phase I, with new final focusing superconducting magnets and the Belle II detector data taking was started from 2018 (Phase II).

3.2 The Belle II Detector

In Belle II[105] mostly the data taking is done in Υ(4S) which is likely to decay to $B\bar{B}$ pairs. This is why Belle II is called a B-factory experiment. The strength of this experiment is that B mesons are produced in pairs. Once one B meson is reconstructed in one of its dominant decay modes, the kinematics of the other B meson are immediately known by exploiting the momentum and charge conservation. So a detector with large solid angle coverage is required for the full reconstruction of the $B\bar{B}$ pairs. In order to measure the decay vertices precisely, high-precision tracking detectors are needed. It

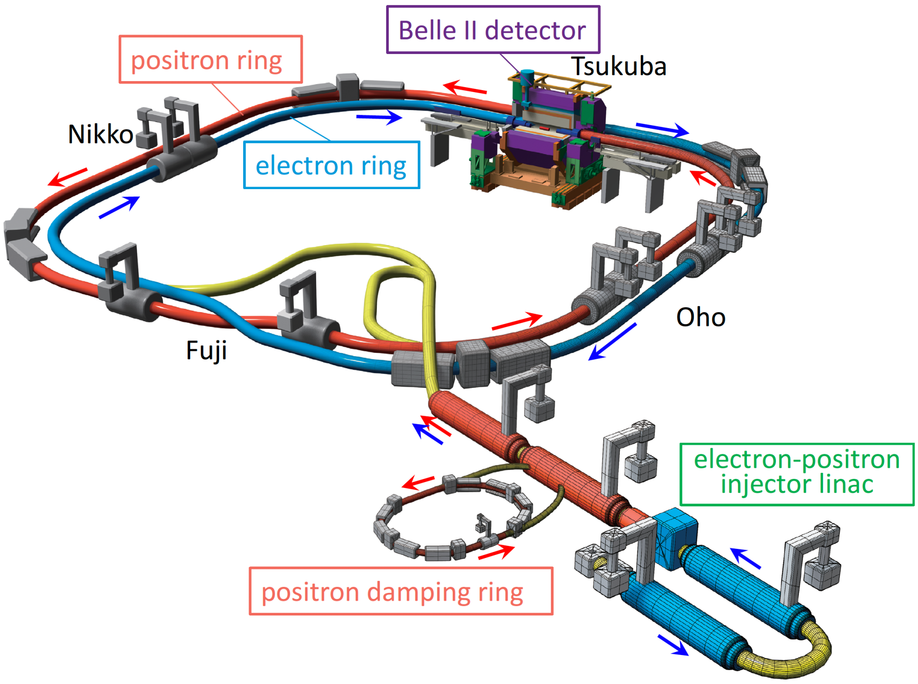

FIGURE 3.1: Schematic diagram of the SuperKEKB collider with its high energy electron ring (HER, blue) and low energy positron ring (LER, red), as well as the added positron damping ring and the Belle II detector. The electron and positron beams collide at the interaction point in the Tsukuba straight section.

has a length of approximately 7.5 m and a height and diameter of approximately 7 m. The following description of the detector follows the technical design report [105] very closely, a more detailed discussion can be found there. A sketch of the Belle II detector is depicted in Fig. 3.2. Different sub-detector serves a different purpose.

3.2.1 Pixel Detector

The high luminosity means a significant increase in background mainly from QED processes. The pixel detector for Belle II must have to face several challenges. The radius of the beam pipe is only 10 mm and the first layer of the sensor is just 14 mm from the interaction point. The proximity of PXD to the interaction point(IP) allows for very precise vertex reconstruction of B meson decays, but because to reach such a goal, the material budget of PXD has to be very minimalistic. On the other hand, huge backgrounds such as near the IP require very radiation-hard technology. All the requirements

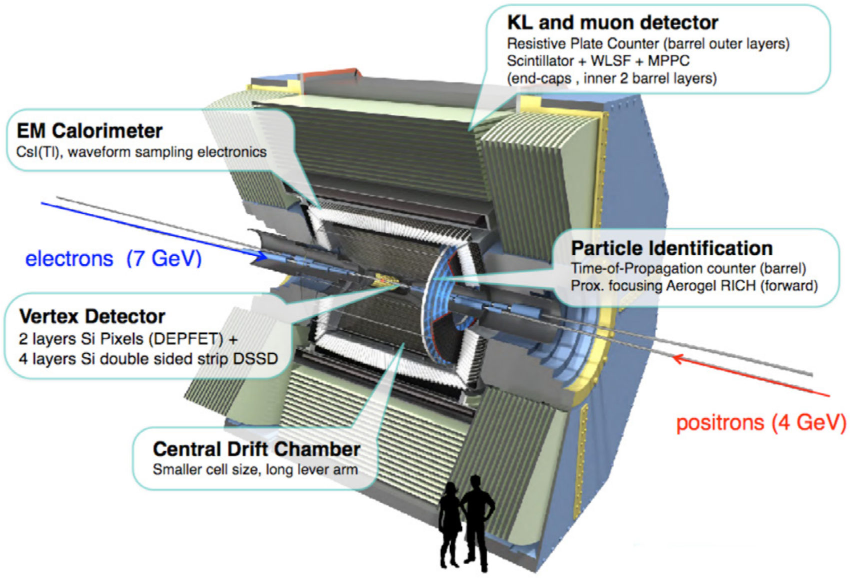

FIGURE 3.2: Layout of the Belle II detector. The inner part is called the vertex detector (PXD and SVD). The vertex detector is enclosed in the Central Drift Chamber (CDC). It is followed by a time of propagation detector (TOP) in the barrel region and a particle identification (PID) detector in the forward direction (to the right-hand side). The next layer is the Electromagnetic Calorimeter (ECL) and the outermost detector is called K_L^0 and muon detector (KLM). The interaction point (IP) is at the center.

are fulfilled by the DEPFET (Depleted Field Effect Transistor) [107] technology, which has been chosen for the pixel detector of Belle II. The DEPFET sensors are arranged into rectangular modules, known as ladders, that make up the two levels of the PXD, with radii of 14 and 22 mm, respectively. The acceptance criteria of the detector establish the sensitivity lengths of each layer: a polar angular coverage of 17° to 155° is ensured. It combines particle detection and amplification within each single pixel in a compact structure. Low capacitance and high signal-to-noise ratio allow for the fabrication of very thin devices. The area of DEPFET applications covers optical photon sensors, X-ray imagers, and particle trackers. The PXD is made up of roughly eight million pixels that are arranged into arrays. Each DEPFET pixel is a cell, which is a monolithic structure with internal amplification, making it significantly smaller than other devices that require external amplification. The pixels have a typical size of 50×50 μm^2 and 50×75 μm^2 for the inner and outer layer, respectively. The readout time of each row of the sensors is 20 μs. It has an impact-parameter resolution of approximately 12 μm and a D meson decay-time resolution of the order of 70 fs[108].

3.2.2 Silicon Vertex Detector

The Belle II experiment is an upgrade of the previous Belle detector. It is designed in such a way that it can perform better than Belle that too in a much-complicated environment that is characterized by a higher beam background and Lorentz boost reduced from $\beta\gamma = 0.4$ to $\beta\gamma = 0.3$. The SVD is crucial for extrapolating the tracks to the PXD to measure the decay vertices with the PXD and point at a region of interest to reduce the PXD data. Other main roles of SVD are the reconstruction of low-momentum charged particles and their particle identification using ionization energy deposits. The SVD is also crucial for vertexing the decay inside the SVD volume, i.e., long-lived particles K_S mesons. The vertex detector of Belle II is designed to provide a better resolution than the Belle silicon vertex detector in order to compensate for the reduced Lorentz boost. This improvement is achieved with more precise point resolution, a reduced inner radius, and a low material budget. Moreover, it must operate in a high background environment with a hit rate of 20 (3) MHz/cm^2 and an integrated yearly dose of 2 (0.2) Mrad at a radius of 14 (40) mm. The schematic diagram of the Belle II SVD is shown in the figure.

The working principle of the SVD is illustrated in Fig. 3.4. The SVD consists of four layers of double-sided silicon strip detectors (DSSDs). The material budget of the SVD is about 0.7% of the radiation length per layer. On the DSSD plane, a local coordinate is defined with the u-axis along the n-side strips and the v-axis perpendicular to the u-axis, i.e., p-side strips and n-side strips provide u and v information, respectively. In the cylindrical coordinate, u and v correspond to $r-\phi$ and z. The SVD consists of three types of sensors: "small" rectangular sensors in layer 3, "large" rectangular sensors in the barrel region of layers 4, 5, and 6, and "trapezoidal" sensors installed slantwise in the forward region of layers 4, 5, and 6.

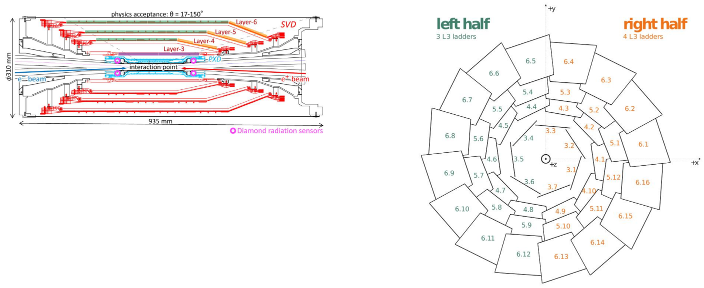

(A) (B)

FIGURE 3.3: (a) The schematic cross-sectional view of the VXD. The SVD is red, the PXD is light blue, and the IP beam pipe diamonds are pink circles. (b) The ladder numbering scheme of the SVD is sketched on the xy plane. Figure courtesy of the Belle II Collaboration.

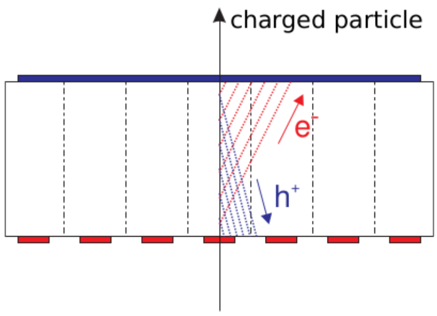

(A)

FIGURE 3.4: Working principle of an SVD sensor. The n-side strips (blue rectangles at the top) are perpendicular to the p-side strips (red rectangles at the bottom). Adapted from [105].

The front-end ASIC, the APV25[109], was originally developed for the CMS Silicon Tracker. The APV25 tolerates more than 100 Mrad of radiation. It has 128 channels with a shaping time of about 50 ns. The chip samples the height of the signal waveform with the 32 MHz clock (31 ns period) and stores each sample in an analog ring buffer. Since the bunch-crossing frequency is eight times faster than the sampling clock, the stored samples are not synchronous to the beam collision in contrast to CMS. In the present readout configuration (the six-sample mode), at every reception of the Belle II global Level-1 trigger, the chip reads out six successive samples stored in the buffers. The six-samples mode offers a wide enough time window (6×31 ns $= 187$ ns) to accommodate large timing shifts of the trigger. In preparation for operation with higher luminosity, where background occupancy, trigger dead-time, and the data size increase, we developed the three/six-mixed acquisition mode (mixed-mode). The mixed mode is a new method to read out the signal samples from the APV25, where the number of samples changes between three and six in each event, depending on the timing precision of the Level-1 trigger signal. For triggers with precise timing, three-sample data are read out with half time window and half-data size compared to six-sample data, reducing the effects due to higher luminosity. This functionality was already implemented in the running system and confirmed by a few hours of smooth physics data-taking. Before starting to use the mixed mode, we assess the performance degradation due to the change in the acquisition mode. The APV25 chips are mounted on each middle sensor with thermal isolation foam in between and the advantage of this method is to reduce the signal propagation length and hence reduce the noise level. To reduce the material budget, the APV25 chips on the sensor are thinned down to 100 μm. The power consumption of the APV25 chip is 0.4 W/chip and 700 W in the entire SVD. The chips are cooled by a bi-phase –20°C CO_2 evaporative cooling system. The SVD detector has been installed in 2018 and has been operated since 2019. The total number of masked strips is about 1%, moreover, the average sensor hit efficiency is greater than 99% and stable with time. The collected signal charge, normalized for the length of traversed sensor thickness, is similar in all sensors and matches the expectation. A very good signal-to-noise ratio is observed in all 172 sensors[110,111].

3.2.3 Central Drift Chamber (CDC)

The Central Drift Chamber (CDC)[112] is the main tracking device and identification of charged particles for the Belle II experiment. The roles of the CDC are measurement of momentum, tracking, provision of trigger signals, and particle identification. The

Belle-II CDC is a cylindrical wire chamber with 14336 sense wires, 2.3 m-length and 2.2 m-diameter. The schematic diagram of CDC is shown in Fig. 3.5. To achieve a low material detector, we use 10 mm thickness Aluminum endplates and 5 mmt and 0.4 mmt CFRP for outer and inner cylinders respectively. The chamber is filled with a low-Z gas, a 50% helium-50% ethane mixture and contains low-mass wires, made of gold-plated tungsten ($\phi 30\mu$m) and aluminum without any plating ($\phi 126$ μm) , to minimize multiple scattering. Table 3.1 shows the comparison of main parameters between Belle CDC and Belle-II CDC. In order to reduce occupancy and wire hit rate from a large beam background, the Belle-II CDC has a smaller azimuthal cell size at the same radius compared with the Belle CDC. The readout electronics system plays a significant role in the performance of the Belle-II CDC at 40 times higher luminosity. The CDC front-end readout system comprises a front-end digitizer close to the backward endplate. The system transfers the digitized analog signal and its timing to the Belle-IIDAQ system via the Rocket I/O link. The ASIC chips, FADC, and FPGA are assembled on a single board. An amplifier, shaper, and discriminator are implemented in the ASIC chip. The digitized data is stored in the ring buffer and sent to the data suppressor block when a trigger signal is received. In order to reduce data size, a sum of ADC values is calculated in the time window adjusted. The suppressed data is transferred using a high-speed data link. Detector and readout electronics were fully upgraded and installed successfully in 2016 and operation with a 1.5-T magnetic field was started in the summer of 2017.

TABLE 3.1: Main parameters of the Belle CDC and the CDC upgrade for Belle II. Taken from [105].

Parameters	Belle	BelleII
Radius of inner cylinder (mm)	77	160
Radius of outer cylinder (mm)	880	1130
Radius of innermost sense wire (mm)	88	168
Radius of outermost sense wire (mm)	863	1111.4
Number of layers	50	56
Number of sense wires	8400	14336
Gas	He-C_2H_6	He-C_2H_6
Diameter of sense wire (μm)	30	30

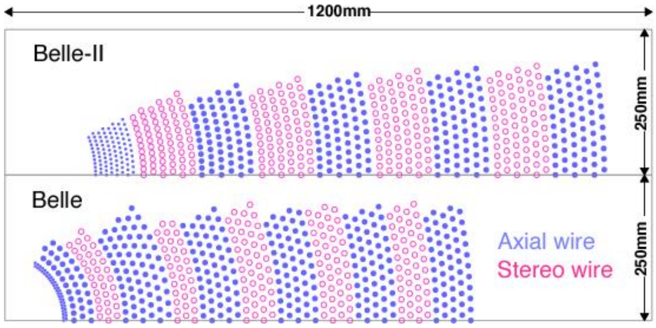

FIGURE 3.5: Wire configuration of Belle-II CDC and comparison with Belle CDC.

3.2.4 Particle Identification Detectors (PID)

Particle identification is subjected to a complete redesign. Earlier Belle had ACC and the TOF which were bigger in dimension and they were replaced by a Time-Of-Propagation counter (TOP) [113] in the barrel and a proximity-focusing Aerogel Ring-Imaging Cherenkov detector (ARICH) [114] in the forward endcap region. This system offers not only an improved discrimination between pions and kaons but also requires less space and material, which allows for a larger CDC volume and a better energy measurement in the electromagnetic calorimeter (ECL). The schematic diagram of particle identification detectors is shown in Fig. 3.6.

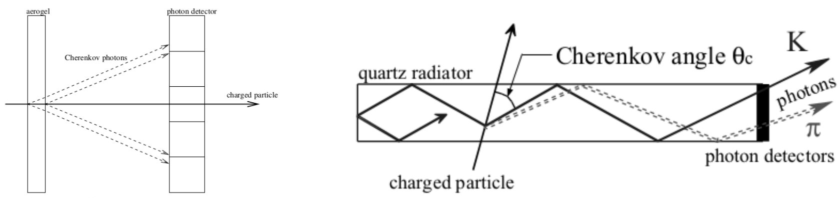

(A) (B)

FIGURE 3.6: Working principle of the ARICH (left) and TOP (right) detectors.

TOP consists of 16 synthetic fused, 2 cm thick silica radiator bars with photo-multipliers [115] at their ends. It measures the time of impact as well as the location where the charged particles enter the optical component. A Cherenkov image is reconstructed from this information and the Cherenkov photons propagate in the quartz bars towards the photomultiplier in a specific time depending on their Cherenkov angle ϕ. Hence, the TOP offers a time-of-flight measurement as well as a velocity measurement based on the equation for the Cherenkov angle $\cos(\phi) = 1/(n\beta)$, where n is the refractive index of the optical component and β is the particle velocity relative to the speed of light in the vacuum. Both measurements are combined into a likelihood for the different final state particle hypotheses. The ARICH detects Cherenkov photons produced in its aerogel radiator which consists of two layers with different refractive indices. Position-sensitive photon detectors reproduce the ring projection of the Cherenkov cone, which is focused due to the decreasing refractive indices. Again, the Cherenkov angle can be determined from the image, thereby providing the velocity of the observed particle. As in the case of the Belle spectrometer, the PIDs allow for the separation between different mass hypotheses in combination with the information from all the tracking detectors. In the backward region not covered by the PIDs, this task is required to be fulfilled by the remaining sub-detectors.

3.2.5 Electromagnetic Calorimeter (ECL)

The Electromagnetic Calorimeter for the Belle II experiment (ECL) will reuse the Belle detector ECL[116] with improved readout electronics. The Belle electromagnetic calorimeter consists of 8736 CsI(Tl) crystals with a typical dimension of $6\times6\times30$ cm^3. The main purpose of the electromagnetic calorimeter is to detect photons and π_0's. The energy of such photons ranges from a few MeV to a few GeV. Energy resolution is very crucial in order to separate signal and background events only with mass distribution. To separate two photons from high momentum π_0, fine granularity is required. Hermeticity is also very important to study final states with neutrinos. The calorimeter has pointing geometry and covers polar angle from $12°$ to $155°$. The scintillation light of the CsI(Tl) crystal has wavelength $\lambda = 560$ nm with a rather slow decay constant of 1.3 μsec but an abundant light output of about 50000 p.e./MeV. The light is read out by two independent sets of silicon PIN photodiodes with a sensitive area of 10×20 mm^2 connected to charge sensitive preamplifier. Two signals from preamplifiers are first added and then processed with two shapers with 0.2(fast) and 1 μsec(slow) shaping times. The readout electronics in Belle were designed to cope with a 300 Hz trigger rate, while in Belle II a rate 100 times higher is expected. Due to the higher background and very high occupancy, in the forward region, the pileup level can severely spoil the energy and time resolution of the detector. The replacement of all or of a part of the crystals with a pure CsI one will allow us to overcome such limitation, thanks to a decay time of 30ns. Fig. 3.7 shows a schematic view and a picture of a crystal equipped with photodetectors.

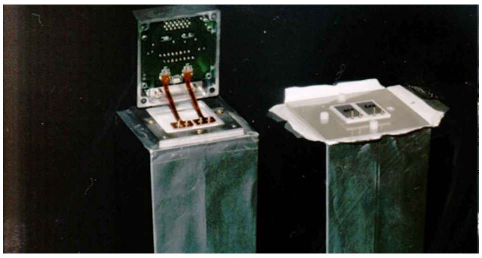

FIGURE 3.7: A schematic view and a picture of a crystal equipped with photodetectors.

3.2.6 Solenoid

A superconducting solenoid provides a magnetic field of 1.5 T in a cylindrical volume 3.4 m in diameter and 4.4 m in length[117]. It radially surrounds the ECL. The return yoke is used as a support and absorber structure for the K_L^0 and muon detector. The yoke is made of iron and split into a fixed barrel and a movable end cap part. The generated magnetic field helps to measure the transverse momentum of the charged particles.

3.2.7 K_L^0 and Muon Detector (KLM)

The muon is an elementary particle that belongs to the lepton family similar to an electron but with a mass 207 times larger. Due to being heavier in mass, they lose less energy flying through the matter and penetrate more into the matter than electrons. K_L^0 is a weak eigenstate of the neutral K meson, which mostly decays to three pions, therefore has a long lifetime and escapes inner detectors easily undetected. So one similar thing between K_L^0 and muon is they can travel long distances without getting undetected inside the Belle II detector. To identify K_L^0 and muons the largest Belle II subdetector is used, KLM. Due to the distance from the interaction point and the amount of metal in the yoke, no other particle but muon and K_L can effectively reach and penetrate KLM. The Belle II KLM is the upgrade of the Belle KLM. The Belle II KLM consists of the barrel part with 15 layers and two endcaps, forward and backward, with 14 and 12 layers, respectively. It is a sandwich-like structure of alternating metal plates and active detector plates. The metal plates have a thickness of 4.7 cm and they serve two purposes: as an absorber to decelerate particles and as the magnetic flux returns the yoke of the magnet. The whole KLM is subdivided into two sections, a barrel part (BKLM) which is aligned in parallel to the beam axis, and an end cape(EKLM) which is normal to the beam. A typical muon will pass through all the KLM layers in the barrel or an endcap, leaving a clean trail of hits to mark its passage. A typical K_L^0 will collide with the iron nucleus, resulting in debris that leaves a cluster of KLM hits. Basically, a traversing charged particle ionizes the gas, frees ions and electrons which are accelerated by the potential, ionizes the gas further, and creates an avalanche of charge carriers. These move towards the electrodes and induce a signal in the readout strips that is strong enough to be measured without amplification. The readout is done with strips on both ends. In EKLM plastic scintillator strips with silicon photomultiplier are used as detector material. The experience from the predecessor experiment Belle has shown that RPCs did not perform well here because of strong rates from beam background, such as neutrons, that saturated the detector. In this environment, it was very hard to find neutral hadrons like K_L^0. EKLM is instrumented with scintillator strips of a length between 885 mm and 2820 mm, a width of 40 mm, and a thickness of 7-10 mm. The working principle of Belle II KLM is shown in Fig. 3.8 and Fig. 3.9.

A muon having momentum higher than $\sim$ 0.6 GeV/c passes through the KLM with a nearly straight trajectory and escapes the detector. On the other hand, a K_L^0 meson is likely to interact with a nucleus of the ECL or the KLM material and initiate a hadronic shower detected by the ECL, the KLM, or both.

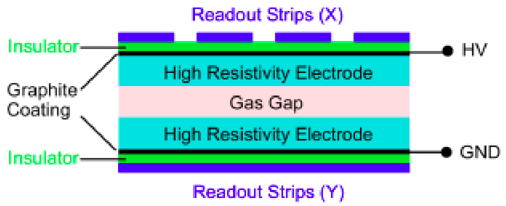

FIGURE 3.8: The sketch of an RPC. Two highly resistive electrodes enclose a gas volume. High voltage is applied to the electrodes.

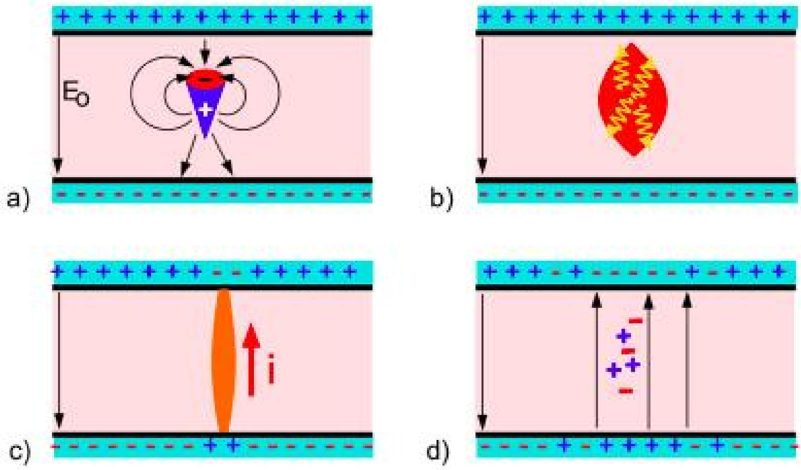

FIGURE 3.9: Depiction of the time development of the signal generation inside a RPC. a) A charged particle ionized the gas forming an avalanche. b) As the avalanche grows photons start to contribute to the avalanche. A streamer mode evolves. c) An avalanche hits the electrodes. d) The electric field on the electrodes is drastically decreased.

3.3 Motivation for Low Momentum Tracking

In this section, we will explain why stand-alone tracking in the VXD is important to the experimental program of Belle II. Apart from many other decay chains of interest, the decays $D^{*\pm} \to D^0\pi^\pm$ are of particular interest since they contain a very distinctive slow pion (π_s), which can be used as an identifier for these channels. $D^{*\pm}$ are very common decay products of $\bar{B}^0$ and B^0. So there are many decay channels where $D^{*\pm}$ are an intermediate state, which are probed to search for the new physics. There are already some deviations found by BaBar, Belle, and LHCb, having a combined deviation of 3.9σ from the theoretical predictions, which could be described by a mediator charged Higgs instead of W boson. Whereas charged Higgs can not be explained by standard model some model based on supersymmetry predicts the existence of charged Higgs bosons. More details could be found in [118–120].

$$R_{D^{(*)}} = \frac{\mathcal{B}(\overline{B} \to D^{(*)}\tau\nu_\tau)}{\mathcal{B}(\overline{B} \to D^{(*)}\ell\nu_l)}(\ell = e, \mu) \tag{3.2}$$

Measurements of the branching fractions of the above-mentioned decay modes suffer from the background $B \to D^{**}\ell\nu_l$ decays, which very often decay to a number of slow pions. Therefore it is crucial to have low-momentum tracking to be able to identify background by the number of the slow pions. Belle II including low-momentum tracking will therefore be able to keep the background lower while having much more events measured than its predecessors. A Monte Carlo based study using VXDTF for reconstructing the decay channels $D^{*\pm} \to D^0\pi^\pm$ found an increase in reconstruction efficiency from 40% to 80% of the slow pions in Belle II than Belle. Roughly a third of all slow pions in that study could only be found by tracking in the SVD. It is also required to study the performance of the SVD as it is crucial to measure the lifetimes of many particles [121–123].

3.4 Study of slow-pion relative tracking efficiency using $B^0 \to D^*\pi$ and $B^0 \to D^*\rho$ decays

We study the decay samples of $B^0 \to D^{*-}\pi^+$ and $B^0 \to D^{*-}\rho^+$ with D^{*-} further decaying to $\overline{D}^0\pi^-$. Our aim is to measure relative efficiency in the low momentum regions and related systematic uncertainty using $B \to D^*\pi$ and $B^0 \to D^{*-}\rho^+$ decays.[1] An earlier measurement of the slow-pion reconstruction efficiency was performed by the

[1] Charge conjugate processes are included unless stated otherwise.

Belle experiment[124] using about 29.1 fb^{-1} data and 0.2 million Monte Carlo (MC) events. High-momentum tracking efficiency measurement using partially reconstructed D decays was also carried out by Belle[125].

We reconstruct ρ^+ from its most favourable mode $\pi^+\pi^0$. We have considered two sets of different final states for $\overline{D}^0$. In the first case , $\overline{D}^0$ decays into the following three clean channels: $K^+\pi^-$, $K^0_s\pi^+\pi^-$, and $K^+\pi^-\pi^-\pi^+$ and in second case, it decays to $K^+\pi^-$, $K^+\pi^-\pi^0$, and $K^+\pi^-\pi^-\pi^+$, respectively. We aim to measure the track finding relative efficiency of the low-momentum charged pion coming from D^* decays, referred to as the slow pion (π_s). The relative tracking efficiency results for the $B^0 \to D^{*-}\rho^+$ mode is attached in the Appendix B.

Reconstructed trajectories of charged particles (tracks) are required to originate from the interaction point (IP) and have a point of closest approach to the latter within 3.0 cm along the e^+ beam axis and 1.0 cm in the transverse plane. These requirements remove tracks not originating from the IP. Additionally, the tracks are required to have at least two hits in the CDC. The final-state charged hadrons (pions, kaons) are identified based on the meausurements in TOP sub-detector and dE/dx measurements. All of this information is combined to form pion and kaon likelihoods, $\mathcal{L}_\pi$ and $\mathcal{L}_K$, respectively. The selection is made on the basis of likelihood ratios, $\mathcal{L}_{i/j} = \mathcal{L}_i/(\mathcal{L}_i + \mathcal{L}_j)$, where i and j are π, K. Kaons and pions are selected by requiring $\mathcal{L}_{K/\pi} > 0.6$ and $\mathcal{L}_{\pi/K} > 0.6$, respectively. The invariant mass of a $\overline{D}^0$ candidate is required to be in the window $|M_{D^0} - M_{D^0}^{\rm PDG}| < 0.04$ GeV (5σ window around the nominal D^0 mass). The mass difference, $\Delta M = M_{D^*} - M_{D^0}$, where M_{D^*} (M_{D^0}) is the invariant mass of the D^{*+} (D^0) candidate, is required to be within $0.143 < |\Delta M| < 0.147$ GeV/c^2(to remove combinatorial backgrounds). The momentum of the D^{*+} candidate in the c.m. frame is required to be greater than 2.5 GeV/c to reduce $q\bar{q}$ and combinatorial backgrounds. We require $|\Delta E| = \sum(E_i$ - $E_{\rm beam})$ to be < 0.2 GeV (5σ window around the nominal ΔE value of zero) where $E_{\rm beam}$ is the beam energy in the c.m. frame and E_i are the energy of the B-decay product in the c.m. frame. A requirement on R2 , the normalized second

Fox-Wolfram moment (R2 < 0.3) is made to reduce continuum background events. The candidates are selected in the range $5.2 < M_{bc} = \sqrt{E_{\mathrm{beam}}^2 - p^2} < 5.29$ GeV/c^2 where p is the momentum of the B-decay product in the c.m. frame. In subsequent analysis, we fit both ΔE and M_{bc} to extract yield.

No particle ID or impact parameter criteria have been applied on the π_s candidate. Owing to this, we expect a poorer signal-to-background ratio in the reconstructed D^* mass distribution and hence apply a tighter requirement compared to the D^0 case. While fitting M_{bc}, we put a tight cut on ΔE to suppress as many combinatorial and peaking backgrounds as possible. While fitting ΔE, we put a tight cut on M_{bc}. We fit M_{bc} and ΔE after applying all those above-mentioned cuts to extract signal yields. The fitting is done in the following four bins of π_s momentum: $0.05-0.12, 0.12-0.16, 0.16-0.20,\text{and } 0.20-0.32$ GeV/c for $B^0 \to D^{*-}\pi^+$ channel. The bins for $B^0 \to D^{*-}\rho^+$ channel are chosen as $0.05-0.12, 0.12-0.16, 0.16-0.20, \text{and } 0.20-0.32$ GeV/c. We keep the binning the same for both modes.

3.4.1 Data and Monte Carlo Samples

We generate 0.2 million simulated events (signal MC) using the present detector condition. The beam background is not taken into account while generating these events. As these events is used only to determine the M_{bc} shape which is later used for fitting data events, it is not crucial to have beam background overlaying. For the background study, we use 100 fb^{-1} of generic Monte Carlo, where beam background is considered in the simulation. The data samples used for our study have luminosity 193.3 fb^{-1}.

3.4.2 Results for $B^0 \to D^{*-}\pi^+$ decays (Clean Channel)

In this section, we present the π_s momentum and M_{bc} distributions along with the results of fits in bins of π_s momentum for $B^0 \to D^{*-}\pi^+$ decays for generic MC, as well as in data events.

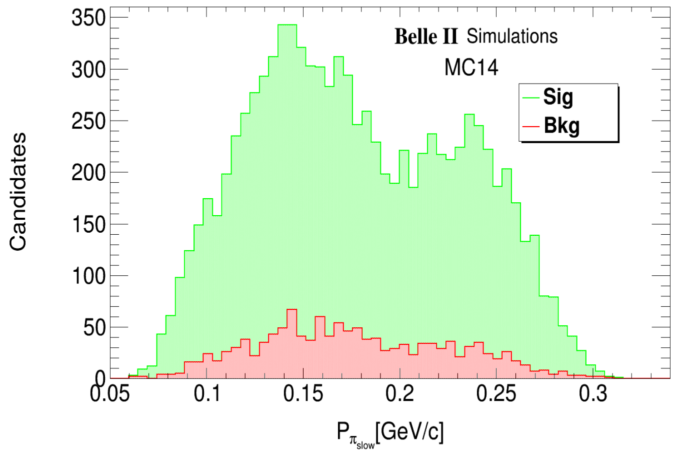

FIGURE 3.10: Distribution of π_s momentum for $B^0 \to D^{*-}\pi^+$ in generic MC events. Signal and background candidates are shown by the blue and red hatched histograms, respectively.

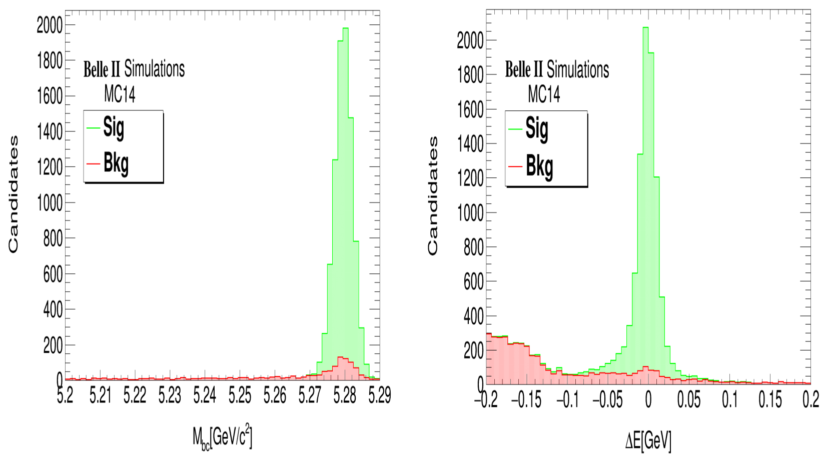

FIGURE 3.11: Distributions of $M_{\rm bc}$ (left) and ΔE (right) for $B^0 \to D^{*-}\pi^+$ in generic MC events. Correctly reconstructed events and backgrounds are shown by the green and red hatched histograms, respectively.

In Fig. 3.10 we present the distribution of π_s momentum for $B^0 \to D^{*-}\pi^+$ in generic MC events. Fig. 3.11 shows the $M_{\rm bc}$ and ΔE plots for the same events. The ΔE distribution does not exhibit any peaking structure beyond the signal peak. We are using generator-level information for the background investigation. We will fit both $M_{\rm bc}$ and ΔE to extract yields. While we fit $M_{\rm bc}$ we use ΔE within range (-0.04, 0.04) GeV and for fitting ΔE we use $M_{\rm bc}$ within range (5.27, 5.29) GeV/c^2. In Fig. 3.12, we present the distribution of $M_{\rm bc}$ for $B^0 \to D^{*-}\pi^+$ in generic MC sample after the background investigation using generator level information. By looking at the distribution the percentage

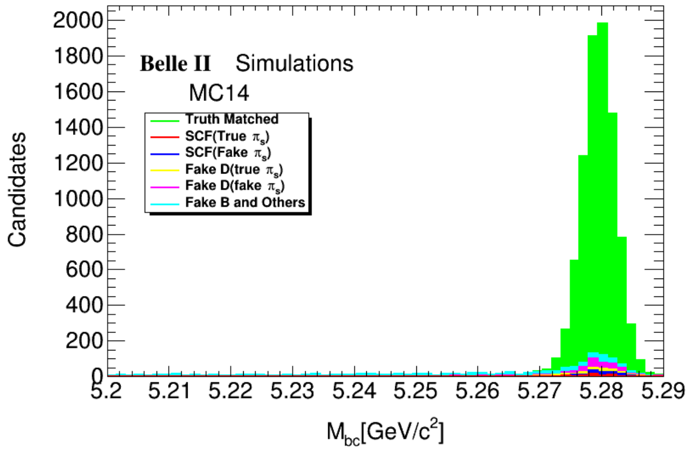

FIGURE 3.12: Distribution of $M_{\rm bc}$ for $B^0 \to D^{*-}\pi^+$ in Generic MC sample after the background investigation using the generator level information.

of background contributing in $M_{\rm bc}$ distribution is listed below in Table 3.2.

TABLE 3.2: Percentage of background contributing in $M_{\rm bc}$ distribution for $B^0 \to D^{*-}\pi^+$ decays where SCF (self-cross feed events) and Fake D corresponds to the mis-reconstructed signal events and the background coming from the wrong D^* and D^0 respectively.

SCF (True π_s)	7 %
SCF (Fake π_s)	7 %
Fake D (True π_s)	10 %
Fake D (Fake π_s)	18 %
Fake B & Other	58 %

3.4.2.1 Using $M_{\rm bc}$ Fitting Method

In Fig. 3.13, the top plot shows the fitted distribution of $M_{\rm bc}$ for $B^0 \to D^{*-}\pi^+$ in generic MC (left) and data (right), and the bottom the points are obtained from an $M_{\rm bc}$ fit in bins of π_s momentum. The Fig. 3.14 shows the fitted distribution of $M_{\rm bc}$ for $B^0 \to D^{*-}\pi^+$ events in generic MC in each momentum bin. The PDFs used for fitting in Fig. 3.14 are the sum of Gaussian (signal) and ARGUS function (background).

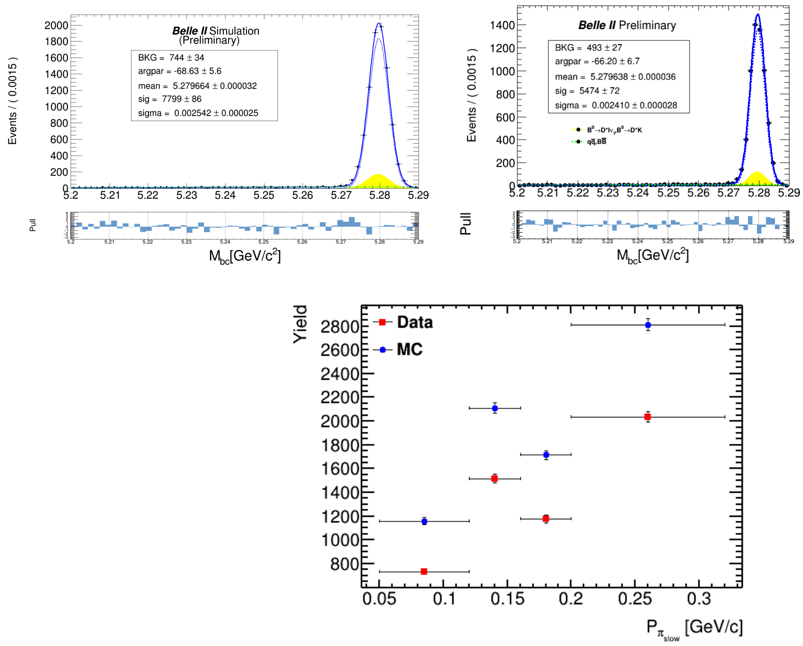

FIGURE 3.13: Top plots show the fitted distribution of $M_{\rm bc}$ for $B^0 \to D^{*-}\pi^+$ in generic MC [left] and data [right]. The PDF for the signal (background) component is shown by the blue (green) dotted curve. The total fit PDF is shown by the solid blue curve. The yellow part shows the peaking background contribution. The bottom plot shows the signal yields obtained from an $M_{\rm bc}$ fit in the bins of π_s momentum. The red error bar corresponds to data yields and the blue error bar corresponds to generic MC yields.

TABLE 3.3: Yields in different bins of slow pion momentum in the generic MC sample for $B^0 \to D^{*-}\pi^+$ decays.

p_{π_s} in GeV	Signal yield
[0.05, 0.12]	1160 ± 33
[0.12, 0.16]	2112 ± 45
[0.16, 0.20]	1714 ± 40
[0.20, 0.32]	2813 ± 52

The Table 3.3 shows the yields in different bins of slow pion momentum in the Generic MC sample for $B^0 \to D^{*-}\pi^+$ decays that are obtained from the fits shown in Fig. 3.14.

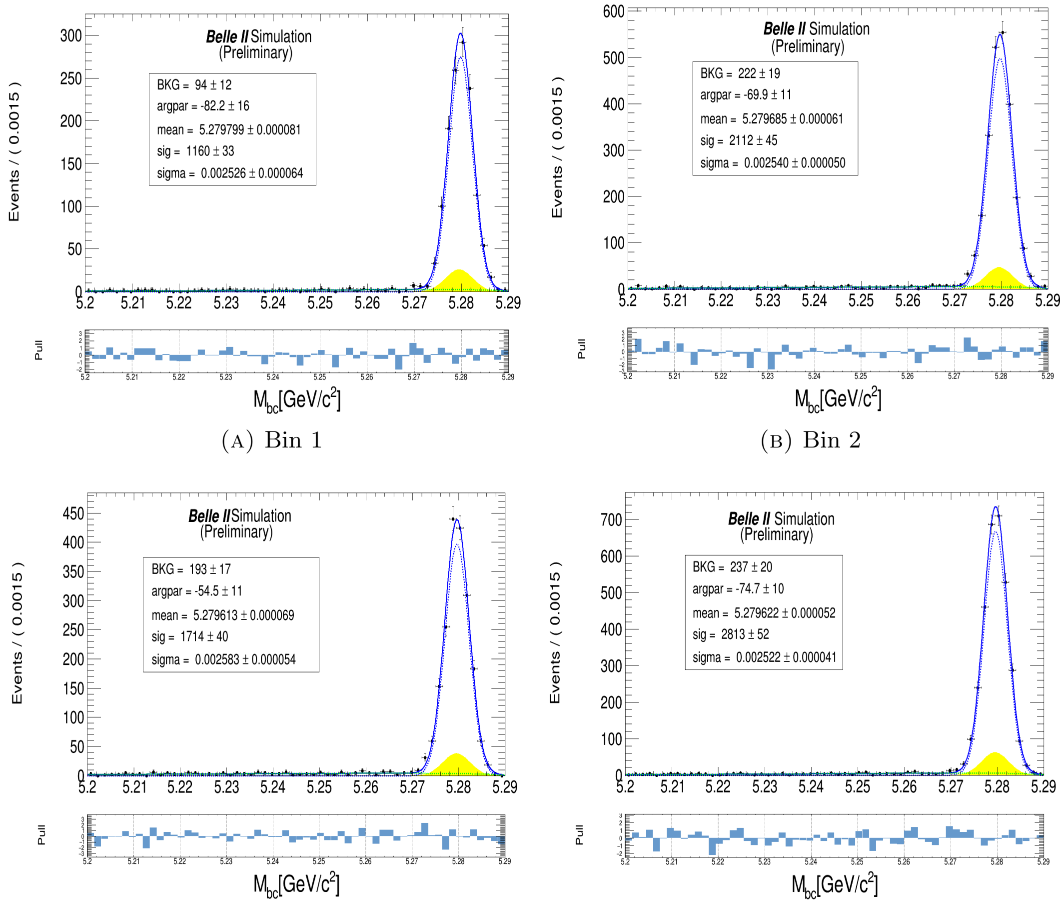

(A) Bin 1 (B) Bin 2

(C) Bin 3 (D) Bin 4

FIGURE 3.14: Fitted distribution of M_{bc} for $B^0 \to D^{*-}\pi^+$ in generic MC in slow pion momentum bins (a) Bin 1, (b) Bin 2, (c) Bin 3 and (d) Bin 4. The points with error bars and all color curves are the same as in Fig. 3.13.

TABLE 3.4: Signal yields in different bins of slow pion momentum in data for $B^0 \to D^{*-}\pi^+$ decays.

p_{π_s} in GeV	Signal yield
[0.05, 0.12]	734 ± 26
[0.12, 0.16]	1517 ± 38
[0.16, 0.20]	1179 ± 33
[0.20, 0.32]	2037 ± 44

The Fig. 3.15 shows the fitted distribution of M_{bc} for $B^0 \to D^{*-}\pi^+$ events in data in each bin of π_s momentum. The PDFs used for fitting in Fig. 3.15 are the Gaussian (signal) and ARGUS function (background). The Table 3.4 shows the yields in different bins of π_s momentum in the data for the $B^0 \to D^{*-}\pi^+$ decays that are obtained from the fits shown in the Fig. 3.15.

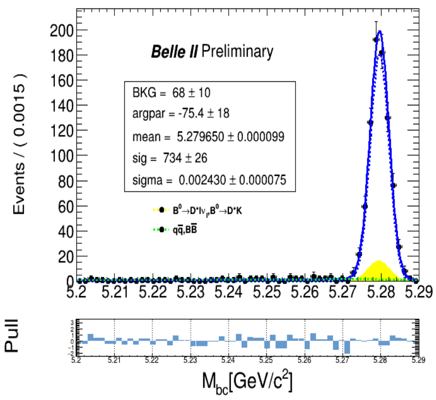

(A) Bin 1

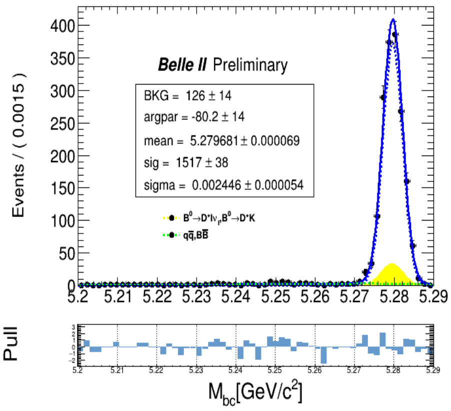

(B) Bin 2

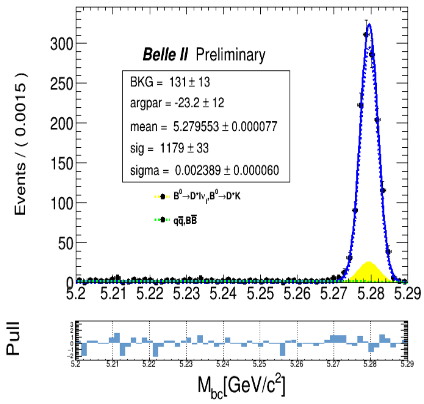

(C) Bin 3

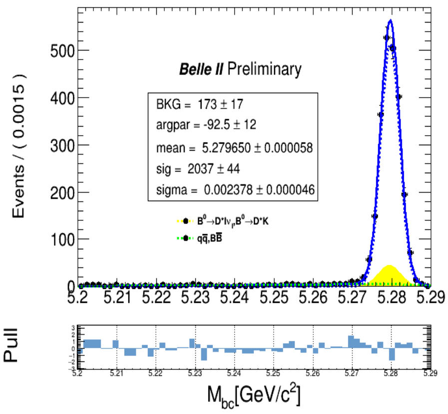

(D) Bin 4

FIGURE 3.15: Fitted distribution of M_{bc} for $B^0 \to D^{*-}\pi^+$ in data in π_s momentum bins (a) Bin 1, (b) Bin 2, (c) Bin 3, and (d) Bin 4. The points with error bars and all color curves are the same as in Fig. 3.13.

The Fig. 3.16 shows the π_s relative tracking efficiency data-MC ratio in bins of π_s momentum for M_{bc} for $B^0 \to D^{*-}\pi^+$. The fraction of events in data and MC ($f^{'}_{Data}$ and $f^{'}_{MC}$) are calculated by dividing the yield in each bin by the total yield. The ratio was normalized to unity in the rightmost bin. We choose the highest momentum bin for normalization as the overall data-MC agreement is expected to be best for this bin. The Table 3.5 summarizes the π_s relative tracking efficiency data-MC ratio in the four bins.

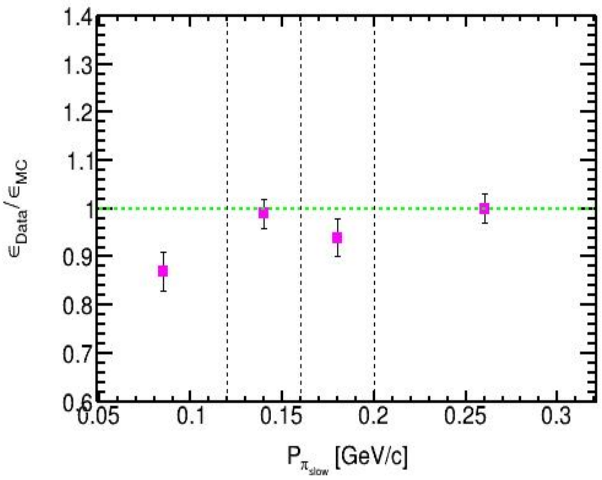

FIGURE 3.16: Slow pion relative tracking efficiency ratio of data to MC in bins of slow pion momentum in lab frame for $M_{\rm bc}$ for $B^0 \to D^{*-}\pi^+$.

TABLE 3.5: Summary of slow pion relative tracking efficiency data-MC ratio in bins of slow pion momentum for $B^0 \to D^{*-}\pi^+$.

p_{π_s} in GeV	$f^{'}_{Data}/f^{'}_{MC}$	$\varepsilon_{Data}/\varepsilon_{MC}$
[0.05, 0.12]	0.90 $\pm$ 0.04	0.87 $\pm$ 0.04
[0.12, 0.16]	1.02 $\pm$ 0.03	0.99 $\pm$ 0.03
[0.16, 0.20]	0.98 $\pm$ 0.04	0.94 $\pm$ 0.04
[0.20, 0.32]	1.03 $\pm$ 0.03	1.00

3.4.2.2 Using ΔE Fitting Method

In Fig. 3.17, the top plots show the fitted distribution of ΔE for $B^0 \to D^{*-}\pi^+$ in both generic MC and data, and the bottom the points are obtained from an ΔE fit in bins of π_s momentum.

The Fig. 3.18 shows the fitted distribution of ΔE for $B^0 \to D^{*-}\pi^+$ events in generic MC. The PDFs used for fitting in the Fig. 3.18 are the sum of double Gaussian (signal) and (exponential + Chebyshev Polynomial of first order) for background.

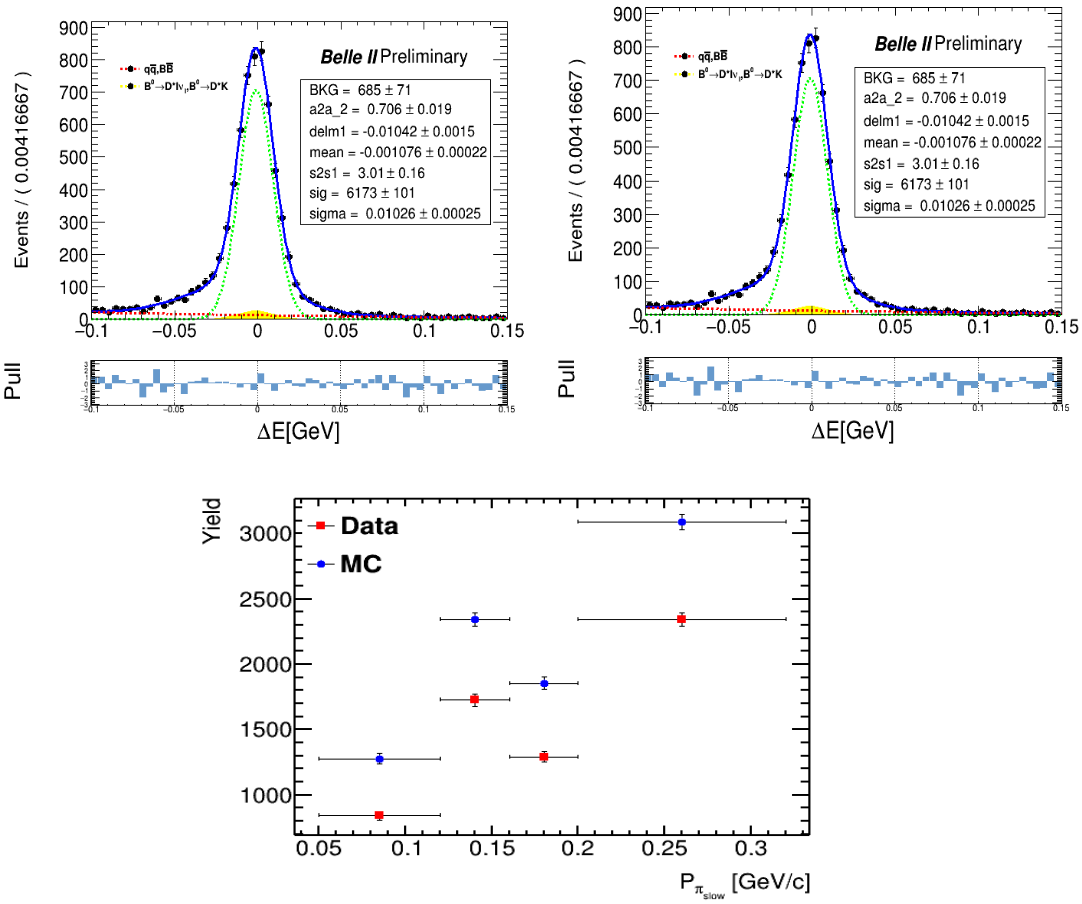

FIGURE 3.17: Top plots show the fitted distribution of ΔE for $B^0 \to D^{*-}\pi^+$ in generic MC [left] and data [right]. The sum of the PDF for signal and background component is shown by the blue dotted curve. The yellow part shows the peaking background contribution. The bottom plot shows the signal yields obtained from an ΔE fit in the bins of π_s momentum. The red error bar corresponds to Data yields and the blue error bar corresponds to MC yield.

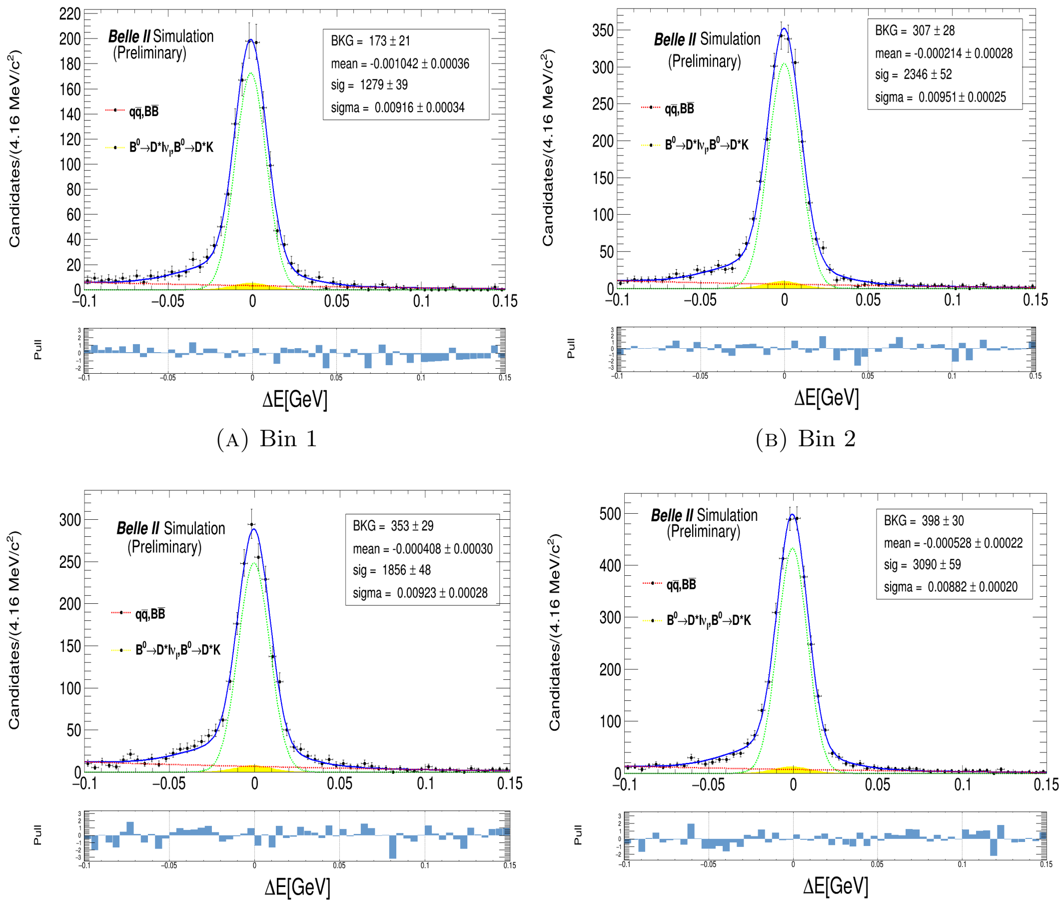

(A) Bin 1

(B) Bin 2

(C) Bin 3

FIGURE 3.18: Fitted distribution of ΔE for $B^0 \to D^{*-}\pi^+$ in generic MC in slow pion momentum bins (a) Bin 1, (b) Bin 2, (c) Bin 3 and (d) Bin 4. The points with error bars and all color curves are the same as in Fig. 3.17.

TABLE 3.6: Yields in different bins of slow pion momentum in the generic MC sample for $B^0 \to D^{*-}\pi^+$ decays.

p_{π_s} in GeV	Signal yield
[0.05, 0.12]	1279 ± 39
[0.12, 0.16]	2346 ± 52
[0.16, 0.20]	1856 ± 48
[0.20, 0.32]	3090 ± 59

TABLE 3.7: Signal yields in different bins of slow pion momentum in data for $B^0 \to D^{*-}\pi^+$ decays.

p_{π_s} in GeV	Signal yield
[0.05, 0.12]	843 ± 32
[0.12, 0.16]	1726 ± 45
[0.16, 0.20]	1294 ± 40
[0.20, 0.32]	2346 ± 52

Table 3.6 shows the yields in different bins of slow pion momentum in the generic MC

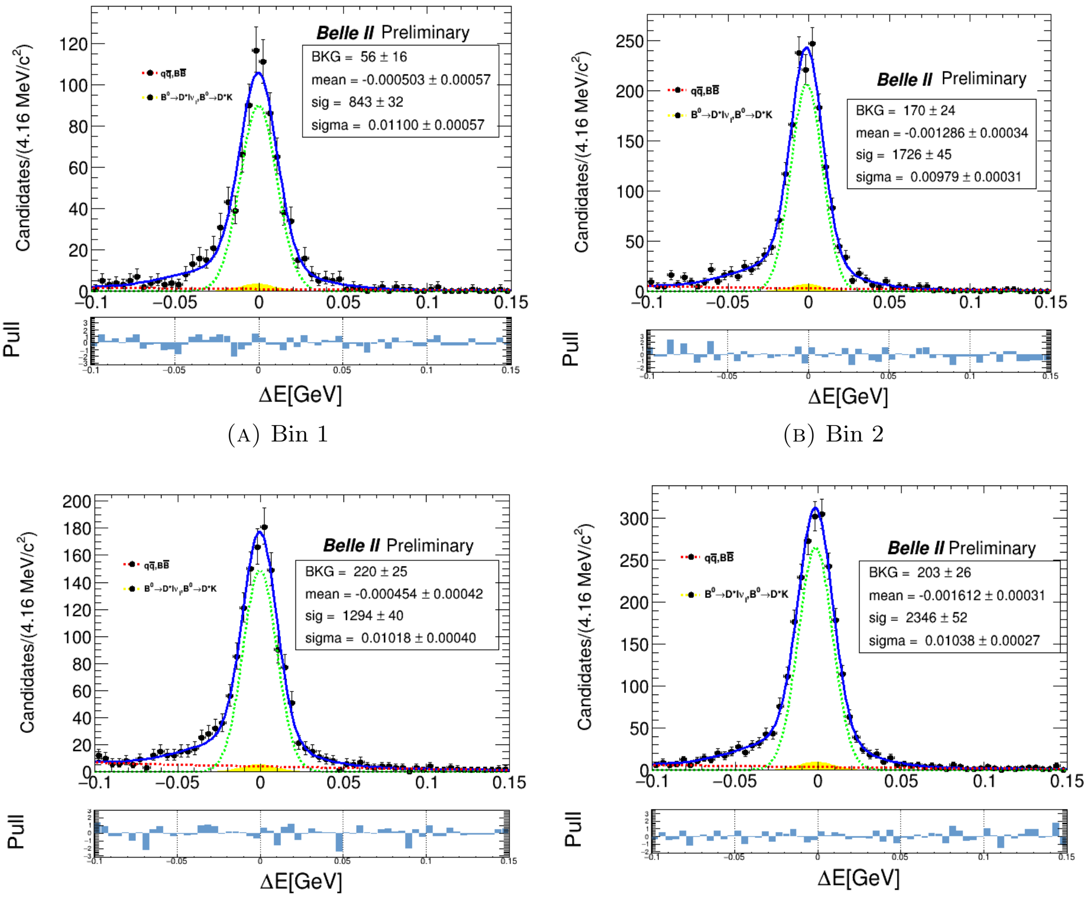

(A) Bin 1 (B) Bin 2

(C) Bin 3 (D) Bin 4

FIGURE 3.19: Fitted distribution of ΔE for $B^0 \to D^{*-}\pi^+$ in data in π_s momentum bins (a) Bin 1, (b) Bin 2, (c) Bin 3, and (d) Bin 4. The points with error bars and all color curves are the same as in Fig. 3.17

sample for $B^0 \to D^{*-}\pi^+$ decays that are obtained from the fits shown in Fig. 3.18. In Fig. 3.17, the top right plot shows the fitted distribution of ΔE for $B^0 \to D^{*-}\pi^+$ in data, and the bottom the points are obtained from an ΔE fit in bins of π_s momentum. The Fig. 3.19 shows the fitted distribution of ΔE for $B^0 \to D^{*-}\pi^+$ events in data in each bin of π_s momentum. The PDFs used for fitting in Fig. 3.19 are the double Gaussian (signal) and the sum of exponential and Chebyshev polynomial of the first order(background). The Table 3.7 shows the yields in different bins of π_s momentum in the data for the $B^0 \to D^{*-}\pi^+$ decays that are obtained from the fits shown in Fig. 3.19. The Fig. 3.20 shows the π_s tracking efficiency data-MC ratio in bins of π_s momentum for ΔE for $B^0 \to D^{*-}\pi^+$. The fraction of events in data and MC (f'_{Data} and f'_{MC}) are calculated by dividing the yield in each bin by the total yield. The ratio was normalized to unity in the rightmost bin. We choose the highest momentum bin for normalization as the overall data-MC agreement is expected to be best for this bin. The Table 3.8 summarizes the π_s relative tracking efficiency data-MC ratio in the four bins.

TABLE 3.8: Summary of slow pion relative tracking efficiency data-MC ratio in bins of slow pion momentum for $B^0 \to D^{*-}\pi^+$.

p_{π_s} in GeV	f'_{Data}/f'_{MC}	$\varepsilon_{Data}/\varepsilon_{MC}$
[0.05, 0.12]	0.90 ± 0.04	0.87 ± 0.04
[0.12, 0.16]	1.01 ± 0.03	0.97 ± 0.03
[0.16, 0.20]	0.96 ± 0.04	0.92 ± 0.04
[0.20, 0.32]	1.05 ± 0.03	1.00

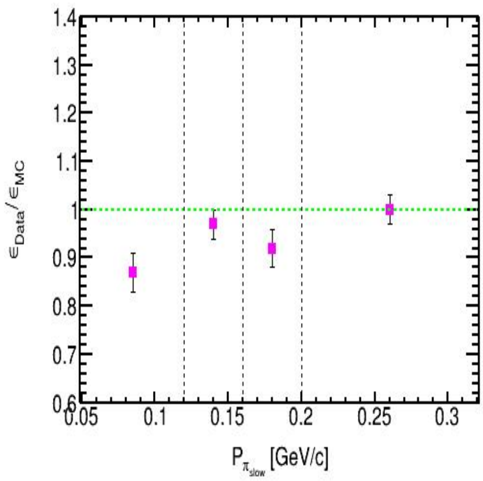

FIGURE 3.20: Slow pion relative tracking efficiency ratio of data to MC in bins of slow pion momentum in lab frame for ΔE for $B^0 \to D^{*-}\pi^+$.

3.4.3 Results for $B^0 \to D^{*-}\pi^+$ decays (π^0 added)

In this section, we represent $M_{\rm bc}$ and ΔE distribution along with the results of fit in bins of π_s momentum for $B^0 \to D^{*-}\pi^+$ decays for generic MC as well as data events. The Fig. 3.21 shows the $M_{\rm bc}$ and ΔE plots for the generic MC events. We are using the generator level information for the background investigation. We fit $M_{\rm bc}$ and ΔE to extract yields. While fitting $M_{\rm bc}$ we have used ΔE within range (-0.1, 0.15) GeV. While fitting ΔE we have used $M_{\rm bc}$ within range (5.27, 5.29) GeV/c^2.

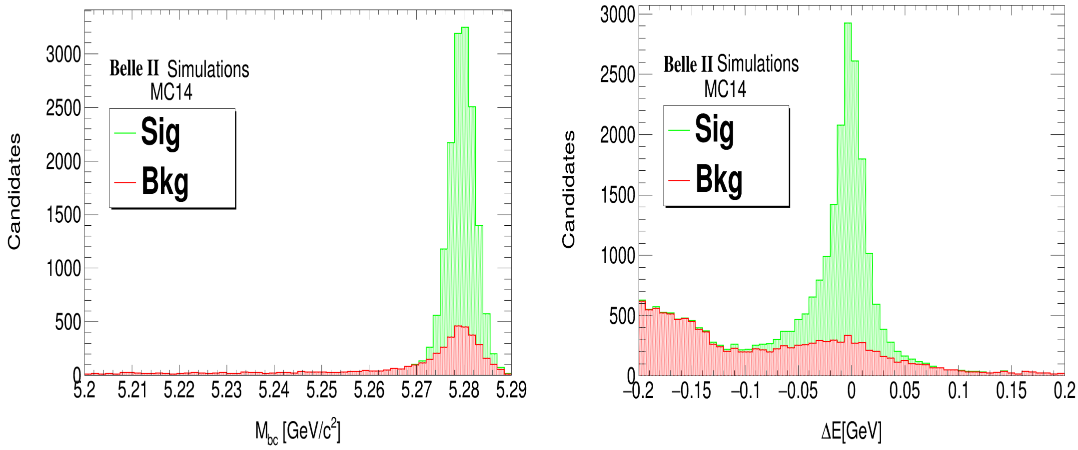

FIGURE 3.21: Distributions of $M_{\rm bc}$ for $B^0 \to D^{*-}\pi^+$ in generic MC events. All and correctly reconstructed events are shown by the blue and red hatched histograms, respectively.

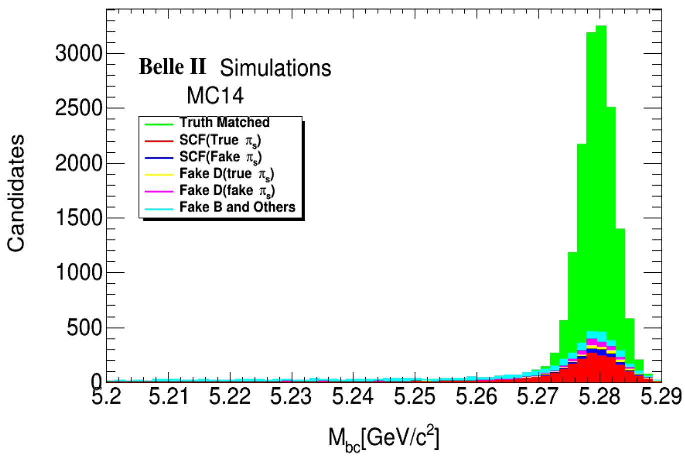

FIGURE 3.22: Distribution of $M_{\rm bc}$ for $B^0 \to D^{*-}\pi^+$ in Generic MC sample after the background investigation using GenMC Tagging tool and isSignal.

In Fig. 3.22, we present the distribution of $M_{\rm bc}$ for $B^0 \to D^{*-}\pi^+$ in generic MC sample after the background investigation using the generator level information. By looking at the distribution the percentage of background contributing in $M_{\rm bc}$ distribution is listed below in Table 3.9.

TABLE 3.9: Percentage of background contributing in $M_{\rm bc}$ distribution for $B^0 \to D^{*-}\pi^+$ decays where SCF (self-cross feed events) and Fake D corresponds to the mis-reconstructed signal events and the background coming from the wrong D^* and D^0 respectively.

SCF (True π_s)	43 %
SCF (Fake π_s)	5 %
Fake D (True π_s)	5 %
Fake D (Fake π_s)	8 %
Fake B & Others	39 %

3.4.3.1 Using $M_{\rm bc}$ Fitting Method

In Fig. 3.23, the top plots show the fitted distribution of $M_{\rm bc}$ for $B^0 \to D^{*-}\pi^+$ in both generic MC and data, and the bottom the points are obtained from an $M_{\rm bc}$ fit in bins of π_s momentum.

The Table 3.10 shows the yields in different bins of slow pion momentum in the Generic MC sample for $B^0 \to D^{*-}\pi^+$ decays that are obtained from the fits shown in Fig. 3.24. In Fig. 3.23, the top right plot shows the fitted distribution of $M_{\rm bc}$ for $B^0 \to D^{*-}\pi^+$ in data, and the bottom the points are obtained from an $M_{\rm bc}$ fit in bins of π_s momentum.

TABLE 3.10: Yields in different bins of slow pion momentum in the generic MC sample for $B^0 \to D^{*-}\pi^+$ decays.

p_{π_s} in GeV	Signal yield
[0.05, 0.12]	1869 ± 41
[0.12, 0.16]	3382 ± 56
[0.16, 0.20]	2618 ± 49
[0.20, 0.32]	4524 ± 64

TABLE 3.11: Signal yields in different bins of slow pion momentum in data for $B^0 \to D^{*-}\pi^+$ decays.

p_{π_s} in GeV	Signal yield
[0.05, 0.12]	947 ± 29
[0.12, 0.16]	1957 ± 41
[0.16, 0.20]	1484 ± 36
[0.20, 0.32]	2712 ± 48

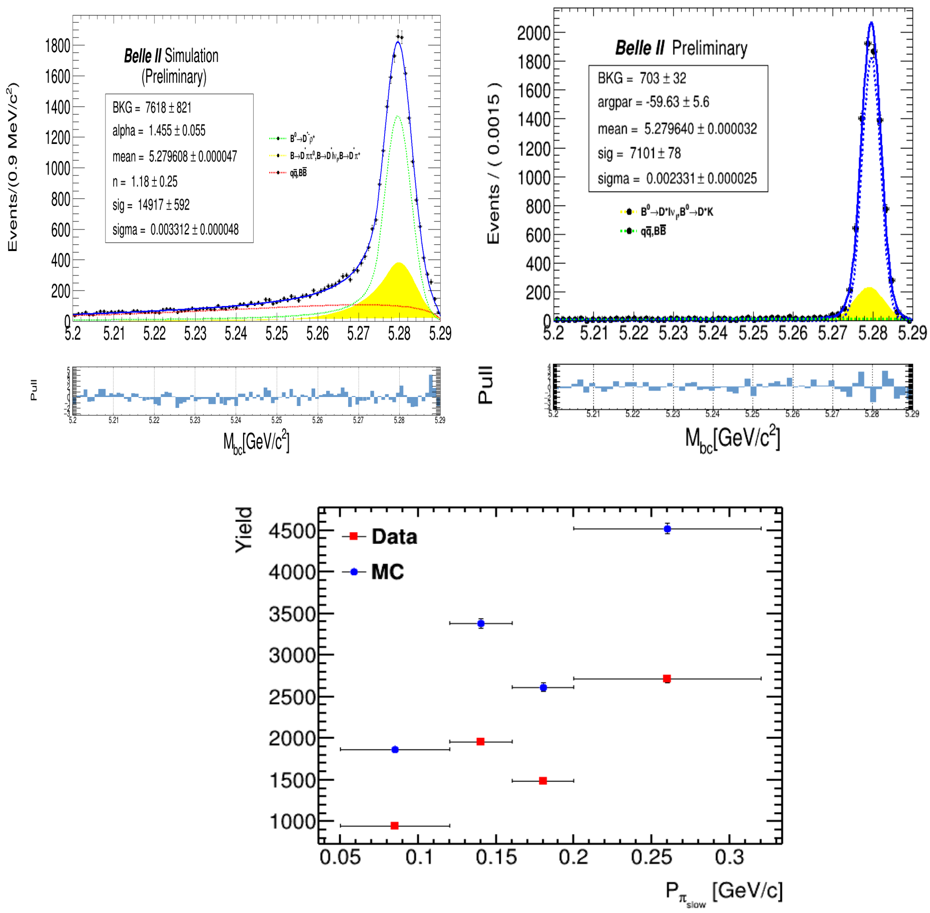

FIGURE 3.23: Top plots show the fitted distribution of $M_{\rm bc}$ for $B^0 \to D^{*-}\pi^+$ in both generic MC (left) and data (right). The PDF for the signal (background) component is shown by the blue (green) dotted curve. The yellow part shows peaking background contribution Total fit PDF is shown by the solid blue curve. The bottom plot shows the signal yields obtained from an $M_{\rm bc}$ fit in the bins of π_s momentum.

Fig. 3.25 shows the fitted distribution of $M_{\rm bc}$ for $B^0 \to D^{*-}\pi^+$ events in data in each bin of π_s momentum. The PDFs used for fitting in Fig. 3.25 are the Gaussian (signal) and ARGUS function (background). Table 3.11 shows the yields in different bins of π_s momentum in the data for $B^0 \to D^{*-}\pi^+$ decays that are obtained from the fits shown in Fig. 3.25.

Fig. 3.26 shows the π_s tracking efficiency data-MC ratio in bins of π_s momentum for $M_{\rm bc}$ for $B^0 \to D^{*-}\pi^+$. The fraction of events in data and MC (f'_{Data} and f'_{MC}) are calculated by dividing the yield in each bin by the total yield. The ratio was normalized to unity in the rightmost bin. We choose the highest momentum bin for normalization as the

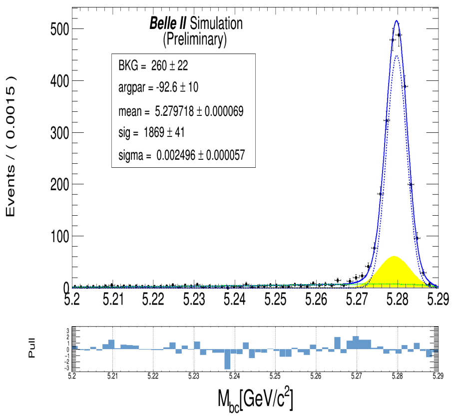

(A) Bin 1

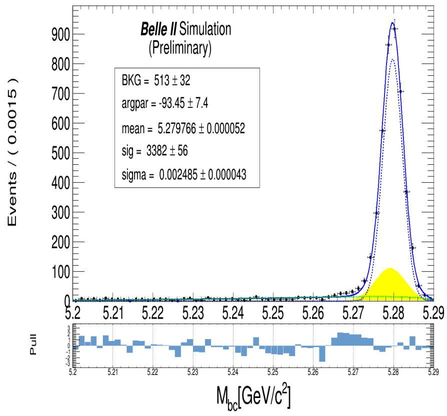

(B) Bin 2

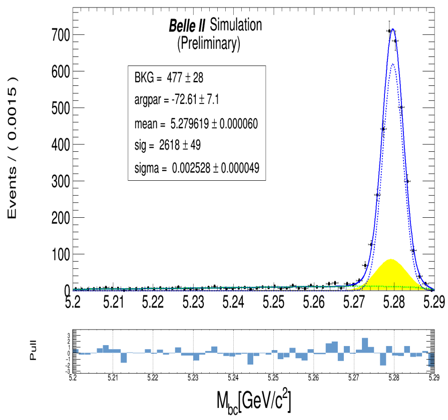

(C) Bin 3

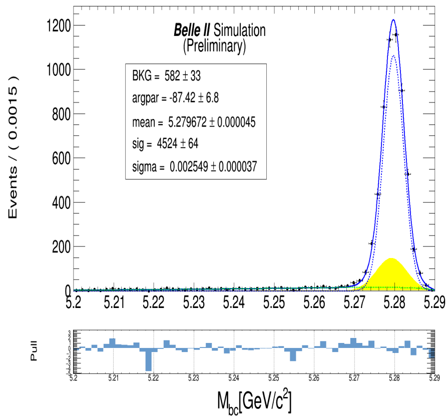

(D) Bin 4

FIGURE 3.24: Fitted distribution of M_{bc} for $B^0 \to D^{*-}\pi^+$ in generic MC in slow pion momentum bins (a) Bin 1, (b) Bin 2, (c) Bin 3 and (d) Bin 4. The points with error bars and all color curves are the same as in Fig. 3.23

overall data-MC agreement is expected to be best for this bin. Table 3.12 summarizes the π_s relative tracking efficiency data-MC ratio in the four bins.

TABLE 3.12: Summary of slow pion relative tracking efficiency data-MC ratio in bins of slow pion momentum for $B^0 \to D^{*-}\pi^+$.

p_{π_s} in GeV	f'_{Data}/f'_{MC}	$\varepsilon_{Data}/\varepsilon_{MC}$
[0.05, 0.12]	0.88 ± 0.03	0.84 ± 0.03
[0.12, 0.16]	1.01 ± 0.03	0.97 ± 0.03
[0.16, 0.20]	0.98 ± 0.03	0.94 ± 0.03
[0.20, 0.32]	1.05 ± 0.02	1.00

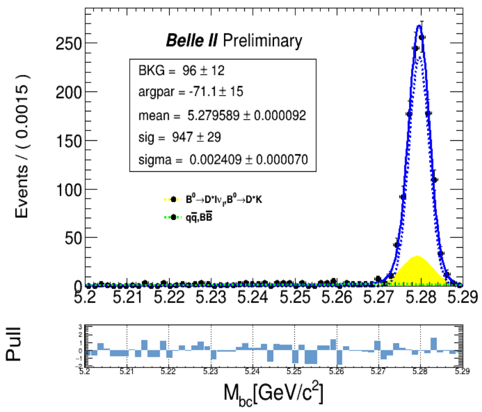

(A) Bin 1

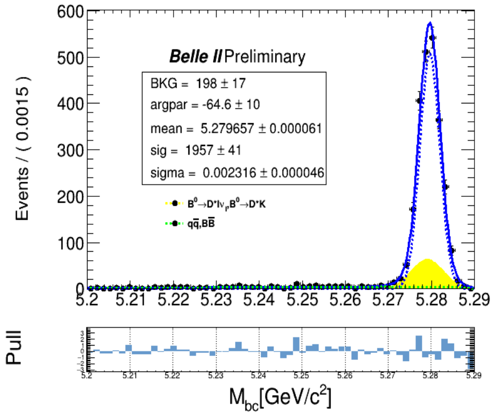

(B) Bin 2

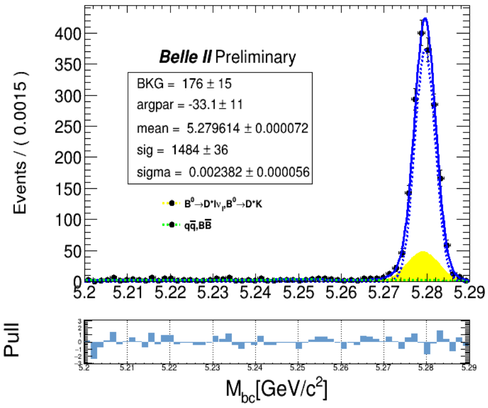

(C) Bin 3

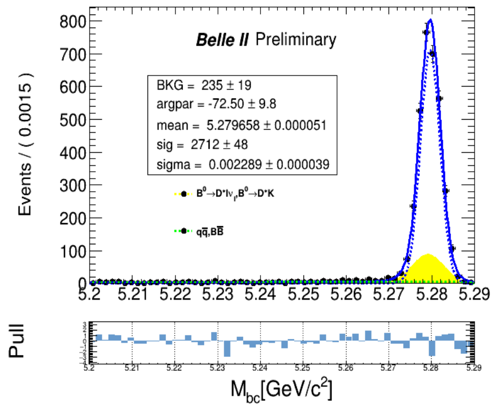

(D) Bin 4

FIGURE 3.25: Fitted distribution of $M_{\rm bc}$ for $B^0 \to D^{*-}\pi^+$ in data in π_s momentum bins (a) Bin 1, (b) Bin 2, (c) Bin 3, and (d) Bin 4. The points with error bars and all color curves are the same as in Fig. 3.23.

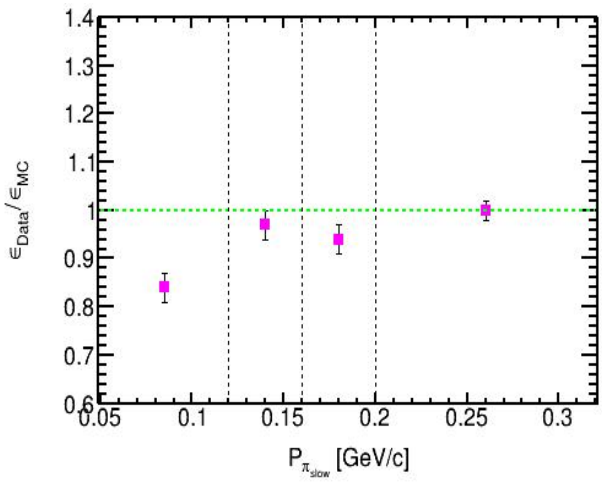

FIGURE 3.26: Slow pion relative tracking efficiency ratio of data to MC in bins of slow pion momentum in lab frame for $M_{\rm bc}$ for $B^0 \to D^{*-}\pi^+$.

3.4.3.2 Using ΔE Fitting Method

In Fig. 3.27, the top plots show the fitted distribution of $M_{\rm bc}$ for $B^0 \to D^{*-}\pi^+$ in both generic MC and data, and the bottom the points are obtained from an ΔE fit in bins of π_s momentum.

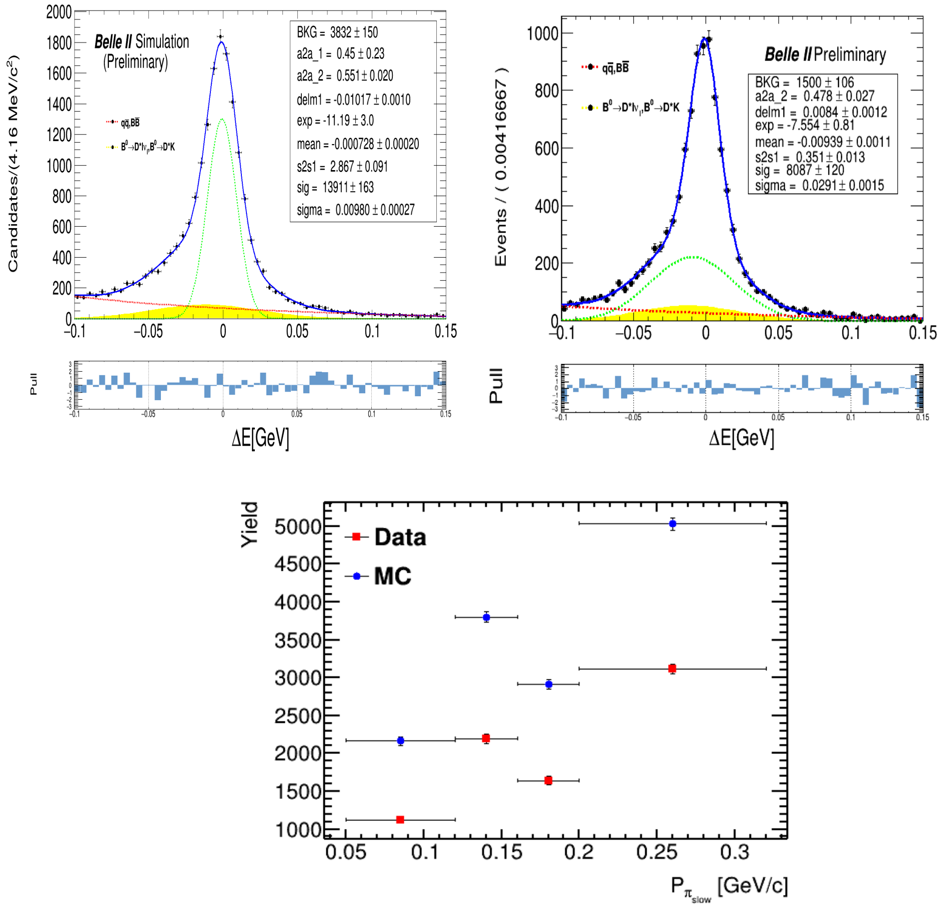

FIGURE 3.27: Top plot shows the fitted distribution of ΔE for $B^0 \to D^{*-}\pi^+$ in generic MC (left) and data (right), respectively. The sum of the PDF for signal and background component is shown by the blue dotted curve. The total fit PDF is shown by the solid blue curve. The bottom plot shows the signal yields obtained from an ΔE fit in the bins of π_s momentum. The red error bar corresponds to Data yields and the blue error bar corresponds to Generic MC yield.

Fig. 3.28 shows the fitted distribution of $M_{\rm bc}$ for $B^0 \to D^{*-}\pi^+$ events in Generic MC. The PDFs used for fitting in Fig. 3.18 are the sum of Double Gaussian (signal) and (exponential + Chebyshev Polynomial of first-order function) for background.

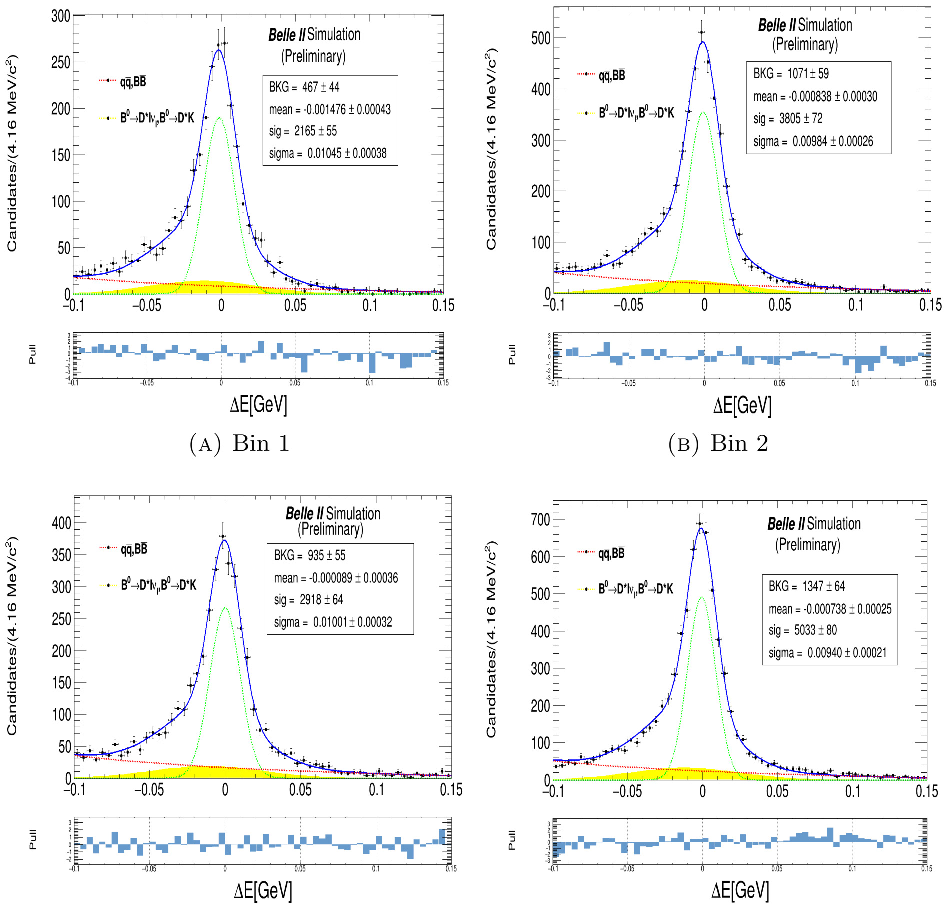

(A) Bin 1

(B) Bin 2

(C) Bin 3

(D) Bin 4

FIGURE 3.28: Fitted distribution of ΔE for $B^0 \to D^{*-}\pi^+$ in generic MC in slow pion momentum bins (a) Bin 1, (b) Bin 2, (c) Bin 3 and (d) Bin 4. The points with error bars and all color curves are the same as in Fig. 3.27

TABLE 3.13: Yields in different bins of slow pion momentum in the generic MC sample for $B^0 \to D^{*-}\pi^+$ decays.

p_{π_s} in GeV	Signal yield
[0.05, 0.12]	2165 ± 55
[0.12, 0.16]	3805 ± 72
[0.16, 0.20]	2918 ± 64
[0.20, 0.32]	5033 ± 80

TABLE 3.14: Signal yields in different bins of slow pion momentum in data for $B^0 \to D^{*-}\pi^+$ decays.

p_{π_s} in GeV	Signal yield
[0.05, 0.12]	1119 ± 43
[0.12, 0.16]	2195 ± 58
[0.16, 0.20]	1644 ± 54
[0.20, 0.32]	3118 ± 67

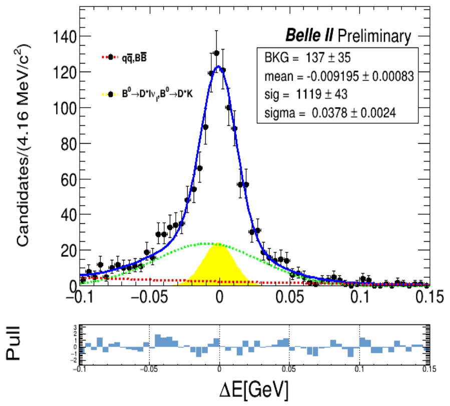

(A) Bin 1

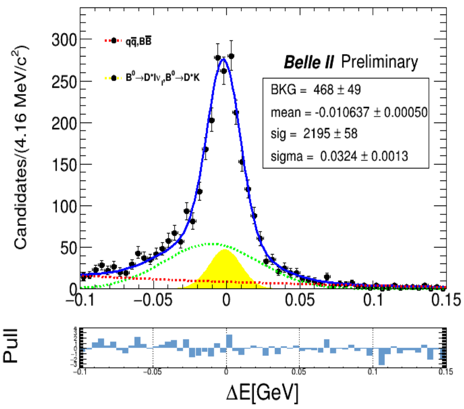

(B) Bin 2

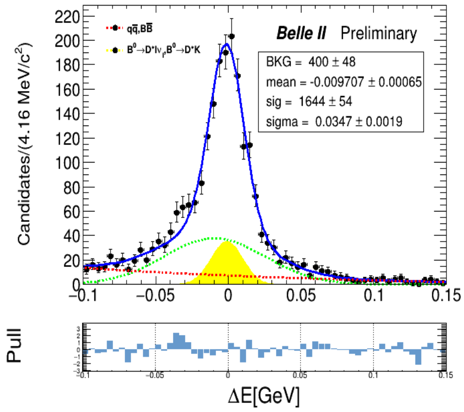

(C) Bin 3

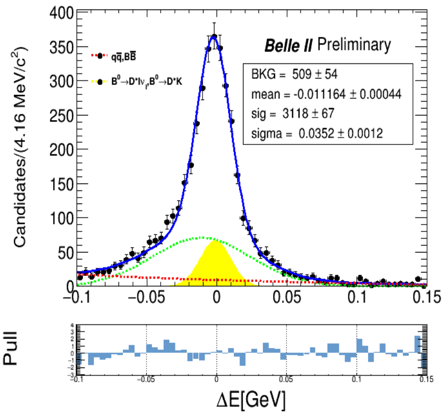

(D) Bin 4

FIGURE 3.29: Fitted distribution of ΔE for $B^0 \to D^{*-}\pi^+$ in data in π_s momentum bins (a) Bin 1, (b) Bin 2, (c) Bin 3, and (d) Bin 4. The points with error bars and all color curves are the same as in Fig. 3.27

The Table 3.13 shows the yields in different bins of slow pion momentum in the generic MC sample for $B^0 \to D^{*-}\pi^+$ decays that are obtained from the fits shown in Fig. 3.28. In Fig. 3.27, the top right plot shows the fitted distribution of ΔE for $B^0 \to D^{*-}\pi^+$ in data, and the bottom the points are obtained from an ΔE fit in bins of π_s momentum. The Fig. 3.29 shows the fitted distribution of ΔE for $B^0 \to D^{*-}\pi^+$ events in data. The PDFs used for fitting in Fig. 3.29 are the Double Gaussian (signal) and the sum of exponential and Chebyshev polynomial of first order (background). Table 3.14 shows the yields in different bins of π_s momentum in the data for $B^0 \to D^{*-}\pi^+$ decays that are obtained from the fits shown in Fig. 3.29.

The Fig. 3.30 shows the π_s tracking efficiency data-MC ratio in bins of π_s momentum for ΔE for $B^0 \to D^{*-}\pi^+$. The fraction of events in data and MC (f'_{Data} and f'_{MC}) are calculated by dividing the yield in each bin by the total yield. The ratio was normalized to unity in the rightmost bin. We choose the highest momentum bin for normalization as the overall data-MC agreement is expected to be best for this bin. Table 3.15 summarizes the π_s relative tracking efficiency data-MC ratio in the four bins.

TABLE 3.15: Summary of slow pion relative tracking efficiency data-MC ratio in bins of slow pion momentum for $B^0 \to D^{*-}\pi^+$.

p_{π_s} in GeV	f'_{Data}/f'_{MC}	$\varepsilon_{Data}/\varepsilon_{MC}$
[0.05, 0.12]	0.89 ± 0.04	0.83 ± 0.04
[0.12, 0.16]	0.99 ± 0.03	0.93 ± 0.03
[0.16, 0.20]	0.97 ± 0.04	0.91 ± 0.03
[0.20, 0.32]	1.06 ± 0.03	1.00

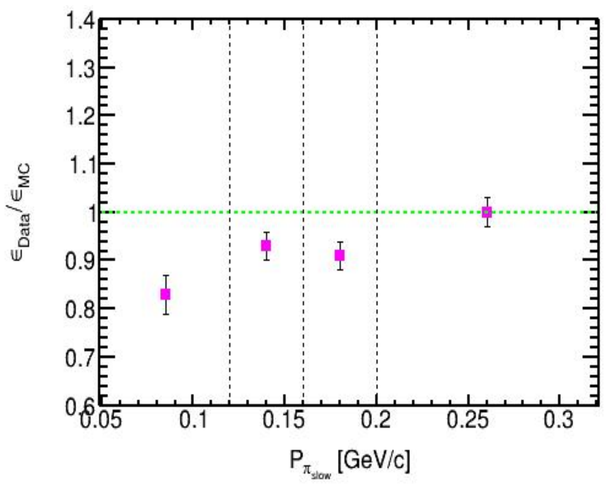

FIGURE 3.30: Slow pion relative tracking efficiency ratio of data to MC in bins of slow pion momentum in lab frame for ΔE for $B^0 \to D^{*-}\pi^+$.

3.4.4 Measured Branching Fraction

We used the simplest equation to calculate the branching fractions of B decay modes, the equation is defined as:

$$\mathcal{B}(B^0 \to D^{*-}\pi^+) = \frac{\text{no. of observed } B^0 \to D^{*-}\pi^+ \text{ events}}{(\text{no. of produced } B \text{ events})\mathcal{B}(D^* \to D^0\pi_s)[\mathcal{B}(\bar{D}^0 \to K\pi, K\pi\pi\pi, K\pi\pi^0/K_s^0\pi\pi)(\%\varepsilon)]} \tag{3.3}$$

The number of produced B events are obtained from the datasets [126]. The branching fractions of $D^* \to D^0\pi_s$, $\bar{D}^0 \to K^+\pi^-$, $K^+\pi^-\pi^0$, $K^+\pi^-\pi^+\pi^-$ and $K_s^0\pi^+\pi^-$ decay modes are equal to (67.7 ± 0.5)%, (3.950 ± 0.031)%, (8.23 ± 0.14)%, (14.4 ± 0.5)% and (2.80 ± 0.18)% respectively [127]. $\%\varepsilon$ is the percentage of reconstruction efficiency which can be calculated as:

$$\%\varepsilon = \frac{\text{no. of reconstructed } B \text{ events}}{\text{no. of generated } B \text{ events}} * 100 \tag{3.4}$$

Each variable in Eq.(3.3) includes a statistical uncertainty or a statistical error. We obtained the branching fractions of B^0 decay modes using both $M_{\rm bc}$ and ΔE methods as shown in Table 3.16 and Table 3.17, with comparing to the Particle Data Group [PDG] branching fraction in 2020 [127].

TABLE 3.16: The Branching fraction ($\mathcal{B}$) of $B^0 \to D^{*-}\pi^+$ (K_s^0 added) decay modes from datasets and PDG [2020]

B decay modes	$\mathcal{B}$ from PDG [2020]	Measured $\mathcal{B}$ from datasets used
$B^0 \to D^*\pi$ ($M_{\rm bc}$ method)	$(2.74 \pm 0.13) * 10^{-3}$	$(2.88 \pm 0.14) * 10^{-3}$
$B^0 \to D^*\pi$ (ΔE method)	$(2.74 \pm 0.13) * 10^{-3}$	$(2.88 \pm 0.14) * 10^{-3}$

TABLE 3.17: The Branching fraction ($\mathcal{B}$) of $B^0 \to D^{*-}\pi^+$ (π^0 added) decay modes from datasets and PDG [2020]

B decay modes	$\mathcal{B}$ from PDG [2020]	Measured $\mathcal{B}$ from datasets used
$B^0 \to D^*\pi$ ($M_{\rm bc}$ method)	$(2.74 \pm 0.13) * 10^{-3}$	$(3.01 \pm 0.12) * 10^{-3}$
$B^0 \to D^*\pi$ (ΔE method)	$(2.74 \pm 0.13) * 10^{-3}$	$(3.02 \pm 0.12) * 10^{-3}$

3.4.5 Systematic study

In addition to the statistical uncertainty, we have estimated the systematic uncertainty for $B^0 \to D^{*-}\pi^+$ decay mode.

TABLE 3.18: Total Systematic Uncertainty of $B^0 \to D^{*-}\pi^+$ (K_s^0 added) mode using $M_{\rm bc}$ fitting method

Bin No.	p range [GeV]	$\varepsilon_{Data}/\varepsilon_{MC}$
1	[0.05-0.12]	$(0.87 \pm 0.04(stat))^{+0.02}_{-0.01}$
2	[0.12-0.16]	$(0.99 \pm 0.03(stat))^{+0.004}_{-0.01}$
3	[0.16-0.20]	$(0.94 \pm 0.04(stat))^{+0.02}_{-0.01}$
4	[0.20-0.32]	$(1.00 \pm 0.03(stat))^{+0.004}_{-0.01}$

TABLE 3.19: Total Systematic Uncertainty of $B^0 \to D^{*-}\pi^+$ (K_s^0 added) mode using ΔE fitting method

Bin No.	p range [GeV]	$\varepsilon_{Data}/\varepsilon_{MC}$
1	[0.05-0.12]	$(0.87 \pm 0.04(stat))^{+0.04}_{-0.003}$
2	[0.12-0.16]	$(0.97 \pm 0.03(stat))^{+0.02}_{-0.001}$
3	[0.16-0.20]	$(0.92 \pm 0.04(stat))^{+0.01}_{-0.002}$
4	[0.20-0.32]	$(1.00 \pm 0.03(stat))^{+0.01}_{-0.004}$

The possible sources of systematic errors for the M_{bc} fitting method are the selection cuts used for the choice of mass difference (ΔM) and ΔE. These applied cuts are varied by $\pm 1\sigma$ for each bin of π_s momentum, and the deviation of the result from the central value is quoted as the systematic uncertainty from the individual source. The possible sources of systematic errors for the ΔE fitting method are the selection cuts used for the choice of mass difference (ΔM) and beam-constrained mass (M_{bc}).

TABLE 3.20: Total Systematic Uncertainty of $B^0 \to D^{*-}\pi^+$ (π^0 added) mode using $M_{\rm bc}$ fitting method

Bin No.	p range [GeV]	$\varepsilon_{Data}/\varepsilon_{MC}$
1	[0.05-0.12]	$(0.84 \pm 0.03(stat))^{+0.02}_{-0.01}$
2	[0.12-0.16]	$(0.97 \pm 0.03(stat))^{+0.04}_{-0.01}$
3	[0.16-0.20]	$(0.94 \pm 0.03(stat))^{+0.01}_{-0.02}$
4	[0.20-0.32]	$(1.00 \pm 0.02(stat))^{+0.04}_{-0.01}$

TABLE 3.21: Total Systematic Uncertainty of $B^0 \to D^{*-}\pi^+$ (π^0 added) mode using ΔE fitting method

Bin No.	p range [GeV]	$\varepsilon_{Data}/\varepsilon_{MC}$
1	[0.05-0.12]	$(0.83 \pm 0.04(stat))^{+0.01}_{-0.004}$
2	[0.12-0.16]	$(0.93 \pm 0.03(stat))^{+0.02}_{-0.01}$
3	[0.16-0.20]	$(0.91 \pm 0.03(stat))^{+0.01}_{-0.02}$
4	[0.20-0.32]	$(1.00 \pm 0.03(stat))^{+0.01}_{-0.003}$

The signal yield is extracted by fitting the experimental data. In order to fit the distributions from the data, we fix some parameters from the monte carlo simulation. These fixed parameters have some uncertainty that may affect the signal yield. In order to estimate this uncertainty, the fixed parameters of PDFs are varied by $\pm 1\sigma$ one at a time. All individual uncertainties are added in quadrature to obtain the total uncertainty. All systematic uncertainties contribution are summarized in Table 3.18 and Table 3.19 for $B^0 \to D^{*-}\pi^+$ mode with K_s^0 added in the final state of $\overline{D}^0$. For $B^0 \to D^{*-}\pi^+$ mode with π^0 added in the final state of $\overline{D}^0$, the systematic uncertainties are listed in Table 3.20 and Table 3.21.

3.4.6 Conclusion

We have obtained the slow-pion relative tracking efficiency in bins of slow-pion momentum using $B^0 \to D^{*-}\pi^+$ decay for the data. The relative tracking efficiencies are checked and there is no difference in results using ΔE and $M_{\rm bc}$ methods. We have calculated the branching fractions in the right-most bin and it is consistent with PDG values. The relative tracking efficiency is consistent with 1 and the corresponding error bars are 4% for $B^0 \to D^{*-}\pi^+$ decay. The associated systematic uncertainties are calculated in the relative tracking efficiency for both $B^0 \to D^{*-}\pi^+$ decay mode. We also validated our results using $B^0 \to D^{*-}\rho^+$ mode which is attached in Appendix B.

Chapter 4

$D \to p\ell$: Future Prospects at Belle II

Charm decays can be particularly interesting in this context because they involve weak interactions mediated by the W boson. While most charm decays do conserve baryon and lepton numbers, there are some rare processes where baryon number and lepton number violations can occur. One example of baryon number violation in charm decays involves the decay of a charmed baryon into final states containing only mesons or the decay of a meson into final states containing only baryons. Lepton number violation in charm decays can occur through processes that produce charged leptons (e.g., electrons, muons, or tau leptons) without the corresponding production of their respective neutrinos. These baryons and lepton number-violating decay searches involve high-energy particle colliders and detectors (Belle, Belle-II, LHCb, BESIII, etc.) capable of precisely measuring the properties of charm particles and their decays. If observed, violations of baryon and lepton number conservation in charm decays could provide important insights into the nature of fundamental particles and their interactions. The decay process $D \to p\ell^-$, where D represents a D meson, p represents a proton, and ℓ^- represents an electron or muon is a particularly interesting case for studying baryon number (B) and lepton number (L) violation. However, it's important to note that these violations, if they occur, are expected to be extremely rare and challenging to detect due to the stringent conservation laws imposed by the Standard Model. Therefore, experiments must be designed with high sensitivity to rare processes and low background noise to observe potential violations. We obtained the most precise upper limit on branching fraction using a dataset of 921 fb^{-1} luminosity collected with the Belle detector. The LHCb experiment at CERN and the Belle-II experiment at KEK are two prominent particle physics experiments that investigate the properties of fundamental particles and the laws governing their interactions. While both experiments share similar research goals, they differ in their specific focus and the types of particles they study. Their complementary nature arises from their different accelerator technologies, collision energies, and detector designs, which allow them to probe different aspects of particle physics and cross-check each other's results. Both LHCb and Belle-II can look for these rare charm decays. Here we discuss the expected sensitivity in the Belle-II of $D \to p\ell$ search.

The Belle-II experiment builds upon the legacy of its predecessor, the Belle experiment, and aims to significantly extend its reach in particle physics research. Belle-II is designed to accumulate a dataset that is about 50 times larger than that of Belle. This increase in statistics provides Belle-II with much greater sensitivity to rare processes and enables more precise measurements of particle properties. much greater sensitivity $D \to p\ell$ at Belle yielded the most stringent upper limit of the order of 10^{-7}. With the 50 ab^{-1} of data to be accumulated at Belle-II, the upper limit and systematics will certainly improve.

For sytematics uncertainty, the sensitivity at Belle measurements is projected to Belle II as,

$$\sigma^{Syst.}_{BelleII} = \sqrt{\sigma^2_{Syst.} \times (\mathcal{L}^{Belle}_{int} / \mathcal{L}^{BelleII}_{int})} \tag{4.1}$$

We have listed the expected systematic in Belle-II and we can also see an improvement by an order at least in upper limit calculations.

TABLE 4.1: Summary of expected systematic uncertainties (%) on $D^0 \to p\ell$ decay modes in Belle-II.

Channel	Systematics
$D^0 \to pe^-$	$^{+0.38}_{-0.33}$
$\bar{D}^0 \to pe^-$	$^{+0.74}_{-0.70}$
$D^0 \to \bar{p}e^+$	$^{+1.71}_{-1.50}$
$\bar{D}^0 \to \bar{p}e^+$	$^{+0.25}_{-0.45}$
$D^0 \to p\mu^-$	$^{+0.48}_{-1.17}$
$\bar{D}^0 \to p\mu^-$	$^{+2.71}_{-1.78}$
$D^0 \to \bar{p}\mu^+$	$^{+3.25}_{-2.76}$
$\bar{D}^0 \to \bar{p}\mu^+$	$^{+1.17}_{-1.31}$

Appendix A

Background details of the $D \to p\ell$ study

A.1 Background details

As expected, the major background originates from the charm sample. The breakdown of backgrounds for each sample is shown in Fig. A.1 and Fig. A.2. In Table 2.14 and Table 2.15 we have already shown the contributions from each sample in the signal enhanced region. In Table A.1 we have listed the contribution from each event type in the whole M_{D^0} and ΔM region.

TABLE A.1: Summary of the background level for each mode in the whole region of M_{D^0} and ΔM.

	B^+B^-	$B^0\overline{B}^0$	charm		uds
Channels	comb.	comb.	peaking	comb.	comb.
$D^0 \to pe^-$	2755	1811	-	2162	1847
$\overline{D^0} \to pe^-$	2596	2660	29800	2596	992
$D^0 \to \bar{p}e^+$	2431	2465	29843	2560	528
$\overline{D^0} \to \bar{p}e^+$	2638	1609	-	1963	1365
$D^0 \to p\mu^-$	3087	2118	-	7569	3203
$\overline{D^0} \to p\mu^-$	2955	2952	27530	10500	3115
$D^0 \to \bar{p}\mu^+$	2695	2877	27730	10488	4181
$\overline{D^0} \to \bar{p}\mu^+$	3051	1966	-	9311	3922

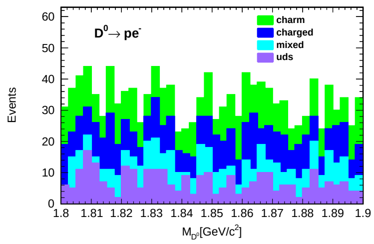

(A) $D^0 \to pe^-$

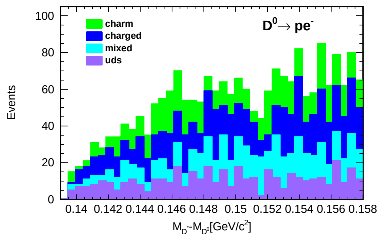

(B) $D^0 \to pe^-$

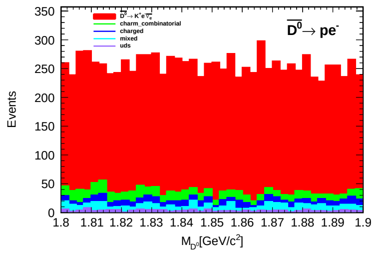

(C) $\overline{D^0} \to pe^-$

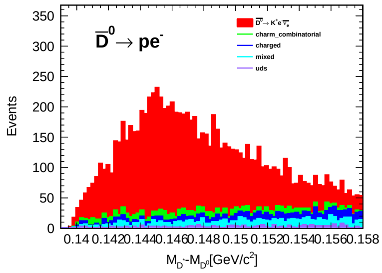

(D) $\overline{D^0} \to pe^-$

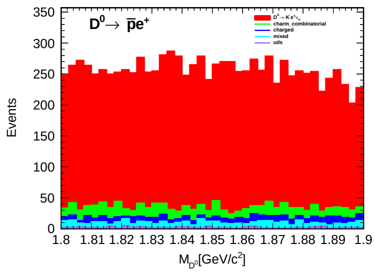

(E) $D^0 \to \bar{p}e^+$

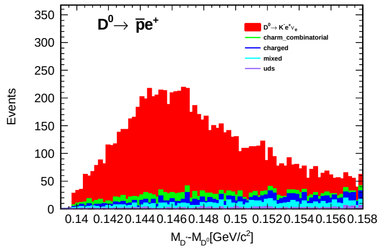

(F) $D^0 \to \bar{p}e^+$

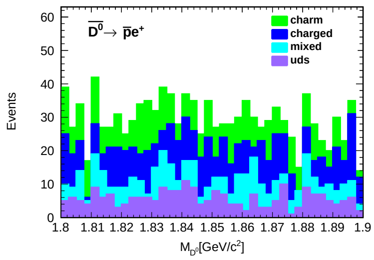

(G) $\overline{D^0} \to \bar{p}e^+$

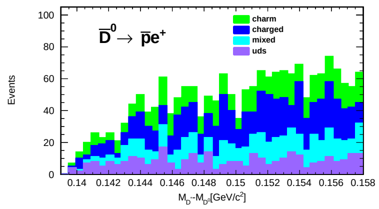

(H) $\overline{D^0} \to \bar{p}e^+$

FIGURE A.1: The breakdown of backgrounds for each sample where left plots are for M_{D^0} and right plots are for ΔM distributions for all the electronic modes.

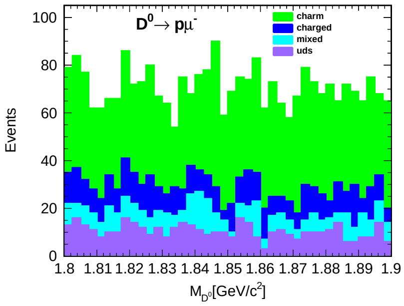

(A) $D^0 \to p\mu^-$

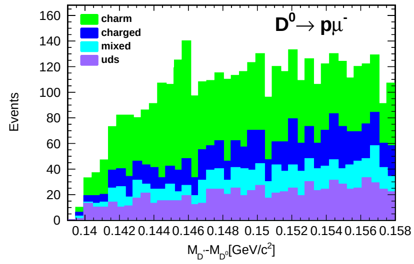

(B) $D^0 \to p\mu^-$

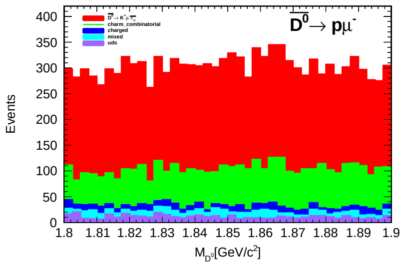

(C) $\overline{D^0} \to p\mu^-$

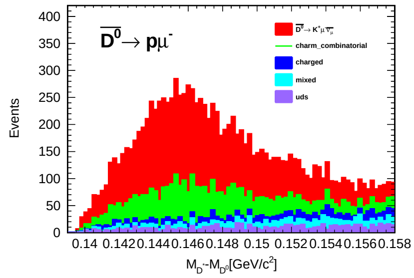

(D) $\overline{D^0} \to p\mu^-$

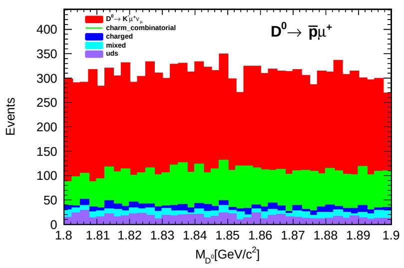

(E) $D^0 \to \bar{p}\mu^+$

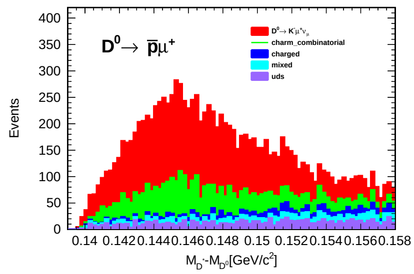

(F) $D^0 \to \bar{p}\mu^+$

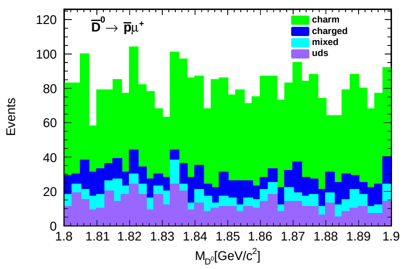

(G) $\overline{D^0} \to \bar{p}\mu^+$

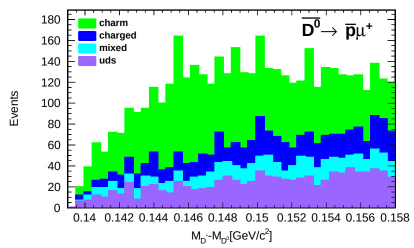

(H) $\overline{D^0} \to \bar{p}\mu^+$

FIGURE A.2: The breakdown of backgrounds for each sample where left plots are for M_{D^0} and right plots are for ΔM distributions for all the muonic modes.

A.2 Background contribution from different samples

Distribution of backgrounds after pre-selection cuts in generic MC are shown in Fig. A.3 and Fig. A.4. We see a peaking component coming from $D^0 \to K^-\pi^+$ mode for the $D^0 \to pe^-$ mode and also $\overline{D^0} \to K^+\pi^-$ mode in $\overline{D^0} \to \bar{p}e^+$. For $D^0 \to p\mu^-$ mode, we see additionally $D^0 \to K^-\rho^+$ and $D^0 \to K^-K^+$ contributions.

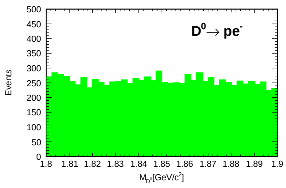

(A) $D^0 \to pe^-$

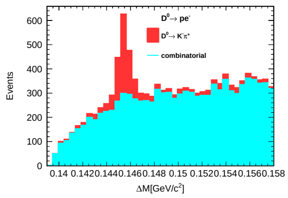

(B) $D^0 \to pe^-$

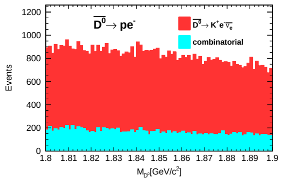

(C) $\overline{D^0} \to pe^-$

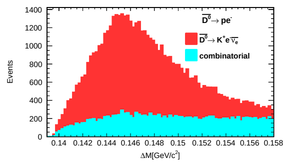

(D) $\overline{D^0} \to pe^-$

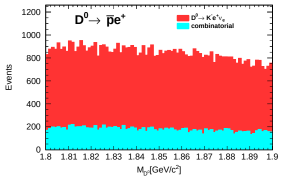

(E) $D^0 \to \bar{p}e^+$

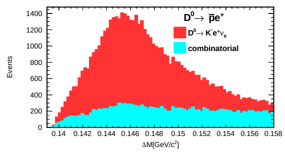

(F) $D^0 \to \bar{p}e^+$

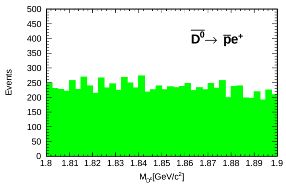

(G) $\overline{D^0} \to \bar{p}e^+$

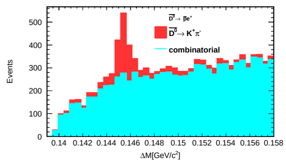

(H) $\overline{D^0} \to \bar{p}e^+$

FIGURE A.3: Distribution of M_{D^0} and ΔM after using pre-selection cuts in generic MC for all the electronic modes.

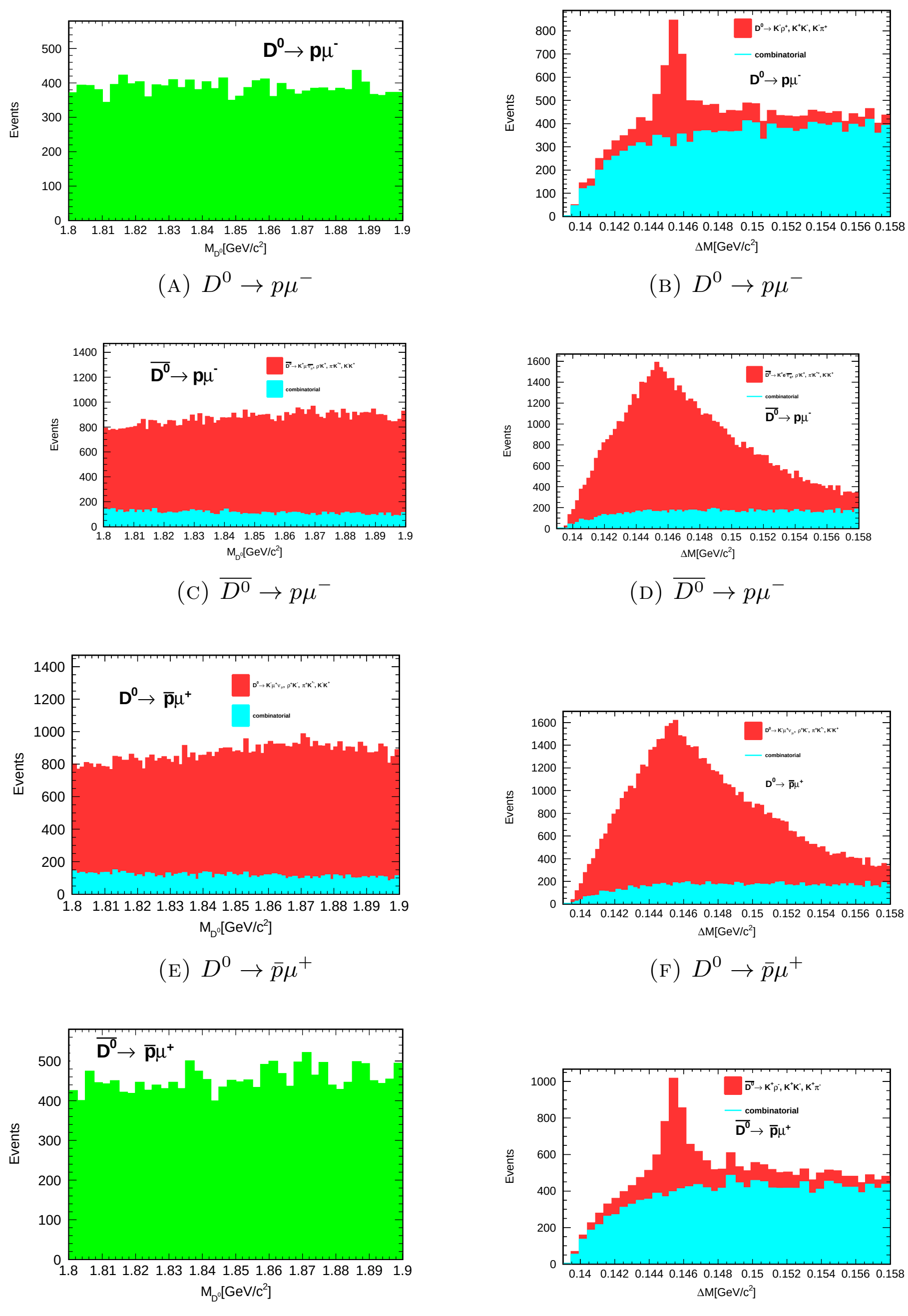

(A) $D^0 \to p\mu^-$ (B) $D^0 \to p\mu^-$

(C) $\overline{D^0} \to p\mu^-$ (D) $\overline{D^0} \to p\mu^-$

(E) $D^0 \to \bar{p}\mu^+$ (F) $D^0 \to \bar{p}\mu^+$

(G) $\overline{D^0} \to \bar{p}\mu^+$ (H) $\overline{D^0} \to \bar{p}\mu^+$

FIGURE A.4: Distribution of M_{D^0} and ΔM after using pre-selection cuts in generic MC for all the muonic modes.

A.3 Significance (Including Systematic)

Systematic uncertainties which affects only signal yield are included in signal significance using marginalization technique[48]. Systematics due to PDF shape and fit bias are included in significance estimation, as these are the only uncertainties which can potentially affect the signal yield. First maximum likelihood curve is obtained by fixing the signal yield zero to the nominal value and the negative log-likelihood minimization curve was obtained with the statistical uncertainties. This likelihood is then smeared with the probability distribution $p_y B$,

$$p_y(\mathcal{B}) = \int_0^\infty e^{-\mathcal{B}S} \frac{1}{\sqrt{2\pi\sigma_S^2}} e^{-(S-\hat{S})^2/2\sigma_S^2}\, dS \tag{A.1}$$

Where, σ_S is the systematic uncertainty on yield (y) and branching fraction ($\mathcal{B}$) is given by $\mathcal{B}$=$y\hat{S}$ and S is the true value of sensitivity (combination of beam flux, detector acceptance etc.).

Appendix B

Relative tracking efficiency for $B^0 \to D^{*-}\rho^+$ decay

In this section, we study the decay modes of $B^0 \to D^{*-}\rho^+$ with D^{*-} further decaying to $\overline{D}^0\pi^-$. D^* mesons are reconstructed using the decay chain $D^* \to \overline{D}^0\pi^-$. ρ^+ meson is reconstructed from π^+ and π^0. We have considered two sets of different final states for $\overline{D}^0$. In the first case, $\overline{D}^0$ decays into the following three final states: $K^+\pi^-$, $K_s^0\pi^+\pi^-$ and $K^+\pi^-\pi^-\pi^+$ (Clean Channel) and in second case, it decays to $K^+\pi^-$, $K^+\pi^-\pi^0$ and $K^+\pi^-\pi^-\pi^+$ respectively. We aim to measure the track finding relative efficiency of the low-momentum charged pion coming from D^* decays. Here, we show π_s momentum and M_{bc} distributions along with the fits in bins of π_s momentum for $B^0 \to D^{*-}\rho^+$ decays for 200 fb^{-1} generic MC sample, as well as data events. In addition to the selection criteria applied for $B^0 \to D^{*-}\pi^+$, we apply following additional requirements to select candidate events:

- We require ρ meson mass to be within the range $0.7 < M_{\rho^+} < 0.9$ GeV/c^2.
- We apply a loose selection criteria in the reconstructed mass of π^0 which is $0.11 < M_{\pi^0} < 0.16$ GeV/c^2.

- The modulus of helicity angle has to within the range $|(cos\theta_{hl}| < 0.8$.

Similar to the $B^0 \to D^{*-}\pi^+$ case, no particle identification or impact parameter criteria are applied on the slow-pion.

B.1 $B^0 \to D^{*-}\rho^+$ decay (Clean channels)

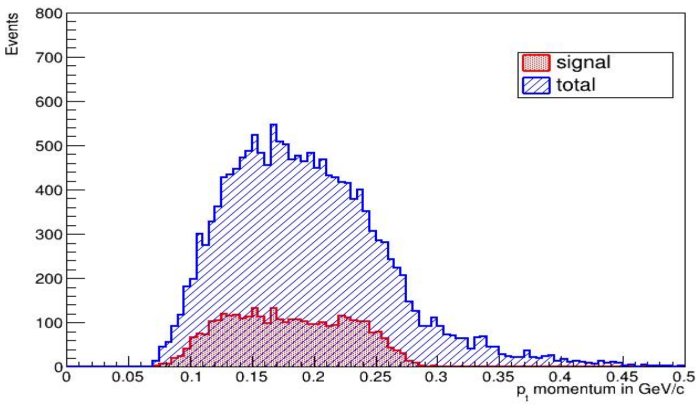

FIGURE B.1: Distribution of π_s momentum for for $B^0 \to D^{*-}\rho^+$ in generic MC events. All (correctly reconstructed) candidates are shown in the blue (red) hatched histogram.

In this section we calculate the relative tracking efficiency for $B^0 \to D^{*-}\rho^+$ by considering $\overline{D}^0$ decays into the following three final states: $K^+\pi^-$, $K^0_S\pi^+\pi^-$, and $K^+\pi^-\pi^-\pi^+$. Because of the presence of π^0 coming from B^0, the ΔE resolution looks worse so we decided to fit M_{bc} only to extract signal yields. In Fig. B.2 we have shown the distribution of ratio of 2nd to the 0th Fox-Wolfram moments(R2), $cos\theta_{hl}$ and M_{bc} for $B^0 \to D^{*-}\rho^+$ in Generic MC sample. By looking at the distribution we decided to take the events where R2 < 0.30 and $| (cos\theta_{hl} | < 0.8$. The major peaking background contribution for $B^0 \to D^{*-}\rho^+$ is coming from $B^0 \to D^{*-}\pi^+\pi^0$ (non-resonant mode). The PDF for the peaking background component is shown by the yellow dotted curve. Fig. B.4. So we model peaking M_{bc} using the Crystal-Ball function and Argus function. Fig. B.1 shows the distribution of π_s momentum for $B^0 \to D^{*-}\rho^+$ in generic MC events.

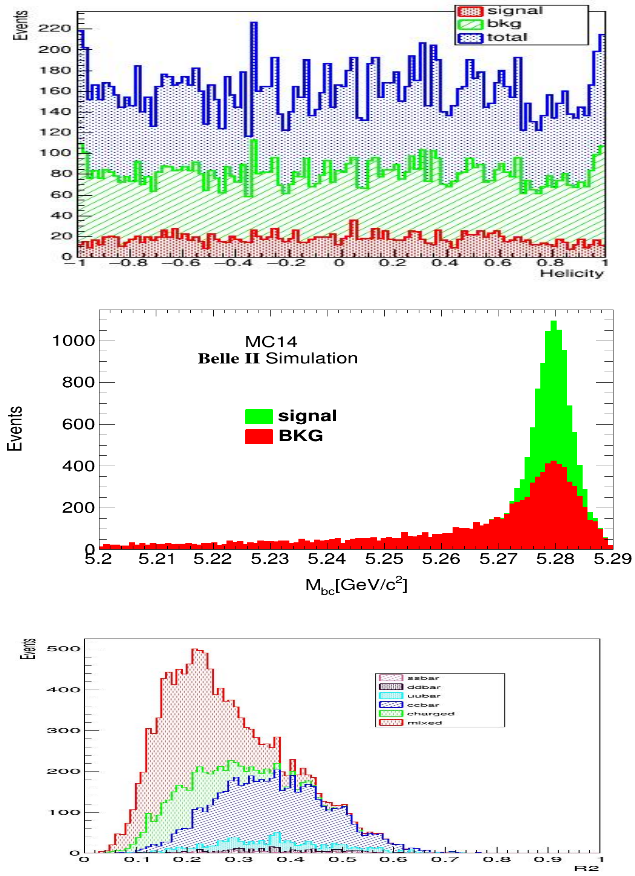

FIGURE B.2: Distributions of $|(cos\theta_{hl}|$, M_{bc} and R2 for $B^0 \to D^{*-}\rho^+$ in generic MC events.

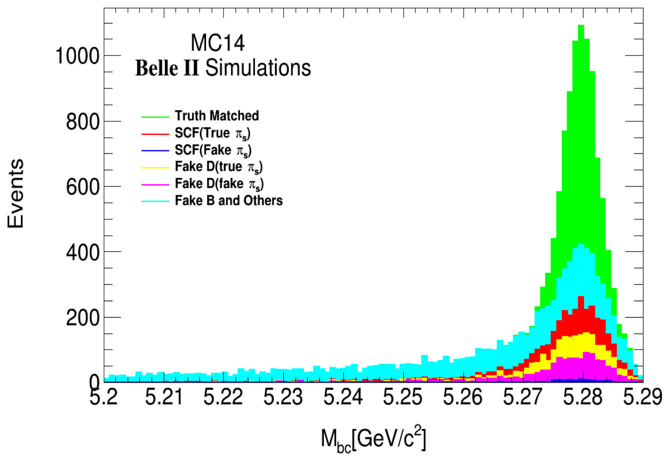

FIGURE B.3: Distribution of $M_{\rm bc}$ for $B^0 \to D^{*-}\rho^+$ decay mode in Generic MC sample after the background investigation using generator level information.

In Fig. B.4, the top plot shows the fitted distribution of $M_{\rm bc}$ for $B^0 \to D^{*-}\rho^+$ in both generic MC and data events, and in the bottom the points are obtained from an $M_{\rm bc}$ fit in bins of π_s momentum. The Fig. B.5 shows the fitted distribution of $M_{\rm bc}$ for

SCF (True π_s)	14 %
SCF (Fake π_s)	1 %
Fake D (True π_s)	10 %
Fake D (Fake π_s)	14 %
Fake B & Others	61 %

TABLE B.1: Percentage of background contributing in $M_{\rm bc}$ distribution for $B^0 \to D^{*-}\rho^+$ decays where SCF (self-cross feed events) and Fake D corresponds to the mis-reconstructed signal events and the background coming from the wrong D^* and D^0 respectively.

$B^0 \to D^{*-}\rho^+$ events for generic MC in each bin of π_s momentum. The PDFs used for fitting in Fig. B.5 are Crystal Ball (signal) + Argus Function (background). The Table B.2 shows the yields in different bins of slow pion momentum in the generic MC sample for $B^0 \to D^{*-}\rho^+$ decays that are obtained from the fits shown in Fig. B.5.

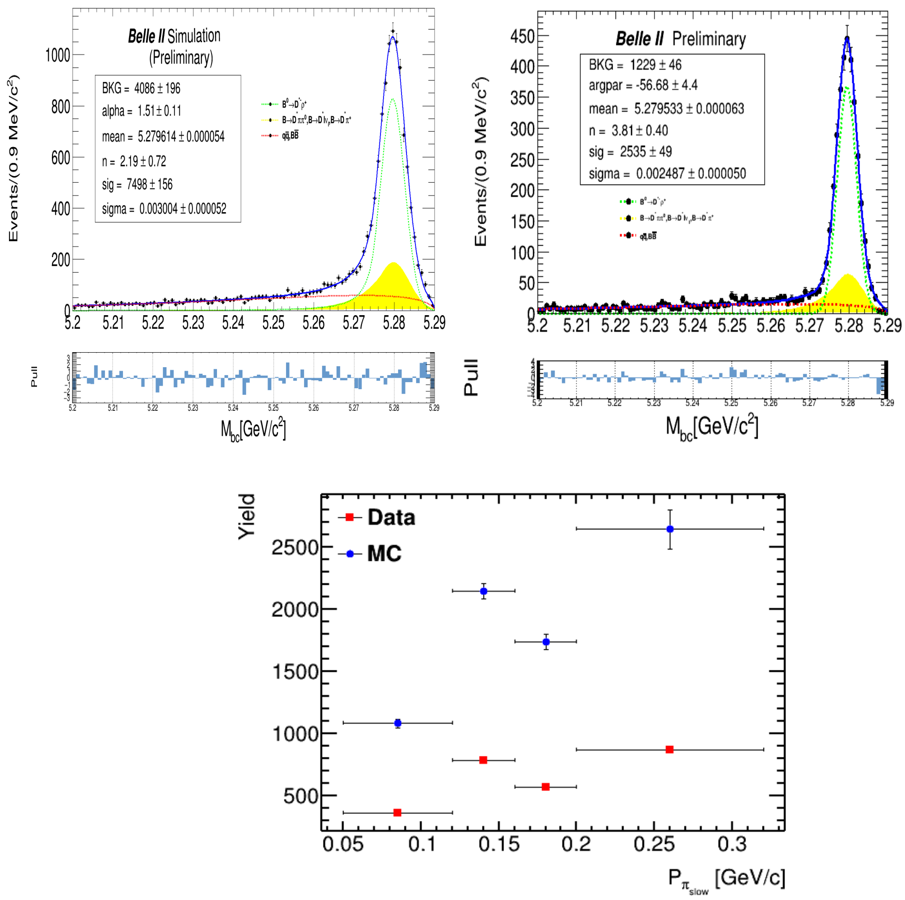

FIGURE B.4: Top plots show the fitted distribution of $M_{\rm bc}$ for $B^0 \to D^{*-}\rho^+$ in both generic MC (left) and data (right). The fit PDFs for signal (background)components are shown in blue (green) dotted curves. The total fit PDF is shown in the solid blue curve. The bottom plot shows the signal yields obtained from an $M_{\rm bc}$ fit in the bins of π_s momentum.

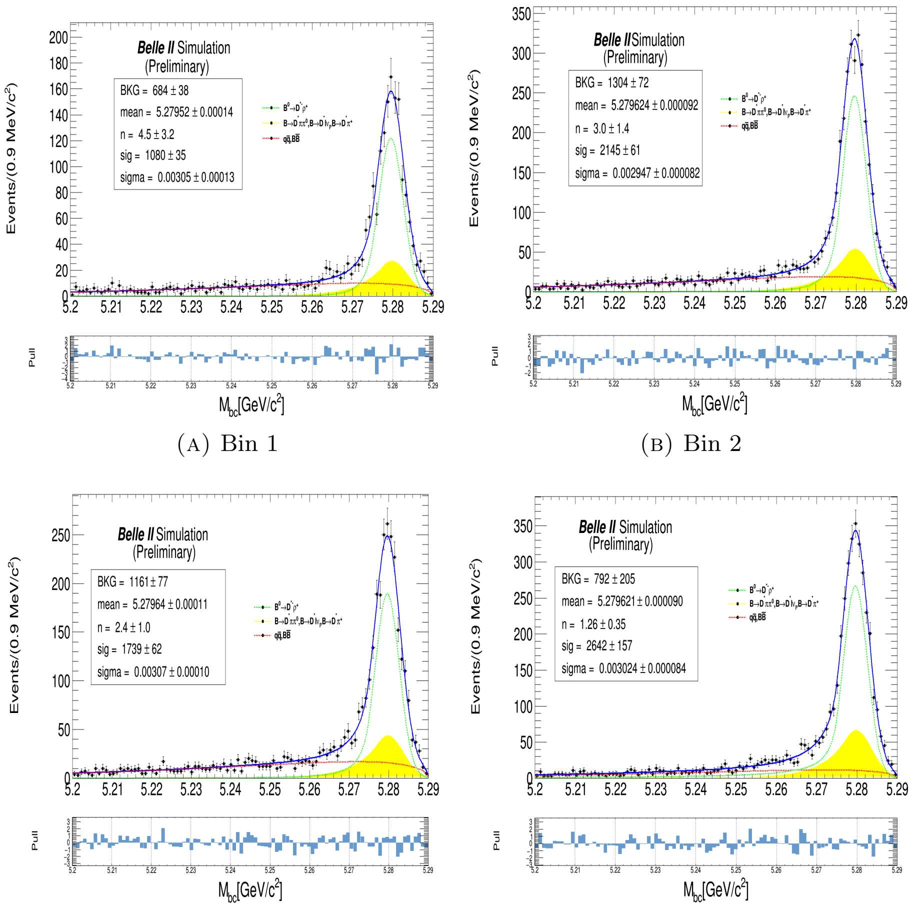

(A) Bin 1 (B) Bin 2 (C) Bin 3 (D) Bin 4

FIGURE B.5: Fitted distribution of $M_{\rm bc}$ for $B^0 \to D^{*-}\rho^+$ in generic MC in slow pion momentum bins (a) Bin 1, (b) Bin 2, (c) Bin 3 and (d) Bin 4. The points with error bars and all color curves are the same as in Fig. B.4.

TABLE B.2: Signal yields in different bins of slow pion momentum in the Generic MC sample for $B^0 \to D^{*-}\rho^+$ decays.

p_{π_s} in GeV	Signal yield
[0.05-0.12]	1080 ± 35
[0.12-0.16]	2145 ± 61
[0.16-0.20]	1739 ± 62
[0.20-0.32]	2642 ± 157

TABLE B.3: Yields in different bins of slow pion momentum in data for $B^0 \to D^{*-}\rho^+$ decays

p_{π_s} in GeV	Yield
[0.05-0.12]	357 ± 17
[0.12-0.16]	785 ± 26
[0.16-0.20]	569 ± 22
[0.20-0.32]	865 ± 27

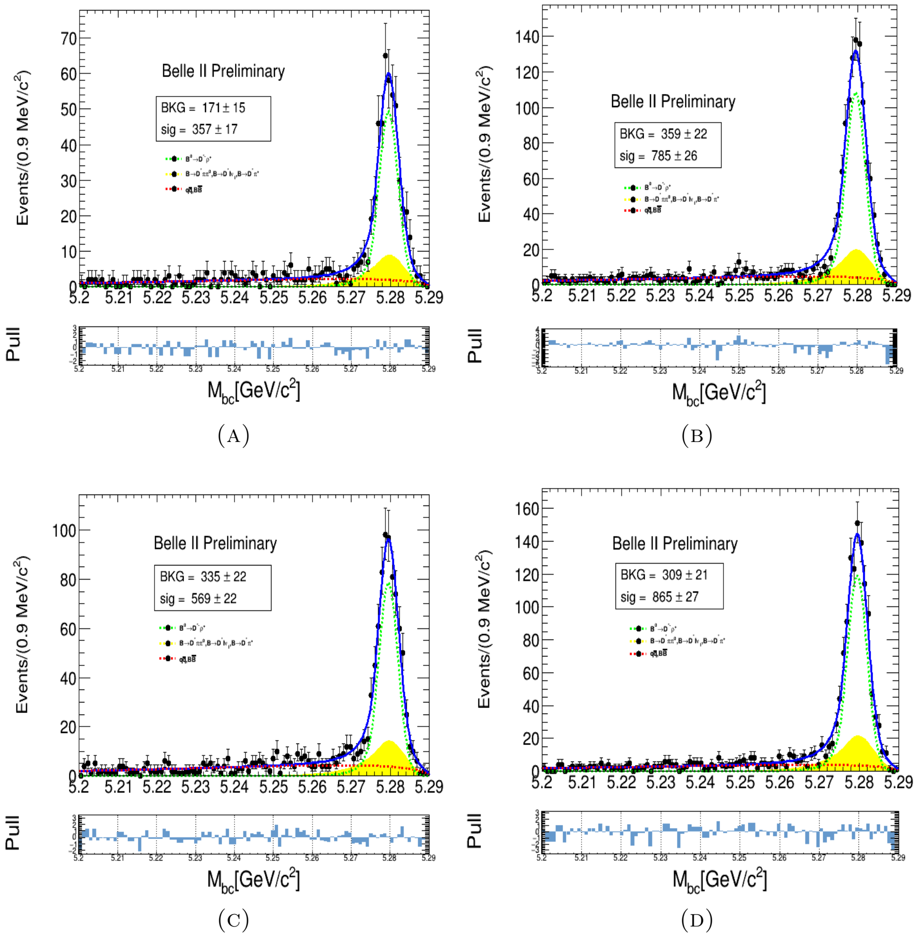

FIGURE B.6: Fitted distribution of M_{bc} for $B^0 \to D^{*-}\rho^+$ in data in slow pion momentum bins (a) Bin 1, (b) Bin 2, (c) Bin 3 and (d) Bin 4.

In Fig. B.4, the top right plot shows the fitted distribution of M_{bc} for $B^0 \to D^{*-}\rho^+$ in data and the bottom plot shows the points are obtained from an M_{bc} fit in bins of π_s momentum. The Fig. B.6 shows the fitted distribution of M_{bc} for $B^0 \to D^{*-}\rho^+$ events for data in bins of π_s momentum. The PDFs used for fitting in Fig. B.6 are Single Crystal Ball (signal) + Argus Function (background).

The Table B.3 shows the yields in different bins of slow pion momentum in the data for $B^0 \to D^{*-}\rho^+$ decays that are obtained from the fits shown in Fig. B.6.

The Fig B.7 shows the π_s relative tracking efficiency data-MC ratio in bins of π_s momentum for M_{bc} for $B^0 \to D^{*-}\rho^+$. The fraction of events in data and MC (f'_{Data} and f'_{MC}) are calculated by dividing the yield in each bin by the total yield. The ratio was normalized to 1 in the right bin. We choose the highest momentum bin for normalization as the overall data-MC agreement is expected to be the best for this bin.

The correction factor for the relative tracking efficiency of the slow pion in bins of slow pion momentum is shown in Table B.4.

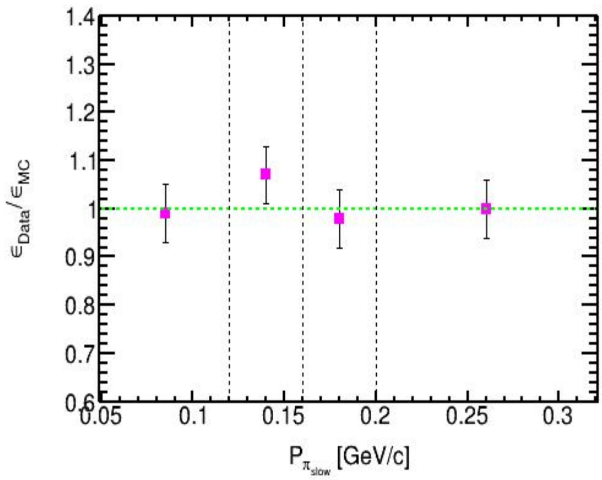

FIGURE B.7: Slow pion relative tracking efficiency ratio of data to MC in bins of slow pion momentum in lab frame for $M_{\rm bc}$ for $B^0 \to D^{*-}\rho^+$.

TABLE B.4: Summary of slow pion relative tracking efficiency ratio of data to MC in bins of slow pion momentum in lab frame for $B^0 \to D^{*-}\rho^+$.

p_{π_s} in GeV	f'_{Data}/f'_{MC}	$\varepsilon_{Data}/\varepsilon_{MC}$
[0.05-0.12]	0.98 ± 0.06	1.01 ± 0.06
[0.12-0.16]	1.08 ± 0.06	1.11 ± 0.06
[0.16-0.20]	0.96 ± 0.06	0.99 ± 0.06
[0.20-0.32]	0.97 ± 0.07	1.00

B.2 $B^0 \to D^{*-}\rho^+$ mode (π^0 added)

In this section we calculate the relative tracking efficiency for $B^0 \to D^{*-}\rho^+$ by considering $\overline{D}^0$ decays into the following three final states: $K^+\pi^-$, $K^+\pi^-\pi^0$, and $K^+\pi^-\pi^-\pi^+$. Because of the presence of π^0 coming from B^0, the ΔE resolution looks worse so we decided to fit M_{bc} only to extract signal yields. The Fig. B.8 shows the distribution of M_{bc} for $B^0 \to D^{*-}\rho^+$ in generic MC events. The major peaking background contribution for $B^0 \to D^{*-}\rho^+$ is coming from $B^0 \to D^{*-}\pi^+\pi^0$ (non-resonant modes). The PDF for the peaking background component is shown by the yellow dotted curve Fig. B.10.

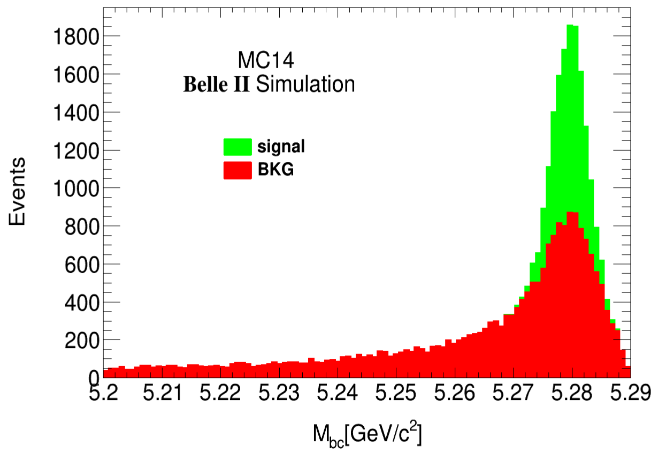

FIGURE B.8: Distributions of M_{bc} for $B^0 \to D^{*-}\rho^+$ in generic MC events.

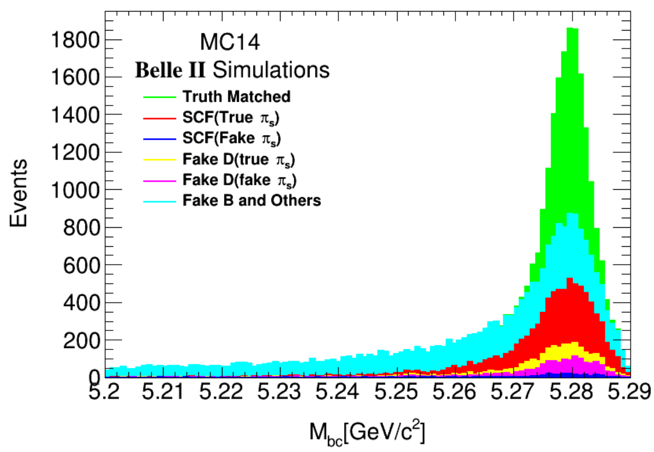

FIGURE B.9: Distribution of $M_{\rm bc}$ for $B^0 \to D^{*-}\rho^+$ decay mode in Generic MC sample after the background investigation using generator level information.

SCF (True π_s)	6 %
SCF (Fake π_s)	1 %
Fake D (True π_s)	15 %
Fake D (Fake π_s)	18 %
Fake B & Others	60 %

TABLE B.5: Percentage of background contributing in $M_{\rm bc}$ distribution for $B^0 \to D^{*-}\rho^+$ decays where SCF (self-cross feed events) and Fake D corresponds to the mis-reconstructed signal events and the background coming from the wrong D^* and D^0 respectively.

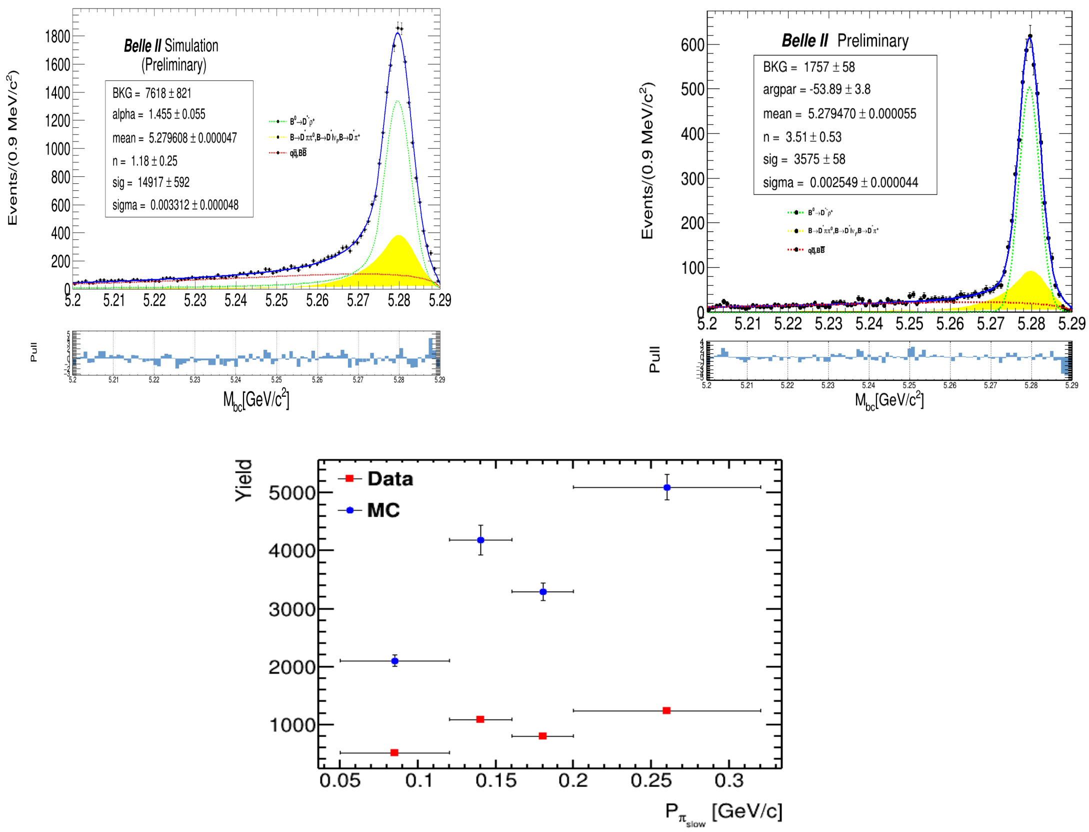

FIGURE B.10: Top plots show the fitted distribution of $M_{\rm bc}$ for $B^0 \to D^{*-}\rho^+$ in both generic MC (left) and data (right). The fit PDFs for signal (background) components are shown in green (yellow) dotted curves. The total fit PDF is shown in the solid blue curve. The bottom plot shows the signal yields obtained from an $M_{\rm bc}$ fit in the bins of π_s momentum.

So we model peaking M_{bc} using the Crystal-Ball function and Argus function. In Fig. B.10, the top plot shows the fitted distribution of $M_{\rm bc}$ for $B^0 \to D^{*-}\rho^+$ in both generic MC (left) and data (right) events, and the bottom plot shows the points are obtained from an $M_{\rm bc}$ fit in bins of π_s momentum.

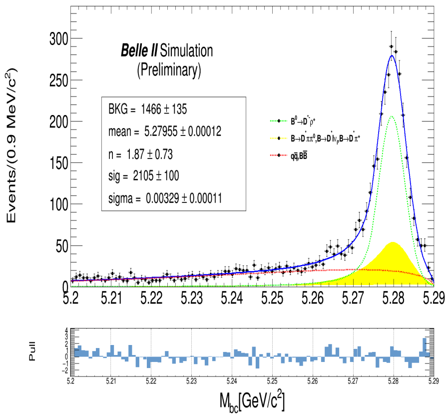

(A) Bin 1

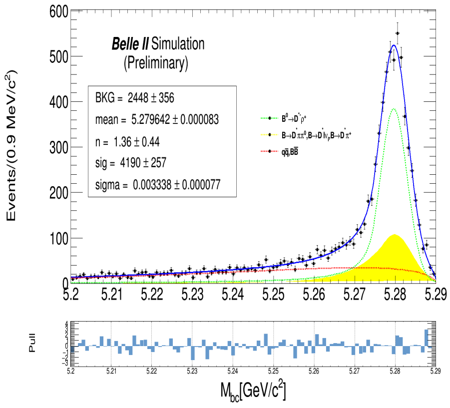

(B) Bin 2

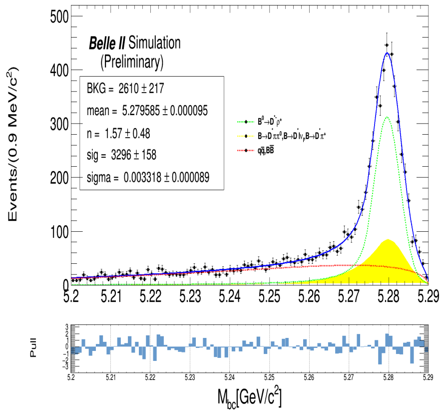

(C) Bin 3

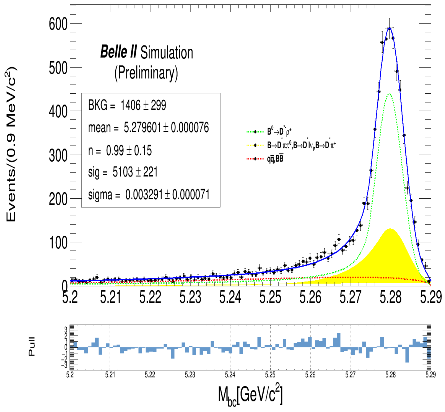

(D) Bin 4

FIGURE B.11: Fitted distribution of $M_{\rm bc}$ for $B^0 \to D^{*-}\rho^+$ in generic MC in slow pion momentum bins (a) Bin 1, (b) Bin 2, (c) Bin 3 and (d) Bin 4. The points with error bars and all color curves are the same as in Fig. B.10.

TABLE B.6: Signal yields in different bins of slow pion momentum in the generic MC sample for $B^0 \to D^{*-}\rho^+$ decays.

p_{π_s} in GeV	Signal yield
[0.05-0.12]	2105 ± 100
[0.12-0.16]	4190 ± 257
[0.16-0.20]	3296 ± 158
[0.20-0.32]	5103 ± 221

The Fig. B.11 shows the fitted distribution of $M_{\rm bc}$ for $B^0 \to D^{*-}\rho^+$ events in generic MC. The PDFs used for fitting in Fig. B.11 are Crystal Ball (signal) + Argus Function (background). The Table B.6 shows the yields in different bins of slow pion momentum in the generic MC sample for $B^0 \to D^{*-}\rho^+$ decays that are obtained from the fits shown in Fig. B.11.

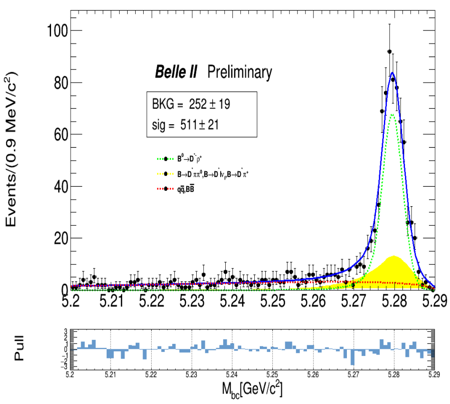

(A)

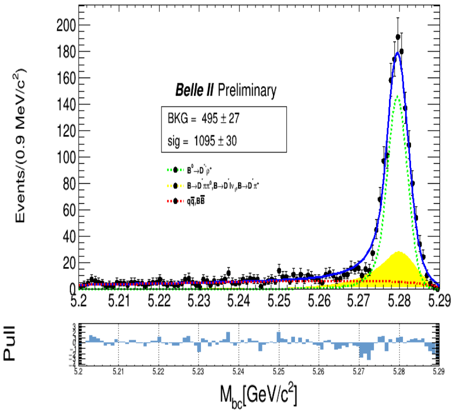

(B)

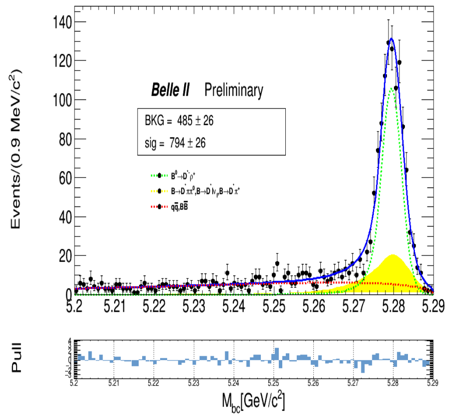

(C)

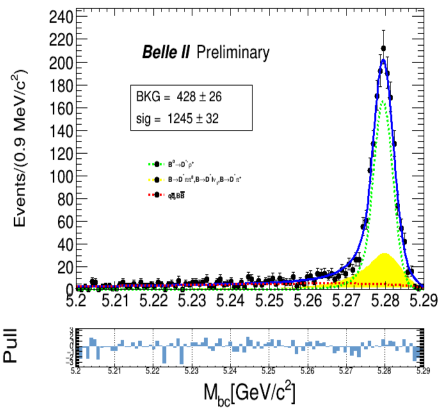

(D)

FIGURE B.12: Fitted distribution of $M_{\rm bc}$ for $B^0 \to D^{*-}\rho^+$ in data in slow pion momentum bins (a) Bin 1, (b) Bin 2, (c) Bin 3 and (d) Bin 4.

TABLE B.7: Yields in different bins of slow pion momentum in data for $B^0 \to D^{*-}\rho^+$ decays

p_{π_s} in GeV	Yield
[0.05-0.12]	511 ± 21
[0.12-0.16]	1095 ± 30
[0.16-0.20]	794 ± 26
[0.20-0.32]	1245 ± 32

The Fig. B.12 shows the fitted distribution of $M_{\rm bc}$ for $B^0 \to D^{*-}\rho^+$ events in data. The PDFs used for fitting in Fig. B.12 are Single Crystal Ball (signal) + Argus Function (background). The Table B.7 shows the yields in different bins of slow pion momentum in the data for $B^0 \to D^{*-}\rho^+$ decays that are obtained from the fits shown in Fig. B.12. The Fig. B.13 shows the π_s relative tracking efficiency data-MC ratio in bins of π_s momentum for $M_{\rm bc}$ for $B^0 \to D^{*-}\rho^+$. The fraction of events in data and MC ($f^{\prime}_{Data}$

and f'_{MC}) are calculated by dividing the yield in each bin by the total yield. The ratio was normalized to 1 in the right bin. We choose the highest momentum bin for normalization as the overall data-MC agreement is expected to be the best for this bin. The correction factor for the relative tracking efficiency of the slow pion in bins of slow pion momentum is shown in Table B.8.

TABLE B.8: Summary of slow pion relative tracking efficiency ratio of data to MC in bins of slow pion momentum in lab frame for $B^0 \to D^{*-}\rho^+$.

p_{π_s} in GeV	f'_{Data}/f'_{MC}	$\varepsilon_{Data}/\varepsilon_{MC}$
[0.05-0.12]	0.98 ± 0.07	0.99 ± 0.06
[0.12-0.16]	1.05 ± 0.07	1.07 ± 0.06
[0.16-0.20]	0.97 ± 0.06	0.98 ± 0.06
[0.20-0.32]	0.98 ± 0.06	1.00

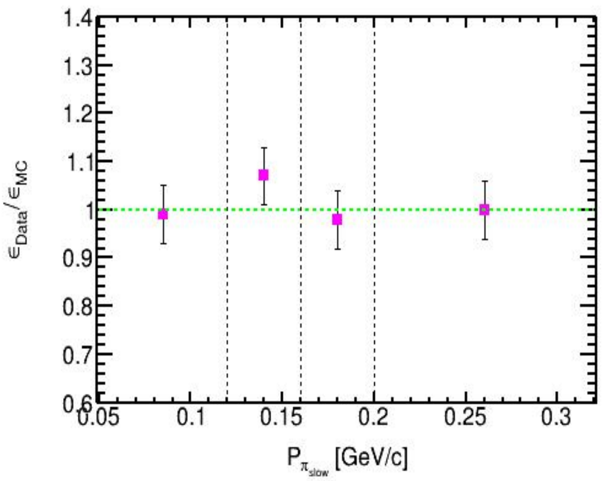

FIGURE B.13: Slow pion relative tracking efficiency ratio of data to MC in bins of slow pion momentum in lab frame for $M_{\rm bc}$ for $B^0 \to D^{*-}\rho^+$.

B.3 Systematic study

In addition to the statistical uncertainty, we have estimated the systematic uncertainty for $B^0 \to D^{*-}\rho^+$ decay mode. The possible sources of systematic errors for the M_{bc} fitting method are the selection cuts used for the choice of mass difference (ΔM) and ΔE. These applied cuts are varied by $\pm 1\sigma$ for each bin of π_s momentum. In order to estimate this uncertainty, the fixed parameters of PDFs are varied by $\pm 1\sigma$ one at a time. All individual uncertainties are added in quadrature to obtain the total uncertainty.All systematic uncertainties contribution are summarized in the Table B.9 and Table B.10 for $B^0 \to D^{*-}\rho^+$ mode with π^0 and K_s^0 added in the final state of $\overline{D}^0$ respectively..

TABLE B.9: Total Systematic Uncertainty of $B^0 \to D^*\rho$ (π^0 added) mode using $M_{\rm bc}$ fitting method.

Bin No.	p range [GeV]	$\varepsilon_{Data}/\varepsilon_{MC}$
1	[0.05-0.12]	$(0.99 \pm 0.06(stat))^{+0.02}_{-0.01}$
2	[0.12-0.16]	$(1.07 \pm 0.06(stat))^{+0.02}_{-0.01}$
3	[0.16-0.20]	$(0.98 \pm 0.06(stat))^{+0.03}_{-0.02}$
4	[0.20-0.32]	$(1.00 \pm 0.06(stat))^{+0.02}_{-0.01}$

TABLE B.10: Total Systematic Uncertainty of $B^0 \to D^*\rho$ (k_s^0 added) mode using $M_{\rm bc}$ fitting method.

Bin No.	p range [GeV]	$\varepsilon_{Data}/\varepsilon_{MC}$
1	[0.05-0.12]	$(1.01 \pm 0.06(stat))^{+0.02}_{-0.04}$
2	[0.12-0.16]	$(1.11 \pm 0.06(stat))^{+0.01}_{-0.02}$
3	[0.16-0.20]	$(0.99 \pm 0.06(stat))^{+0.03}_{-0.02}$
4	[0.20-0.32]	$(1.00 \pm 0.06(stat))^{+0.01}_{-0.02}$

Bibliography

[1] N. Cabibbo, Phys. Rev. Lett. **10**, 531 (1963).

[2] M. Kobayashi, T. Maskawa, Prog. of Theor. Phys. **49**, 2, 1973, 652–657.

[3] R.L. Workman *et al.* (Particle Data Group), Prog. Theor. Exp. Phys. **2022**, 083C01 (2022).

[4] S. Lola and G. G. Ross, Phys. Lett. B **314**, 336 (1993); N.Polonsky, arXiv:hep-ph/0108236v1; H. E. Haber in Ref. [4].

[5] J. C. Pati and A. Salam, Phys. Rev. D **8**, 1240 (1973); H.Georgi and S. L. Glashow, Phys. Rev. Lett. **32**, 438 (1974); S. Raby, arXiv:hep-ph/0608183v1; R. N. Mohapatra and R. E. Marshak, Phys. Lett. **91B**, 222 (1980).

[6] K. Biswal, L. Maharana, and S. P. Misra, Phys. Rev. D **25**, 266 (1982).

[7] G. Lazarides, C. Pangiotakopoulos, and Q. Shafi, Nucl.Phys. **B278**, 657 (1986); C. Schmidhuber, arXiv:hep-th/0207203.

[8] "The Gaia Project – technique, performance and status". Astronomische Nachrichten. **329**, (9–10): 875–880. arXiv:0811.2345.

[9] S. L. Glashow, D. Guadagnoli, and K. Lane Phys. Rev. Lett. **114**, 091801 (2015).

[10] N. Košnik, arXiv:2002.01041.

[11] P. Langacker, Rev. Mod. Phys. **81**, 1199 (2009).

[12] R. Aaij *et al.*, (LHCb collaboration), Phys. Rev. Lett. **115**, 111803 (2015).

[13] W. Altmannshofer, P. Stangl, and D. M. Straub, Phys. Rev. D **96**, 055008 (2017).

[14] B. Capdevila, A. Crivellin, S. Descotes-Genon, J. Matias, and J. Virto, J. High Energy Phys. **093**, 01 (2018).

[15] T. Hurth, F. Mahmoudi, D. Martínez Santos, and S. Neshatpour, Phys. Rev. D **96**, 095034 (2017).

[16] G. D'Amico, M. Nardecchia, P. Panci, F. Sannino, A. Strumia, R. Torre, and A. Urbano, J. High Energy Phys. **09**, 010 (2017).

[17] L.-S. Geng, B. Grinstein, S. Jäger, J. M. Camalich, X.-L. Ren, and R.-X. Shi, Towards the discovery of new physics with lepton-universality ratios of $b \to s\ell\ell$ decays, Phys. Rev. D **96**, 093006 (2017).

[18] M. Ciuchini, A. M. Coutinho, M. Fedele, E. Franco, A. Paul, L. Silvestrini, and M. Valli, On flavourful easter eggs for new physics hunger and lepton flavour universality violation, Eur. Phys. J. C **77**, 688 (2017).

[19] R. Aaij *et al.*, (LHCb collaboration), Int. J. Mod. Phys. **A30**, 1530022 (2015).

[20] R. Aaij *et al.*, (LHCb collaboration), JINST **9**, P09007 (2014).

[21] T. Abe et al. (Belle II Collaboration), arXiv:1011.0352.

[22] A. Abada, M. Abbrescia, S. AbdusSalam, *et al.*, Eur. Phys. J. Spec. Top. **228**, 1109–1382 (2019).

[23] The Future Circular Collider. arXiv:2203.06520.

[24] H. Georgi and S. L. Glashow, Phys. Rev. Lett. **32**, 438 (1974).

[25] R.L. Workman *et al.* (Particle Data Group), Prog. Theor. Exp. Phys. **2022**, 083C01 (2022).

[26] W. Buchm¨uller, R. R¨uckl, and D. Wyler, Phys. Lett. B **191**, 442 (1987).

[27] Y. Amhis et al., [HFLAV Collaboration], Eur. Phys. J. C. **77**, 895 (2017), updated results and plots available at https://hflav.web.cern.ch/.

[28] A. T. Fienberg, P. Alonzi, A. Anastasi, R. Bjorkquist, D. Cauz *et al.*, Nucl. Instrum. Methods Phys. Res., Sect. A **783**, 12 (2015).

[29] K. S. Khaw, M. Bartolini, H. Binney, R. Bjorkquist, A. Chapelain *et al.*, (Muon g - 2 Collaboration), Nucl. Instrum. Methods Phys. Res., Sect. A **945**, 162558 (2019).

[30] J. Kaspar, A. T. Fienberg, D. W. Hertzog, M. A. Huehn, P. Kammel *et al.*, JINST **12**, P01009 (2017).

[31] E. Gibney, Nature. **544**, 7649, 145-146, (2017).

[32] T. Endoh, T. Morozumi, A. Purwanto, Phys. Lett. B **515**, 111 (2001).

[33] K. Cheung, Phys. Rev. D **64**, 033001 (2001).

[34] P. F. Pérez and M. B. Wise, Phys. Rev. D **88**, 057703, (2010).

[35] J. M. Feller *et al.*, IEEE Transactions on Nuclear Science, **25**, 1, 304-308, 1978.

[36] R. Aaij, *et al.*, (LHCb collaboration), Phys. Rev. Lett. **131**, 079901, (2023).

[37] D. J. Gross and F. Wilczek, Phys. Rev. Lett. **30**, 1343 (1973).

[38] T. Nakano and K. Nishijima, Prog. of Theor. Phys., **10**, 581–582 (1953).

[39] J. Heitger, F. Joswig, and Kuberski, J. High Energ. Phys. **288**, 101007 (2021).

[40] S. Prelovsek, https://doi.org/10.48550/arXiv.1310.4354.

[41] C. Ratti, *et al.*, Nuclear Physics A, Volumes 904–905, Pages 869c-872c, (2013).

[42] R. C. Verma, J. Phys. G: Nucl. Part. Phys. **39**, 025005 2012.

[43] J. Laiho, R. Van de Water and E. Lunghi, Phys. Rev. D **81**, 034503 (2009).

[44] G. Lazarides, C. Pangiotakopoulos, and Q. Shafi, Nucl. Phys. B **278** 657 (1986); C. Schmidhuber, arXiv:hep-th/0207203.

[45] J. D. Barrow, M. S. Turner, Nature Physics. **291** (5815), 469–472, 1981.

[46] A. Davidson, Phys. Rev. D **20**, 776 (1979).

[47] Jonathan M. Arnold, Pavel Fileviez Pérez, Bartosz Fornal, and Sogee Spinner, Phys. Rev. D **85**, 115024 (2012).

[48] A. D. Sakharov JETP Lett.-USSR **5**, 24 (1967).

[61] W. S. Hou, M. Nagashima, and A. Soddu, Phys. Rev. D **72**, 095001 (2005).

[62] P. Rubin et al. (CLEO Collaboration), Phys. Rev. D **79**, 097101 (2009).

[63] R. Arnowitt and P. Nath, Phys. Rev. Lett. **62**, 2225 (1989).

[64] R. Barbier et al., Phys. Rep. **420**, 1 (2005).

[65] R. Godang et al. (CLEO Collaboration), Phys. Rev. D **59**, 091303 (1999).

[66] M. E. McCracken et al. (CLAS Collaboration), Phys. Rev. D **92**, 072002 (2015).

[67] P. del Amo Sanzhez et al. (BABAR Collaboration), Phys.Rev. D **83**, 091101 (2011).

[68] M. Artuso et al., Nucl. Instrum. Methods Phys. Res., Sect. A **502**, 91 (2003); D. Peterson et al., Nucl. Instrum. Methods Phys. Res., Sect. A **478**, 142 (2002).

[69] M. Ablikim et al. (BESIII Collaboration), Nucl. Instrum. Methods Phys. Res., Sect. A **614**, 345 (2010).

[70] S. Kurokawa, E. Kikutani, Nucl. Instrum. Meth. A 499, 1 (2003), DOI: 10.1016/S0168-9002(02)01771-0.

[71] T. Abe *et al.*, PTEP 2013, 03A001 (2013). doi:10.1093/ptep/pts102.

[72] A. J. Bevan *et al.*, [BaBar and Belle Collaborations], Eur. Phys. J. C 74 (2014) 3026 doi:10.1140/epjc/s10052-014-3026-9 [arXiv:1406.6311[hep-ex]].

[73] J. Brodzicka *et al.*, [Belle Collaboration], PTEP 2012, 04D001 (2012) doi:10.1093/ptep/pts072 [arXiv:1212.5342 [hep-ex]].

[74] K. Kanazawa *et al.*, Nucl. Instrum. Meth. A 499, 75 (2003).

[75] T. Abe *et al.*, Conf. Proc. C 070625, 27 (2007) [arXiv:0706.3248 [physics.ins-det]].

[76] U. Tamponi, https://belle.kek.jp/belle/theses/doctor/2015/Tamponi2015.pdf

[77] A. Abashian *et al.*, (The Belle Collaboration), Nucl. Instrum. Meth. A **479**, 117 (2002). doi:10.1016/S0168-9002(01)02013-7

[78] G. Alimonti *et al.*, (The Belle Collaboration), Nucl. Instrum. Methods Phys. Res., Sect. A 453 (2000), 71.

[79] Y. Ushiroda Nucl. Instrum. Meth. A **511** (2003), 6.

[80] H. Hirano et al., Nucl. Instr. Meth. A **455**, (2000) 294;

[81] S. Uno *et al.*, Nucl. Instrum. Meth. A **330**, (1993), 55.

[82] T. Iijima *et al.*, Nucl. Instrum. Methods Phys. Res., Sect. A **453**, (2000), 321.

[83] I. Adachi *et al.*, Nucl. Instrum. Meth. A **335**, (1995), 390.

[84] T. Iijima *et al.*, Nucl. Instrum. Meth. A **453**, (2000), 321.

[85] H. Kichimi *et al.*, Nucl. Instrum. Meth. A **453**, (2000), 315.

[86] H. Ikeda *et al.*, Nucl. Instrum. Meth. A **441**, (2000), 401.

[87] M.Z. Wang *et al.*, Nucl. Instr. Meth. A **455**, (2000), 319.

[88] K. Hanagaki *et al.*, Nucl. Instrum. Meth. A **485**, (2002), 490.

[89] A. Abashian *et al.*, Nucl. Instrum. Meth. A **449**, (2000), 112.

[90] R. Akhmetshin *et al.*, Nucl. Instr. Meth. Phys. Res. Sect. A 455 (2000) 324.

[91] S. Bahinipati, https://belle.kek.jp/belle/theses/doctor/2008/Bahinipati.pdf.

[92] P. Rubin *et al.*, (CLEO Collaboration), Phys. Rev. D 79, 097101.

[93] M. Ablikim *et al.*, (BESIII Collaboration), Phys. Rev. D 105, 032006.

[94] D. J. Lange, Nucl. Instrum. Methods Phys. Res., Sect. A **462**, 152 (2001).

[95] T. Sjöstrand, S. Mrenna and P.Z. Skands, Comput. Phys. Commun. **178** 852 (2008).

[96] E. Barberio and Z. Was, Comput. Phys. Commun. **79**, 291 (1994); P. Golonka and Z. Was, Eur. Phys. J. C **45**, 97 (2006); **50**, 53 (2007).

[97] R. Brun *et al.*, GEANT 3.21, CERN Report DD/EE/84-1 (1984).

[98] R. Itoh, Internal Belle Note 161.

[99] G. Punzi, PHYSTAT2003, SLAC Sep. 8-11, 2003.

[100] T. Junk, Nucl. Instrum. Methods Phys. Res., Sect. A **434**, 435 (1999).

[103] K. Akai, K. Furukawa and H. Koiso, Nucl. Instrum. Meth. A **907**, (2018) 188.

[104] N. Toge *et al.*, KEKB B-factory design report KEK Report 95-7 (1995). S. Kurokawa and E. Kikutanu, Nucl. Instrum. and Meth. A 499 (2003), 1.

[105] Belle II collaboration, Belle II technical design report, 1011.0352.

[106] LHCb collaboration, Technical Proposal, CERN-LHCC-98-004, http://cdsweb.cern.ch/record/622031.

[107] J. Kemmer, E. Belau, U. Prechtel, W. Welser and G. Lutz, Nucl. Instrum. Meth. A **253**, (1987) 378.

[108] Belle II collaboration, Phys. Rev. Lett. **127**, (2021) 211801 [2108.03216].

[109] M. French *et al.*, Nucl. Instrum. Meth. Phys. Res. A **466**, 359 (2001).

[110] Christoph Schwanda **et al.**, In: PoS Vertex2019 (2020), p. 014. doi: 10.22323/1.373.0014 (cit. on p. 26).

[111] K. Adamczyk *et al.*, In: (Jan. 2022). arXiv: 2201.09824 [physics.ins-det] (cit. on p. 26).

[112] "Letter of intent for KEK Super *B* Factory". In: (June 2004). Ed. by S. Hashimoto et al. (cit. on p. 27).

[113] K. Inami, Nucl. Instrum. Meth. Phys. A **595**, 1 (2008).

[114] T. Iijima *et al.*, Nucl. Instrum. Meth. Phys. A **548**, 3 (2005).

[115] Kodai Matsuoka *et al.*, "Performance of the MCP-PMT for the Belle II TOP counter". In: PoS PhotoDet2015 (2016), p. 028. doi: 10.22323/1.252.0028 (cit. on p. 29).

[116] K. Miyabayashi, Nucl. Instrum. Meth. Phys. Res. A **494**, 298 (2002).

[117] Y. Makida *et al.*, Adv.Cryog.Eng. **43**, (1998) 221-228.

[118] J. P. Lees *et al.*, (BABAR Collaboration) Phys. Rev. Lett. **109**, 101802 (2012); Phys.Rev.D **88**, 072012 (2013).

[119] A. Abdesselam *et. al.*, (Belle Collaboration), arXiv:1904.08794.

[120] R. Aaij *et al.*, (LHCb Collaboration), Phys. Rev. Lett. **115**, 111803 (2015); Erratum Phys. Rev. Lett. **115**, 159901 (2015).

[121] F. Abudinén *et al.*, (The Belle II Collaboration), Phys. Rev. Lett. **130**, 071802 (2023).

[122] F. Abudinén *et al.*, (The Belle II Collaboration), Phys. Rev. D **107**, L031103 (2023).

[123] F. Abudinén *et al.*, (The Belle II Collaboration), Phys. Rev. Lett. 127, 211801 (2021).

[124] T. Aushev, Belle Note 480.

[125] B. Bhuyan, Belle Note 1165.

[126] C. Cecchi *et al.*, BELLE2-NOTE-PH-2019-

[127] P. A. Zyla *et al.*, (Particle Data Group), Prog. Theor. Exp. Phys. **207**, 083C01 (2020).

[101] M.C. Chang "Observation of B deays to $J/\psi\eta$, Internal Belle Note 884.

[102] S. Ryu *et al.*, (Belle Collaboration), Phys. Rev. D **89**, (2014) 072009, arXiv:hep-ex/1402.5213.

[51] J. Schechter and J. W. F. Valle, Phys. Rev. D **25**, 2951 (1982).

[52] P. Minkowski, Phys. Lett. 67B, **421** (1977).

[53] R. N. Mohapatra and G. Senjanovic, Phys. Rev. Lett. **44**, 912 (1980).

[54] M. Gell-Mann, P. Ramond, and R. Slansky, Supergravity Workshop Stony Brook, New York, September 27-28, 1979, Conf. Proc. C790927, **315** (1979), arXiv:1306.4669 [hep-th].

[55] S. Davidson, E. Nardi, and Y. Nir, Phys. Rept. **466**, 105 (2008), arXiv:0802.2962 [hep-ph].

[56] Z. Berezhiani and L. Bento, Phys. Rev. Lett. **96**, 081801 (2006), arXiv:hep-ph/0507031.

[57] B. Dutta, Y. Mimura, and R. N. Mohapatra, Phys. Rev. Lett. **96**, 061801 (2006), arXiv:hep-ph/0510291.

[58] K. S. Babu, R. N. Mohapatra, and S. Nasri, Phys. Rev. Lett. **97**, 131301 (2006), arXiv:hep-ph/0606144.

[59] K. S. Babu, P. S. Bhupal Dev, and R. N. Mohapatra, Phys. Rev. D **79**, 015017 (2009), arXiv:0811.3411 [hep-ph].

[60] M. Baldo-Ceolin *et al.*, Z. Phys. C **63**, 409 (1994).

[49] P. del Amo Sanchez *et al.*, (BABAR Collaboration) Phys. Rev. D **83**, 091101(R), 2011.

[50] R. Aaij *et al.*, (LHCb Collaboration) Phys. Rev. D **108**, 012021, 2023.